SHRP-A-682

Application of Acoustic Emission to Study the Cohesive and Adhesive Strength of Asphalt

W.V. Chang

Department of Chemical Engineering
University of Southern California

Strategic Highway Research Program
National Research Council
Washington, DC 1994

SHRP-A-682
Contract A-002B
Product No.: 1012

Program Manager: *Edward T. Harrigan*
Project Manager: *Jack Youtcheff*
Production Editor: *Marsha Barrett*
Program Area Secretary: *Juliet Narsiah*

February 1994

key words:
asphalt thin-film
asphaltic concrete
blister test
cavitation
compression test
contact angle measurements
mechanical properties
shear stress
strain rate
tensile strength
tension test
thermal scanning test

Strategic Highway Research Program
National Academy of Sciences
2101 Constitution Avenue N.W.
Washington, DC 20418

(202) 334-3774

425/NAP/294

Acknowledgments

The research described herein was supported by the Strategic Highway Research Program (SHRP). SHRP is a unit of the National Research Council that was authorized by section 128 of the Surface Transportation and Uniform Relocation Assistance Act of 1987.

Contents

List of Figures

List of Tables

Abstract

A combined acoustic emission/poker chip test was developed to measure the mechanical behavior of, and cavitation in, asphalt thin films. Combining results of the test with the appropriate stress analysis and fractography allows us to understand the controlling fracture mechanism of geometrically confined asphalt thin films. The test successfully differentiates different SHRP asphalts. The test provides a logical link among asphalt bulk rheological properties, microstructure in asphalt thin films, and performance properties of asphalt/aggregate mixtures. A laser contact angle goniometry technique and a modified blister test were developed to characterize, respectively, the asphalt surfaces and the adhesive strength between asphalt and aggregate surfaces.

Executive Summary

Asphalt is present in pavements in the form of thin films. The performance properties of asphaltic concretes are very much controlled by asphalt properties in thin films. The respectable rigidity and strength of asphaltic concretes depend on the bulk modulus, the viscoelastic behavior in shear and the cavitation resistibility in the asphalt phase, and the asphalt/aggregate interface. Because the asphalt thin film in a mix is confined by the neighboring aggregate particles, its apparent mechanical properties and its resistibility to cavitation differ from the properties of asphalt in bulk.

The objectives of this work are the following:

1. To develop novel performance-related tests for asphalt binders.
2. To elucidate mechanisms that control the rigidity, cohesive strength, and adhesive strength of geometrically confined asphalt thin films.
3. To develop quantitative acoustic emission (AE) techniques for microdamage detection and cumulative damage quantification.

By accomplishing the above objectives, we hope to provide rational bases for the highway community in its effort to improve binder selection and qualification procedures, asphalt mix preparation conditions, and pavement rehabilitation programs.

At the center of the experimental program is the poker chip test, which allows us to simulate the cohesive properties of the binder in asphalt concretes. A quantitative AE technique is employed to monitor the microfracture processes. Discussed are the effects of speciment thickness, aspect ratio, different preparation conditions, and test conditions. The use of a nonlinear elastic analysis of the poker chip test permits the evaluation of the stress state in the binder phase as a function of the geometric shape factor of the specimen, the Poisson's ratio of the material (which depends on the air content in asphalt), and the applied load. By combining information obtained from mechanical tests, AE analysis, fractography, and stress analysis, we attempt to elucidate mechanisms that control the mechanical behavior of asphalt.

A limited effort was directed toward the development of new techniques for characterizing the interfacial interactions and adhesive strength between asphalts and aggregates.

A simple test procedure based on laser contact angle goniometry was developed to characterize asphalt surfaces. AE technique was used to identify the critical pressure at which rapid debonding starts. The potential of this new test was demonstrated, and a nonlinear elastic analysis of the blister test was conducted.

The principal conclusions of this research are as follows:

1. The usefulness of the asphalt thin-film, poker chip test in simulating the stress state and the resultant cumulative damages in asphalt pavements has been established. The stiffness and the tensile strength as determined from the poker chip test are consistent with those of asphalt/aggregate mixtures.
2. Cavitation initiation and growth is the dominant mechanism that greatly affects the stiffness, fatigue behavior, low-temperature cracking resistance, and the tensile strength of asphalt thin films. Using the concept of caviation control, the thin-film tensile properties of AAK were shown to improve upon addition of a small amount of reclaimed rubber.
3. AE is a very sensitive and reliable technique for monitoring microdamage and healing processes in a poker chip specimen. The AE/poker chip test can successfully rank different asphalts.
4. Further research should be conducted in order to understand quantitatively the cavitation and healing kinetics as well as ways to control and mitigate cavitation. The successful conclusion of this research will provide a key link between fundamental chemical properties of binders and performance properties of asphalt concretes. The research will provide valuable guidelines for future performance related specifications procedures for binders and mixes, and will also assist in the formulation of rehabilitation procedures for distressed asphalt pavements.

Chapter 1

Introduction

1.1 Problem Definition

1.1.1 Asphaltic Concrete–A Complex Material

Asphaltic concrete has a highly complex structure. At the microstructure level, an asphalt paving mixture can be considered as a three-phase system, containing a high concentration of aggregates, up to 90% by volume, several percent of air and a small amount of asphalt binder. It may behave as a two-phase system if air is homogeneously dispersed as small, colloidal-size pockets in the asphalt phase. In addition to asphalt, the binder may also contain fines as well as a variety of other modifiers. Asphalt itself is a complex mixture consisting of many organic and inorganic compounds. The composition of asphalt varies with the source of the crude oil and the refining technology employed. The various compounds making up the asphalt will have different chemical affinities as well as different hardnesses. The result is a very complex morphological state, which may vary with the thermal and mechanical histories of the sample.

The potential economic benefits of improving asphalt pavement performance has long been recognized by highway agencies. Despite many years of research, costly and embarrassing failures continue to occur. Because of the complexity of the material, existing specifications, design methods, and construction techniques are mainly based on empiricism rather than fundamental scientific and engineering principles. It is not uncommon to hear complaints by highway engineers on the inferior performance of recent-year asphalt compared with that of the good old days. Many attribute these deteriorating properties to the removal of the "juicy stuff" during the refinery process. Although this may be the case, one can also partially attribute the poor performance to changing and often more severe traffic conditions. In any case, it is a futile debate if one cannot identify what constitutes the "juicy stuff." This requires an unequivocal definition of performance criteria, properties, and key structural variables and a clear understanding of the interplays between them.

A perennial challenge to asphalt scientists and engineers is to relate the performance properties of asphalt paving mixtures to the fundamental structure of asphalt. Although properties of asphalt paving mixtures should ultimately depend on the chemical structure and composition of its ingredients, this dependence is not likely unique and straightforward. Highway engineers who are directly responsible for design and selection of the best systems are most concerned with performance involving a length scale of a meter or larger. On the other hand, the molecular scale is in the order of nanometers. In between, there are many intermediate structures such as colloidal structure and microstructure, which are important in any attempt to relate the behavior of asphaltic concrete in a highway environment and the molecular composition of asphalt. A logical approach that gives proper perspective to the interrelations between the properties and structures of different scales is necessary. This requires balanced and properly ordered considerations from different scientific disciplines, such as surface chemistry, rheology, engineering analysis, testing, and pavement engineering. The problem is complex and the challenge is enormous. Successful solution of this problem depends on our ability to cut through the complex facade and identify the key variables.

1.1.2 Cavitation and Reynolds Dilatancy

Dry aggregate is a granular medium. As pointed out by O. Reynolds in 1885, granular media possess a singular fundamental property, which he called "dilatancy" because this property consists of a definite change in volume when the medium is subjected to a change of shape[1]. Based on geometrical consideration, Reynolds asserted that in a state of maximum density the volume of a granular material increases with shear deformation. Recently, Goddard presented a new interpretation of Reynolds dilatancy based on the modern theory of internally constrained continua[2]. He provided an elegant discussion of the coupling of the shear work and the volume work. His theory helps to rationalize some difficult-to-accept experimental facts, such as the shear-induced volume dilatation in a granular medium even when the mean stress in the medium is negative[3].

Without asphalt, mineral aggregate is a noncoherent, loose mass. After addition of a small amount of asphalt and compaction, the mix shows respectable rigidity on the order of one hundred thousand to one million psi and strength. Where does this change come from? It is unlikely that it can be directly attributed to the shear viscosity of asphalt, which, although high, cannot nearly account for the magnitude of the change. Since the volume of the aggregate in a mix is close to its maximum packing, volume dilatation must accompany any deformation. Indeed, this is what has been observed in asphaltic concretes, even when they are subjected to a stress state where the pressure component is as high as four atmospheres[4]. Compared with asphalt, aggregate is much more rigid, and hence the necessary volume change must come from either the asphalt phase or the asphalt-aggregate interface or the air phase, if indeed there is a recognizable one. In other words, the *enhanced rigidity and strength must depend on the bulk modulus and the cavitation resistibility in the asphalt phase and the asphalt-aggregate interface.* We achieve this understanding in part because of our experience with cavitation and debonding in highly filled elastomers[5-12].

1.1.3 Asphalt Thin-Film Properties–A Key Link Between Performance and Fundamentals

It is usual to correlate the usefulness of an asphalt as a binder with its properties in mass, such as viscosity or penetration and ductility. However, as pointed out by Mack 34 years ago, asphalt is present in pavements in the form of thin films, and the apparent properties of asphalts in thin film may differ significantly from their properties in mass[13]. The difference may be due to one or more combinations of the following factors: confinement of asphalt imposed by the aggregate, thermal stress, void content, or colloidal structure and molecular orientation. Compared to other means for evaluating asphalt properties, relatively few studies have been directed at evaluating tensile properties of asphalt thin films.

Cavitation in tensile loaded asphalt thin films was observed as early as 1911 by Budgett[14] and later by Kumler[15]. Most of the research on tensile behavior and fracture characteristics of asphalt thin films were carried out between the late 1950s and the late 1960s[16-22]. Mack, in his pioneering work on the physical behavior, first reported the strong dependence of tensile strength on the thickness of asphalt thin films[13]. This observation was later confirmed by others[17-22]. He reported that as the thickness of asphalt thin film decreases, its failure mode changes from flow to uniform, solid-like fracture and to cavitation. He demonstrated the existence of a correlation between the film strength and the bearing strength of sand-asphalt mixtures. He also proposed a theoretical model based on the Lennard-Jones equation for binary intermolecular interactions. Herrin's research group[18,19] conducted a very extensive experiment program on the effects of thickness, temperature, and deformation rate. In the thick-film region, he interpreted his results in terms of the prediction of the Stefan equation, which relates the force required to separate a Newtonian fluid thin film between two parallel rigid plates at different separation rates. In the thin-film region, which he termed "the brittle fracture region," he adopted Mack's model. Majidzadeh's technique was adopted by Marek to study the effects of asphalt consistency and source of the asphalt material[19,22]. Sisko[21] studied the effect of aging on the film strength.

Through the cumulative efforts of the previous researchers, it is fair to say that we have acquired significant empirical information and a good qualitative understanding of different microstructural processes. However, we feel that the importance of the cavitation process on a number of thin-film physical behaviors, other than just the tensile strength, has not been fully appreciated. Important issues need to be addressed such as: where the cavitation occurs, when it occurs, how it grows, ways in which it affects the rigidity of the specimen, and whether or not it heals and, if so, how to promote healing. I believe that the answers to these questions have important practical applications to the highway community. Therefore, in this research we have attempted to record accurate and complete histories of stress, strain, and temperature of a given specimen. The thin-film mechanical behavior can be related to the rheological behavior of the asphalt with the help of micromechanical analysis. It is important to exhaust all the microstructural causes before embarking on any molecular-level explanations. An innovative acoustic emission (AE) technique was used to monitor cavitation initiation and spreading, which was shown to be promising in our earlier research on elastomers[5–8].

1.2 Purpose

The objectives of this work are as follows:

1. To develop novel contractor performance-related tests for asphalt binders in support of the A002A.
2. To elucidate mechanisms that control the rigidity, cohesive strength, and adhesive strength of geometrically confined asphalt thin films.
3. To develop quantitative AE techniques for microdamage detection and cumulative damage quantification.

By accomplishing the above objectives, we hope to provide rational bases for the highway community in its effort to improve binder selection and qualification procedures, asphalt mix preparation conditions, and pavement rehabilitation programs.

1.3 Research Approach

The previous discussion on the logical connection between pavement distressed modes, asphalt mix composition and asphalt thin-film properties are summarized in Figure 1.1. In order to elucidate the mechanisms of microprocesses in materials as rheologically complex as asphalts, many probes are needed to monitor the material. Therefore, quantitative AE techniques have been integrated with such supplementary tasks as mechanical testing, stress analysis, deformation profile monitoring, fractography, and surface property study. The research approach is summarized in Figure 1.2. At the center of the experiment program are two tests: (1) the poker chip test, which permits the simulation of the cohesive properties of the binder in asphalt concretes; and (2) the blister test, which determines the adhesive strength between asphalt and aggregate phases. The charge was not to measure many asphalt systems, but to understand the fundamental mechanisms by conducting carefully integrated experiments on selected asphalts.

1.4 Organization

Chapter 2 presents mechanical properties of confined asphalt thin films as measured by the poker chip test. Our objective is to elucidate mechanisms of plastic deformation, microdamage, and fracture in thin films. Discussed are the effects of specimen thickness, aspect ratio, different preparation conditions, and test conditions. Chapter 3 presents results of acoustic emission analysis of the poker chip test. By combining information obtained from mechanical tests, AE analysis, fractography and stress analysis, we conclude that cavitation is one of the most important mechanisms for controlling the mechanical behavior of asphalt. Chapter 4 proposes a new test, thermal mechanical scan, for a quick evaluation of asphalt binders' thermal cracking resistance. Using the concept of cavitation control, we demonstrate that thin-film thermal cracking properties of AAG can be improved by addition of a small amount of reclaimed rubber. Chapter 5 demonstrates the utility of acoustic emission in monitoring damage in asphalt concretes. Chapter 6 shows a simple, innovative test for characterizing asphalt surfaces, using laser contact angle goniometry. Chapter 7 discusses a modified blister test for the characterization of adhesive strength of asphalt/aggregate systems. Chapters 8 and 9 present finite element calculations of nonlinear elastic analyses for poker chip and blister tests, respectively. Although asphalt is a nonlinear viscoelastic material, our elastic analysis provides useful clues for understanding micro-mechanical processes in the two tests. Chapter 10 summarizes key conclusions and recommendations of this research.

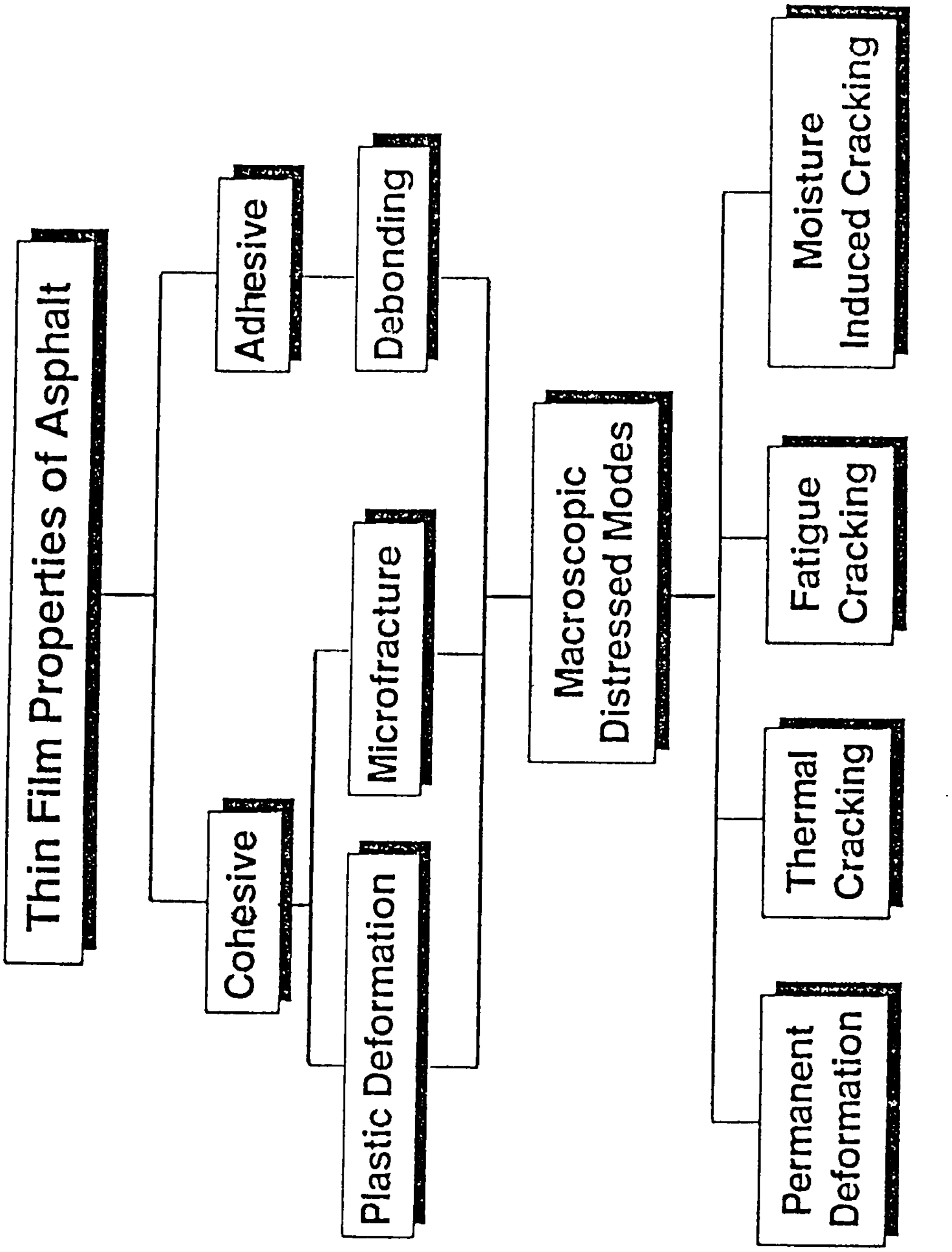

Figure 1.1: Thin film properties of asphalt.

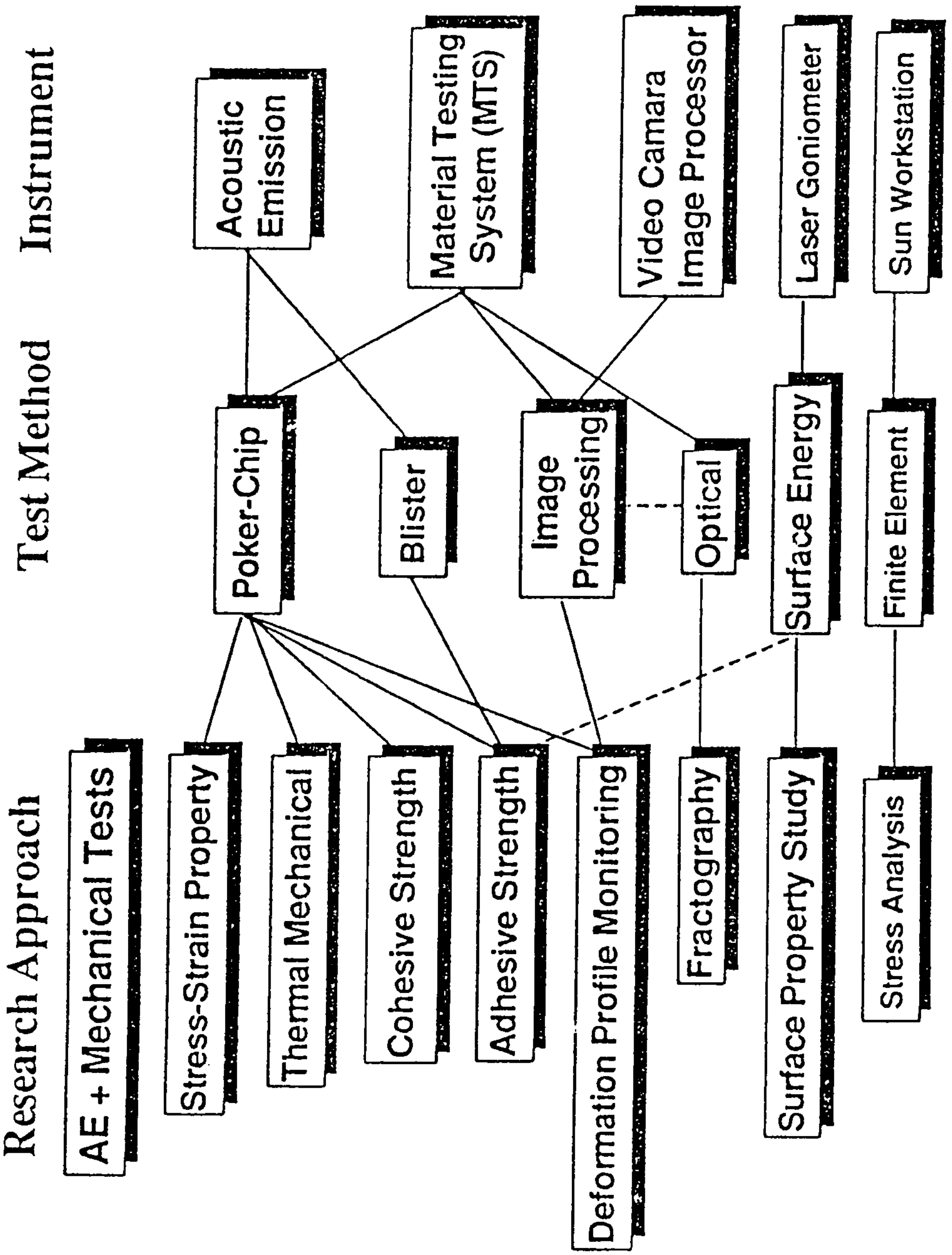

Figure 1.2: Research approach, test methods and instrumentation used

References

1. O. Reynolds, *Philosophical Magazine* **20**, 469 (1885).
2. J. D. Goddard and Y. M. Bashir, Chapter 2 in *Recent Developments in Structured Continua*, eds. D. DeKee and P. N. Kaloni (Longman Scientific and Technical/J. Wiley, 1990).
3. X. Zhuang, Master's thesis, Department of Chemical Engineering, University of Southern California, May 1991.
4. C. A. Bell, Ph.D. thesis, Department of Civil Engineering, University of Nottingham, September 1978.
5. W.V. Chang, *Proceedings IUPAC 28th Macromol Symposium*, 545 (1982).
6. W. V. Chang, B. Wijayarathna and R. Salovey, *Advances in Chemistry Series* **206**, 233 (1984).
7. P. Kakavas and W. V. Chang, "Detection and Spectrum Analysis of Microcavitation in Bonded Elastomer Disc" (129th Rubber Division Meeting, ACS, New York, 1986).
8. P. Kakavas, Ph.D. thesis, Department of Chemical Engineering, University of Southern California, December 1987.
9. P. Kakavas and W.V. Chang, *Journal of Applied Polymer Science* **42**, 1997 (1991).
10. P. Kakavas and W.V. Chang, *Journal of Applied Polymer Science* **45**, 865 (1992).
11. R. L. Denecour and A. N. Gent, *Journal of Polymer Science* **A276**, 1853 (1968).
12. T. Shinomura and M. Takahashi, *Rubber Chemistry Technology* **43**, 1015 (1970).
13. C. Mack, *Industrial and Engineering Chemistry* **49**, 422 (1957).
14. H. M. Budgett, *Proceedings of the Royal Society (London)* **A86**, 25 (1911).
15. W. D. Kumler, *Journal of Physical Chemistry* **44**, 612 (1940).
16. P. R. Wood and H. C. Miller, *HRB Bulletin, National Research Council* **270**, 38 (1960).
17. K. Majidzadeh and M. Herrin, *Highway Research Report, Highway Research Board* **67**, 98 (1965).
18. C. R. Marek and M. Herrin, *AAPT* **37**, 386 (1968).

19. R. C. G. Haas, written discussion submitted to the Marek-Herrin paper.

20. A. W. Sisko, *Highway research Report, Highway Research Board* **231**, 62 (1968).

21. C. R. Marek, *Journal of Materials*, JMLSA **5**, 3 (1970).

Chapter 2

Mechanical Property Measurements of SHRP Asphalts

2.1 Introduction

The underpinning philosophy of this research is that the performance of asphaltic concretes depends on the asphalt thin film properties. Asphalt thin film properties may not be the same as asphalt bulk properties because of the following causes:

1. geometrical constraints, the effects of which can be explained in terms of micromechanical analysis and bulk rheological properties;
2. microfracture, which may exhibit different modes and different size from those in the bulk state;
3. preferential adsorption/absorption, which may alter the effective composition of asphalt thin film and/or lead to the formation of a weak boundary layer; and
4. molecular orientation of component molecules in asphalt at the asphalt-aggregate interface.

It is important to exhaust all the micromechanical explanations before resorting to any molecular-level explanations. In this chapter, experiments are conducted to investigate the micromechanical factors which control the mechanical properties of asphalt thin films. The relevant micromechanical analysis is given in Chapter 7.

2.2 Materials

Asphalts used in the experiments were obtained from two sources: the SHRP Material Research Laboratory (MRL) and the Los Angeles County Road Department. Included were core SHRP asphalts AAD-1, AAG-1, AAK-1, and AAM-1 and the two grades of California asphalts, an AR4000 and an AR8000. Characterization of asphalts used in the experiments are listed in Table 2.1.

2.3 Experimental

2.3.1 Specimen Preparation

Specimens used in the mechanical experiments have a poker chip geometry, (i.e., the asphalt cement is used to bind two rigid steel plates together). This specific geometry of the test specimen can simulate and adequately represent the processes of deformation and fracture of a highly filled asphalt system in the pavement.[1] When the Acoustic Emission (AE) measurement is involved, each steel plate has two holes for mounting the AE sensors.

The physical state of the asphalt cement and the geometry of the specimens necessitates the use of different preparation methods for asphalt specimens of different thickness. Table 2.2 summarizes the various methods used to prepare the test specimens. A set procedure was used in handling the core asphalt cement and preparing the steel plates for all experiments. Asphalts, obtained in standard 5-gal cans, are cooled by liquid nitrogen and cracked into small pieces, then transfered into smaller containers (5 oz). The asphalt is stored at room temperature for one week prior to use in experiments. This provided time for any water condensed on asphalt surfaces or embedded inside the asphalt upon warming to room temperature to evaporate out. This also minimizes the presence bubbles in asphalt, when it is heated to 180°F. The steel plates (of 20 mm thickness) are cleaned with kerosene and rinsed with pentane. A fine sandpaper is used to remove any rust present on the surface of the steel plates prior to cleaning with the solvents.

It should be mentioned that the method suggested by the MRL for handling the asphalt cement is modified in this laboratory. The MRL method requires heating the asphalt in the 5-gal can to the melting point. Since only a fraction of the 5 gallons was used each time specimens were prepared, only the required quantity of asphalt in the 5-oz container was heated to the melting point. Had the MRL procedure been strictly followed, the unused asphalt would be heated again to high temperature when preparing future poker chip specimens. We are afraid that some volatile compounds in asphalt will be lost during multiple heating processes.

Details on each individual method are given below.

Method 1: Casting. This method was used to prepare thicker specimens (thickness $\geq$ 5 mm). To make an asphalt/steel poker chip specimen, two pieces of steel plates are used as grips. Other equipment requirements include an oven, a vacuum pump, a steel funnel and an aluminum hoop.

The steel plate is 15.24 cm (6 in.) in diameter and 2 cm (0.8 in.) in thickness. A threaded hole with thread size of 1/14" and depth of 1 cm (0.4 in.) is located on the center of one side of the plate. It is used to mount the plates on the loading rods of the Material Testing System (MTS) machine. The environment chamber that covers a wide range of temperature (-100°F to +600°F) is used as an oven to prepare the test piece. The hoop made from shell aluminum is designed specifically for molding asphalt. There are two holes on the hoop. The bigger one, with its diameter being the specimen thickness and fitting the outlet of a steel funnel, serves as an inlet for pouring hot asphalt. The smaller one (5 mm in diameter) serves as a vent for vacuuming during the molding process. Two pairs of bolts and nuts at the ends of the hoop are tightened together against the lateral surfaces to two steel plates. Sufficient frictional force has to be generated to maintain a constant separation between the two plates during molding and mounting of the specimen. To facilitate the removal of the hoop from the specimen after it has been molded and to avoid damaging the edge of the asphalt specimen during removal of the hoop, aluminum foil is used to cover the inside surface of the hoop. A dry lubricant, such as GW-3, may be sprayed gently on the foil if necessary. Hoops with different widths and hole sizes have been made to mold specimens of different thicknesses. Basically, the procedure for preparing thick asphalt, steel poker chip specimens is as follows:

- Mount the steel grips (plates) on the extension rods of the MTS machine. Adjust the distance between the two plates to the desired specimen thickness by means of displacement control.

- Apply the hoop around the steel plates and tighten it using the bolt-nut pairs. This forms a grip unit, the two plates are separated with the desired specimen thickness and hooped together.

- Put the asphalt and the grip unit in the environment chamber at 290°F for at least 20 min. Then attach the grip unit vertically to a laboratory table. Apply vacuum to the inside of the unit from the small hole and pour in hot asphalt through the bigger hole with a steel funnel.

- Seal the vent and inlet holes once the grip unit is completely filled with asphalt. Let the specimen cool down under ambient condition for at least 3 hr prior to use.

The preparation of special specimens (e.g., air bubbled and vacuumed) follows the same procedure as above, except that air bubbles are mixed into the cement by stirring the asphalt melt before pouring into the grip unit, and vacuumed cement is obtained by putting a certain amount of asphalt in vacuum (760 mmHg) at 65°C for 2.5 hrs so that no visible bubbles are exuded from the asphalt cement.

Method 2: Compression with Spacer Control. In specimen preparation with the *compression* method, the precompression procedure is fixed for all the specimens. Asphalt and the two steel plates are heated in the environmental chamber to a temperature of 185°F and kept at this temperature for about 2 hr. The asphalt is then poured carefully onto the lower grip plate, and the whole system is cooled to ambient conditions by keeping the door of the environmental chamber open. Once the desired temperature is reached, the compression process is initiated.

For specimens with thickness less than 2 mm and larger than 120 μm, the thickness is controlled by four small steel spacers. In order to study the effect of compression pressure in the preparation stage on the final properties of the poker chip specimen, two pressures are used: 3.4 and 9 psi. The pressure is increased linearly from zero to the final value in 30 min. During compression, the poker chip specimen is cooled by natural convection. The temperature at which asphalt cement is compressed is about 5°F higher than the softening point of the specific asphalt (120-130°F). The compression period is about 2 hr.

Method 3: Compression with Extensometer Control. For thin specimens, thinner than 120 μm, it is very difficult to control the thickness with spacers. Instead, the following procedure is followed. First, the specimen is prepared as above in method 2, except that very low pressure is used to bring the two plates containing 120 μm together. Axial extensometers are then mounted on the edges of the two grip plates. Following this, the spacers are removed and the desired pressure is applied and kept constant. The specimen is cooled to room temperature while being compressed continuously with the control of the extensometer, until the desired thickness is reached. Figure 2.1 shows the thickness change and the temperature history for asphalt AAK specimen in preparation after the spacers are removed. The loading system used to prepare the thin poker chip specimens has a preloading clamp. During the compression process, the clamp is removed, so that, once a specimen reaches the desired thickness, the pressure can be immediately released.

Specimens for Studying Effect of Preparation Conditions. Based on the knowledge that the preparation conditions may have significant influences on the mechanical behavior of asphalts in poker chip tests, we designed a series of tests to investigate the effects of preparation conditions associated with method 2 and method 3 described above. A detailed description of the procedure and conditions is given in Section 2.4.3.

2.3.2 Experimental Variables

Asphalt binders in pavements are subjected to complex stress fields. The triaxial tension test of a poker chip specimen of asphalt simulates the pavement environment. The rheological behavior of asphalts under tensile stress is affected by many factors, including the rate of loading, temperature, and thickness of the specimen. In our tests, we find that not only the previous three factors but also the condition for preparation of the specimen and *conditioning time* during which asphalt stabilizes at a certain temperature once a poker chip specimen is prepared can significantly affect the mechanical behavior of the material. Consequently, they are all included as testing variables which are summarized in Table 2.3.

2.3.3 Mechanical Test

Two types of test, axial tension and compression, were performed on asphalt poker chip specimens to determine the mechanical and rheological behavior of asphalts. Because asphalt has a low thermal conductivity, each specimen is placed on the loading system (free of mechanical force) and maintained at the test temperature for at least three hours before testing to ensure temperature equilibrium. The AE measurement was involved in many mechanical tests for evaluating the cohesive and adhesive behavior and the occurrence of cavitation.

The primary output of the mechanical tests are load, stroke displacement, and local strain measured with extensometer as functions of time. From these outputs, we can obtain the apparent modulus, the tensile strength and strain, the yield behavior, and the failure behavior of asphalt binder in the poker chip geometry. These main mechanical parameters provide information that can be used to relate the poker chip specimen of asphalt to that of the mixture containing asphalt and aggregate. The parameters are defined as follows:

- Nominal stress, σ_{nom}, is simply the applied force, F, divided by the undeformed cross section area, $A = \pi R^2$, of the specimen. $\sigma_{nom} = F/A$.
- Nominal strain, ϵ_{nom}, is the total displacement, Δh, divided by the initial thickness, h_o, of a specimen. $\epsilon_{nom} = \Delta h / h_o$.
- Apparent stiffness modulus of a poker chip specimen, E_s^{app} is defined as the ratio of nominal stress and nominal strain, $E_s^{app} = \sigma_{nom}/\epsilon_{nom}$.
- Tensile strength is the stress value at which the specimen is broken.

The healing behavior of asphalt was also investigated via mechanical testing. The apparent moduli and the yield behavior were compared, although the AE accumulated energy is a better INDEX for evaluating the healing behavior of asphalt cement (Chapter 3).

All mechanical tests were conducted on the MTS 710 machine. The machine is equipped with load, stroke, and extensometer controls; a multifunction generator; a load frame and an environmental chamber (Figure 2.2). The loading system for a specimen consists of stainless steel extension rods, thread rods, nuts, and clamps. Shown in Figure 2.3 (a) are two loading systems used in the experiments. System A is connected through the coupling nut, and system B through a preloading clamp. The clamp makes it easy to mount the specimen and disassemble the system.

Compliance of the Loading System. When the specimens are thin, their apparent moduli are very high. In our tests, the apparent modulus of an asphalt poker chip specimen was as high as 10^5 psi and only two orders of magnitude less than the Young's modulus ($\sim 3 \times 10^7$ psi) of stainless steel, when the thickness is as thin as 250 μm. Furthermore, if the diameter of the specimen is 15.24 cm and the loading system A in Figure 2.3 (a) is 100 cm long and 4.445 cm ($1\frac{3}{4}$ in.) in diameter, a displacement as long as 200 μm of the loading system could be induced for 1 μm of axial deformation of the asphalt film.

Measurement of Deformation and Apparent Stiffness. The measurement of deformation and initial stiffness of asphalt specimens, especially while the specimens are very thin is difficult for the following two reasons. First, the load-deformation curve for a thin film specimen is nonlinear due to the viscoelastic effect and cavitation in the asphalt thin film. Second, the compliance of the measuring system may not be negligible when the specimen stiffness is as high as mentioned in the paragraph above, and the readout from the stroke linear vertical differential transformer (LVDT) is no longer a good measure of the strain in the asphalt thin film. To measure the real asphalt displacement precisely, strain gages and two extensometers were employed. To implement the measurement, two Wheatstone bridges and three DC amplifiers with low-pass filters were built. The extensometer (MTS model 632.11B-20) was directly fixed on steel plates by rubber bands (Figure 2.3 (b)). It has been shown that there is no slip between its knife edges and the plates. The extensometer was calibrated by means of an improved micrometer (graduation 1 μm). With the signal amplification, it is able to give a resolution of 5 $\mu\epsilon$ (microstrain) of its 2.54 cm (1-in) gauge length. The strain gages were fixed across the two plates with the specified adhesive. But the practice of displacement measurements indicated that they are not suitable in the poker chip specimen system because of the alignment problem of the strain gauge on the edges of the plates.

2.4 Preliminary Tests on California Asphalts

Two batches of local California asphalts; AR4000 and AR8000, were used in our preliminary mechanical tests. All specimens used were of a 1-cm thickness and a 15.24-cm diameter. The purpose was to evaluate the feasibility of mechanical tests on our MTS system and to impartially measure the sensitivity of our tests in differentiating different types of asphalt materials.

The mechanical response of the poker chip speciment under uniaxial tension for both asphalts are shown in Figure 2.4. Both asphalts are strongly viscoelastic and show a well-defined yield point. The yield stress and yield strain increase with the strain rate. AR8000 is stiffer and has higher yield strength than AR4000 at the same temperature and deformation rate. For example, referring to Figure 2.4, AR8000 shows a nominal yield strength of 70 psi and yield strain of 4% when the nominal strain rate is 2.5%/sec, whereas AR4000 has an average yield strength of 48 psi and yield strain of 4%. However, AR4000 seems to be more rate sensitive. Its yield strength increases to 88 psi when the strain rate is 5%/sec, whereas for AR8000 yield strength is 97 psi.

In load-controlled tension tests, the hysteresis behavior of asphalts is very different from that of common polymer solids. Figure 2.5 shows the test result at room temperature. The load was gradually increased from zero to the desired value, for example 5% of full operating range (10 KIPS), at a constant rate (5 sec) and then decreased to zero at the same rate. As we can see, AR8000 asphalt shows a strong hysteresis even in the case of small maximum loading (18 psi) and slow loading rate (3.6 psi/sec). Hence, at room temperature (~ 82°F), the asphalt behaves more like a viscoelastic liquid.

Cyclic Deformation and Loading. Cyclic ramp was chosen as an input to simulate the behavior of asphalt under low rate deformation. The ramp period (up and down) we used was 10 sec. Figure 2.6 shows the cyclic mechanical response of AR8000 asphalt. In this test we applied different maximal strain, but kept the same ramp period. As we can see, the larger the deformation, the faster the deformation, and the earlier the yield point appears. However, the yield strain increases with the stroke rate. As is shown in Figure 2.6, the load time trace curves change very little from one cycle to another. It suggests that very little permanent damage has been incurred.

Deformation Rate Influence: Rates of deformation in tension tests significantly affect the yield stress of the 10 mm asphalt specimen. The result obtained from AR8000 oil asphalt is shown in Table 2.4, which presents the proportional relationship of the yield stress to the deformation rate. But the yield strain is less, affected by the rate of deformation. For example, the yield strain increases from 4% to 4.5% whereas the rate of deformation varies from 15 mm/min to 30 mm/min for the 10 mm-thick poker chip specimen of AR8000 asphalt.

Temperature Influence: To evaluate the temperature effect on the mechanical response of asphalt, uniaxial tension and compression tests were conducted on AR8000 asphalt at 32°F and at room temperature (82°F). In tensile tests with a strain rate of 2.5%/sec, there was no distinct difference in the nature of stress–strain curves obtained at room temperature and 32°F, except that the California asphalt became very stiff and brittle at 32°F, and the specimen cracked prematurely. The failure was at the interface of asphalt and one of the steel plates. The surface of the asphalt was smooth. On the other hand at room temperature, tensile failure occurred in the asphalt phase. The fracture surface of asphalt was very rough. Contrary to the tensile tests, compression tests of AR8000 asphalt poker chip specimens, at room temperature and 32°F, behaved distinctly different in terms of stress–strain curves, as shown in Figure 2.7. At room temperature, AR8000's compression stiffness decreases with strain in the strain range tested and shows a large hysteresis. At 32°F, however, the asphalt's compression stiffness increases with strain, and the stress–strain curve indicates very little hysteresis, and the relation is almost linear, suggesting that the material is nearly Hookean.

2.5 Mechanical Measurements of SHRP Asphalts

2.5.1 Stress-Strain Characteristics and Observations of Failure

Like other viscoelastic materials, the stress-strain patterns of asphalts are time, strain, and temperature dependent. When asphalt is present as a thin film, the stress-strain curve is also thickness-dependent.[6,7] For all tensile tests conducted in our laboratory of asphalt poker chip specimens, the stress-strain curves shown in Figure 2.13 are typical. It is clear that the stiffness of asphalt before yield is very high. For example, the initial apparent stiffness of a 5-mm-thick specimen could be as high as 2.7×10^4 psi when evaluated at 0.15% of strain (2 sec) under specific test conditions. Once past the yield point, the load decreases rapidly with increasing strain. The asphalt becomes very soft and behaves much more like a viscoelastic liquid. This can be also seen from the very large hysteresis loops (Figure 2.14 and curves II and III in Figure 2.13).

Four distinct types of failure of asphalt cements have been observed in our mechanical tests as shown in Figure 2.8. They are classified into brittle, semibrittle (tenacious), semiflow, and flow failures. The mode of failure depends on many factors, such as specimen thickness, test temperature, loading rate, stabilization time, and control mode of test (load control/stroke control). Typical stress-strain curves corresponding to different failure modes are illustrated in Figure 2.13.

Brittle fracture is characterized by a complete and instantaneous separation of test specimens at the maximum stress and a near linear relation of stress and strain (curve I in Figure 2.13). It can occur in a thin specimen (e.g., 40 μm) or in a thick specimen (e.g., 5 mm). The fractured surface of brittle failure is, in most cases, well divided into two semicircular parts (Figure 2.8 (a)). In the case of a thick specimen, a very smooth fracture surface with few cavities is observed. In the case of a thin specimen, one-half part is filled by asphalt totally, and no cavitations are observed. The other half has most likely a "monolayer" of asphalt coated on the steel surface, and small cavities with outward tails may be observed.

Curve III in Figure 2.13 is related to the tenacious and the semiflow failures. The low initial stiffness of this curve indicates that the specimen was heavily damaged tue to previous loadings. Both failures are characterized by a gradual drop off in strength after the attainment of the maximum load value, more cavities than the brittle failure, and a well-ordered network (honeycomb pattern, Figure 2.8 (c)) made up of individual structural units (cells) on the surface of a broken specimen. But there are still some differences in fracture surfaces of specimens. Lower, flatter, and wider ridges form to separate irregular polygonal cavities in tenacious failure. More small cavities are observed in tenacious failures than in semiflow failures. Semiflow failure is also characterized by the formation of multiple asphalt threads and limited necking of asphalt. Under test conditions with thicker specimens, higher temperature, and lower deformation rate (stroke control), an asphalt poker chip specimen's behavior follows curve II in Figure 2.13, which corresponds to the so-called flow failure. This type of failure is mainly caused by a viscous flow of asphalt cement and is characterized by the beginning of inward flow, extreme necking, and large asphalt threads.

In brittle fracture and tenacious fracture of asphalt, it is observed that there exist both adhesive failure and cohesive failure. But only cohesive failure is observed in the other two types of failure.

2.5.2 Comparison of Different SHRP Asphalts

In this section, attention is focused on the responses of different SHRP asphalts at selected temperatures. SHRP asphalts are also characterized in the laboratory by using the thermal scanning test, which is reported in Chapter 4.

2.5.2.1 Uniaxial Tension

Uniaxial tension tests of asphalt poker chip specimens were conducted on five core SHRP asphalts AAA-1, AAD-1, AAG-1, AAK-1, and AAM-1 and over a range of specimen thickness from 35 μm to 10 mm. The testing temperatures used were 50° and 60°F; the effective loading rates studied were from 4.5 to 800 psi/sec. Because of the geometric constraints imposed by the rigid plates on the asphalt thin film, the initial stiffness* of the poker chip specimen is very high, at least 10^3 psi order of magnitude. The apparent initial stiffness is very sensitive to the aspect ratio of the specimen, as defined by the ratio of diameter to four times the thickness of the specimen. For a detailed theoretical analysis please refer to Chapter 8.

The MTS machine allows an input of constant stress rate or constant stroke (displacement) rate. Due to the high initial stiffness of the specimen and the thin film nature of the asphalt layer, the deformation due to the compliance of the loading system can be

---

*The initial apparent stiffness of asphalt in poker chip test is defined as $S_i(t_e) = \sigma(t_e)/\epsilon(t_e)$, where t_e is a evaluation time. In this report, $t_e = 0.5$ sec, unless mentioned otherwise.

significant (Section 2.2.3). The strain in the asphalt thin film cannot be directly read from the stroke movement of the MTS machine. Hence, a constant stroke rate input does not result in a constant strain rate in the asphalt thin film. For this reason, a constant loading rate input provides better control of the mechanical history of the specimen.

Yield Strength. Yield stress is the most reliable parameter that can be used to compare the strength of different asphalts. Asphalt poker chip specimens of 6-in. diameter and three thicknesses (0.5, 5, and 10 mm) are used for the comparison. It is done by grouping same-thickness specimens of different asphalts together and diverging them by plotting the yield stresses as functions of the apparent loading rate at the yield point. The result at 60°F is presented in Figure 2.9. The obvious rate dependence of yield strength, as shown in Figure 2.9 (a), is observed for 10-mm-thick specimens of AAA-1 and AAD-1 asphalts. From the figure, we can see that AAD-1 asphalt has higher yield points than AAA-1. For 5-mm-thick specimens (Figure 2.9 (b)), AAG-1 is much stronger than AAM-1, and AAK-1 has a little bit higher yield point than AAD-1, when evaluated at similar apparent loading rates. In comparing AAD-1, AAK-1, and AAM-1 (Figure 2.9 (c)), one can anticipate that both AAD-1 and AAK-1 will have yield strength values higher than AAM-1's, but lower than AAG-1's, by considering the rate effect for asphaltic materials. Large AAK-1 specimens of 0.5-mm thickness are mainly used to study the healing behavior of asphalts and to evaluate the reproducibility of mechanical tests. Regardless of the mechanical aging and other variables that may affect the yield behavior, the yield points, with stress values ranging from 75 to 185 psi, are obtained for 0.5-mm-thick AAK-1 specimens. However, when considering only the virgin specimens, an average value of 168 psi with a standard deviation of 7.6% is obtained. As in the case of 5-mm-thick specimens, this value is still lower than that (> 200 psi) of AAG-1 specimens of the same thickness (Figure 2.9 (d)). By examining Figure 2.9 overall, we can rank the five SHRP asphalts in the sequence of AAG-1 $>$ AAK-1 $>$ AAD-1 $>$ AAA-1 $\geq$ AAM-1 with respect to yield strength at 60°F.

Initial Apparent Stiffness. The toughest thing, perhaps, is to determine the initial apparent stiffness in our mechanical tests. The main difficulty is contributed by the great compliance of the loading system, as discussed earlier. With the assistance of extensometers, however, it is possible to calibrate the system compliance and to get the direct readout of asphalt deformation more accurately for thicker specimens. Data listed in Table 2.5 are the test results for 5-mm-thick specimens of AAD-1, AAG-1, AAK-1, and AAM-1 asphalts. Among these asphalts, AAG-1 is the stiffest. Its initial apparent stiffness could be higher than 10^5 psi. From the table, one can basically gain a similar sequence as the comparison with the yield strength before, that is, AAG-1 $>$ AAK-1 $>$ AAD-1 $\geq$ AAM-1. This ranking is consistent with the ranking of shear relaxation modulus of these asphalts at 60°F and 0.5 sec. as calculated from A002A dynamic shear modulus data.[2]

Tensile Strength. A series of load controlled tension tests are conducted on 2-in. specimens of AAD-1, AAG-1 and AAK-1 asphalts with 800 psi/sec of loading rate and under 60° F. The related experimental information is listed in Table 2.8. The specimen thickness varies from 30 μm to 120 μm. Because asphalt will become extremely stiff when it is in the form of thin film, the comparison of different SHRP asphalts is established on the relation of break strength and thickness of thin-film specimens, as presented in Figure 2.10. As we can see, asphalt binder is very strong. The apparent tensile strength could be as high as, 1200 psi when the thickness is less than 40 μm. Contrary to the comparison result for thick specimens, a sequence of AAD-1 $\geq$ AAK-1 $>$ AAG-1 can be drawn for thin-film specimens of asphalts. We believe that the tensile strength of a very thin film is controlled by the cavitation tendency of the asphalt. It seems that the bubble nucleation rate of AAD is least among the three asphalts. More research is needed to further confirm the hypothesis.

The results above are summarized as follows:

- For specimen thickness greater than 0.5 mm, we have $\sigma_y^{AAG-1} > \sigma_y^{AAK-1} > \sigma_y^{AAD-1} > \sigma_y^{AAM-1} \geq \sigma_y^{AAA-1}$ in terms of yield stress and initial apparent stiffness.
- For specimen thickness less than 120 μm, we have $\sigma_b^{AAD-1} \geq \sigma_b^{AAK-1} > \sigma_b^{AAG-1}$ in terms of break (or tensile) strength when tested at a high loading rate (800 psi/sec).

2.5.2.2 Uniaxial Compression

Less comparable test results are obtained in uniaxial compression for SHRP asphalts. All available data for five core asphalts are listed in Table 2.6. Though it is difficult to tell which asphalt is stiffest among AAD-1, AAK-1, and AAM-1, we can say that AAG-1 asphalt is still the strongest one and AAA-1 the weakest.

2.5.2.3 Dynamic Loading

Dynamic mechanical tests were preliminarily conducted on two specimens of mechanically aged AAK-1. The main objective was to evaluate the effect of accumulated damage on the fatigue life of the asphalts. The waveform of the input load was sinusoidal, and the tension load amplitude was selected such that the damage caused by microcavitation under a single cycle loading is not significant. The strain and strain rate in Figures 2.11 and 2.12 are calculated from the stroke directly (uncalibrated).

Tests were performed at a temperature of 60° F and under load control, with no preloading on the specimens (the minimum value of the apparent normal tension stress is zero). The frequencies employed in the dynamic tests were 0.2, 0.5, and 1 Hz. Figure 2.11 shows the typical stroke response of an AAK-1 butt-joint specimen (AAK06) to the dynamic load at a frequency of 0.2 Hz and an amplitude of apparent normal tension stress of 27.6 psi. Another run that caused specimen failure at a frequency of 0.5 Hz and an amplitude of apparent stress of 68.2 psi is shown in Figure 2.12. The figures clearly show that the residual strain increases with time until the specimen is ruptured. The increase in strain could be attributed to the linear viscoelastic bheavior of the material and the cumulative damages caused by the cavitation in the specimen. The latter will be further examined in this study.

2.5.3 Influence of Specimen Preparation Conditions

Asphalt cement is such a complex material that any variation in the specimen preparation may affect the property measured. As mentioned in Section 2.3, many experimental variables are involved in our tests. A series of tensile tests are designed for the study of the influence of preparation conditions on the forming process of an asphalt poker chip specimen and the consequent effect on its mechanical behavior. Preparation method 2 (compression with spacer control) and method 3 (compression with extensometer control) are employed. All tests are conducted with the same loading rate of 8.1 psi/sec and at the same temperature of 60° F. The main variables involved in the preparation are described in the following:

Starting Compression Temperature. Temperature is a very important factor, which determines the physical state of the asphalt subjected to compression. The influence of temperature is studied by controlling the temperature at which compression starts and by using natural cooling during the compression. Three starting temperature points were selected: 175° F, 125° F, and 98° F.

Compression Mode. According to the loading function selected, compression process can be classified into two modes, *step* compression (mode I) and *ramp* compression (mode II). In mode I, the loading is a square wave function. At the beginning of compression, the pressure reaches the preset level immediately and is kept at this value thereafter for a specific period (2 to 3 hr.), then released to zero. The variable for this mode is the selected pressure level. Two pressure levels, 9 and 150 psi, are used in the preparations associated with mode I. This compression mode is only used in the preparation with higher starting temperature (175°F), and the specimen thickness is controlled by spacers. In mode 2, the pressure increases gradually to a given value in 1 hr. and then is kept constant for another 1 hr. before being released. The variable for mode II is the maximum pressure. Two maximum pressure values, 150 and 500 psi, were used in the preparation associated with mode II. This compression mode is mainly selected for the preparation of specimens with lower starting temperature (98°F) and without spacers (except specimen AK60) to achieve different thicknesses.

Initial Thickness. Initial thickness is only associated with compression mode II. It is controlled by inserting spacers of known thickness between the upper and lower steel plates before compression. When the temperature reaches the desired starting point, the spacers are removed and compression initiated. Two initial thicknesses, 1.5 and 0.114 mm, were selected for the specimens.

Diameter of Specimens. Specimens with diameters of 15.24 cm (6 in.) and 5.08 cm (2 in.) were prepared. The final thickness of all the larger specimens are controlled by spacers. For the 5.08 cm specimens, both methods (with and without spacers) are used.

The detail of the preparation parameters for each specimen are listed in Table 2.7. For specimens prepared with compression mode II, two extensometers are mounted on the steel plates in opposite positions to monitor the thickness change of the specimen during compression. This enables analysis of the influence of various factors on the preparation process of the specimens.

Figure 2.15 shows the thickness-pressure-time curves during preparation of two specimens with same diameter (15.24 cm), same initial thickness (1.5 mm), and same compression mode (mode II, P_{max} = 150 psi), but with different starting temperature (98° and 125°F). For both specimens, a change in thickness occurs mostly in the initial stages of compression. The change in thickness is faster at the higher starting temperature (AK60) than that of the specimen with the lower starting temperature (AK70). One thousand seconds after compression starts (this corresponds to a pressure level of about 43 psi), specimen AK60 reaches the limiting thickness of the spacers, and the change in thickness of specimen ceases. The thickness of AK70 also tends to be stable at constant pressure.

For specimens with same diameter (5.08 cm), same compression mode, and same starting temperature (98°F), but with different initial thickness, the curves of thickness change are apparently distinct, as shown in Figure 2.16. This is due to the geometry constraint on the flow behavior for different initial thickness.

Specimens AK6[0-4]S are all of the same diameter (5.08 cm) and prepared with same starting temperature (98°F), initial thickness (0.114 mm) (specimen AK60S was thicker ([1.5 mm]), over same compression mode but different maximum pressure. Figure 2.17 shows the comparison of thickness curves between AK61S (P_{max} = 150 psi) and AK64S (P_{max} = 500 psi). The initial part of the two curves almost coincide with each other, but deviate as the compression process proceeds. The effect of the maximum pressure is reflected in final thickness of the specimens.

For specimens prepared with mode I, based on the high starting temperature (175°F) and observation of thickness change curve of AK60 during preparation, it is reasonable to believe that their thickness equals the thickness of the spacers. It is confirmed by the observation on the fractured surfaces that there is no asphalt between the spacers and the steel plates.

The test result is presented in Figure 2.18, and the data inside the dot-lined ellipse is compiled in Table 2.9. The specimens in the figure are classified into three groups corresponding to curve I (125°F, near the softening point), curve II (98°F, below the softening point), and those in the dot-lined ellipse (125 and 175°F). The compression pressure/modes (section 2.3) for these three groups are 32 psi for mode I, 32 to 500 psi for mode II, and 9 to 150 psi for mode I, respectively.

From the two obviously distinct curves in Figure 2.18, we find that the influence of preparation temperature on the tensile strength of specimens is significant. The tensile strength of thin specimens prepared with starting compression temperature of 125°F is much higher than those specimens prepared at 98°F. In thicker specimens, higher preparation temperature results in lower tensile strength, as shown in Table 2.9.

Observation of fracture surfaces of specimens corresponding to 98°F series (curve II in Figure 2.18) indicates that the thinner the specimen, the smaller the size of the cavities and the more interfacial failure involved (see Figure 2.20). In Figure 2.18, the thickness effects on tensile strength are listed. The AK50S101 specimen shows less tensile strength than other 2-in.- diameter specimens. The starting temperature in preparation of AK50S101 is 176°F, higher than others. The fracture surface shows a lot of large cavities (see Figure 2.21).

Within the pressure range used in our tests, the conditioning temperature has a greater effect than preparation pressure. Under the condition of high temperature and high pressure, the tensile strength maybe reduced greatly as a result of combining the temperature and pressure effects. As we can see from Table 2.9, the AK5001 and AK5101 specimens have similar preparation conditions except that the compression pressure for AK5101 is much higher than that for the AK5001. The tensile strength of AK5101 is only half of the value of AK5001. Comparing the deformation curves of these two specimens (Figure 2.19), we find that AK50 is much stiffer than AK51. Bending of the grip plates, indicated by the negative extensometer reading, occurs during the tension of AK50. This suggests that AK50 has a very high stiffness. Examining the fracture surfaces of AK5001 and AK5101, shown in Figure 2.22, one noted that there are many cavities spreading over the surfaces of these two specimens. The AK5101 specimen shows higher density of the cavities and less tendency to interfacial failure than the AK5001 specimen. At high starting temperature, the high preparation pressure on the AK5001 specimen causes the lower tensile strength and weaker cohesive strength.

2.5.4 Effect of Stabilization and Hardening

Because asphalt is a time-dependent material, we expect that the stabilizing and equilibrium time may affect the mechanical property appreciably. Thus, instead of making the asphalt specimen in equilibrium at the desired test temperature (for about 2 to 3 hr) right after it was cooled to room temperature, specimens were allowed to equilibrate (14 to 1,200 hr) at a certain temperature. The mechanical test results indicate that this longer stabilizing time gives rise to strong effects on the mechanical properties and the failure behavior of asphalt poker chip specimens. We believe that the so-called physical hardening effect was introduced by a longer stabilizing time. It is largely due to the formation of physical structure and is reversible under thermal conditions.

The influence of stabilization time on mechanical properties of asphalts can be clearly seen from Table 2.10, which lists three series of runs on 0.5-mm-thick specimens of AAK-1 asphalt. Series AK04-AK06 stabilized in less than 2 hr; series AK07-AK14 stabilized over 12 hr; and series AK25-AK26 stabilized near 1,170 hours. The first two series were tested under stroke control, and the last series was controlled by load. It is easy to see that the stiffness increases with the stabliziation time. In addition to the difference in stiffness, the failure behavior and the fracture surface of the specimens show a significant difference (Figure 2.23). Series AK04-AK06 showed semiflow failure, and the failure occurred in bulk asphalt (i.e., cohesive failure). In contrast, a tenacious failure, with appreciable interfacial contribution, was observed in series AK07-AK14 (see Figure 2.8 for four types of failures that have been observed in the uniaxial tension tests of poker chip specimens). We believe that there must be two types of AE characteristics corresponding to adhesive failure and cohesive yielding/failure. This will be investigated by analyzing the spectrum of AE signals. Refer to Chapter 3 for a detailed account of AE characteristics.

From Table 2.10, we can also see that the mechanical parameters related to large deformations, such as yield stress and tensile strength, are also affected by stabilization of asphalt as the initial apparent stiffness modulus, especially for yield strain, which decreases significantly with increasing time of stabilization.

2.5.5 Influence of Deformation/Loading Rate

As mentioned before, asphalt is a very time-dependable material. The deformation and loading rates in the compression and tension tests of poker chip specimens must affect the mechanical parameters, such as break strength, appreciably. In order to determine the magnitude of the dependence of the tensile and compressive properties of SHRP asphalts on the rate of deformation and the rate of loading, series of tension and compression tests are conducted on AAK-1, AAA-1, AAD-1, and AAG-1 asphalts.

For AAK-1 asphalt, Figure 2.27 shows the result of the strain rate study on uniaxial compression in terms of mean modulus and stroke rate. The tests are carried out with different rates of strain varying from 1.2% per second to 9% per second and at 60°F. The specimen thickness is 5 mm. The mean modulus is taken as the slope of a straight line in Part B of Figure 2.37. The results indicate that the faster the strain rate, the greater the mean modulus of compression. Notice that the value of the modulus changes slowly in the range of the stroke rate selected. If it were presented in real strain rate, the change of modulus would be faster than that in the figure.

In studying the influence of deformation/loading rate on the tensile properties of AAK-1 asphalt, tension tests were conducted on 6-in. diameter specimens at 60°F with both stroke control and load control. The compression starting temperature for all specimens is 125°F. The result for the large specimens is plotted in the break strength versus loading rate and shown in Figure 2.24. The *effective* load rate at yielding $[\sigma_y(t)/t_y]$ is used for the stroke-controlled tests. It is easy to see that there is a trend for the influence of loading rate on the break strength, similar to cases of common polymers. The larger the load rate, the higher the break strength. The fluctuation of data in the figure can be contributed to other variables (e.g., the stabilization time for virgin specimens and healing time for nonvirgin specimens) and the void content in specimens. In terms of yield strength, Figure 2.25 shows the result for the stroke-controlled tests in Figure 2.24.

Tension tests are also conducted for 2-in. diameter specimens of AAK-1 asphalt with load control (loading rate 15 to 630 psi/sec) and at room temperature ($\sim$ 78°F). A similar result to that for 6-in.-specimens, is obtained as shown in Figure 2.26. A very high break strength ($>$ 600 psi) is observed first in this series even though the thickness is 0.24 mm, a relatively large number compared with the typical thickness of asphalt cement in paving concretes.

2.5.6 Influence of Specimen Thickness and Diameter

It has been well confirmed that there exists a "strength-thickness" rule, which indicates the dependence of the tensile strength of materials on the magnitude of the film thickness when tested in thin film.[7] According to this rule, the tensile strength (not stiffness) of thin films of a material, when tested in tension, increases as the film thickness decreases. Figure 2.28, which consists of plots of stress and strain versus time under stroke control, shows the influence of specimen thickness on the mechanical properties of AAK-1 asphalt. Numbers inside the parentheses are specimen thickness. As we can see, the "strength-thickness" rule holds true for the relatively thick film range used. This rule even holds as the overall trend shown in Figure 2.30 for the results obtained from both stroke- and load-controlled tests (see Section 2.5.3 and Section 2.5.5 for details about group A and groups B and C, respectively). In addition, Figure 2.29 presents the fracture patterns of AAK-1 specimens with different film thickness (0.5 and 0.32 mm). The thinner the specimen, the smaller the bubbles, and the higher the bubble density. This kind of phenomena may be attributed to the specific poker chip geometry.

In load-controlled tests for studying the influence of thickness on the tensile properties of asphalt cements in thin films, specimens with 2- and 6-in. diameters were used. For tests of specimens of 2-in. diameter, it is very interesting to note that there are two distinct curves corresponding to two compression temperatures in the specimen preparation (Figure 2.18). The details about the influence of temperature are discussed in Section 2.5.3.

tion 2.5.3. An alternative presentation considering the shape factor ($S = D/4h$) is shown in Figure 2.31. A micromechanical calculation would predict that the mechanical properties, such as modulus or stress, at a given strain are the same for a 2-in. diameter specimen and a 6-in. diameter specimen, if they have the same shape factor. This prediction is true as long as the constitutive properties of asphalt thin films in the two specimens are the same. This assumption is not valid if different microdamages are introduced during the deformation in the two specimens. Except for the two curves identical to the ones in Figure 2.18, one can see that there are two regions characterized by the tensile strength. Region A corresponds to specimens of 2-in. diameter and has higher tensile strengths, whereas Region B corresponds to specimens of 6-in. diameter and has lower tensile strengths. By evaluating the fracture patterns, the same relationships of bubble size and bubble density to film thickness exist. For the same shape factor, 6-in. diameter specimens are three times as thick as 2-in. diameter specimens. Hence, the size of bubbles generated in the 6-in. diameter specimen is much larger than in the 2-in. diameter specimen, resulting in a lower tensile strength for the 6-in. diameter specimen.

2.5.7 Influence of Testing Temperature

We have already seen the influence of testing temperature on the compressive properties in the preliminary tests of local California AR8000 asphalt in Section 2.4 (Figure 2.7). For the tensile test, Figure 2.32 shows the test result of AAK-1 specimens with 5-mm thickness tested at 60° and 50°F. It is clear that temperature significantly affects the tensile properties of the asphalt. In terms of apparent stiffness modulus, for example, curve I (60°F) is 1.5×10^4 psi and Curve II (50°F) is 3.4×10^4 psi, evaluated at 2 sec and the initial effective loading rates are 22.9 and 18.6 psi/sec, respectively.

2.5.8 Influence of Void Content in Asphalt Cement

In this section, the evaluation of the effect of void content on the mechanical behavior of asphalt is presented. Three kinds of extremely different asphalt cements are used: asphalt with induced air bubbles, normal asphalt and vacuumed-treated asphalt. The preparation of air bubbled and vacuum-treated specimens is described in method 1 of Section 2.3. From the test results, we conclude that the cavitation is the main contributor to the softening of asphalt. The detailed results are presented below.

Comparison of Normal and Bubbled Asphalts. It is expected that the asphalt containing more bubbles will be softer than one having less bubbles. The softening effect should be reflected by such tensile properties as initial apparent stiffness and maximum yield point. A comparison of AAD-1 asphalts with and without air bubbles in tension tests at 60°F is illustrated in Figure 2.33. As we can see, air bubbles greatly decrease the stress level of yield point. It is difficult for us to experimentally quantify the influence of air bubbles to the initial apparent stiffness modulus, due to our experimental error range. A theoretical analysis of the effect of air bubbles, in terms of the change in Poisson's ratio of asphalt, is presented in Chapter 8.

Comparison of Normal and Vacuum-Treated Asphalts A comparison of mechanical measurements for vacuumed and normal AAK-1 asphalt in tension tests at 60°F is illustrated in Figure 2.34. As predicted, the vacuum-treated specimen shows a larger tensile strength than the normal one. But in terms of apparent stiffness modulus, AK09 is softer than AK12 (and other normal specimens) at the initial stage, though its strain rate is a little faster. The reason is not clear at this moment. The corresponding AE energy vs. count plot is shown in Figure 3.19 (comparison of AE amplitude distribution of a regular and a vacuumed-treated specimen) of Chapter 3, Section 2.3.2. From a photograph of fractured specimens (Figure 2.35), we can easily see that bubbles in the specimen made from vacuum-treated asphalt are smaller than those in the specimen made from normal asphalt.

2.6 Application of Linear Viscoelastic Theory

Viscoelastic properties of asphalts and asphalt concrete have been studied by many researchers using different testing methods and conditions.[9] Most commonly used methods include the dynamic mechanical test and the creep test. In our laboratory, the viscoelastic phenomena have been observed over all asphalt poker chip specimens with larger deformation in tension tests. To evaluate the viscoelastic behavior of asphalt cements, the linear viscoelastic (LVE) theory and the time-temperature superposition principle are applied to AAK-1 asphalt tested at small deformation (strain less than 1%).

The following approximation, which is derived from the principle of linear superposition,[10] has been used:

$$\sigma(t) \doteq 3\int_0^t G(t-\tau)\,\dot{\epsilon}(\tau)\,d\tau, \tag{2.1}$$

where $G(t)$ is the shear modulus and τ is any time before the current time t. In the equation above, asphalt cements have been considered as incompressible materials. As we can see, either value stress and strain can be calculated easily from the other once the shear modulus is given. In our calculation, the shear modulus of AAK-1 asphalt is from the data presented in the report of A-002A[11] and converted to our testing temperature (T) using WLF equation and the principle of time-temperature superposition:

$$\log a_T = \frac{-C_1(T-T_\circ)}{C_2+T-T_\circ} \tag{2.2}$$

$$G(T, t) = G(T_\circ, t/a_T) \tag{2.3}$$

where, a_T is the shift factor, C_1 and C_2 are constants for a perticular asphalt, and $T_\circ = 25°\mathrm{C}$, is the reference temperature used in A002A's data. In fact, constants C_1 and C_2 are not universal for asphalt materials.[12] The values used in the calculation are 11.28 and 106.60, respectively.

Calculations has been done for both load control (stress input) and stroke control (strain input). Figure 2.36 illustrates the comparison of a calculated stress-strain curve, obtained with a input of ramp loading (rate = 18.5 psi/s) and temperature of 60°F, with the one of AAK-1 asphalt in tensile test conducted on 5 mm thick poker chip specimen with load control (same load rate as above) and the same temperature. Due to the difference of simple tension (LVE calculation) and triaxial tension (poker chip test), the calculated strain is much higher than the nominal strain measured in the test. The values of strain for the test and the calculation have been normalized with respect to their maximum values. It is easy to see that the calculated result is in good agreement with the experimental one, indicating that the linear viscoelastic theory is applicable to asphalt cements under small strain (at least upto 1% under our experimental conditions). Furthermore, if we define the ratio of two maximum strain values $(\epsilon_{max}^{(LVE)}/\epsilon_{max}^{(PC)})$ as the strain magnification factor, we will find that the factor is about 134. This is close to the value of 117 obtained from the lubrication theory (cf. Chapter 8).

2.7 Mechanical Damage and Healing Behavior of Asphalt

An important property of asphalt is that the material can self-heal after a relatively large degree (say, passed yield point) of mechanical damage (or aging). Healing is a complicated issue, and its quantification depends on the properties monitored. In terms of AE measurement, healing of asphalt cements can be characterized by the AE accumulated energies (See Chapter 3). From the mechanical point of view, it can be evaluated by monitoring the initial apparent modulus and the yield behavior of asphalt poker chip specimens.

To study the healing behavior of SHRP asphalt mechanically, the following approach is incorporated into our test routines. We select a proper deformation rate for the first run. After waiting for a certain time period (varying from 5 to 60 min), we take the next run, and so on. After a series of runs, we compare the stress–strain curve for all runs to study the difference of the mechanical response and determine the healing time of the asphalt specimen. Both uniaxial tension and uniaxial compression modes have been used to study the healing behavior of SHRP asphalts.

Uniaxial Compression. A series of uniaxial compression tests on the same 5-mm-thick specimen of AAK-1 asphalt (run number, AK0101xx) is listed in the first part of Table 2.12. In the table, Δt is the time interval between runs; $\overline{E}_c$, the mean compression modulus, is defined as the slope of the straight line region in the stress–strain curve. A definite softening effect on an asphalt specimen is found to occur between the runs. The graphic presentation is shown in Figure 2.37. The data presented in this figure was obtained at a temperature of 60°F, with a strain rate of $0.0067 \pm 1.5\%$ and a maximum strain of $12 \pm 1\%$.

Data shown in Figure 2.37 indicate that there are two main regions to the compression stress–strain curves. Region A appears in the small strain range. Following the test run by run, the compression stiffness of asphalt decreases. This indicates that there is a strong softening effect, especially at the initial region. The asphalt cannot heal perfectly in a short time. In turn, this tells us that we cannot use the same specimen to establish the relationship between the initial stiffness (or modulus) and the deformation rate by running experiments at short time intervals (less than 60 minutes). The second region, (B) consists of a straight line of stress-strain curves that exists in the larger strain range. Here, we define the slope of the straight line as a kind of *mean modulus* (or apparent modulus). By analyzing the mean modulus of different runs of the same strain rate $5.7 \pm 2\%$/sec, we it relative error is $\pm 1.5\%$. This indicates that we can use the same specimen to evaluate the influence of the rate of deformation in term of our mean modulus by taking a proper time interval (20 to 30 min) between runs.

How much time does the asphalt need to heal perfectly, at least for the mechanical properties, after a run? To answer this question, we did the following test. After the AAK-1 specimen (AK010201) of 5-mm thickness was run through the test several times, we waited almost two weeks, and then ran the test on it at same conditions again. During the waiting period, the specimen was not taken off the load frame of the MTS machine, and four C-clamps were used to hold the grips to ensure constant specimen thickness. The obtained result is shown in Figure 2.38. As we can see from the figure, the two curves are overlapped except near the maximum test strain. This indicates that the asphalt would take quite a long time to heal perfectly under temperature conditions.

Uniaxial Tension. AAK-1 poker chip specimens with 0.5-mm thickness were used to study the healing behavior and accumulated damage of the asphalt in uniaxial tension tests. Other test control parameters were stroke rate (1 mm/min) and environmental temperature (60°F).

Table 2.11 shows the healing process of AAK-1 in terms of initial modulus. The data presented in this table were obtained in the test conditions above, and with a maximum strain of about 8%, the asphalt being in the LVE region. The absolute waiting time used in the table is defined as the time with respect to the virgin run for each specimen. As we can see, the initial modulus is well reproducible. In fact, the initial stress-strain curves of tension follow almost the same trace for different runs of the same specimen, indicating complete recovery, or negligible internal damage, or mechanical aging of the asphalt in small deformation. This is consistent with the result obtained from uniaxial compression tests in terms of the mean compression modulus. When the specimen has been extended beyond the maximum yield point, it can not completely recover. However, given a sufficiently long resting time (over 100 hr), it recovers substantially, as shown in Figure 2.39. In contrast, AE measurement indicates a different story. Most microcracks occurring after a tension run (Chapter 3) are hard to heal, in both linear and nonlinear regions. Figure 2.39 shows the healing process of a series of runs (AK05010x) in terms of the mechanical healing index. Full stress-strain curves, including both linear and nonlinear regions (maximum strain = 105%), are presented in Figure 2.40. It is clearly shown by both figures that the specimen significantly recovers if the resting time between runs is long enough (e.g., curves 7 and 8). But if the resting time is very short, the healing process of the asphalt will not be significant and the accumulated internal damage of the microstructure results in a lower stress response to a particular strain (e.g., curves 4 and 5). As a matter of fact, Figure 2.39 shows the competition between the accumulated internal damage and the self-healing of asphalt cement. Also shown in Figure 2.40 are the AE accumulated energies corresponding to each tension test. The AE signals will not recover to the state of the previous run, even with a long resting time.

Superhealing of Asphalt Cements. A superhealing effect of asphalt cements was observed on AAK-1 and AAD-1 asphalts when a long resting time was allowed for mechanically test aged specimens. For example, in case of tensile tests of 5-mm-thick AAD-1 poker chip specimens, the yield stresses of a virgin specimen (AD300110) and the second run specimen (AD300111) were 56.5 and 55 psi, respectively; and the yield stress of the third run specimen (AD300112) was as high as 86 psi, whereas the rest time was 19 hr after the first run and 1,226 hr after the second run.

2.8 Conclusions

- For specimen thickness greater than 0.5 mm, we have $\sigma_y^{AAG-1} > \sigma_y^{AAK-1} > \sigma_y^{AAD-1} > \sigma_y^{AAM-1} \geq \sigma_y^{AAA-1}$ in terms of yield stress and initial apparent stiffness.
- For specimen thickness less than 120 μm, we have $\sigma_b^{AAD-1} \geq \sigma_b^{AAK-1} > \sigma_b^{AAG-1}$ in terms of break (or tensile) strength, when tested at a high loading rate (800 psi/sec).
- The mechanical properties of asphalt poker chip specimens are strongly affected by the specimen preparation temperature. The relationship between the temperature and tensile strength is well established. The effect of preparation pressure is not significant within the pressure range used in our experiments.

- Four types of failure are observed in the mechanical testing of asphalt poker chip specimens. They are brittle fracture, tenacious rupture, semiflow rupture and failure by flow, based on the stress-strain characteristic and the nature of fracture surface. Depending on the test conditions, brittle fracture can occur in thin and thick specimens; flow failure mainly occurs in thick specimens; and tenacious and semiflow ruptures can occur in intermediate specimens.

- The tensile property of an asphalt cement at small deformation is significantly affected by its stabilization time. Long stabilizing/equilibrium time introduces the so-called physical hardening effect, which is reflected by the greater stiffness, the tendency of interfacial failure, and the brittle bulk failure of poker chip specimens.

- The film thickness of poker chip specimens in tensile tests strongly affects the tensile property of asphalt cements. The tensile strength increases as the film thickness decreases. For the range of thicknesses studied, the tensile strength-film thickness relationship for poker chip specimens of asphalts is linear. When a specimen is very thick, however, depending on the test conditions, the tensile strength can approach quite a small value.

- The mechanical properties of asphalt in poker chip geometry subjected to a stress significantly lower than the yield stress can be described by the linear viscoelastic (LVE) model. The LVE calculation results agree with experimental results. The enhancement in stiffness of asphalt thin film as compared to its Young's modulus in bulk can be predicted from the shape factor of the specimen based on stress analysis (Chapter 8).

- As the loading increases, microdamage in the asphalt film occurs and leads to the eventual failure of the specimen. Strength properties of poker chip specimens depend on the asphalt's resistivity to cavitation.

- Asphalts have strong healing behavior. Unbroken specimens, after several test runs, can recover their original behavior, both mechanically and acoustically if allowed to rest for relatively long times. This depends on the healing temperature and mechanical histories.

Table 2.1: Inspection of Test Asphalts

Asphalt	Penetration (100g,5s,77°F,0.1mm)	Viscosity (140°F,Poises)	R&B Softening Point (°F)	Source
AAD-1	135	600	118	SHRP MRL
AAG-1	53	1862	120	
AAK-1	70	3256	121	
AAM-1	64	1992	125	
AR4000	30*			LA County Lab.
AR8000	20*			

*Test on residue.

Table 2.2: Preparation Methods of Poker-Chip Asphalt Specimens*

Method	Control	Pressure (psi)	Note
Pouring	Spacer and Hoop	N/A	Thickness (h) $\geq$ 5mm
C.S.†	Spacer and Stroke	5.3, 19.1 and 32 psi	$120\mu m \leq h \leq 1mm$
C.E.†	Spacer and Extensometer	9 and 32psi	$40\mu m < h < 120\mu m$

* Melting temperature of asphalt: 180 ~ 200°F; Temperature at compression: 130 ~ 140°F

† C.S.: Compression with spacer control; C.E.: Compression with extensometer control

Table 2.3: Experimental Variables

Type of Asphalt		AAD-1, AAG-1, AAK-1 and AAM-1
Test Temperature		50°F, 60°F and RT(78°F)
Starting Temperature*		60°F and 130°F)
Aspect Ratio of Specimen $S = D/4h$	Thickness(h)	40μm ~ 10mm
	Diameter (D)	2in and 6in
Loading Rate	Stroke	60 ~ 250μm/s
	Load	4.3psi/s ~ 650psi/s
	Temperature*	~ 2°F/min.
Specimen History	Stabilization	2hrs. ~ 1173hr. at RT and $55 \pm 5°F$
	Healing	0 ~ 1226hrs. at RT, 55 and 60°F
Test Mode		Axial Tension and Compression, Thermal Scanning

* Thermal scanning test.

Table 2.4: Strain Rate Influence to the Yield Strength of AR8000 Asphalt

Strain Rate (1/s)	Yield Stress (psi)	Yield Strain
0.0250	70.7	0.040
0.0375	88.4	0.045
0.0500	97.3	0.045

* Specimen thickness: 10 mm; Test temperature: RT (~ 75°F).

Table 2.5: Apparent Stiffness of SHRP asphalts in Tension[a]

Asphalt (Run Number)	Thickness (mm)	Loading Rate (psi/s)[b]	Apparent Stiffness (psi)[b]	
AK010121	5	104.9	6.2×10^3	
AK010220	5	20.7	3.4×10^3	
AM050101	5	78.8	1.9×10^3	linear
AM050102	5	95.5	2.5×10^3	linear
AK300101-06	5	18.4	5.8×10^4	± 16.5%
AD300110-11	5	17-20	3.1×10^4	± 25.4%
AG660106	5	14	$> 1.1 \times 10^5$	
AG660107	5	100	$> 1.4 \times 10^5$	
AG660201	5	100	$> 2.1 \times 10^5$	

a. Uniaxial tension tests of Poker-Chip specimens under 60°F.

b. Evaluated at 0.5 seconds of loading.

Table 2.6: Apparent Stiffness of SHRP Asphalts in Compression[a]

Asphalt (Run Number)	Thickness (mm)	Loading Rate (psi/s)[b]	Apparent Stiffness (psi)[b]	
AA010101-06	10	20-80	1.7×10^3	8.0%
AD600101-05[c]	10	30-65	3.8×10^3	7.0%
AK010101	5	98.0	3.2×10^3	[d]
AK010201	5	18.9	2.7×10^3	
AG660101-02	5	99.0	$> 5.0 \times 10^4$	
AM050201	5	104.5	3.6×10^3	

a. Uniaxial compression tests of Poker-Chip specimens under 60°F.

b. Evaluated at 0.5 seconds of loading.

c. Estimated from 50°F tests (AD60).

d. Estimated value at 1.0 second of loading.

Table 2.7: Parameters Characterizing Specimen Preparation

Test NO.	T_{start} (°F)	Compression P (psi)	Compression Mode	Initial Thickness (mm)	Final Thickness (mm)	Break Stress (psi)
AK5001	175	32	step	-	0.114	250
AK5101	175	160	step	-	0.114	125
AK50S1	175	32	step	-	0.114	300
AK6101	125	160	ramp	1.5	0.114	270
AK60S1	98	160	ramp	1.5	0.200	420
AK7001	98	160	ramp	1.5	0.200	277
AK61S1	98	160	ramp	0.114	0.055	560
AK62S1	98	500	ramp	0.114	0.045	600
AK63S1	98	500	ramp	0.114	0.036	700
AK4101	125	9	step	-	0.114	282
AK4201	125	9	step	-	0.114	272
AK40S1	125	32	step	0.114	0.041	1025
AK41S1	125	32	step	0.114	0.080	719
AK42S1	125	32	step	-	0.114	410
AK43S1	125	32	step	0.114	0.076	745

* Loading rate is 8.1 psi/s. Test temperature = 60°F. Spacer thickness = 0.114 mm

Table 2.8: Parameters Characterizing Specimen Preparation for High Rate Tested Thin Specimems

Test NO.	T_{start} (°F)	Compression P (psi)	Initial Thickness (μm)	Final Thickness (μm)	Break Stress (psi)*
AK64S1	98	500	114	55	900
AK65S1	125	96	-	114	600
AG64S1	98	160	-	114	560
AG65S1	98	160	114	55	750
AD65S1	98	160	114	30	1200

* Tensile loading rate: 800 psi/s

Table 2.9: Influence of Preparation Condition on Tensile Strength*

Specimen No.	Diameter (in.)	Preparation Temperature (°F)	Preparation Pressure (psi)	Tensile Strength (psi)
AK41	6	125	9	282
AK42	6	125	9	272
AK61	6	125	160	270
AK50	6	175	32	250
AK51	6	175	160	125
AK42S	2	125	32	410
AK50S	2	175	32	300

* Loading rate is 8.1 psi/s. Specimen thickness is $120\mu m$.

Table 2.10: Hardening Effect on Mechanical Properties of AAK-1 Asphalt

Test Number*	Stabilization		Effective§	Initial§	Yield Point	
	Time (hr)	Temp (°F)	$\dot{\sigma}_o$ (psi)	E_s^{app} (psi)	σ (psi)	ϵ
AK040101(3)	~ 2	RT	6.8	1.14×10^3	187.0	25.4%
AK050101(3)			7.8	1.43×10^3	172.3	30.0%
AK060101(9)			7.8	1.26×10^3	158.6	46.7%
AK120101(1)	~ 14	RT	7.8	5.25×10^3	145.8	15.9%
AK140101(1)			8.3	4.30×10^3	164.9	19.7%
AK250101(1)	1168	50	8.1	$> 5 \times 10^3$	275	3.5%
AK260101(1)	1172		8.1	$> 5 \times 10^3$	240	3.6%

* Stroke control: AK04,05,06,12,14; Load control: AK25,26.

§ Evaluated at 1 second of pulling for stroke control.

† Estimated from the error band of the stress – strain curve.

Table 2.11: Initial Modulus in Studying Behavior of AAK-1 Asphalt

Run Number	Abs. Waiting Time (hr)	Eff. $\dot{\sigma}$ (psi/s)	Initial E (psi)	Evaluation	
				Time (sec.)	Strain
AK040101	0.0	6.82	968.0	10.0	7.0%
AK040102	59.9	7.41	967.0	10.0	7.7%
AK040103	166.1	7.13	1104.0	10.0	6.5%
AK050101	0.0	6.96	1038.0	5.0	3.4%
AK050102	50.2	7.18	820.0	5.0	4.4%
AK060101	0.0	7.47	1051.0	5.0	3.6%
AK060102	3.2	7.48	959.3	10.0	7.8%
AK060103	9.5	7.65	1098.7	10.0	7.0%
AK060104	58.0	7.42	1020.0	10.0	7.3%
AK060105	58.6	7.53	1011.0	10.0	7.4%
Average		7.31 ± 3.5%	1003.7 ± 7.8%	Time and Strain upto that loading rate and modulus evaluated.	

Table 2.12: Compression Test Data from Runs of AK0101 and AK0102 Series

Run Number	Δt (min.)	Strain Rate (1/s)	$\overline{E}_c$ (10^7 Pa.)	Average $\overline{E}_c$
AK010101		0.012	1.07	for $\dot{\epsilon} =$
AK010103	25	0.024	1.16	$0.057 \pm 0.01 s^{-1}$
AK010104	15	0.033	1.29	1.33 ± 0.02
AK010105	10	0.043	1.32	
AK010106	10	0.058	1.32	
AK010108	10	0.074	1.49	
AK010109	15	0.090	1.56	
AK010111	5	0.057	1.31	
AK010112	36	0.056	1.35	
AK010113	25	0.057	1.35	
				for $\dot{\epsilon} =$
AK010202	60	0.055	1.38	$0.054 \pm 0.01 s^{-1}$
AK010210	25	0.055	1.30	1.34 ± 0.04
AK010211	40	0.053	1.34	

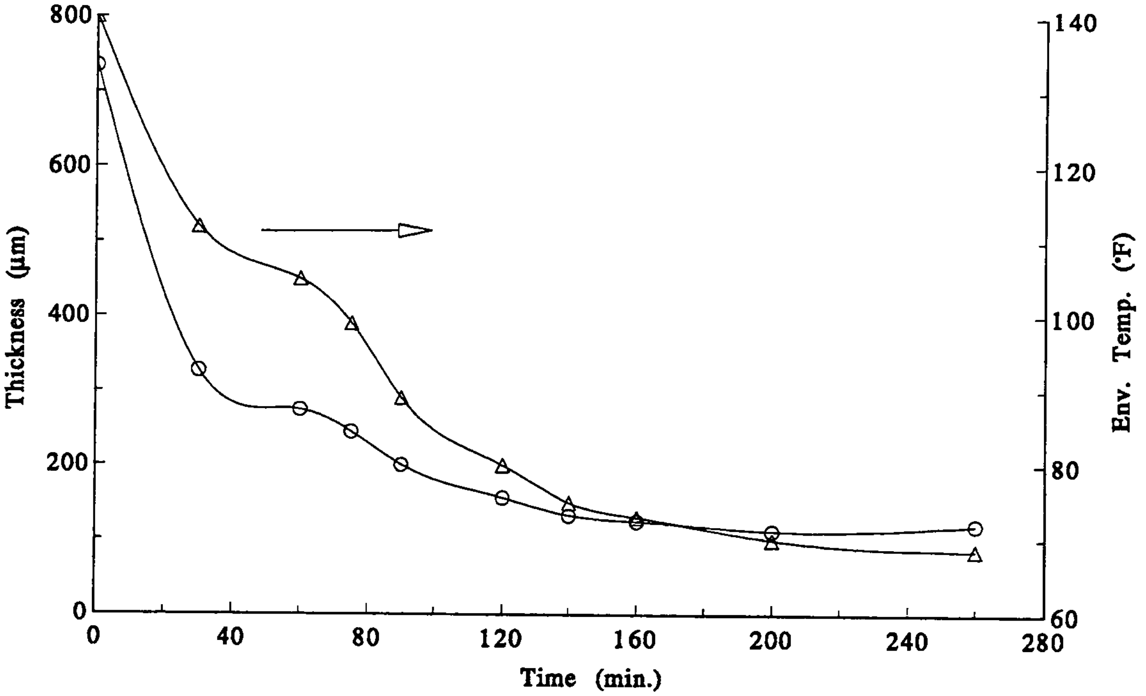

Figure 2.1: Compression process: Thickness and temperature change during preparation.

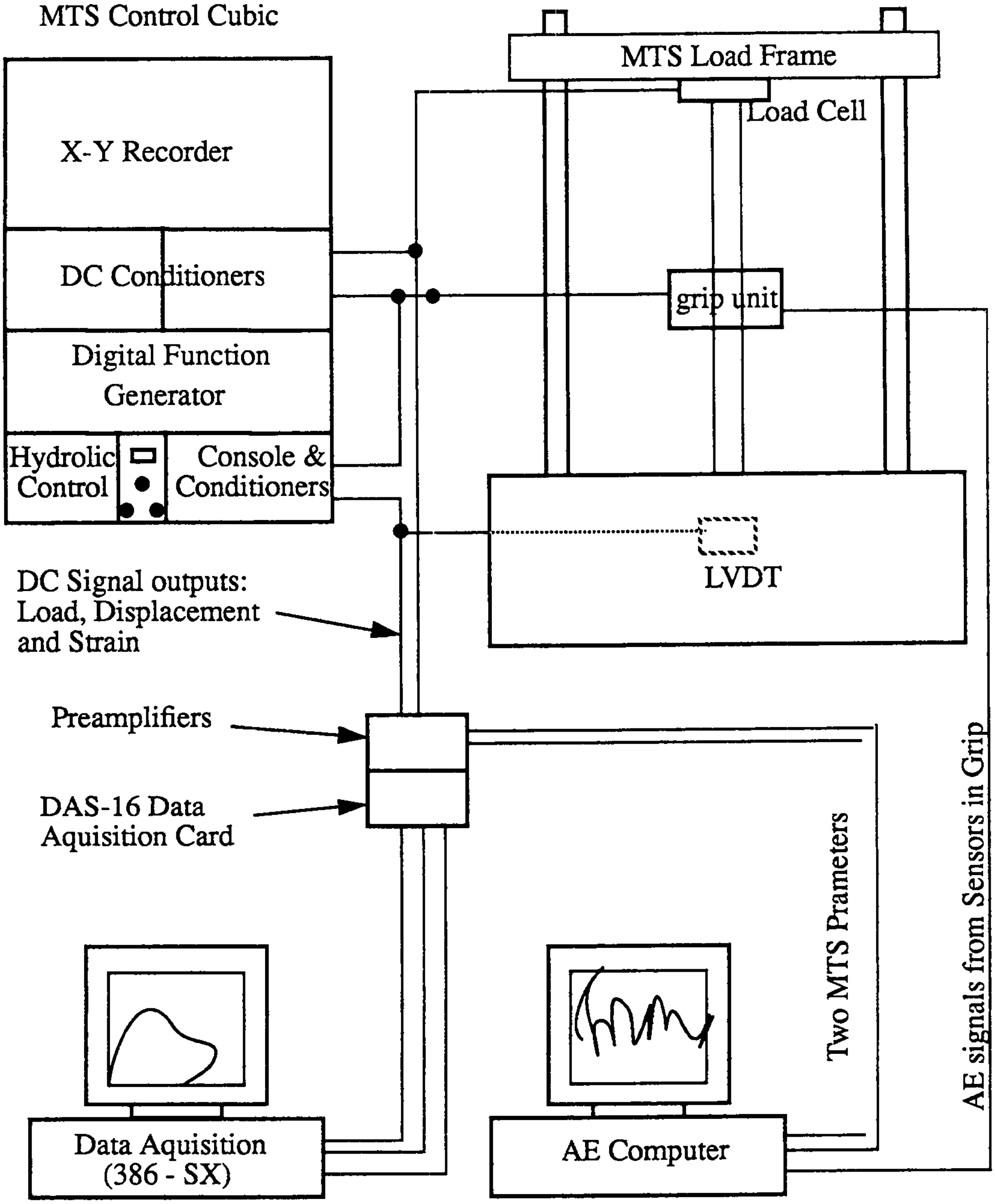

Figure 2.2: Schematic of test setup and equipment.

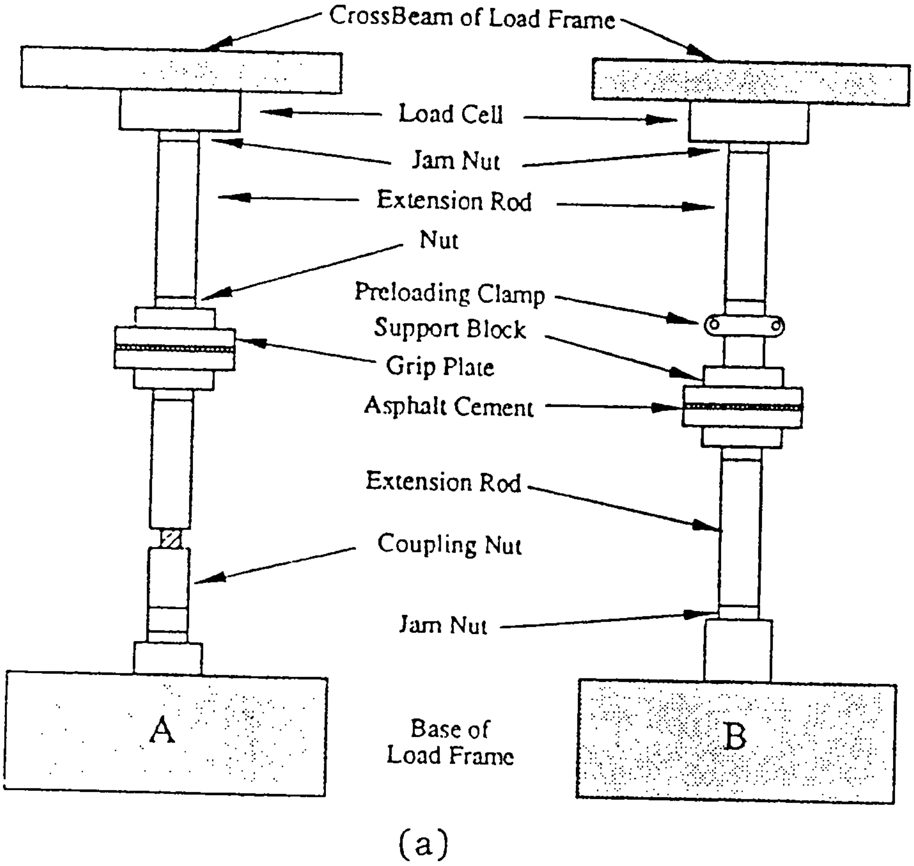

Figure 2.3: (a) Schematic of specimen loading system.

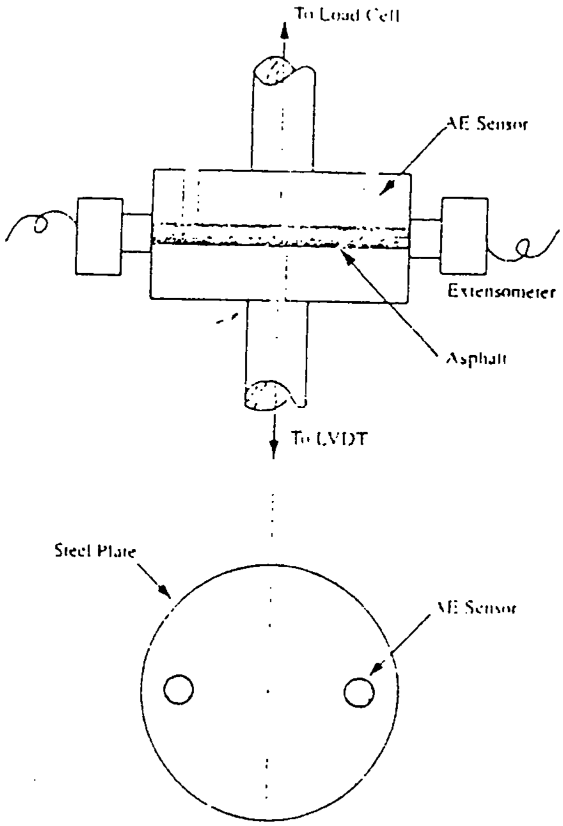

(b)

Figure 2.3: (b) Schematic of grip unit.

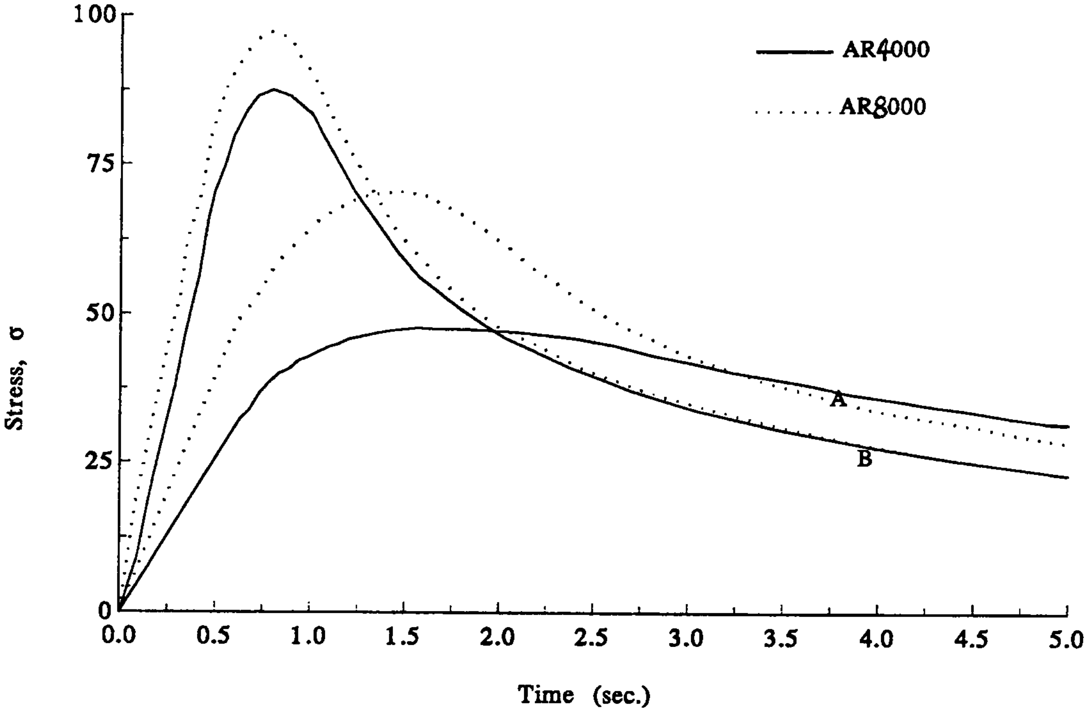

Figure 2.4: Comparison of AR4000 and AR8000 in tension test. Specimen diameter = 6in, thickness = 0.4in. Strain rate is 0.025/s for Set **A** and 0.05/s for Set **B**.

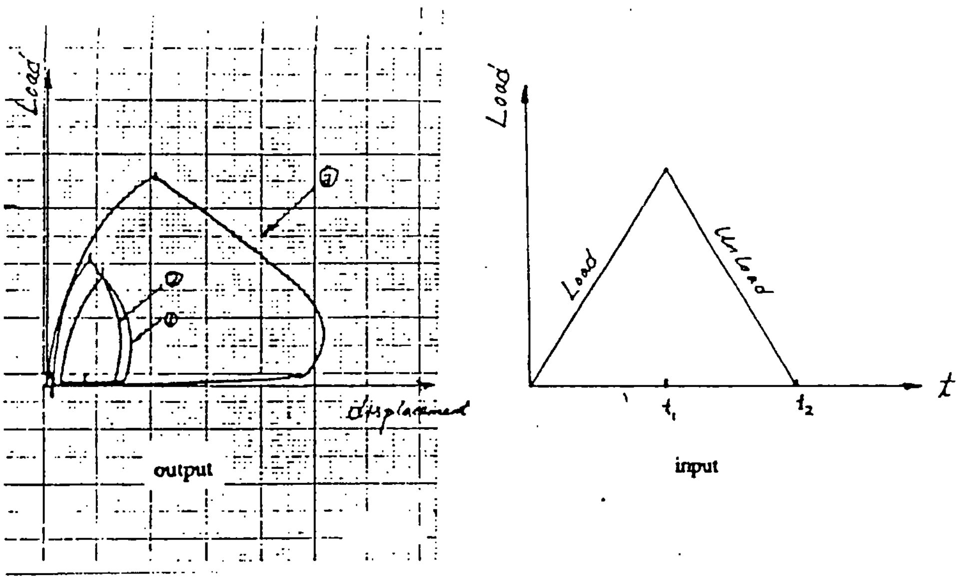

Figure 2.5: Cyclic load tests of California asphalt AR8000 (peaks corresponding to time t_1). (1) 5%, (2) 6%, (3) 10% of operating range (10 KIPS) of load.

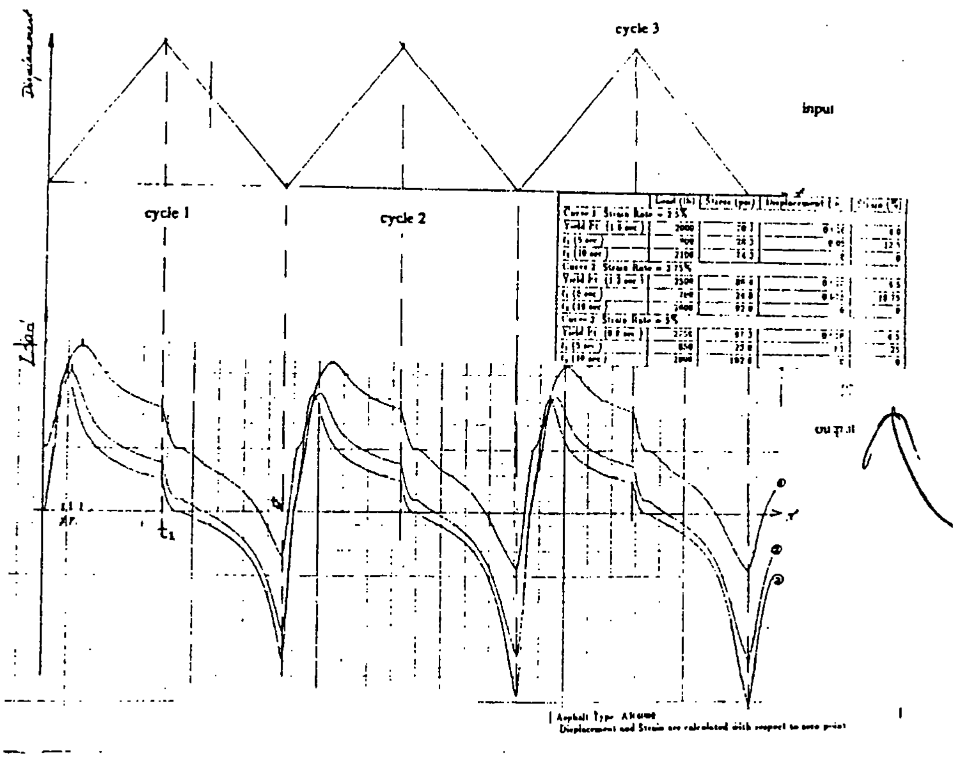

Figure 2.6: Cyclic deformation (ramp) test of AR8000.

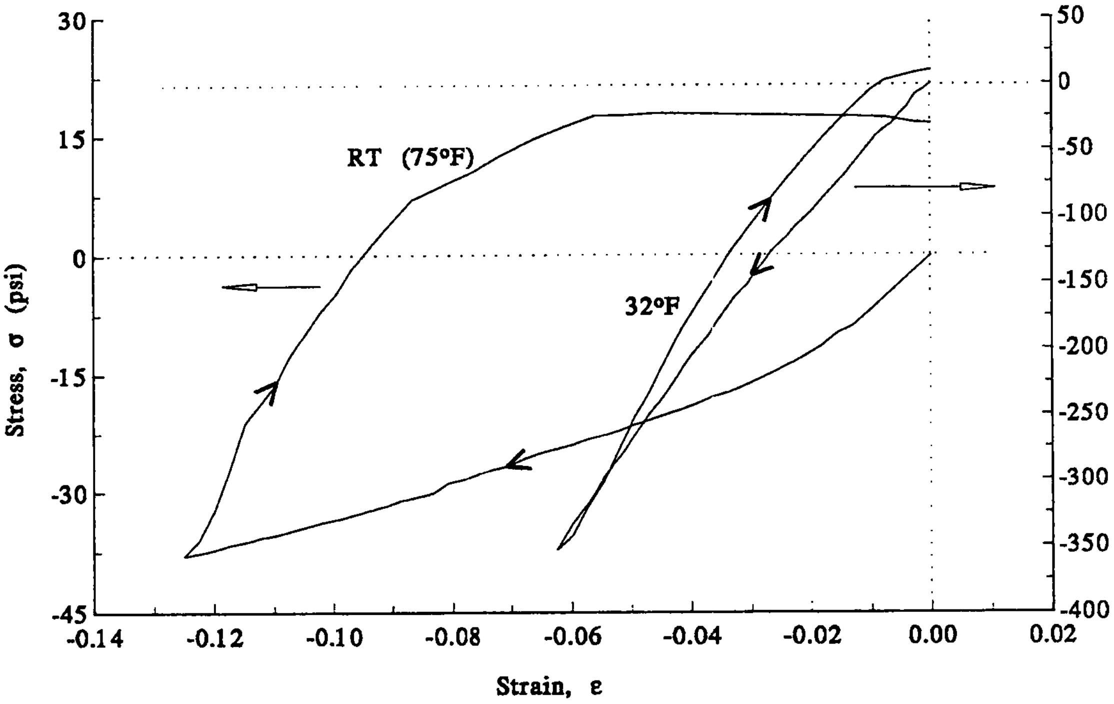

Figure 2.7: Uniaxial compression and tension (CTC) of AR4000 at different testing temperature.

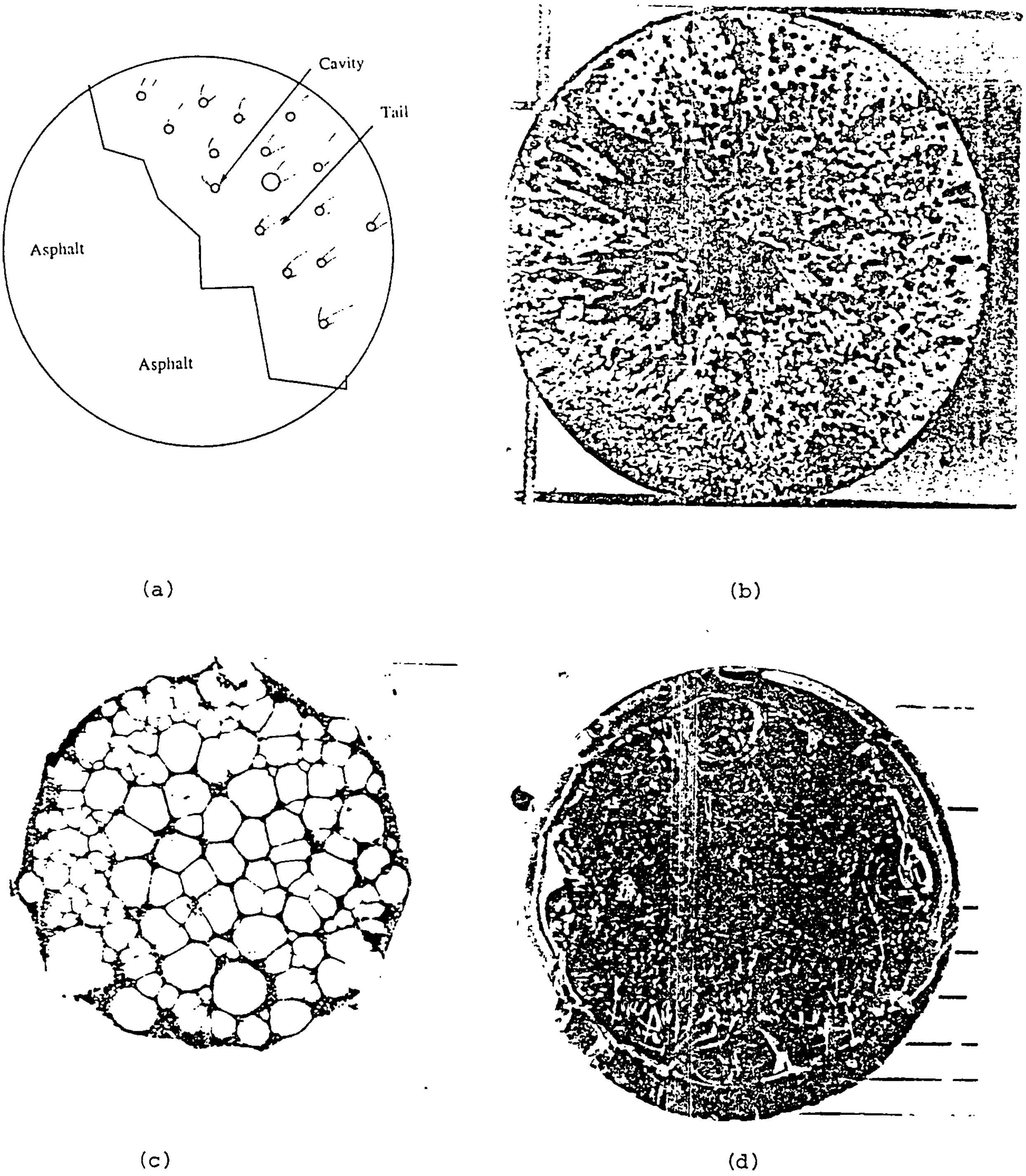

Figure 2.8: Fracture patterns observed in four failure modes of asphalts.

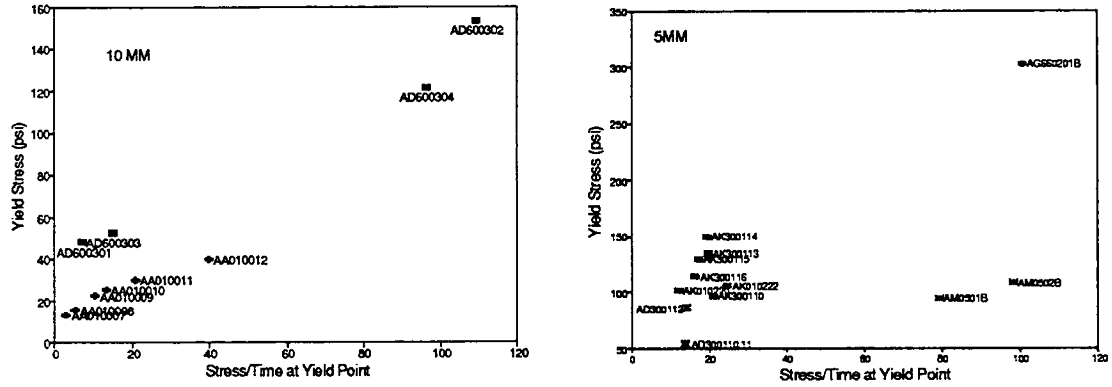

(a) Thickness: 10 mm

(b) Thickness: 5 mm

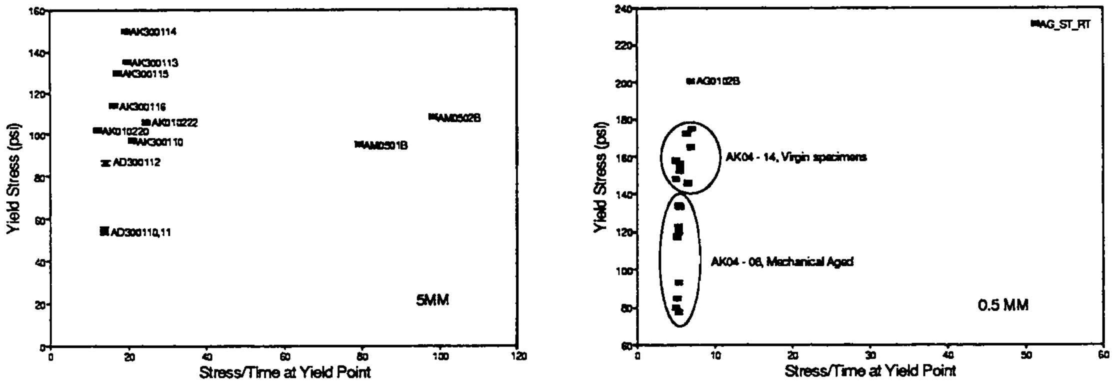

(c) Thickness: 5 mm

(d) Thickness: 0.5 mm

Figure 2.9: Comparison of yield strength at 60°F in tension tests for different asphalts.

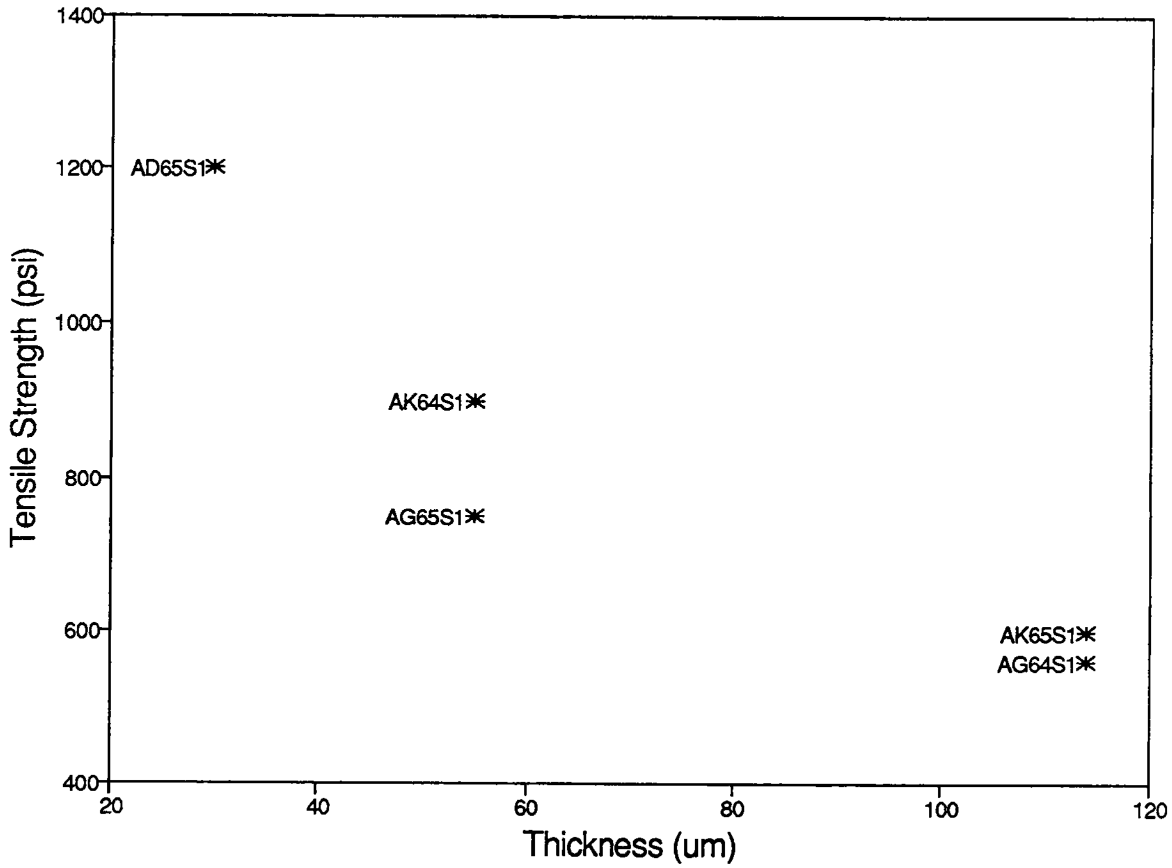

Figure 2.10: Comparison of tensile strength of different SHRP asphalts. Tests are controlled by stress and loading rate is 800 psi/s. Refer to Table 2.8 for details of specimen preparation.

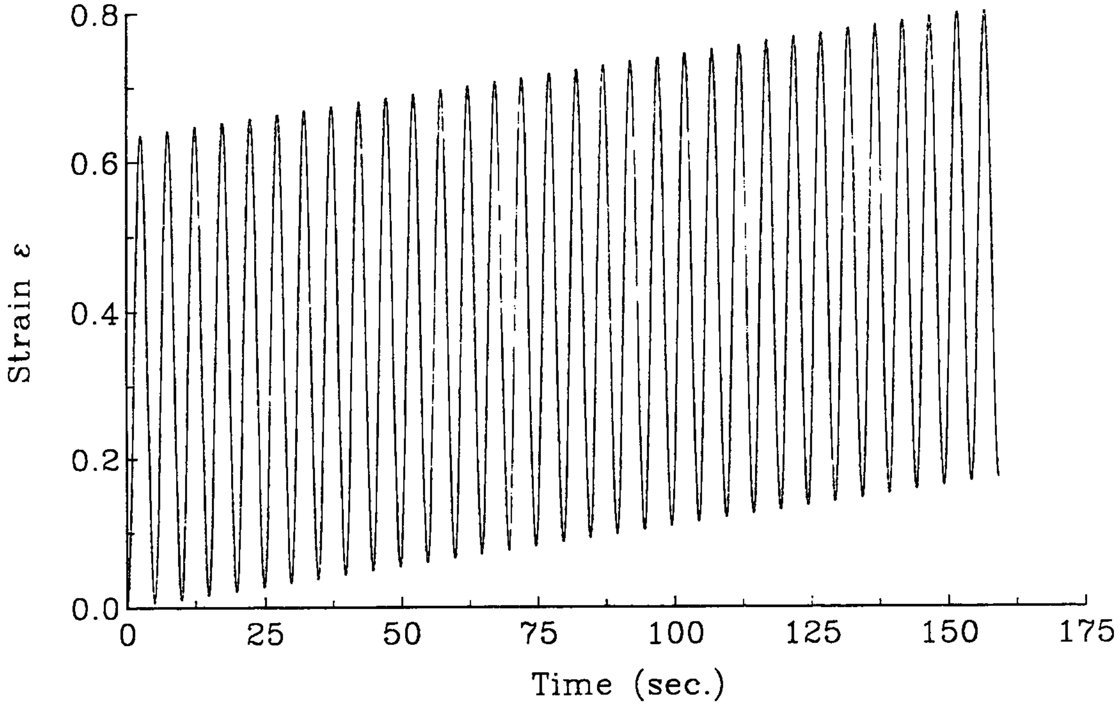

Figure 2.11: Stroke responses to Haver sinusoidal load of AAK-1 asphalt (AAK06) (frequency = 0.2 Hz, Temperature = 60°F, Loading Amplitude = 1.9×10^5 Pa).

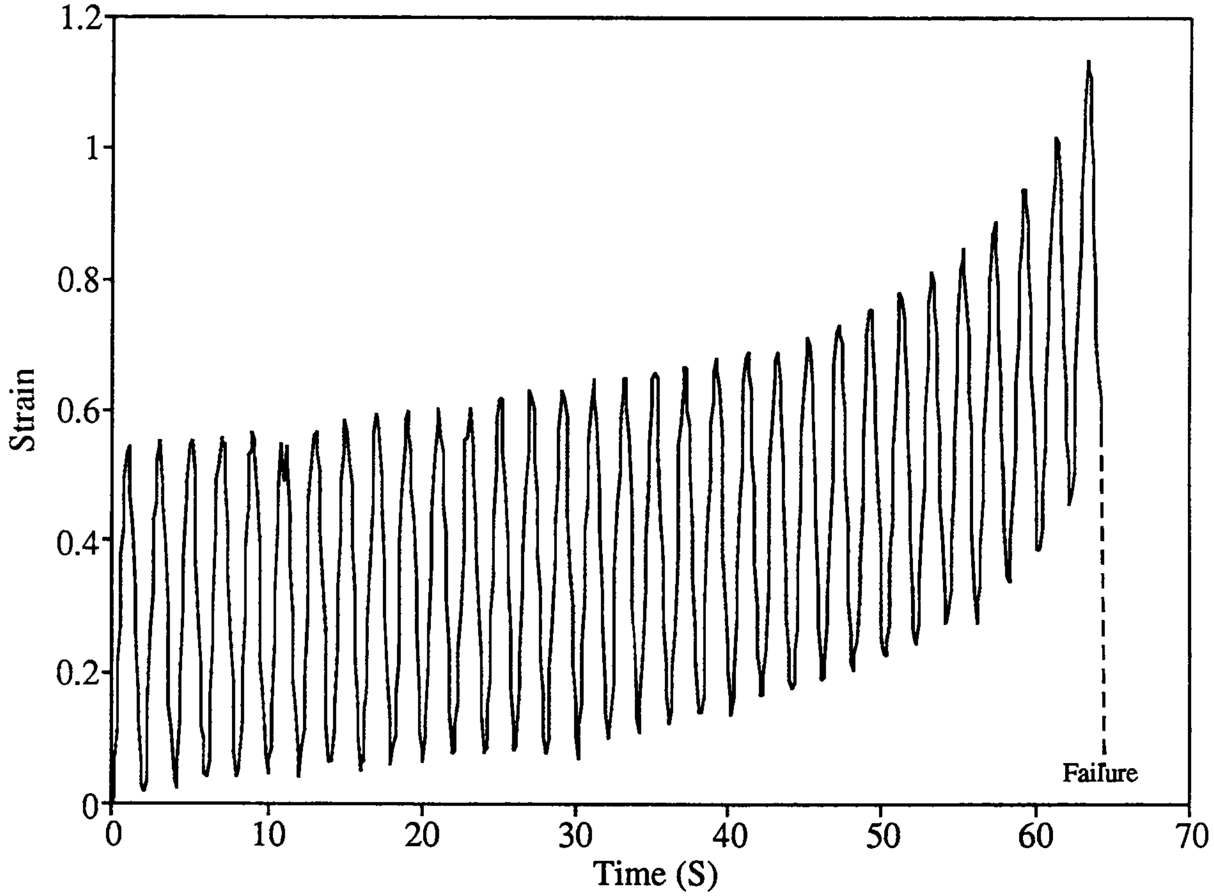

Figure 2.12: Stroke responses to Haver sinusoidal load of AAK-1 asphalt (AAK06) (frequency = 0.5 Hz, Temperature = 60°F, Loading Amplitude = 4.7 × 10^5 Pa).

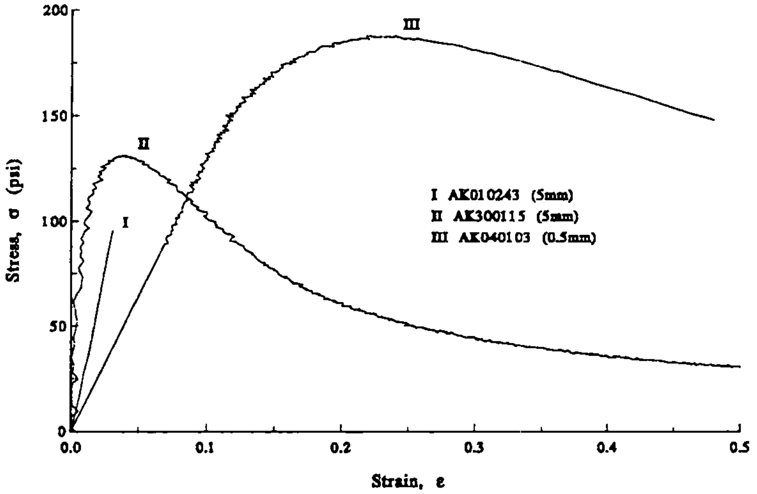

Figure 2.13: Characteristic stress–strain curves of asphalt Poker-Chip specimens

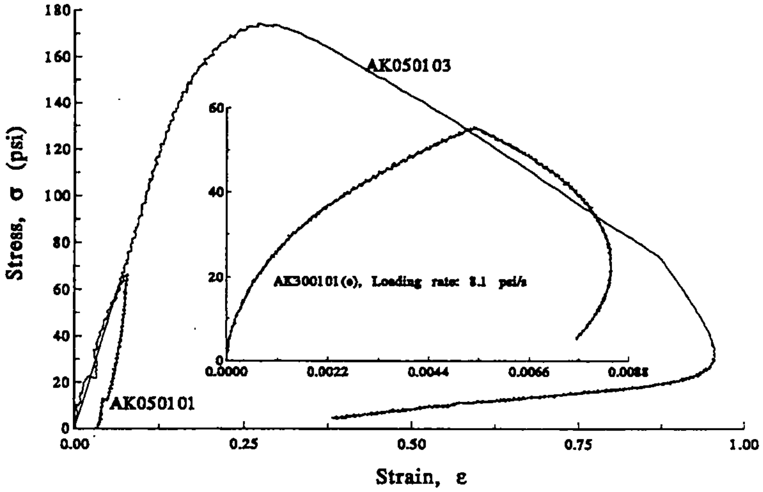

Figure 2.14: Hystereses of AAK-1 asphalt tested under stroke control and load control

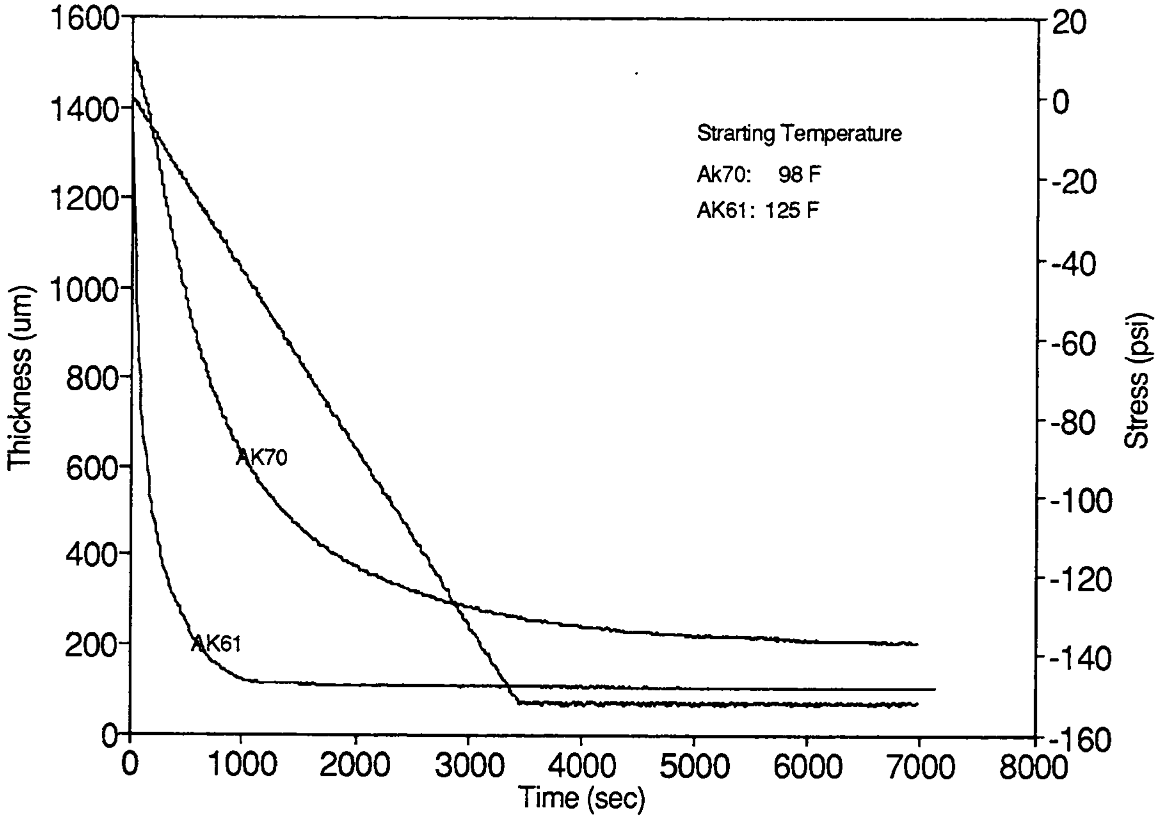

Figure 2.15: Evaluation of poker chip specimen preparation conditions–effect of casting temperature of specimen subject to load.

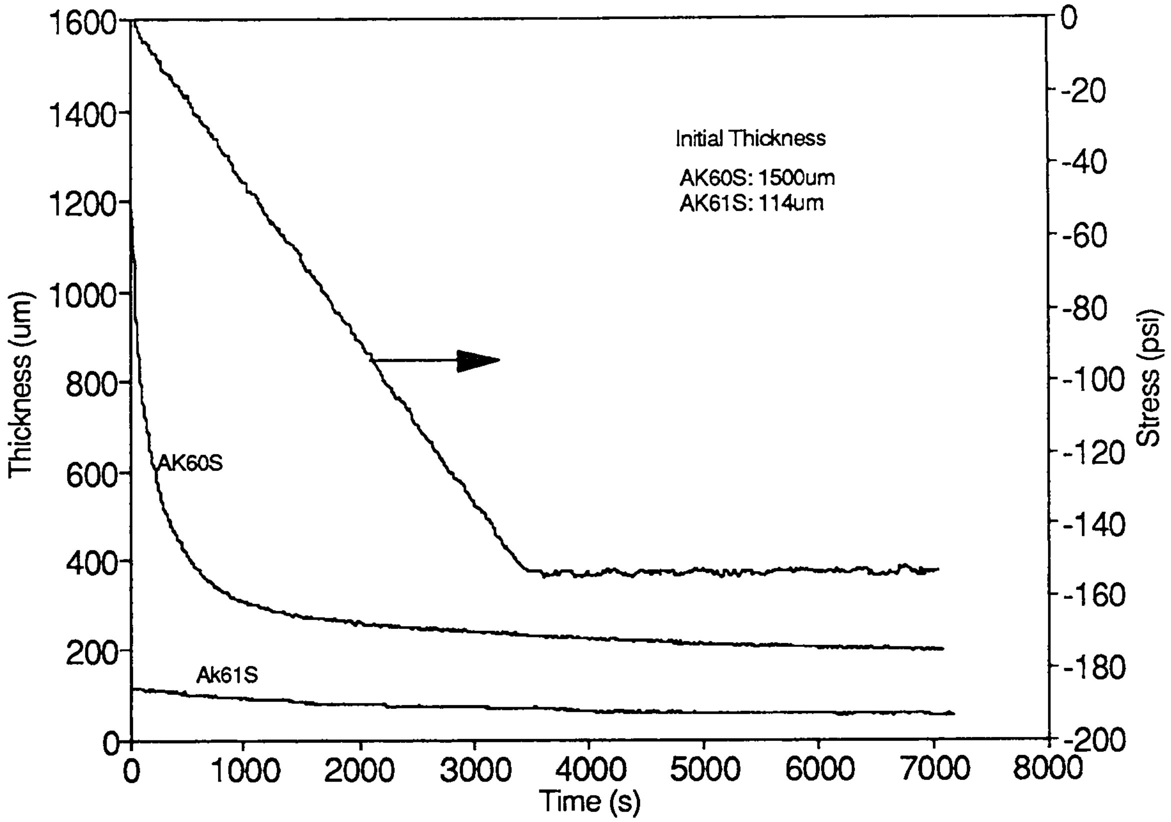

Figure 2.16: Evaluation of poker chip specimen preparation conditions–effect of film thickness when subjected to load.

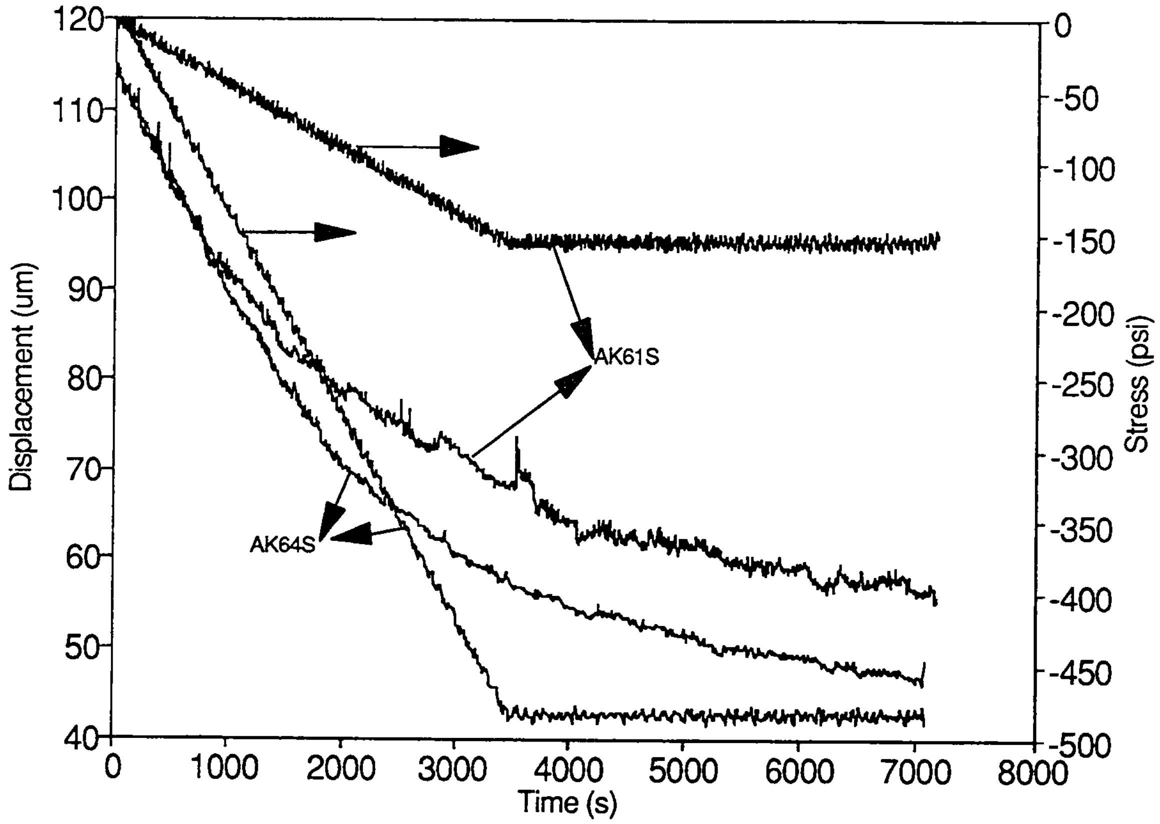

Figure 2.17: Effect of two different loading histories on amount of displacement.

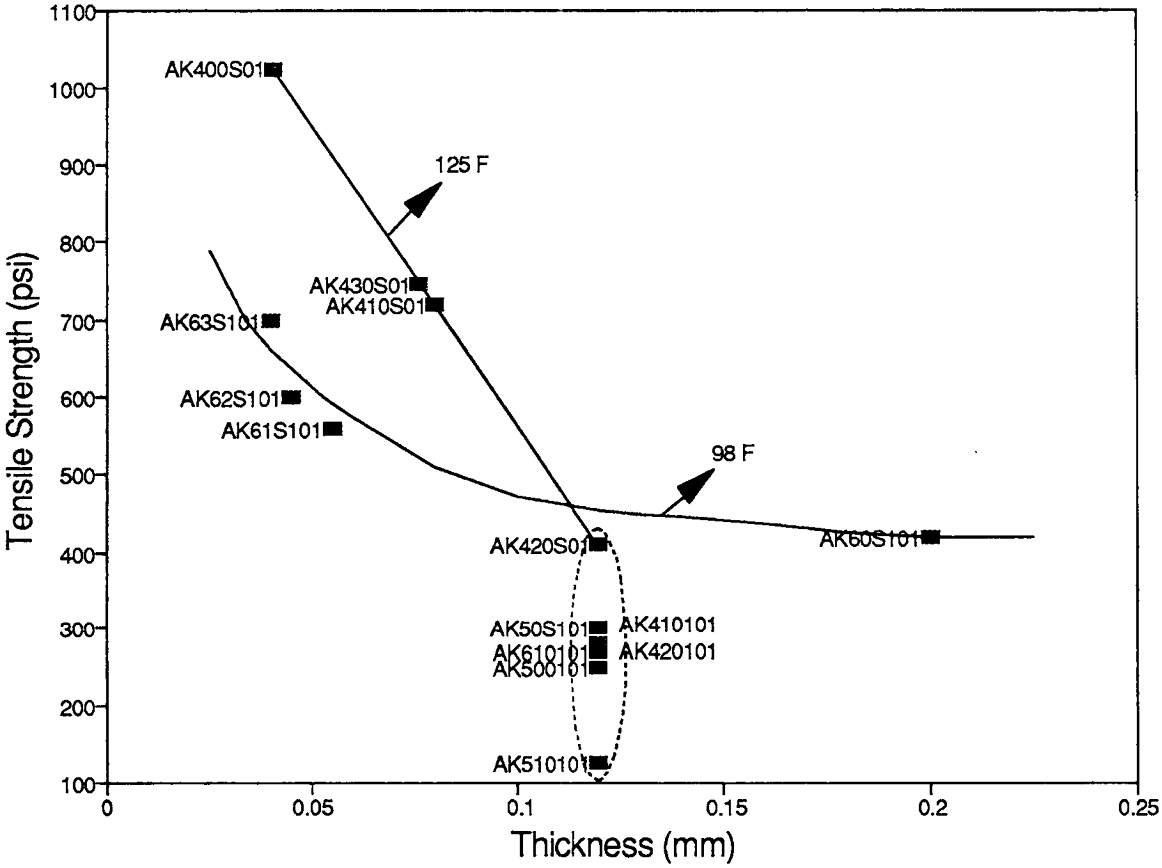

Figure 2.18: Influence of initial compression temperature in specimen preparation on the strength – thickness relation for AAK-1 asphalt. The numbers pointed by the arrows are the compression temperatures in specimen preparation. (cf. Section 2.5.3 and Table 2.9 for details about the data inside the dot-lined ellipse).

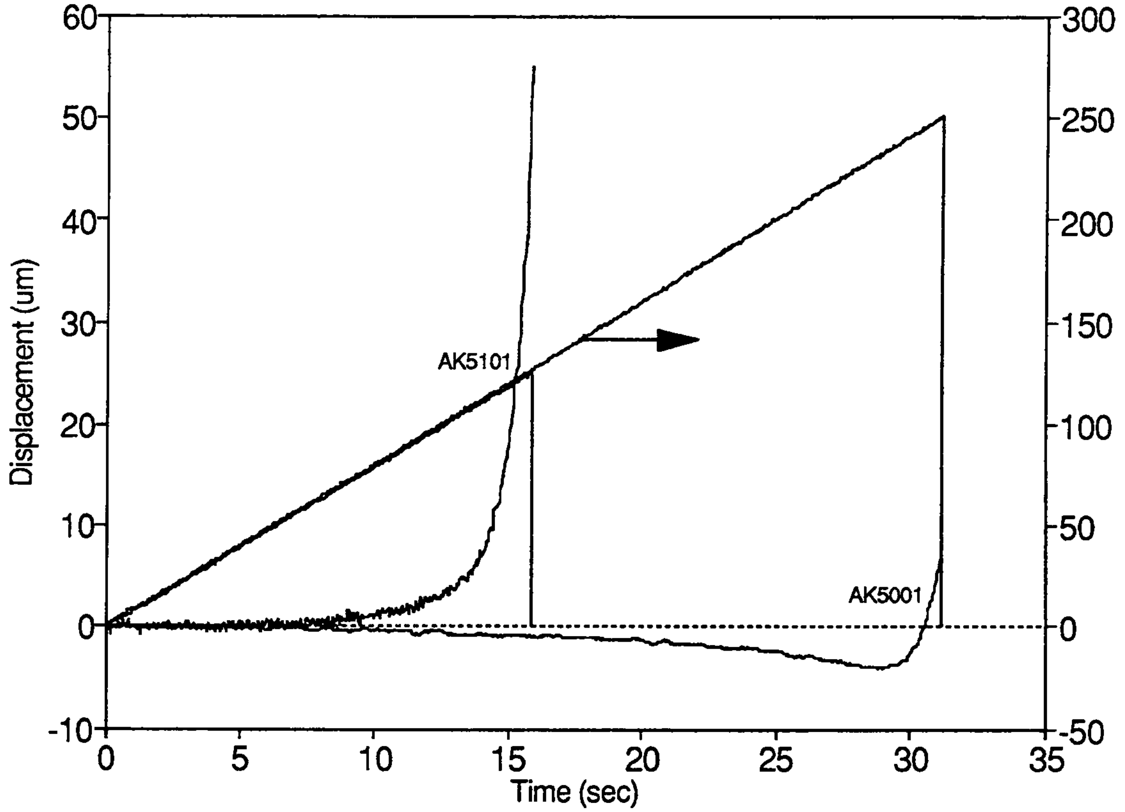

Figure 2.19: Tension tests for specimens of 6 in. diameter and thickness of 0.114 mm.

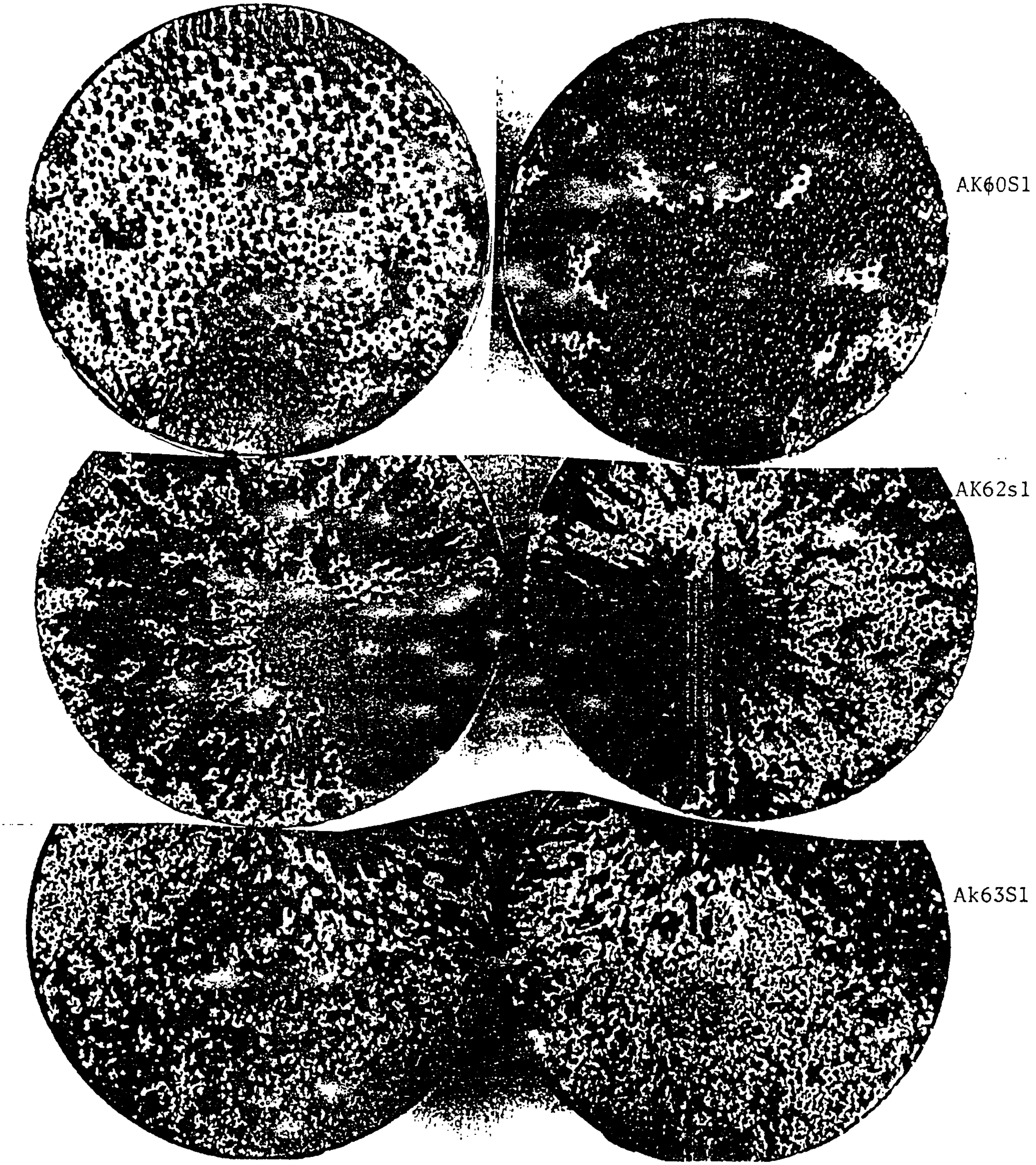

Figure 2.20: Variation of fracture pattern with thickness for 2 in. diameter specimens of AAK-1 asphalt.

Figure 2.21: Fracture pattern of AK51S prepared at high temperature (175°F).

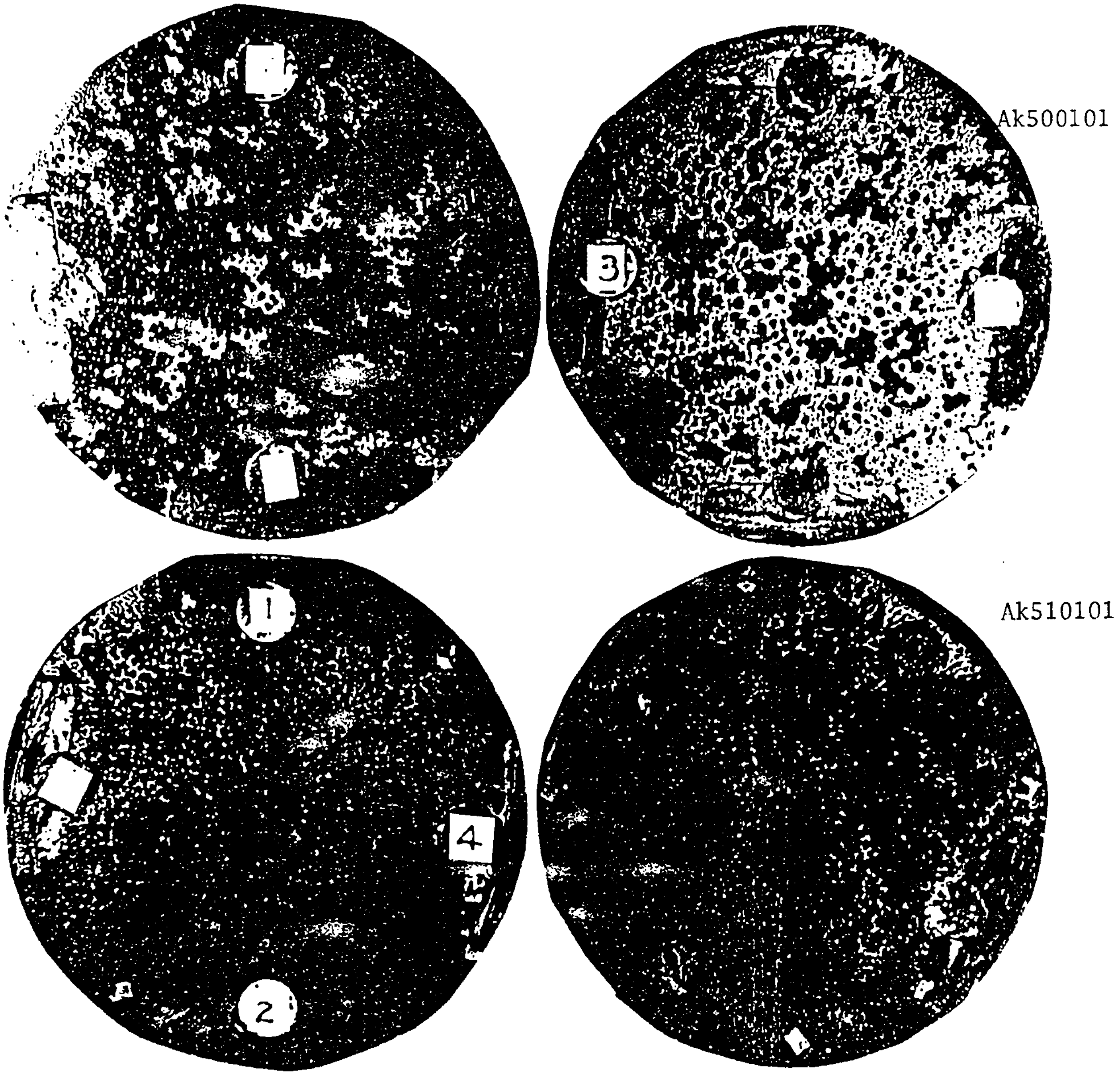

Figure 2.22: Fracture pattern of AK50 and AK51. Ak51 shows higher density of cavities.

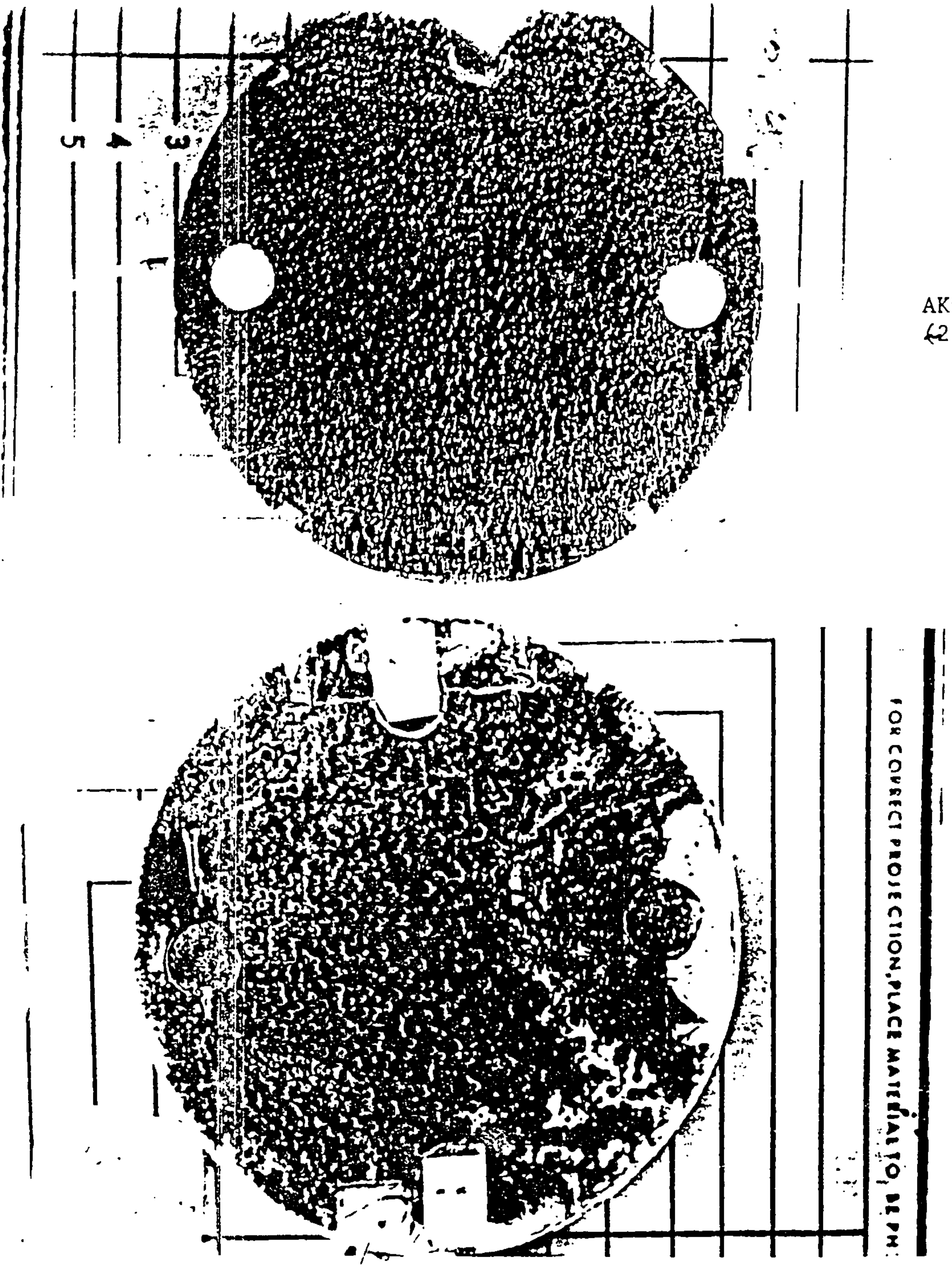

AK04
(2 hrs.)

AK07
(14 hours)

Figure 2.23: Effect of stabilization time on fracture surface of AAK-1 asphalt. Stabilization time for AK04 is about 2 hours, and AK07 about 14 hours.

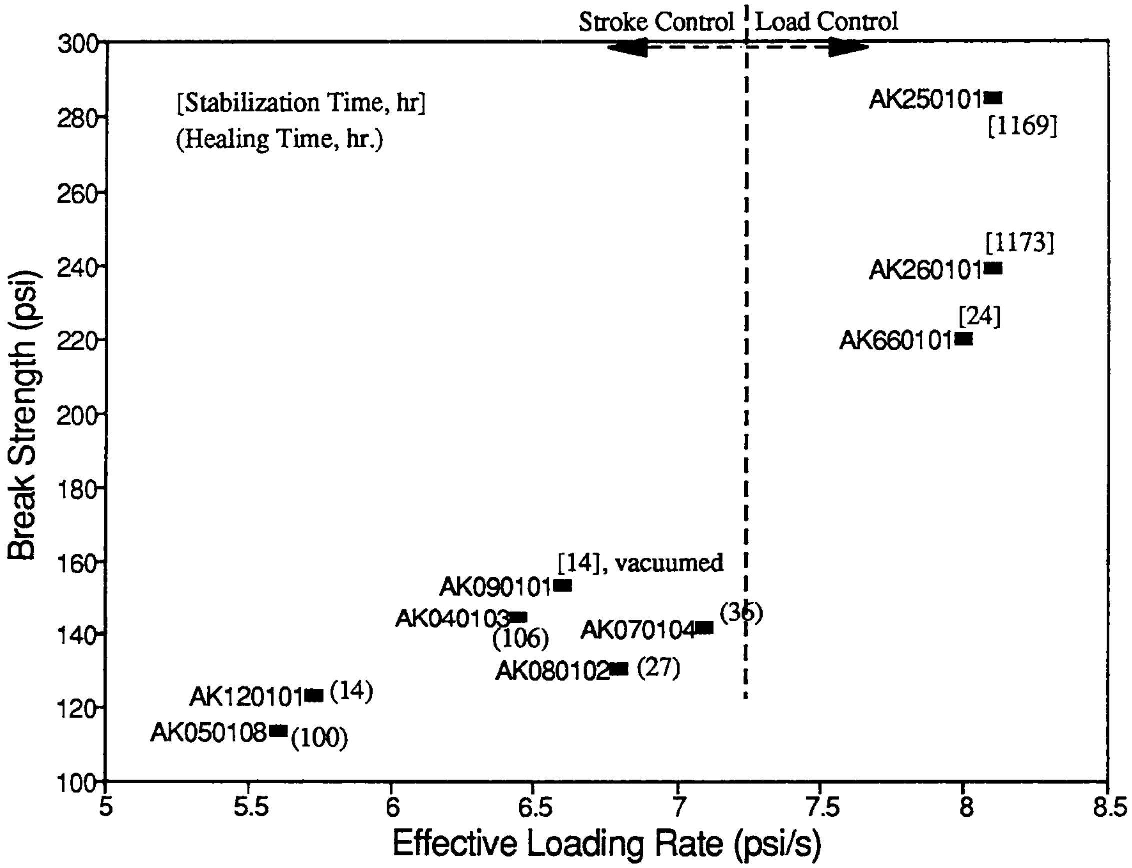

Figure 2.24: Influence of loading rate on break strength for 6 in. diameter and 0.5 mm thick specimens of AAK-1 asphalt. $\dot{\sigma}_{eff} = \sigma_y/t_y$ for stroke controlled tests.

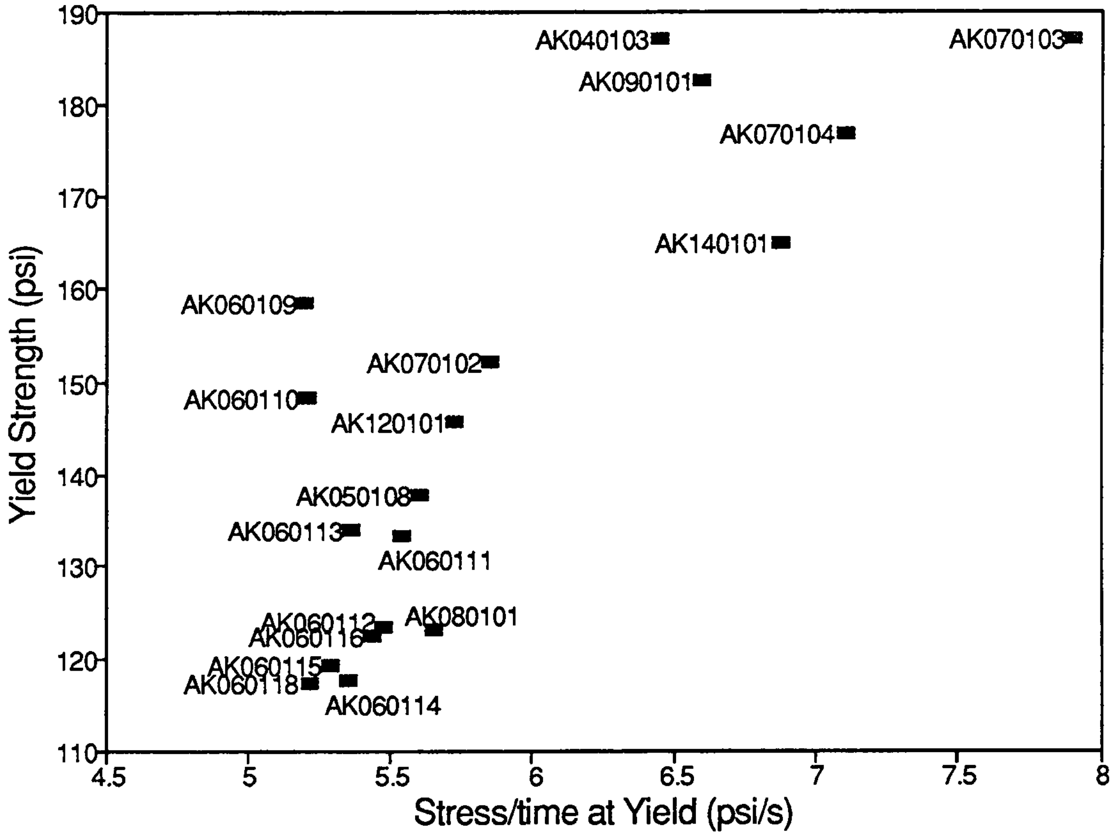

Figure 2.25: Influence of effective loading rate on yield strength for 6 in diameter and 0.5 mm thick specimens of AAK-1 asphalt in tension tests at 60°F. $\dot{\sigma}_{eff} = \sigma_y / t_y$.

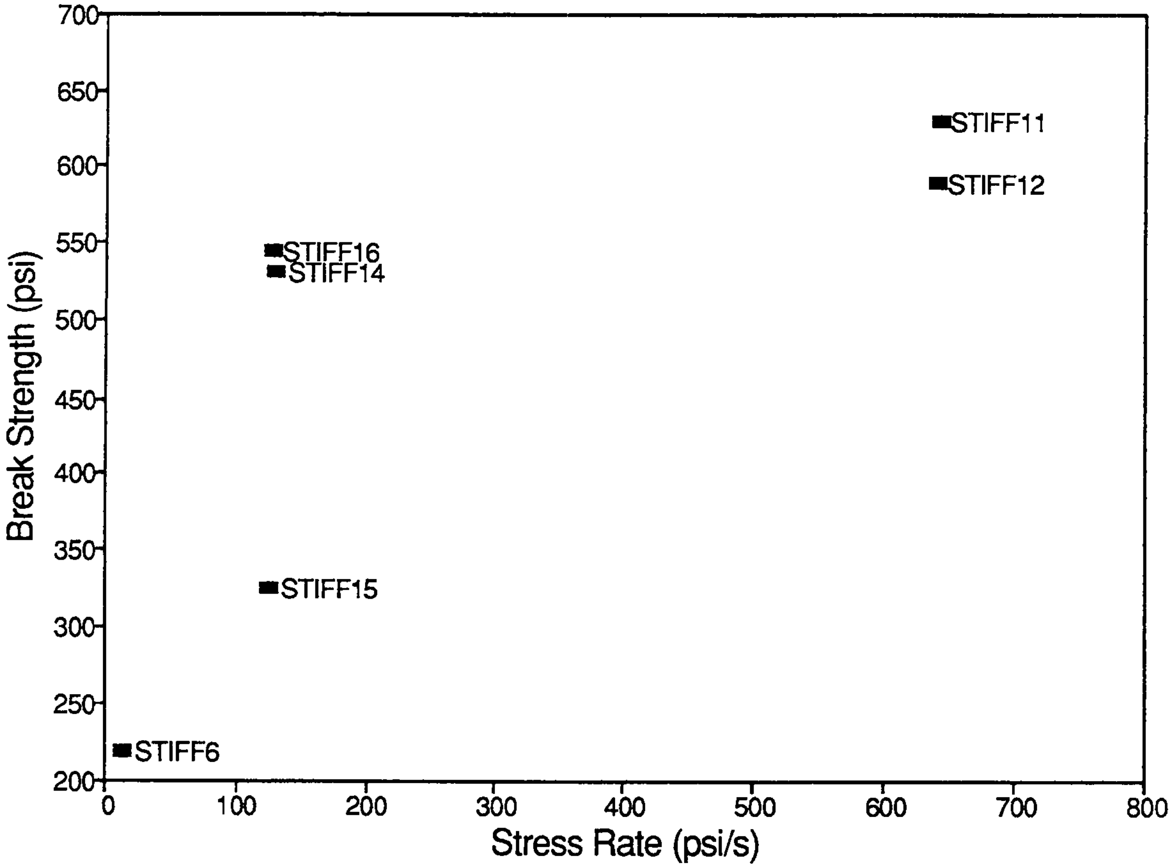

Figure 2.26: Influence of loading rate on break strength for 2 in. diameter and 0.24 mm thick specimens of AAK-1 asphalt tested at room temperature (~ 78°F).

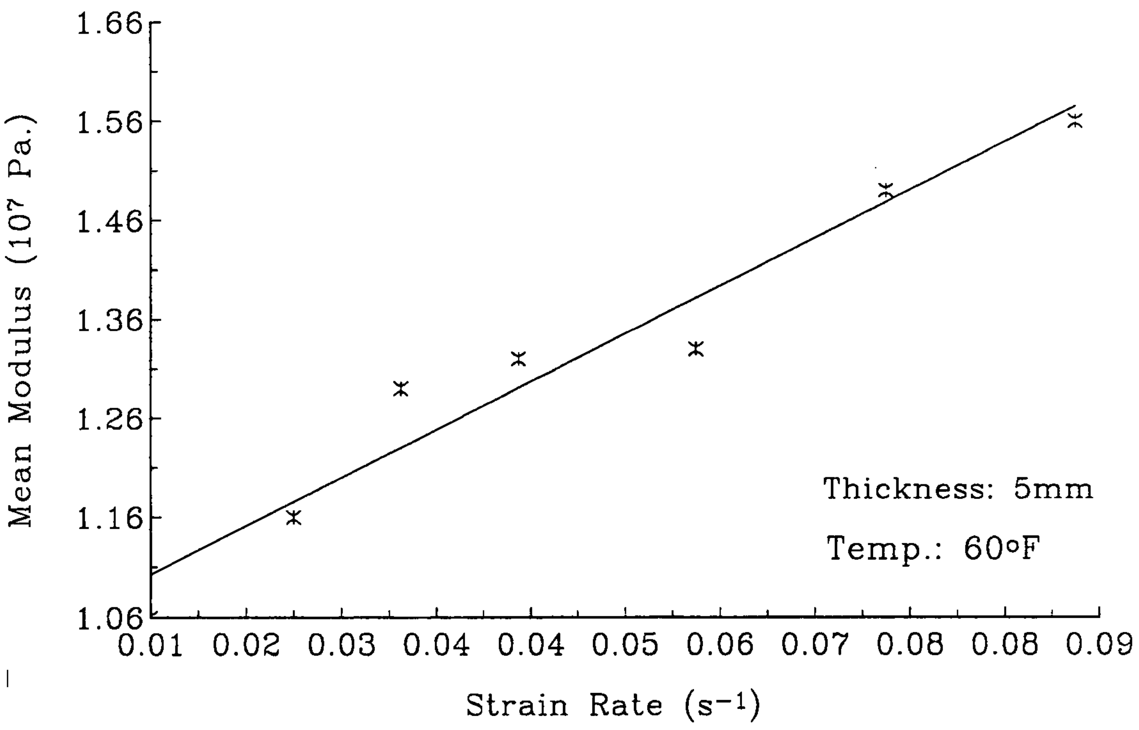

Figure 2.27: Stroke rate dependence of mean modulus of AAK-1 asphalt in compression tests.

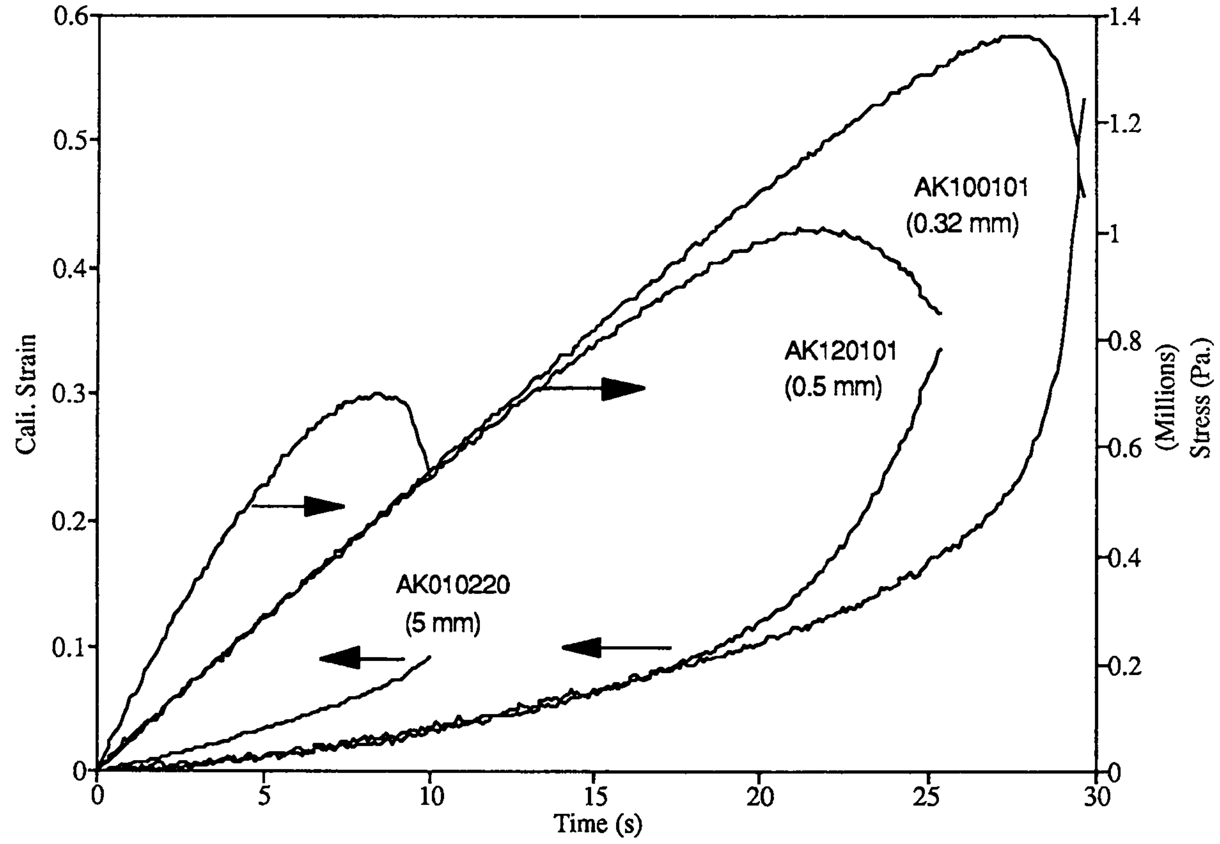

Figure 2.28: Influence of specimen thickness on mechanical properties of butt-joint AAK-1 specimen. Numbers inside the parentheses are specimen thickness.

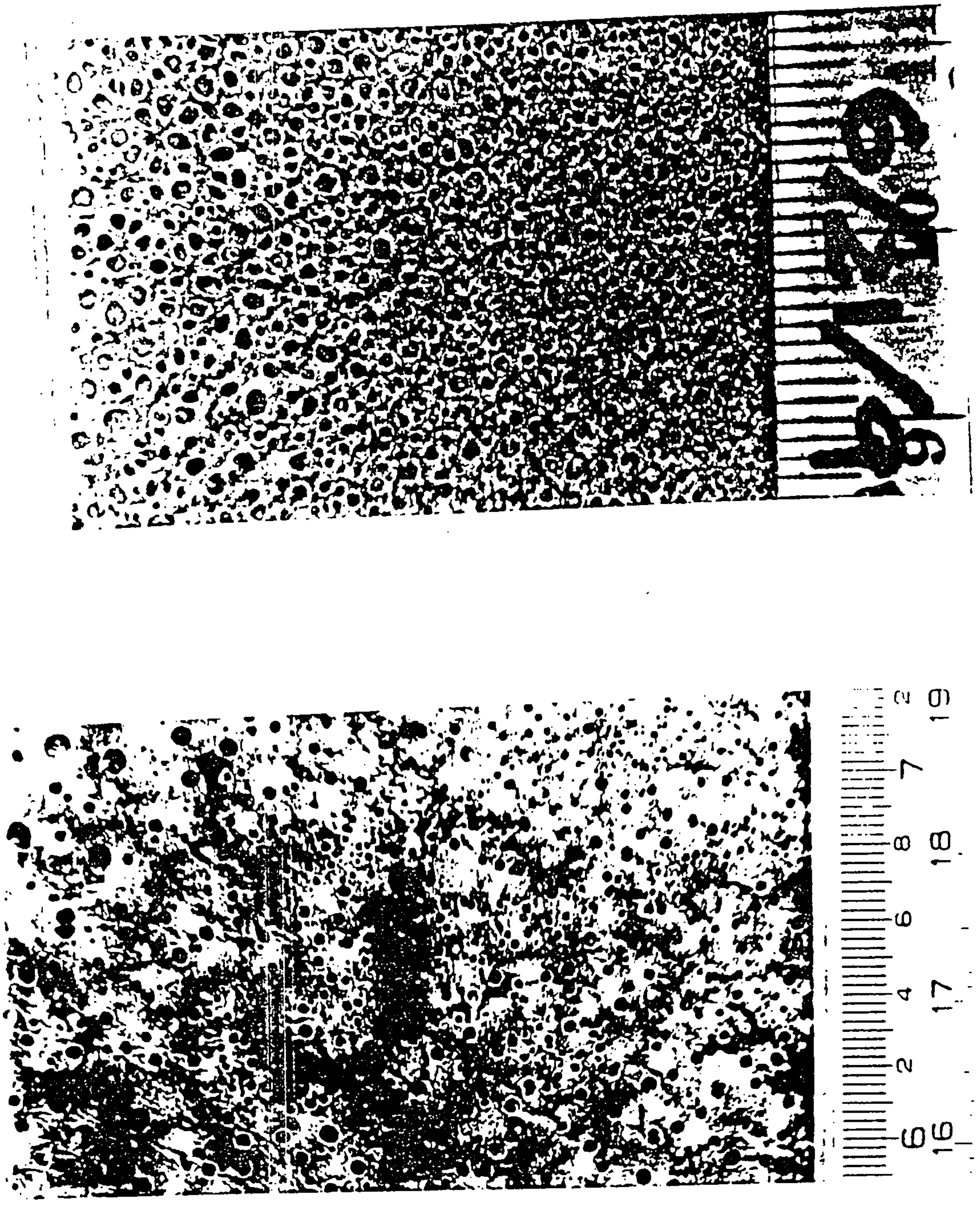

AK10
(0.32mm)

AK09
(0.5mm)

Figure 2.29: Fracture surfaces of AAK-1 specimens with different thickness.

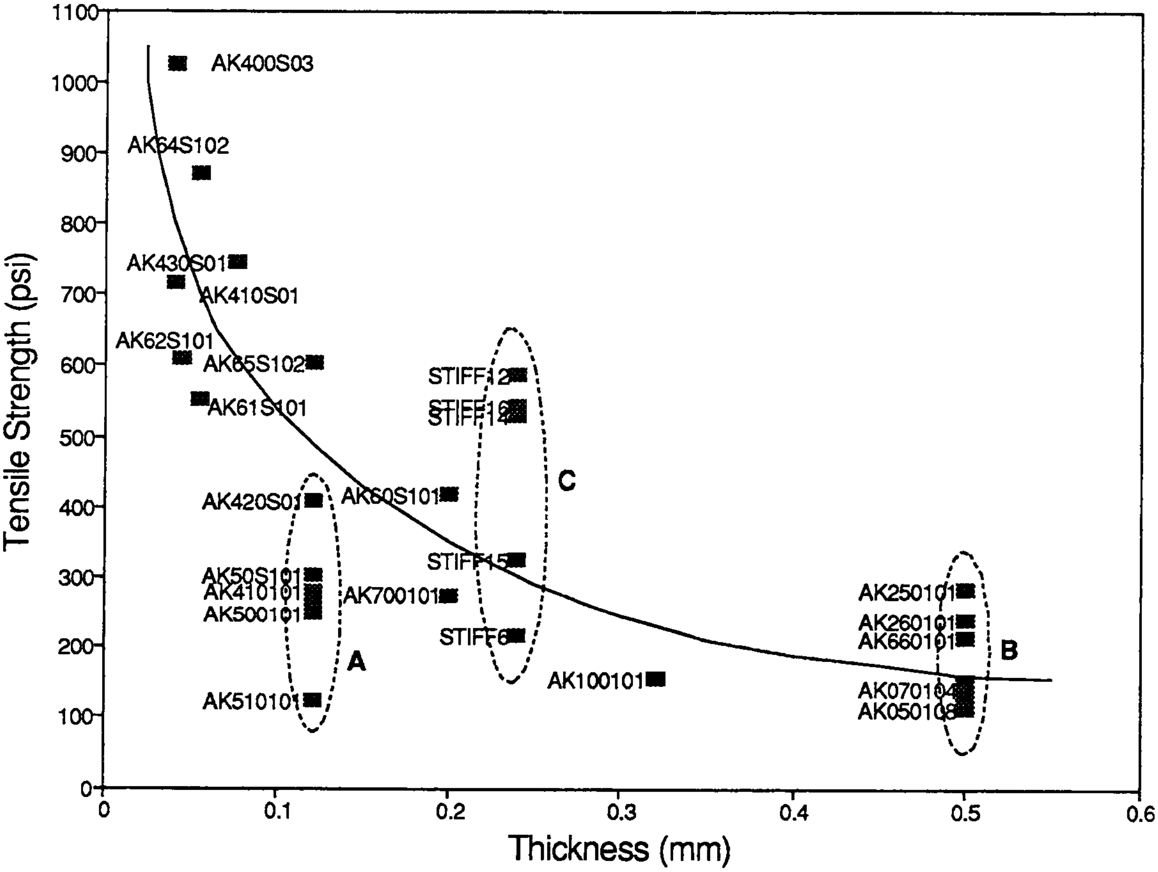

Figure 2.30: The overall trend of the influence of thickness on the break strength of AAK-1 asphalt in tensile tests. (cf. Section 2.5.3 and Table 2.9 for details about Group **A**, Section 2.5.5 and Figures 2.24, 2.26 for Groups **B** and **C**.)

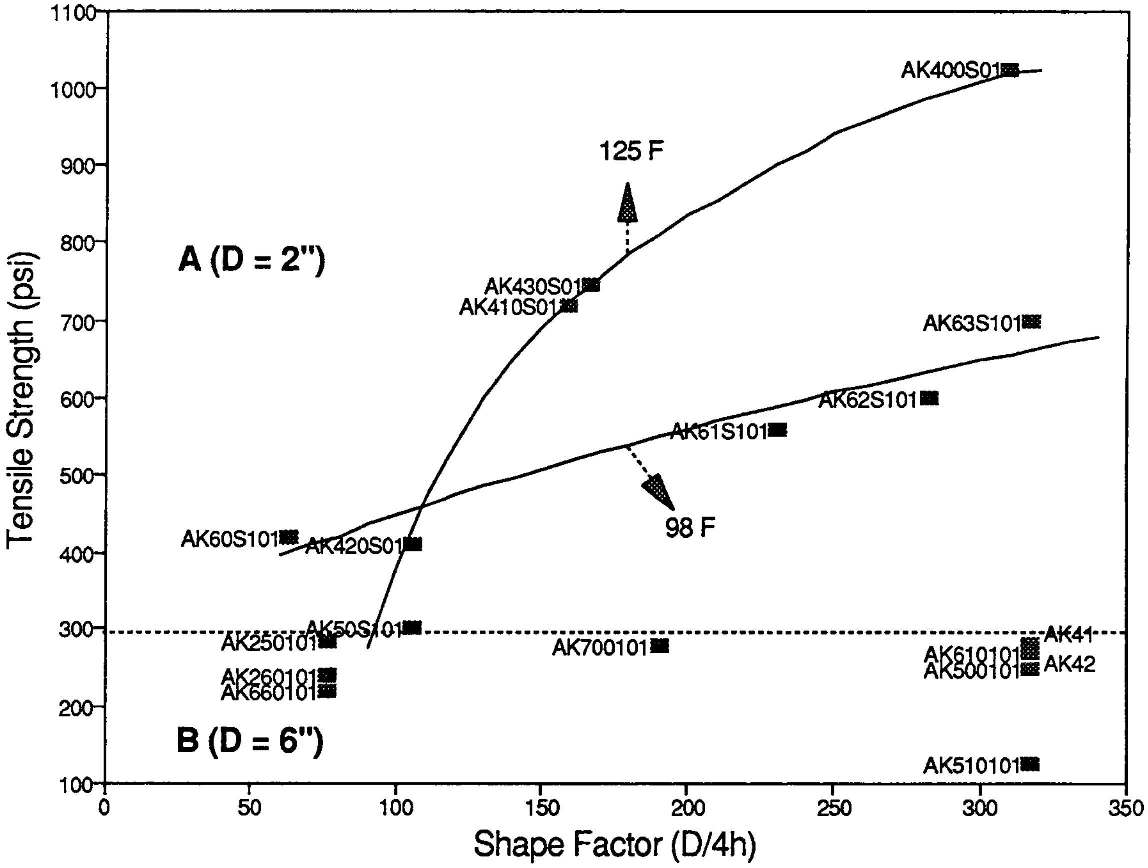

Figure 2.31: The break strength change of AAK-1 asphalt with shape factor in load controlled ($\dot{\sigma} = 8.1$ psi/s) tensile tests at 60°F. The numbers pointed by the arrows are the compression temperatures in specimen preparation.

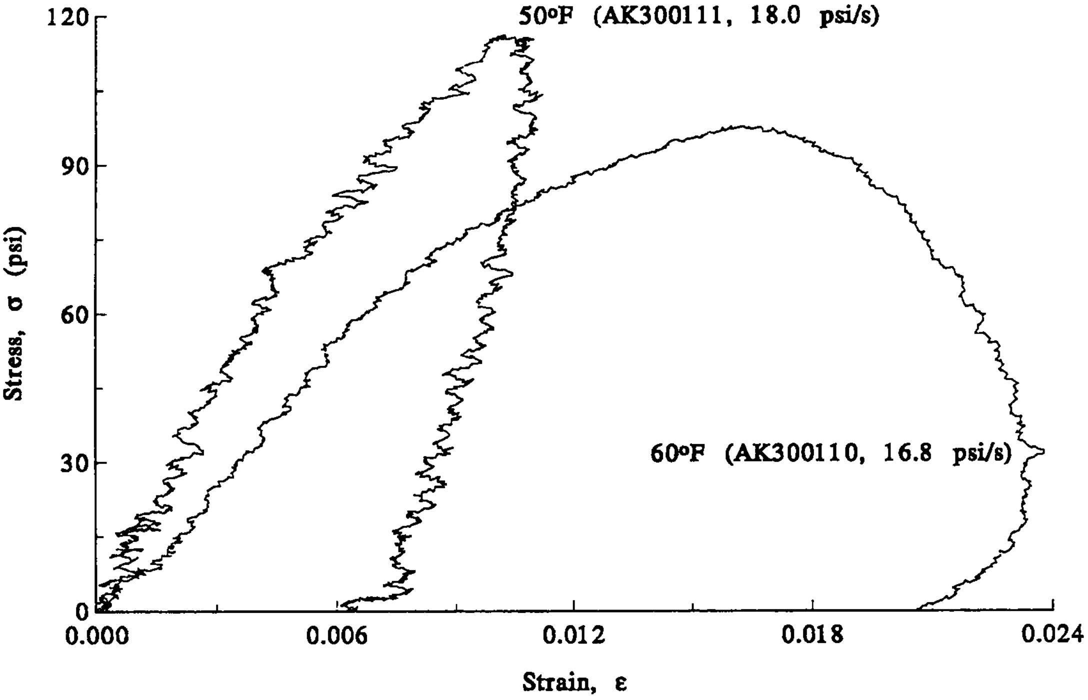

Figure 2.32: Influence of temperature on the tensile property of AAK-1 asphalt. Data inside parentheses are the effective loading rates upto one second of pulling.

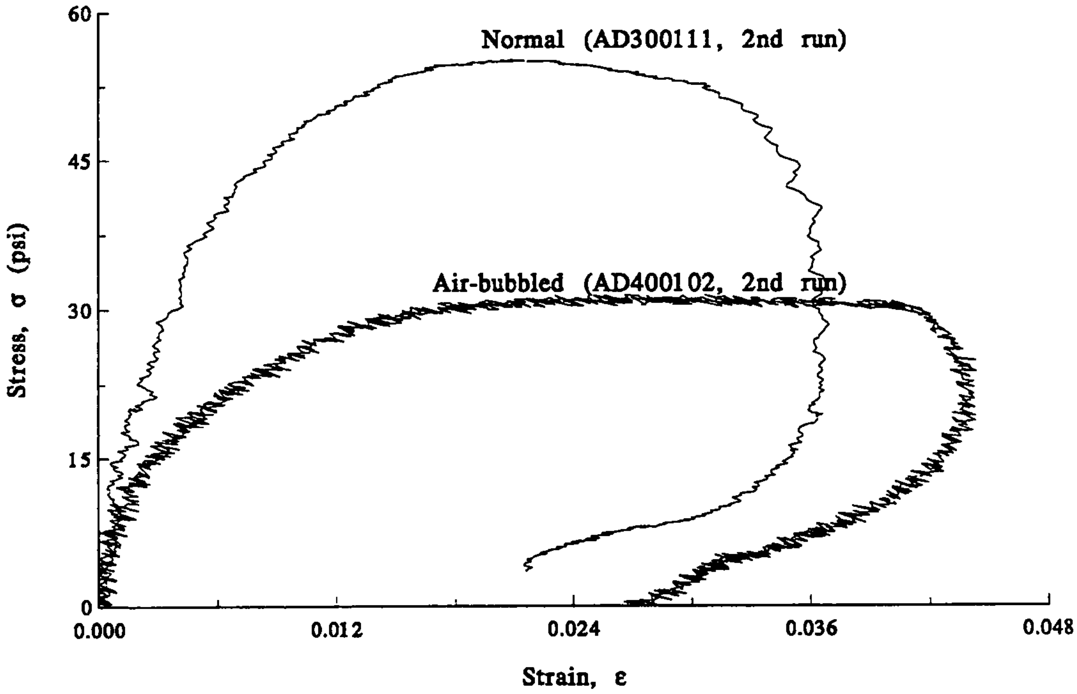

Figure 2.33: Influence of air bubbles to the tensile property of AAD-1 asphalt.

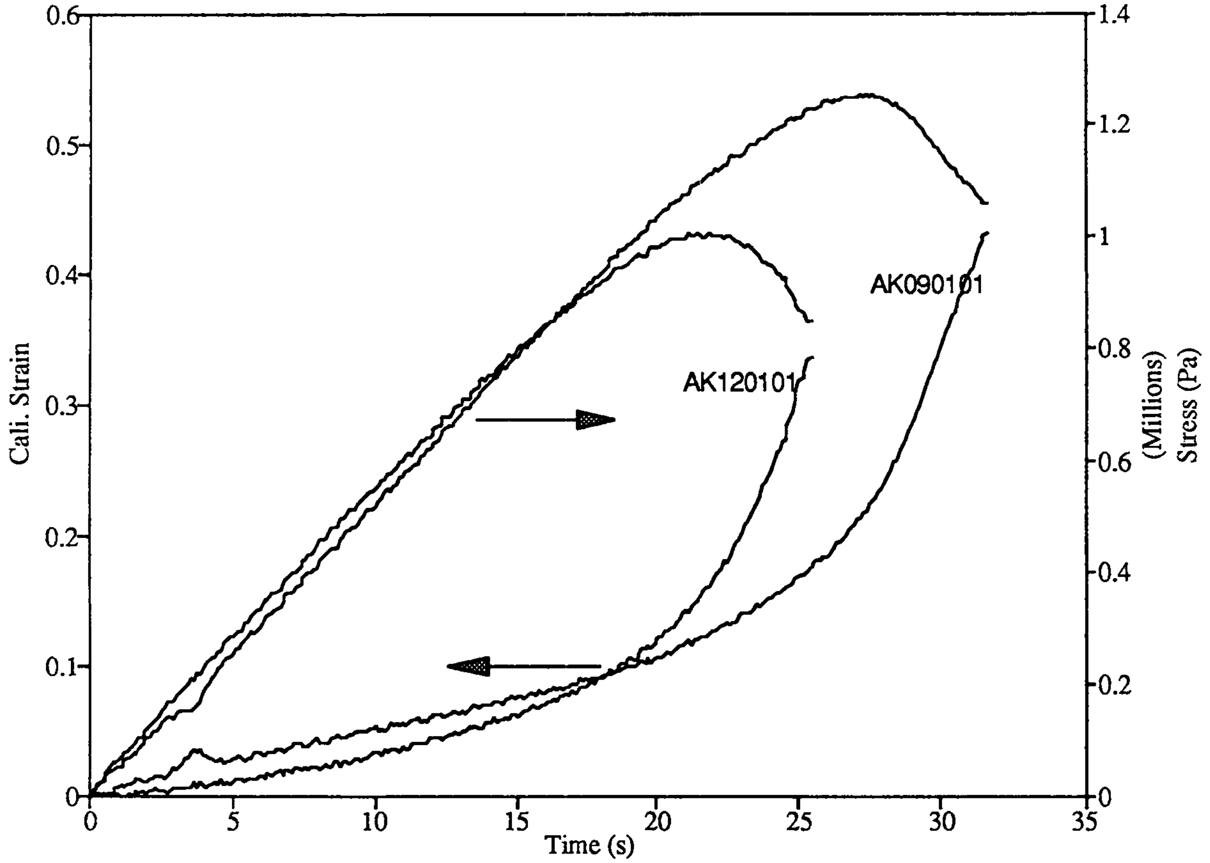

Figure 2.34: Comparison of mechanical behavior for regular and vacuumed AAK-1 asphalt (0.5mm thickness) in butt-joint tension test.

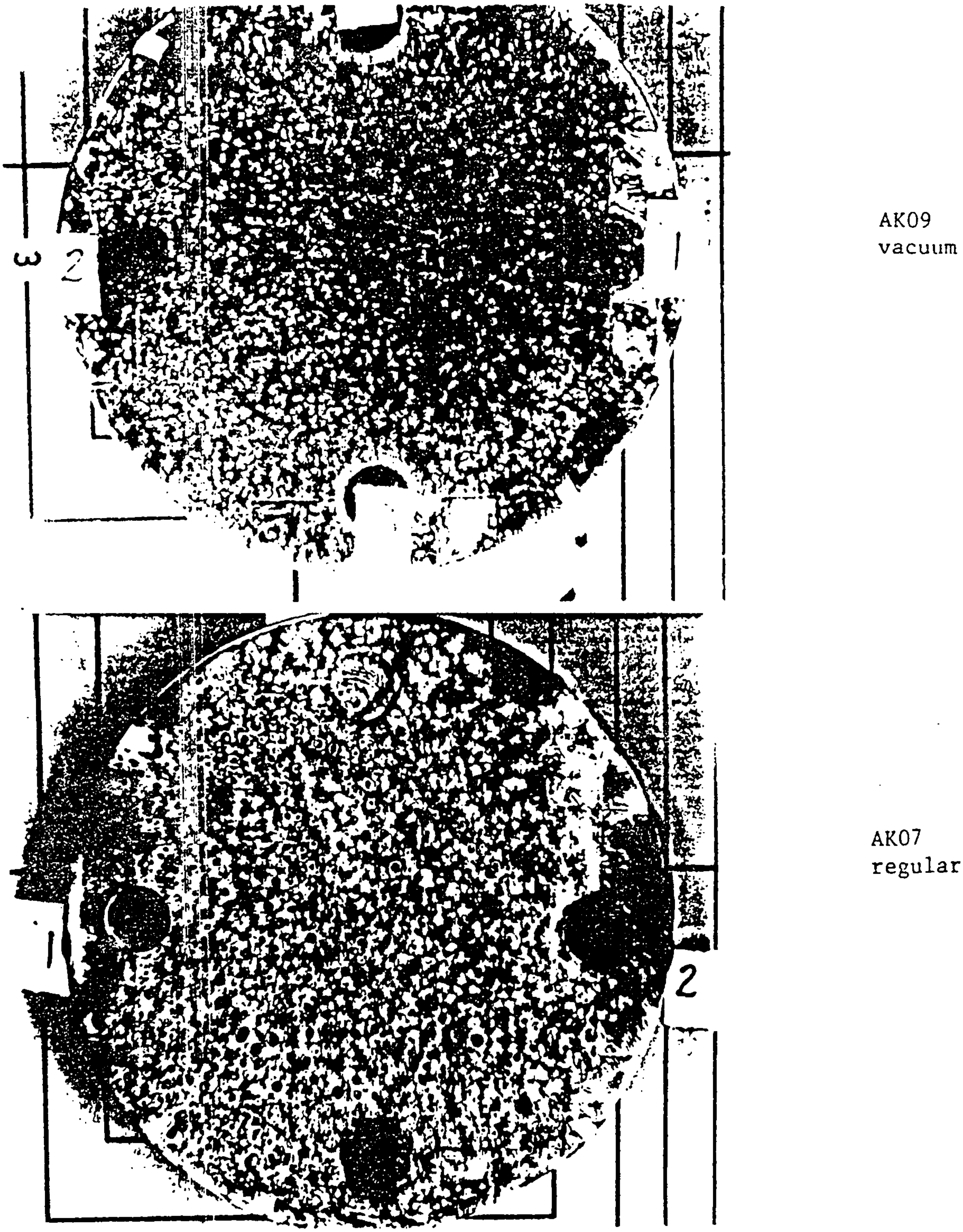

Figure 2.35: Size and density of air bubble showed in fracture surfaces for regular and vacuumed AAK-1 asphalt.

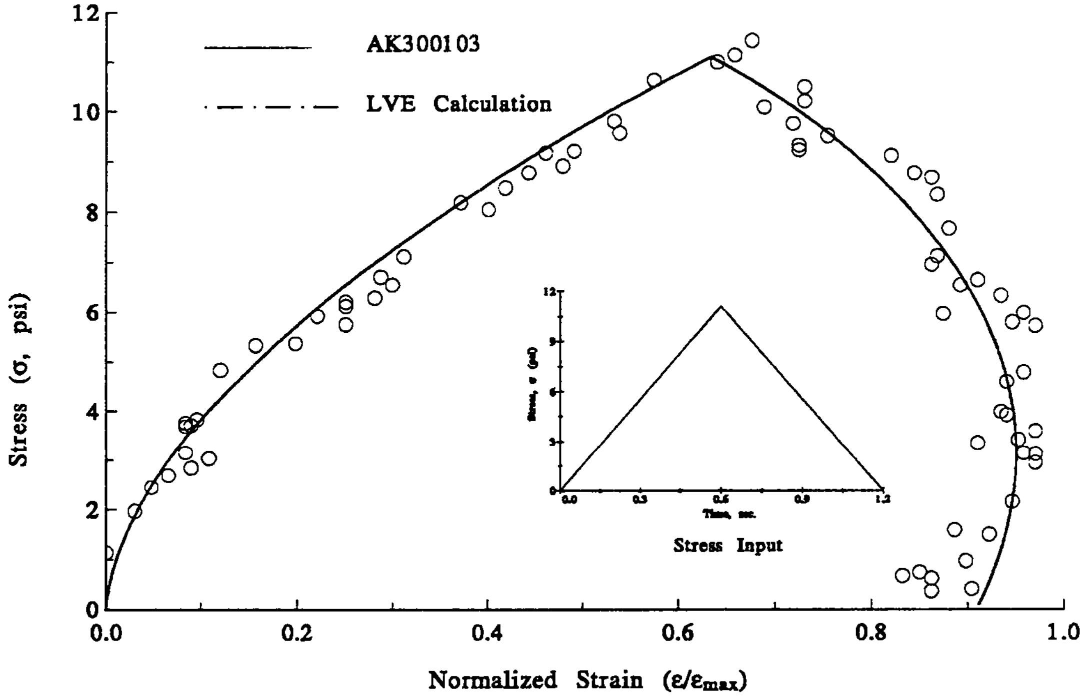

Figure 2.36: Comparison of linear viscoelastic (LVE) calculation with stress – strain relation of AAK-1 asphalt in the tensile test (AK300103) controlled by load. Both have the same loading rate (18.5 psi/s) and the same time scale.

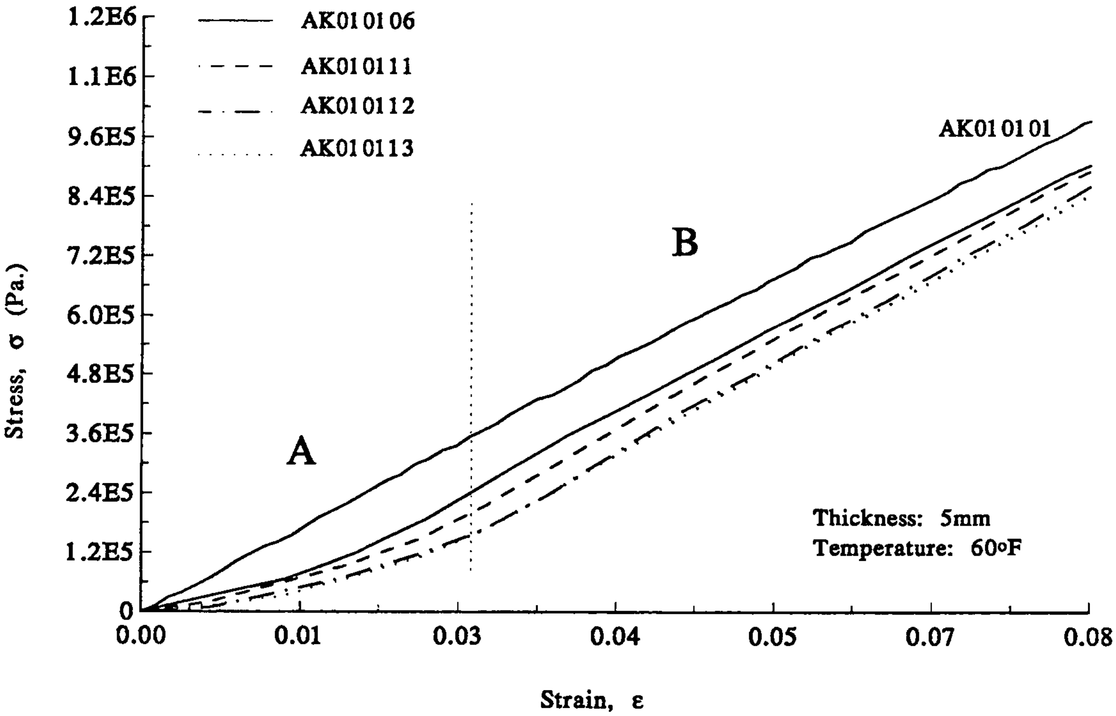

Figure 2.37: Compressive stress-strain curves for different runs of the same specimen of AAK-1 asphalt.

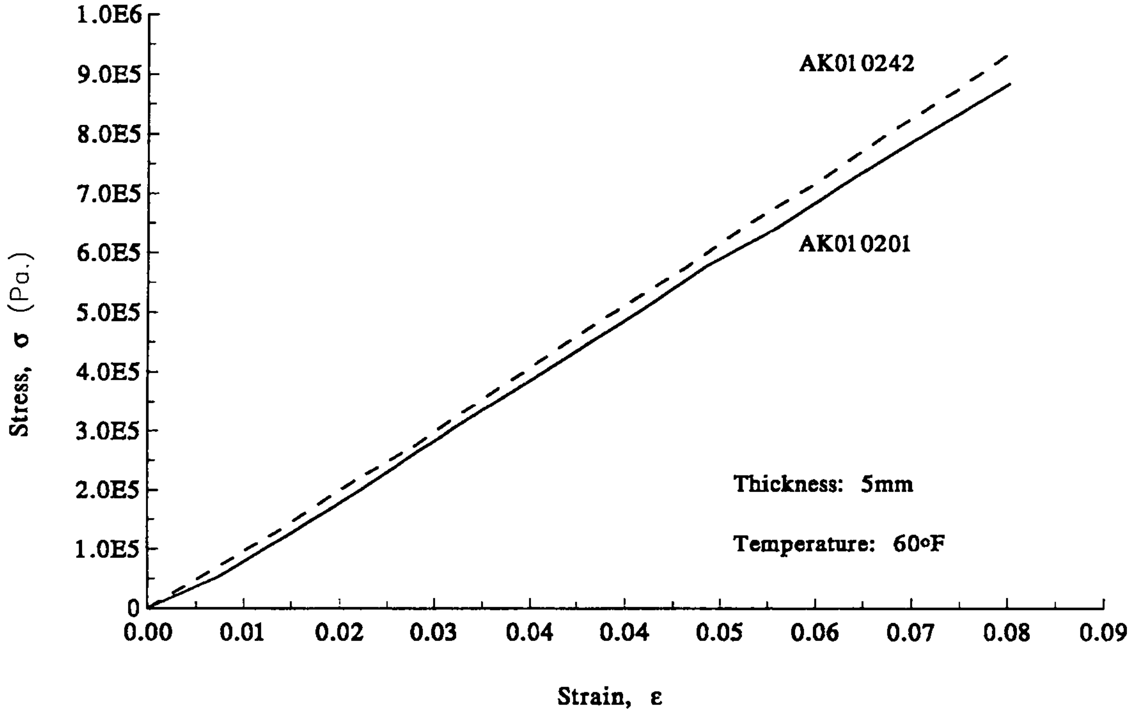

Figure 2.38: Compressive stress-strain curves for different specimens of AAK-1 asphalt.

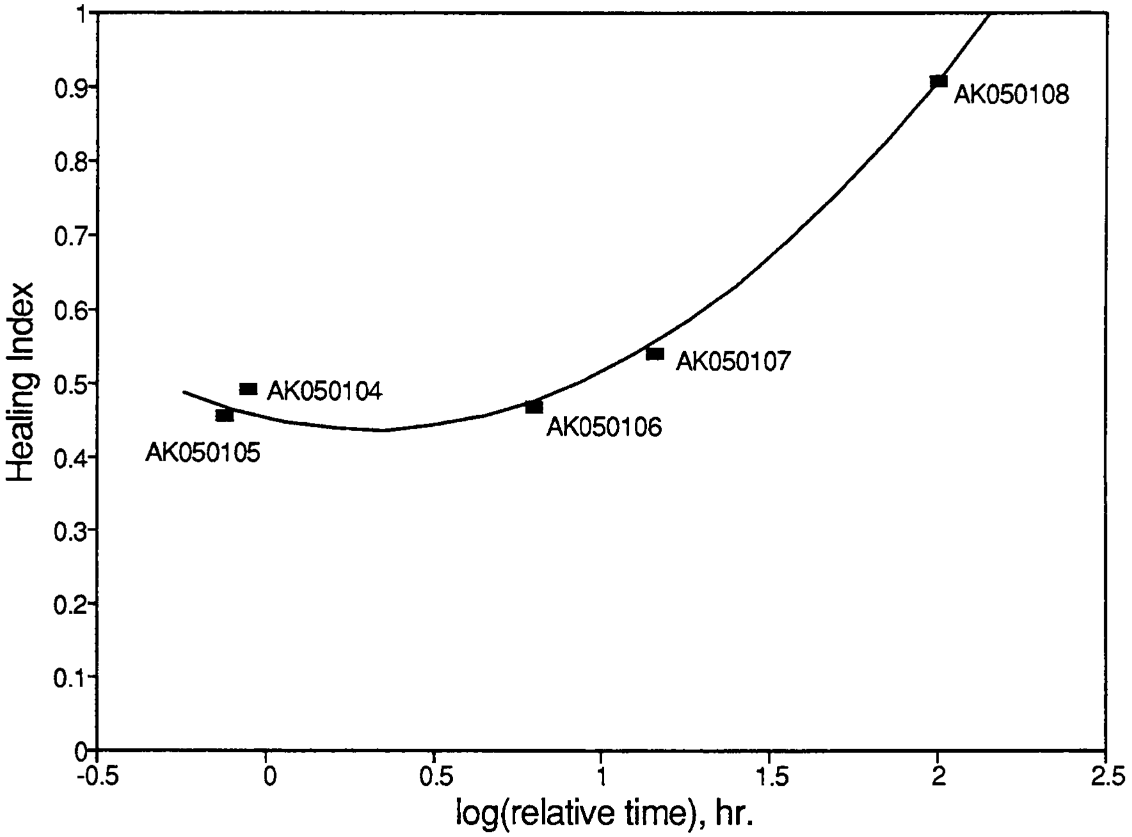

Figure 2.39: The healing process of AAK-1 asphalt (AK05010n). The healing index defined as $\sigma_y(n)/\sigma_y(n_\circ)$, where n is the run number and $n_\circ$ is the first run past yield point.

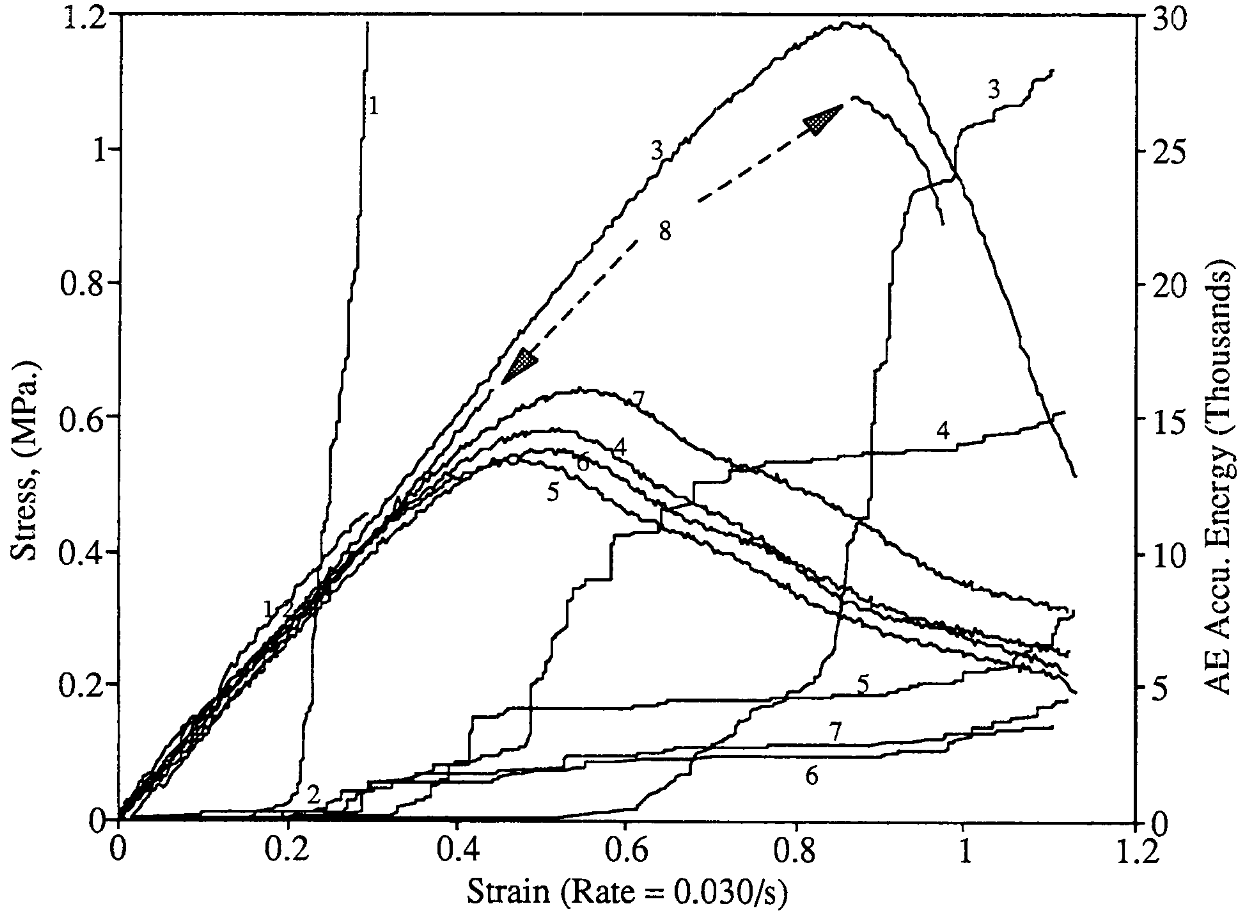

Figure 2.40: The healing process of AAK-1 asphalt (AAK05010n) characterized by the AE energy and the mechanical behavior. The healing time is presented in Figure 2.39 as the x-coordinate.

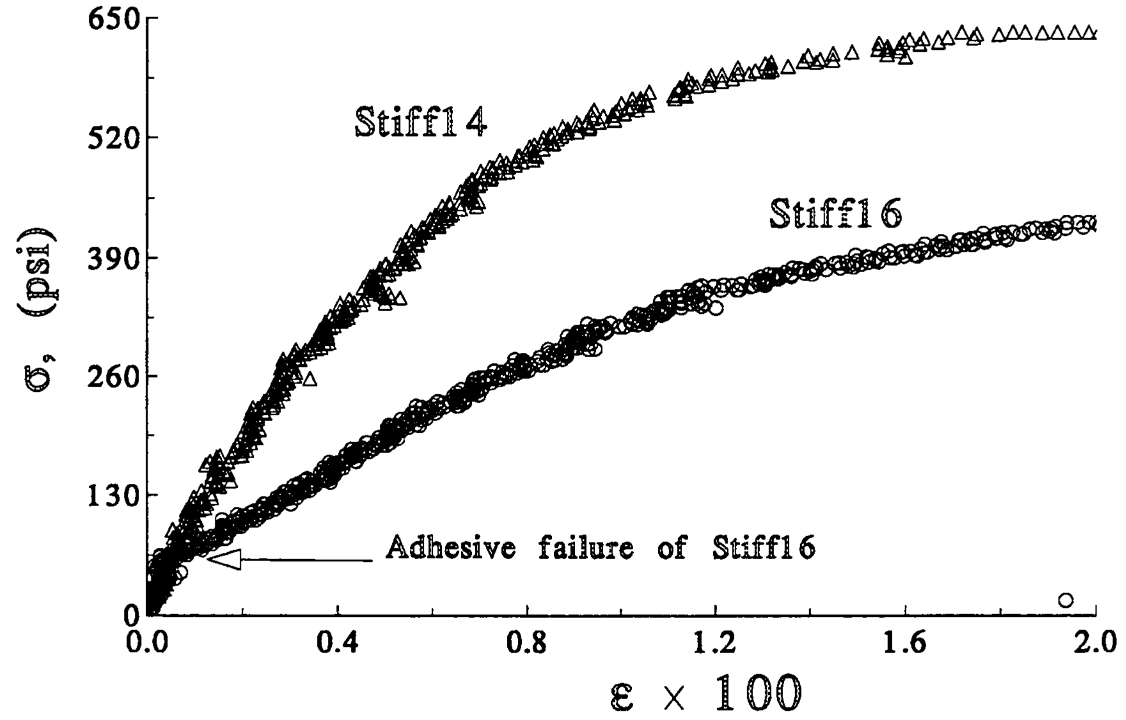

Figure 2.41: Stress-strain curves of 2 inch diameter specimens of AAK-1 asphalt in the tension test of Poker-Chip specimen with load control ($\dot{\sigma}$ = 127 psi/s) and at room temperature (~ 78°F).

References

1. SHRP A-002B (USC), "Application of Acoustic Emission to the Studies of Cohesive and Adhesive Strength" *Quarterly Report*, January 1989.
2. SHRP A-002A, "Binder Characterization and Evaluation" *Quarterly Report*, June 1989.
3. T. F. Yen, "Asphaltic Materials" *Encyclopedia of Polymer Science and Engineering*, 2nd ed., Index Volume, p 1.
4. J. V. Evans, "Asphalts", *Encyclopedia of Chemical Technology*, 2 ed., **2**, 284 (19 ?).
5. C. Mark, *Industrial and Engineering Chemistry* **49**(1), 442 (1957).
6. C. R. Marek and M. Herrin, *Proceedings*, Association of Asphalt Paving Technologists, **37** (1968).
7. K. Majidzadeh and M. Herrin, "Modes of Failure and Strength of Asphalt Films Subjected to Tensile Stresses."
8. C. R. Marek, *Journal of Materials* **5**(1), 3 (1970).
9. Transportation Research Board, *State of the Art Report 7* (1978).
10. J. D. Ferry, *Viscoelastic Properties of Polymers*, 3rd ed. (1980).
11. SHRP A-002A, *Quarterly Report*, July 1990.
12. G. R. Dobsen, *Journal of the Institute of Petroleum* **58**(559), 14 (1972).

Chapter 3

Analysis of Cavitation in Confined Asphalt Thin Films

3.1 Introduction

Acoustic emission (AE) is the sudden generation of transient elastic waves in materials by the rapid release of energy. The transient elastic waves are usually generated when the material is subjected to varying stresses. AE is unique among the nondestructive testing (NDT) techniques in the sense that it is the message directly sent by the material itself. The ability to understand the message is very important for the investigators to diagnose the general condition of the material. All messages carried by each acoustic event can be related to the nature of the source. Therefore, analysis of the individual acoustic emission event allows us to identify the various source mechanisms[1–3].

Asphaltic concrete in many ways is very similar to highly filled elastomers; it contains high concentrations of fillers (small-size rock and fine, up to 90% by volume) and binder (asphalt). Our experience with highly filled elastomers suggests that failure starts either by microcavitation in the binder phase or by debonding at the filler-binder interface[4–6]. Asphalt's resistance to microcavitation and to debonding depends, respectively, on its cohesive strength and the binder-filler adhesive strength. We need to quantitatively understand the microfracture processes. Real asphaltic concretes may not be the best systems for the initial study because they involve too many uncontrolled variables. A better approach is to design a model system which not only retains all the essential mechanical characteristics of the asphaltic concretes but is simple enough for monitoring microfracture by acoustic emission. We simulate this system by bonding a circular disc of asphalt binder between two circular plates of steel. This is the so-called "poker chip" specimen. The rationale for selecting the poker chip specimen is discussed in Chapter 1.

In this chapter, we centered our efforts on the AE analysis of cavitation in thin film poker chip specimens.

3.2 Experimental

3.2.1 AE Equipment

The AE equipment used in this study was the 3900 Locan-AT manufactured by Physical Acoustics Corporation (PAC). The Locan-AT system supports four independent channels as well as an attached Tra2.5m module, a transient wave recorder. The AE sensors (PAC WD broad-band type, for studying the signal spectrum) with operating frequency range from 100 kHz to 1 MHz were coupled to the poker chip specimen with couplant. Signals were fed into PAC 1220A preamplifiers (40 or 60 dB selectable gain) with a 100–1000 kHz bandpass filter and then into the Locan-AT. The schematic diagram is shown in Figure 3.1.

Each independent channel can record the absolute arrival time (resolution 0.25 μsec), the count (number of times the acoustic emission signal exceeds a present threshold), the energy, the signal duration, and the maximum amplitude. Figure 3.2 is the AE signal from a cavitation in a poker chip specimen under a tension load (triaxial tension state). Figure 3.3 (a) shows the general form of an AE signal and Figure 3.4 illustrates some of the AE parameters characterizing an AE signal[7]. All the provided definitions of the AE terminology have been designated by American Society for Testing and Materials[8]. The Locan-AT also provides two outside parameter inputs at the sampling rate of 10 Hz. The stroke or load output signals from MTS can be digitized and stored with the AE parameters in Locan-AT.

The Tra2.5m is a kind of transient wave recorder. The Tra2.5m digitizing boards employ high speed analog-to-digital converters (running at 32 MHz) and very high memory setups (2 M samples). The post-test analysis functions can calculate the frequency spectrum of a signal through an FFT (fast Fourier transform) algorithm(Figure 3.3 (b))[9]. All the information can be stored in digital form on the computerized Locan-AT.

The AE system was upgraded in 1990, and an expansion chassis with four more channels was added to the main system. This upgrading provided us with greater ability to conduct the AE measurement on wave speed determination and the three dimensional source location.

3.2.2 AE System Calibration

For system calibration, a transparent PMMA disk (Plexiglas, acrylic plastic sheet) was chosen as the simulated poker chip specimen. The PMMA circular disk was shaped 6 in. diameter by 0.25 in. thickness. Several steel balls (of 0.125 in. in diameter) coated by asphalt or pure asphalt droplets about 0.07" in diameter were put in the different positions inside the transparent PMMA disk.

A Nd:YAG pulsed laser is applied to hit the steel sphere and the signal of the resulting thermoelastic wave is captured by the sensors firmly glued on the PMMA specimen (Figthermoelastic wave is captured by the sensors firmly glued on the PMMA specimen (Figure 3.5) or on the steel plates which bind the PMMA disk. The wave length of laser is 532 nm (green, visible, peak power is 50mJ and pulse duration is 10 nsec) and the PMMA is nonabsorptive at this frequency. The sphere hit by the laser is a simulated dilation source event[10].

There are four sensors put on the metal plates or PMMA specimen. The sensor arrangement can be referred to in Figure 3.6. From the absolute arrival time recorded by the four channels in Locan-AT, the wave speed of the acoustic wave can be defined by the known sphere position. The Tra2.5m also recorded the waveform of the thermoelastic wave generated from the steel ball by the Nd:YAG pulsed laser.

3.2.3 Modifying the Grips and Mounting AE Sensors

From the result of AE system calibration, a better way of mounting transducers in order to correctly determine the location of a source event was defined: the sensors are directly placed on the specimen itself rather than on the steel plates. In the AE measurement of the asphalt poker chip specimen, all the plates are modified by introducing bores and placing transducers in the bores. The face of the sensor is therefore directly in contact with the asphalt specimen. This design removes the noise and interference generated by the reflection and vibration of the steel plates. The schematic diagram is shown in Figure 3.7.

In the system calibration, the sensors were glued by a couplant (commercial name "Krazy Glue," recommended by PAC). Asphalt itself is also a good couplant in our poker chip specimen. In the initial studies of AE measurement on asphalt, the asphalt was applied as the couplant. Once an experiment on thin-film asphalt was underway, the ceramic faces of the sensors were taken off in the tension period. From then on, a water soluble couplant (Sperry multi-purpose ultrasonic couplant) and high-vacuum grease (Dow Corning) were applied to decrease the tension load as well as to provide good wave transmission.

3.2.4 Computer Software

All the AE data stored in Locan-AT were in binary format. Locan-AT provides some software packages to display the AE data based on histogram or distribution. To achieve a better understanding of AE parameters at different time, load, or displacement ranges, all the binary data had been transformed to ASCII format by a C language program. It makes it easier to manipulate the AE parameters as one wishes. A source location identification program and a three-dimensional, animated presentation software has already been developed.

The AE transient waveform data file recorded by Tra2.5m can also be transformed into an ASCII format file. These data have been linked with a commercial software package to carry out the FFT and obtain the digitized value for each signal waveform spectrum.

3.2.5 Specimen Preparation and Mechanical Test

See the related sections of Chapter 2.

3.3 Results and Discussion

3.3.1 AE System Calibration

Source Location. The initial AE system calibration, the schematic diagrams for mounting the transducers to the two types of specimens are given in Figure 3.7. Several PMMA specimens were prepared with steel balls placed at the center, 1, 2, and 2.75 inches from the center, respectively. We used the Locan-AT to identify the source location in each type of specimen.

For the specimen of PMMA sandwiched between two steel plates, there are two transmission media: polymer and metal plates. Wave transmission in such a system is very complicated. It is very difficult to define an overall wave speed for the location function of the Locan-AT. At different wave speeds, Locan-AT predicted different source location. By setting wave speed equal to 140,000 in./sec, we obtain relatively good predictions for steel balls located at the center, and 1 and 2 in. from the center, but at the edge (2.75 in.), the prediction shows a great deviation. Using other wave speeds, the predictions were even worse.

For the case where sensors are attached directly to PMMA, the prediction of source locations are reasonably good for spheres located at center, and at 1 and 2 in. from the center, when the wave speed is set to equal to 80,000 in./sec. However, the edge one shows a deviation of about 0.5 in., which can be greatly decreased at the expense of increasing error at the other locations by choosing the wave speed as 100,000 in./sec.

Overall, the identification of source location becomes more reliable if sensors are attached directly to PMMA surface rather than to the steel plates. Hence, we have to modify the configuration of our butt-joint specimen by drilling holes into the steel plates to house the transducers in direct contact with the asphalt phase.

The subsequent experiments were conducted in several ways. The test schematic diagram is shown in Figure 3.8. There are four types of tests, namely, type 0, type I, type II, and type III. There are also two different sizes of the source: a 0.125-in. steel ball covered by asphalt, and pure asphalt of about a 0.07 in. diameter. The targets with asphalt better absorb the laser energy. The laser beam is directed to hit the target in different directions, as shown in Figure 3.8. In the early work of system calibration, the sources at the center were exactly located by Locan-AT, so we centered our interest on the case of the sources not in the center. In the case of type 0, the asphalt was exposed directly to the laser beam, and we only wanted to make sure that the asphalt had good absorption of this wavelength laser beam. The testing device of type III was simulated by being bound between two metal plates, in order to evaluate the different results of the other types. If the signals with AE energy are under 10 counts, then they are deleted from the graph. The location results are shown in Figure 3.9. We compared the results of different-size metal bearings and different laser directions. The location prediction is better for smaller spherical bearings, as well as the stronger AE events. Generally speaking, types I and III have better prediction results than type II, and the difference between the predicted location and the actual source in the simulated case, type III, is no more than 1 cm.

System Response. Due to the geometry of the butt-joint specimen, an acoustic emission signal is very complex when it arrives at the sensor. To describe the characteristics of an AE event, we have to remove the effects from the testing system. By FFT of the output AE signals, the waveform spectrum can be shown. The function implements the transformation given by

$$X(k+1) = \sum_{n=0}^{n-1} x(n+1) W_N^{kn} \ . \tag{3.1}$$

where $W_N = \exp[-j(2\pi/N)]$ and n is the n-point FFT. N is the number of x input[11]. Here, x is the voltage of the amplitude.

From system calibration by a pulsed laser, the system response spectrum can be obtained. The output waveform spectra are reproducible, and the waveform spectra have similar peaks occurring at some specified frequencies. Though the Tra2.5m records a signal from only one channel at a time, we still get the complete spectrum for the four channels by hitting the specimen four times because of the good reproducibility of laser. This provides us with a very important basis to get the frequency response of the testing system. Figure 3.10 shows the spectra for type I for the small pure asphalt ball from the four sensors. They show peaks at frequencies of about 100, 240, 280, 390, 450, and 510 kHz, but, at over 500 kHz the spectra do not agree. The high-frequency component is much affected by the material properties and system geometry[12]. We also observe that each spectrum is independent of laser energy. One thing we should note is that if the output signal energy counts are too low or too high, the peak on the spectrum will not be sharp enough. This can be explained by the resolution (8 bits) and input range (-10 to 10 v) of the Tra2.5m digitizer. Basically, in our experiments, if the signal energy is between 50 and 100 (counts), the output spectrum will have fairly high resolution.

3.3.2 AE Measurement on SHRP Asphalts

3.3.2.1 Observations of AE Signals with Mechanical Parameters

In the initial study on SHRP* asphalts, the AAK-1 specimen with 0.5 mm in thickness was tested under three different kinds of mechanical conditions at 60°F. The MTS control mode was stroke control, and the estimated initial loading rate was 8 psi/sec. The time intervals (healing time) between the first test and second test, the second and third tests were 309.8 hr and 2.0 hr, repectively (Table 3.2).

Figure 3.11 shows the AE output signals corresponding to the mechanical behavior. The first run (AK010301†, I) and the second run (AK010302, II) have almost the same mechanical response if the strain is less than 0.1. The AE results in these two tests differ greatly in this strain range; that is, the first run had much more AE exerted than did the second run. However, when the stress in AK010302 was greater than the maximum stress point in AK010301, the AE signals again became more active. In the second test, when the stress level reached the yield point, some more damage occurred. In the third run (AK010303, III) of AK0103, the stress-strain curve deviated from the two curves of the first two runs and reached maximum stress at a strain of 0.25. The AE signal kept "quiet" in the initial range between 0 to 0.25, but rose abruptly as the strain level rose above 0.25, and then emitted no signal until it reached a strain level of 1.05.

Some features can be observed: (1) there exists a threshold load beyond which the AE signals occur inside the sample; (2) before the yield point, if the stress does not reach the level of the previous run, there would be no significant AE; and (3) at the yield region, the high intensity of AE energy indicates the extensive damage in the asphalt.

The AE location distributions for these three tests are shown in Figure 3.12 (a) and (b) and Figure 3.13. The overall distribution of AE events on AK0103 specimen is shown in Figure 3.14. Compared with the first three plots, the AE sources occurred in different parts of the poker chip specimen.

Some failure surfaces of the poker chip specimen have been recorded by camera. We integrated the information from MTS, AE and fractography. Comparing the AE source locations of AK0103 specimen to the photographs of fracture surface, we gain significant insight into the microfracture process. Figure 3.12 shows the progression of AE event distribution over the specimen. These events began in the left section (Figure 3.12 [a]), moved through the lower right area (Figure 3.12 [b]), then rose into the right central region (Figure 3.13). The final diagram Figure 3.14 shows the overall distribution of the AE events as they occurred. When these diagrams are compared with the actual photograph

---

*SHRP (Strategic Highway Research Program) is a unit of the National Research Council that was authorized by section 128 of the Surface Transportation and Uniform Relocation Assistance Act of 1987.

†The first two characters in test code represent the asphalt specification. "AK"is for AAK-1, "AD" for AAD-1, "AA" for AAA-1, etc. The numerical digits are the combination of the specimen number and run number.

taken, the agreement is quite remarkable, as can be seen in Figure 3.15. In this case, the spatial distribution of cavities shown in Figure 3.15 agrees well with the predicted AE source locations. Locan-AT can pinpoint the microfracture caused by cavitation and the direction of fracture propagation can be defined.

We can conclude that: (1) the mechanical loading history is very important for AE measurement; (2) the healing is not complete even after a two-week period (the healing effect may not show up in a short-time mechanical property test); and (3) the damage from different locations of AE events for each test can be accumulated and has long-term effects on mechanical properties such as fatigue.

3.3.2.2 Uniaxial Tension

AAK-1 Asphalt with 0.5-mm thickness or less. A series of tension tests were performed on two AAK-1 specimens with 0.5-mm thickness, namely, AK04 and AK05, at 60°F with different healing time intervals (Table 3.2). Figure 3.16 shows the AE output signals corresponding to the mechanical behavior for each test on AK04 specimen. The AE results of AK04 show the same phenomena as specimen AK0103. The AE parameters cannot return to the original values and can be related to the previous loading history. There are always some strong AE signals occurring when the applied load reaches the yield point (Figure 3.19). Figure 3.17 shows the sources with energy greater than 100 located by Locan-AT for every test on AK04 specimen. The AK04 sample was ruptured in the AK040103 test. Even after eight days, test AK040201 (the fourth test on the AK04 specimen) still showed only some very weak signals. The real fracture surface is shown in Figure 3.20. It shows that all of the fractures are due to cavitation.

A similar plot for AK05 specimen can be referred to in the part of the Chapter 2. One interesting thing is the AE signal from the first run of AK04 specimen, which, though in the linear range, emitted signals sooner than AK050101, and the signals were much stronger. In the second run (still in the linear range) of both specimens, the AE outputs were very quiet. For the third run in AK04 and AK05, the same strain rate (0.03/sec, MTS stroke control) and the estimated loading rate (8 psi/sec) were applied. AK04 ruptured at the strain point 0.54, and AK05 survived up to the maximum imposed strain of 0.6 (see Chapter 2). The accumulated AE energy in AK040103 is much greater than that in AK050103, at the maximum stress of about 1.2 MPa. That presented us with an important clue: before the material failure, AE gave us some early warnings that could not be detected from mechanical results. If a specific proof load range is chosen, it may be possible for us to evaluate the specimen and to anticipate specimen fatigue life. More cases of mechanical and AE measurements on AAK-1 specimen are discussed below.

Figure 3.21 shows the AE accumulated energy along different stress level for specimen AK09 (0.5-mm thickness, vacuum treated), AK10 (0.32-mm thickness, regular), AK12 (0.5-mm thickness, regular), and AK14 (0.5-mm thickness, regular) in unaxial tension test at loading rate of 8 psi/sec. The mechanical properties of AK09 (vacuumed, tensile strengh 1.28 MPa) and AK10 (0.32-mm thickness, tensile strengh 1.35 MPa) are better than the ones of AK12 (regular, tensile strengh 0.94 MPa) and AK14 (regular, tensile strengh 1.08 MPa) specimen. The AE onset load for these four specimens are 0.53, 0.72, 0.41, and 0.17 MPa, respectively. There was a tendency for specimens with higher AE onset stress to have higher tensile strength. A concept of "proof testing" can be applied to access the integrity of the butt-joint specimen[13]. The load range of 0.7 MPa (3,000 lb on a 6-in.-diameter specimen) to 0.96 MPa (4,000 lb on a 6-in.-diameter specimen) can be chosen as a criterion to monitor the AE change in this load range. The AE energy increse rate in this load range for the four specimen are 10, 105, 500, and 270. The greater the emitted AE energy in this range, the closer the failure approached. These values seem much more valuable for investigators to assess the butt-joint specimen integrity. The proof load should be chosen according to the specimen thickness, loading rate, etc.

Figure 3.22 is the AE accumulated energy count changes with time, at the loading rate of 8 psi/sec with specimen thickness from 0.12 mm (AK41, AK50, and AK51) to 0.2 mm (AK70). The AE onset load for the AK51 specimen is much lower than for the others. In Chapter 2, the effect of different specimen preparation conditions has been discussed. Because of its high starting preparation temperature and the high preparation pressure, the AK50 specimen shows lower tensile strength and lower AE onset load. The proof load for specimen with thickness from 0.12 to 0.2 mm can be chosen from 0.96 to 1.20 MPa (4,000 to 5,000 lb on 6-in.-diameter specimen). The emitted AE energy for AK41, AK50 and AK70 at this load range are 0, 5, and 12, respectively. The AK51 specimen cannot survive up to this load range.

AAK-1, AAM-1 and AAG-1 Asphalt with 5mm-Thickness. Several specimen with 5-mm thickness were cast from AAK-1, AAM-1, and AAG-1 asphalts. The loading rates for these tests were around 100 psi/sec at 60°F. The AE signals corresponding with the mechanical response are shown in Figure 3.23. The tensile strength for AAG-1 is greater than for AAK-1 and AAM-1. The load at the onset of AE signal for AAM-1 and AAK-1 are less than the load for AAG-1. The accumulated AE traces with loads for AAM-1 are much different from those for AAK-1 and AAG-1 specimen. The AAG-1 specimen possesses a very high load at the onset of AE signal. That is the reason AAG-1 has so high a tensile strength (270 psi). The accumulated AE energy traces for the AAM-1 continue higher and higher with the increase of the applied load. For the load range of from 60 to 90 psi, the AE signal growing rate for the AAM-1 specimen was greater and greater. On the other hand, the AE growing rates for AAK-1 and AAG-1 specimens were pretty "flat" at this load range. As the load reaches 90 to 100 psi, the AAM-1 specimen ruptured, and the AAK-1 and AAG-1 specimens still "survived." This provided an important message: at the load range of 60 to 90 psi in 5-mm-thick specimens, the AE output signals can tell us the materials' integrity.

Figure 3.24 shows the AE source location distribution over the poker chip specimen for AAM-1 asphalt. Different labels denote different intensities of the AE sources. The loading history has been divided by two or three regions, and the direction of AE signals propagation (the arrows in Figure 3.24) can be defined.

Based on the above results of AE measurements on SHRP asphalt specimens, Table 3.1 tentatively lists the proof load and the criteria of AE energy counts for asphalt poker chip specimens in "healthy" condition with various thickness. For thinner specimens, the applied proof load will be higher, and the criteria of AE energy occuring in this proof load range will be smaller.

3.3.2.3 Uniaxial Compression

AAA-1, AAG-1, and AAM-1 Asphalts. The compression tests on AAA-1, AAG-1 and AAM-1 asphalts has been conducted. Due to the resolution of the MTS control system, the compression tests can only be applied on thick specimens, that is, those at least 5 mm thick.

In the initial study on SHRP asphalts, the AAA-1 was tested in different kinds of mechanical conditions. The experiment was run at 60°F, and the thickness of the poker chip specimen was 10 mm. Twenty different runs with varied strain rates in compression, tension, and cyclic tests were conducted. The cyclic compression test with test code AA010020 (MTS control mode: stroke) is illustrated here. Figure 3.25 shows the load and stroke along with the AE energy count data for cyclic compression tests on AAA-1 specimens 10 mm thick. The AE signals from the poker chip specimen are greatly related to the load. There exists a threshold load beyond which the AE signals occur inside the sample. When the compression load reaches a maximum, the AE signals reach a maximum. But there are fewer signals detected at the intervals when the load goes from maximum (compression) back to 0. The AE signals continuously arise as the specimen undergoes a tension load. After the load reaches a maximum, almost no AE signals are observed for the rest part of the first cycle. The observed AE signals were far fewer in the following cycles than in the first cycle. We postulate that the AE signals emitted during the first compression were from collapsing voids in the specimen. Since the maximum tensile load in the experiment was only a fraction of the maximum compression load, all the unstable nuclieation sites for cavitation corresponding to the tensile load had been removed. Therefore, very few AE signals were emitted in the tensile loading region.

The AE sources located by Locan-AT are shown in Figure 3.26. The AE events spread over the poker chip specimen and the larger hits (AE energy greater than 10) had a tendency to be more central than peripheral. This is consistent with the results of finite element analysis from the chapter of Stress Analysis that in poker chip specimen, the mean stress is much higher in the center than the edge on a poker chip specimen.

Figures 3.27 and 3.28 show the AE outputs and mechanical parameters. Similar to what is shown in Figure 3.23, the AE signals for AAM-1 show more gradual increases with load than AAG. Figure 3.28 shows strong AE signals during half of each loading cycle. The AE increase rate at the initial ranges in Figures 3.28 (a) and (b)-(d) show some differences. The AE onset load for Figure 3.28 (a) is lower than the others. The phenomenon has been observed in uniaxial tension tests on asphalt butt-joint specimens. This is due to the virgin specimen in the test of Figure 3.28 (a). Comparing the four graphs in Figure 3.28, (c) shows the largest AE output and permanent deformation. The only explanation of the phenomenon is the low loading rate, 20 psi/sec for graph (c) and 100 psi/sec for the other three. The viscoelastic behaviors play a role in testing the SHRP asphalts at low loading rates. The lower the loading rate, the more AE signals (damages).

3.3.3 Evaluating the Healing behavior

Crack healing in polymeric materials has been investigated by many researchers. Lin et al.[14] reviewed the literatures and found that the phenomena of healing in polymeric materials occurred at temperatures above the glass transition temperature T_g. Asphalt possesses a special healing ability. Some of the damage to the asphaltic specimen can heal if it has been left alone for a certain period of time at room temperature. This self-healing ability can be evaluated from the output AE parameters by loading the materials. To evaluate the healing effect on the same specimen, what first has to be done is to choose a suitable AE parameter as an index for the evaluation. Generally speaking, AE counts and AE energy are good parameters to represent the size of each AE event. According to our experimental results, they have the same tendencies. AE energy is less affected by the threshold setting[14]. The AE accumulated energy was taken as a basis to monitor all AE events during the testing period. The hypothesis for healing monitored by AE is this: if the specimen does fully heal, the AE accumulated energy from the successive test would possess the same traces with load as the virgin specimen.

In the three tests on the AK0103 specimen (Figure 3.11), the healing time between tests I and II and tests II and III are 309.8 and 2.0 hr, respectively. The AE accumulated energy for test II in linear range is less than that of test I. The AE signals rise abruptly in the yield point of test III and almost no AE signal at the load range at which tests I and II exhibit linear mechanical properties. The source location of the three tests also provides some more information about healing. Figures 3.12 (a) and (b) and 3.13 (a) and (b) show the progression and the overall of AE event distribution over the specimen. The AE events began in the left section (test I), moved through the lower right area (test II), then rose into the right-central region (test III) (Figure 3.14). The overlapped area of AE events from tests I and II contains many more AE events than the overlapped area of AE events from tests II and III. One more important observation is that most of the AE events occuring at the load range at which tests I and II exhibited linear mechanical behaviors are located in the overlapped region of AE events from test I & II. The AE events occuring outside the overlapped region is present at and near the yield and beyond the yield point of test II. The healing process of asphalt poker chip specimens monitored by AE is related to the location. This finding enhanced the value of AE techniques to evaluate the healing process of asphalt cement.

In Table 3.2, all the test parameters used to evaluate the healing effect are tabulated. The first column contains the specimen index. The second column are the labels of different tests. The fourth column is the absolute time referred to the virgin test (the first run on the specimen). The third column is the healing interval, that is, the waiting time between two tests. In the remaining columns, the accumulated AE energy for each test on different stress levels are listed.

The Kaiser effect[‡], and the Felicity ratio[§] are both used in practical AE testing to assess the integrity of materials. The concrete beam integrity (CBI) ratio, the ratio of the load at onset of AE and the maximum prior load, was presented as an effective criterion to measure the severity of damages induceed in repaired concrete beams[16].

Here, the asphalt healing index (AHI), given below, is proposed as a criterion to evaluate the healing behaviors of poker chip asphalt specimen:

$$\mathrm{AHI}_{\text{at a certain stress level}} = \frac{\text{AE energy from an aged specimen}}{\text{AE energy from a virgin specimen}} \ . \tag{3.2}$$

For the first test on an AD30 specimen (AD300110), the AE signals start at the stress level of 15 psi, and the accumulated AE energy at a maximum stress of 60 psi is 3,000. After 18.9 hr, the second test (AD300111) gives the onset AE at a stress of 45 psi, and the accumulated AE energy is 1,050 at the maximum stress of 60 psi. Compared with the AE output of the two tests on an AD30 specimen, the healing phenomenon can be quantified by AE output energy for different stress levels.

There are no AE signals at the stress interval of 10 to 30 psi in the test of AD300111. This means that the AHI at this stress interval is 0. At higher stress levels (not exceeding the yield point), the AHI values are 0.01 for the stress interval of 30 to 45 psi and 0.53 for the stress interval of 45 to 60 psi. The AHI for different specimens at varied stress levels are given in Table 3.3.

This result tells us that damage happening in the low-stress-level range is not as easy to heal as the damage happening in the higher stress level. It is believed that the healing in the higher stress range is related to the return path of the tension test (owing to the viscoelasticity of the material, the specimen in tension at the return path would be in compression). The number of AE signals detected at the return path was due to the collapsing of the existing cavities in the asphalt butt-joint sample[17].

[‡] The Kaiser effect is the absence of detectable AE at a fixed sensitivity level, until previously applied stress levels are exceeded[8].

[§] The Felicity ratio is the ratio of load at which AE begins on a successive load cycle to the maximum load on the previous cycle[15].

Asphalt healing at room temperature (about 78°F) increases with the healing time. If a very long healing time was allowed for a damaged specimen, a "superhealing" effect was observed on an asphalt poker chip specimen. For the third run on an AD30 specimen (AD300112), the waiting interval was 1,226 hr. The first AE happens in the beginning of the test. The AHI value is greater than 1 (at stresses no greater than 30 psi). This is because the healing time is so long that the damage experienced in the small stress range has healed. Some existing damages already in the virgin specimen that cannot be detected in the first run also heal during the long waiting time. This can also be verified by the mechanical results. The yield stresses of the virgin specimen (AD300110) and the second run specimen (AD300111) were 56.5 and 55.0 psi, respectively; and the yield stress of the third run specimen (AD300112) was as high as 86 psi, whereas the rest time was 19 hr after the first run and 1,226 hr after the second run.

Some results of the study on asphalt healing can be epitomized as follows. First, before the yield point, asphalt showed an almost complete healing from previous damage based on linear viscoelastic properties. Yet, AE would show that the specimen can heal to some extent at a high-stress (15–60 psi) range and can hardly heal in low-stress (0–15 psi) range. It is believed that this lack of complete recovery would greatly affect the fatigue life of the specimen. Second, near and beyond the yield point, serious damages happened to the specimen. The accumulated AE energy can quantitify the healing process. When the specimen was allowed a very long healing time (100 to 1,000 hr, depending on the previous mechanical history), some existing damages already in the virgin specimen that could not be detected in the first run healed in the long waiting time, and the "super healing" was observed. Third, the healing process in asphalt poker chip specimens monitored by AE also provide information on the location effects. The AE sources can represent the location of damages, and the AE events that happened in the same area on poker chip specimens can be explained as the healing. Combined with the stress-stain data, the healing process can be carefully studied according to time, location, and mechanical behavior. A good illustration is seen in an AK0103 specimen (Figures 3.11 and 3.14).

3.3.4 Effect of Sample Preparation Conditions

AE is a useful tool to monitor the integrity of materials as well as to evaluate the healing behaviors of asphalt specimen. AE was also used to monitor the different kinds of sample preparation conditions. The detailed procedures are referred to Chapter 2. The effects of hardening and void content on AE measurements are discussed below.

3.3.4.1 Stabilization and Hardening

The AE results for specimens with different stabilizing times (the period between sample preparation and test) showed wide variance. For example, the accumulated AE energy at the same stress, 0.3 MPa, in AK05 (with a stabilization time of 2 hr) and AK07 (with a stabilization time of 14 hr) returned values of 5,000 and 50,000, respectively. The AE signals were so strong for AK07 and AK08 specimen that the data acquisition boards on Locan-AT were saturated. The AE measurement is very sensitive to the effect of hardening.

3.3.4.2 Effect of Void Content in Asphalt Cement

As in our previous work, it was found that almost all the cohesive failures were due to cavitation failure. We suspect that microvoids in the specimens affect the mechanical properties of asphalt. We therefore performed studies on microvoid effects. In these tests, before we prepared the sample, the asphalt was put in a vacuum oven for 3 hr at 80°F. Although we could not see distinct differences in density or mechanical behavior, the failure surface shows the differences (Figures 3.29 and 3.30). The cavities are very close to one another in the regular untreated asphalt. However, for the sample that underwent the vacuum process, the large visible cavities are not nearly as dense as in the untreated sample. We attempted to explain this phenomenon via the AE event distribution with amplitude. Figure 3.31 shows the event count with the amplitude for an untreated sample of AK12 and a vacuum-treated sample of AK09. The samples do not exhibit the same amplitude distribution. The vacuum-treated sample has more events in the low-amplitude region than the untreated sample. More cavitation occurs in the vacuumed specimen at the lower stress region, indicating that it contained mor unstable cavitation sites. As shown in Figure 2.35 the tensile strength of the vacuumed specimen is less than that of the regular specimen. We suspect that because of the high viscosity of the asphalt, the vacuum time was not long enough to remove most of the less stable cavitation sites, yet it was long enough to destabilize other cavitation sites. Consequently, vacuumed specimens contain more less stable sites.

3.3.5 Temperature Effect on AE measurement

Asphalt is a thermal-sensitive material. The apparent stiffness modulus of an AAK-1 specimen 5 mm thick at 50°F (34,000 psi) is higher than that at 60°F (15,000 psi) described in the Chapter 2. Figure 3.32 shows the AE signal output with the mechanical parameters, and Figure 3.33 shows the AE source location of two tests on AAK-1 specimen with different temperatures. The total AE output signal for test at 60°F is higher than the test at 50°F. Cavitation starts at higher stress level at 50°F than that at 60°F. The AE source location for the tests at these two different temperature have a similar tendency of the source distribution. More detailed study on temperature effects can be referred to in Chapter 4.

3.3.6 Viscoelastic Effect on AE measurement

Asphalt rheology is related to the study of physical or mechanical stability of the asphalt colloid system under varying states of time, stress, pressure and temperature.[18] From our experience in mechanical tests on asphalt specimens with low loading or stroke rate at 60°F, viscoelastic behaviors can be easily observed. Figure 3.34 shows four consecutive tests on a AAK-1 specimen (5 mm thick) with a very large deformation (6 mm) at a very low strain rate (0.012/sec). The mechanical results show strong hysteresis, similar to what we show in Figure 2.9. The AE occurs at a "threshold load" of around 50 psi and then rises abruptly. The testing period has been divided into five regions in order to study the different AE sources. Figures 3.35 and 3.36 shows the location distribution of AE events. The arrows show the direction of the propagation of an AE event.

In region I, of Figure 3.34 (a) the AE signal occur at the stress reaching about 50 psi (total load 1,414 lbs.), and then rise abruptly. The AE growth rate became lower at region II. There are almost no signals in region III. In region IV, the materials experience a compression load, and the AE rises gradually, in a way very similar to those in observations of AE tests in uniaxial compression tests. In region V, the materials start the relaxation process, and almost no AE is observed. The AE source locations in Figure 3.35 showing the sources in different loading ranges also show different source locations. The direction of AE event propagations are not the same either. The yield stress for each test was progressively lower and the damage to the specimen was progressively more serious.

If the apparent yield behavior is associated with the cavitation process, once a cavity is formed it will continue to grow as long as the pressure in the cavity is higher than the mean stress of the surrounding medium. Consequently, the volume of the poker chip specimen will increase significantly after the yield point. On the other hand, if the yield phenomenon is a consequence of nonlinear elastic instability, then the volume dilation of the specimen will decrease after the yield point as predicted by our theoretical analysis (see Figure 8.26). AE data suggest that the yield phenomenon is closely associated with the cavitation process. In order to further support the thesis, we decided to follow the change in the lateral surface profile of the specimen as it was deformed, with a camera. We then calculated the volume dilation as a function of time. We observed that, first, the volume increase is significant and it increases even after the yield point. For example, the test of AK300117 showed a volume increase of less than 5% near the yield point at 8 sec, increased to 15% at 30 sec and increased to 20% at 50 sec.

3.3.7 AE Source Characteristics

Due to the geometry of the butt-joint specimen, an AE signal is very complex when it arrives at the sensor. To describe the characteristics of an AE event, we have to remove the response spectra from the testing system. By FT of the output AE signals, the waveform spectrum can be shown. From system calibration by a pulsed laser, the system response spectrum can be obtained. Ideally, the system response spectra should be subtracted from the frequency spectra of each AE event to get the source frequency distribution.

The waveform spectra from the AE events of the tests at AK010301, AK010302, and AM050101 has been closely analyzed, and two typical kinds of spectra can be classified, as shown in Figures 3.37 (c) and 3.38 (c). They do not show tendencies similar to the system response spectra (refer to Figure 3.10). We can get very distinct spectra of the source itself by subtracting the spectra of the system response from the graph, in Figures 3.38 (c) and 3.39 (c). The first kind of spectra was discovered in all the tests for AK010301, AK010302, and AM050101. The second kind of spectra only showed up in the test of AM050101. There is no interfacial failure in the AK0103 specimen (three tension tests have been done on AK0103 specimen, namely, AK010301, AK010302, and AK010303). The AM0501 specimen showed some failures at the interface of carbon steel and asphalt. After we checked the original AE hit data of two of the second type of spectra, one was a large source location and occurred in the position X=3.1, Y=3.5 (only about .50 in. from the center of the grip). The other predicted source location was out of the grip; that is, the AE signal for this event had been interfered. Upon reexamination of the specimen, there were some exposed carbon steel areas around the middle of the grip or near the sensors. We tentatively conclude that Locan-AT has the potential to differentiate the cohesive and adhesive failures in poker chip specimens. Although we can get two typical types of spectra, still more spectra analysis is needed.

We believe that the frequency spectra not only relate to the source mechanism, but are also a function of loading mode, mechanical history, source location, and sample thickness. Therefore, we assembled a library of all the spectra related to position and loading history (tension or compression mode). This was done primarily to determine when and where the AE event happens. We divide the time history into four major stages: during the initial stage, during the nonlinear range, at the yield point, or during the recovery interval. Some typical cases are shown in Figures 3.37 and 3.38. The purpose of setting up the library is to compare different kinds of microdamage: cavitation, adhesive debonding, plastic zone propagation, etc. However, a careful examination and analysis of the library remains to be carried out in the future.

Comparing mechanical history, AE source location, and AE signal waveform spectra with the failure surface of the butt-joint specimen, we found that most major failures were caused by cavitation, and minor failures were from brittleness. In Chapter 2, the failure patterns were classified into brittle, semibrittle (tenacious), semiflow, and flow failures. The type of failure depends on several factors, such as specimen thickness, test temperature, loading rate, stabilizing time, and control mode of test (load control or stroke control).

A general waveform spectrum for cavitation failure is shown in Figure 3.37 (c). Although the other kinds of spectra have been observed in several tests, it is not as obvious as defining microdamages from the library database. The other observation was the AE signal with the characteristics of cavitation occuring mostly in the process of tension testing. Near or at the rupture point, some very large AE signals were observed. These signals came from specimen ruptures and happened all of a sudden. The signals with various characteristics from different locations on the specimen were mixed and it was very difficult to distinguish them by AE. We believe the fast ruptures include brittle failure in the asphalt itself, the asphalt-steel interfacial failure, cavitation, and other kinds of fracture mechanism.

In the third test on the AK0103 specimen, the maximum strain shown in Figure 3.11 is up to 1.6. The AE signals kept almost "quiet" in the strain range from 0.2 to 1.2. In this region, some damages (cavitation) had already happened in the previous mechanical history, and the displacement of the specimen was still increasing. This phenomenon was tentatively explained as follows: the size of the existing cavities was larger and larger in this range of strain, and no detected AE signals implied that no new cavitation occured. The growing of a specified cavity might emit a stress wave; however, the signal was not strong enough to reach the threshold voltage set in the AE system. Before the specimen ruptures, the "forming" of cavities can emit much stronger AE signals than the "growing" of the cavities. The ductile behavior of asphalt cement can account for the low intensity of emitted signals. A similar observation in tests of AK300115 to AK300118, with very large deformation, can support the explaination (Figure 3.34).

The other point of view on AE source characteristics of compression and tension tests on AAG-1 specimens 5 mm thick at 60°F are show in Figures 3.39 (a) and (b). The amplitude distribution for compression tests have a larger fraction of hits with low amplitude (graph [a]). Figure 3.39 (b) is the accumulated amplitude distribution for tension and compression testing. The AE signals from compression testing show a large number of hits; however, the signal intensity for each hit was very low. The AE signal from the compression test is so small that the waveform spectrum did not show distinct peak. This is due to the resolution of the Tra2.5m Transient Recorder Analyser.

3.3.8 Wave Speed Determination

Choosing the proper wave speed in the poker chip specimen is very important for AE source location. In the previous work of system calibration, the wave speed was easily obtained from the known source position and arrival time difference for each AE channel. In the butt-joint asphalt specimen, unlike in transparent PMMA, we cannot see anything inside the core asphalt. As the AE source occurred, the wave propagated in all directions. Locan-AT records four sets of absolute arrival time data as the wave reaches each sensor. Theoretically, there are three independent time differences to determine three variables; namely, X and Y position and wave speed. A method of predicting the wave speed from some special case of time difference data has been developed. In this speed calculation algorithm, an initial guess value of wave speed and two arrival time differences were input to get the source location. The third time difference was used to iterate wave speed until the error was very close to zero.

The approximate wave speeds are 48,000, 54,000, 58,000, and 59,000 in./sec for some special cases in poker chip asphalt specimens AAA-1, AAD-1, AAK-1, and AAM-1, respectively. The thickness of the specimens are 10 mm for AAA-1 and 5 mm for the others. In mechanical measurement on SHRP asphalt with specimen thickness less than 0.5 mm, the $\sigma_y^{AAK-1} > \sigma_y^{AAD-1} > \sigma_y^{AAM-1} \geq \sigma_y^{AAA-1}$ in terms of yield stress and initial apparent stiffness had been reported. There was an irregularity on AAM-1 asphalt, whereas the wave speed for these SHRP asphalts were related to the yield stress. Futher investigation is needed to explain the irregularity.

While 0.25 μs arrival time error was introduced in a channel, the calculated wave speed deviates up to 10,000 in./sec for some source located along paths rotated 45° from the diagonal paths. On the diagonal paths, the deviation is no more than 1,000in./sec. Thus, for different positions, the deviation of calculated wave speed will take on various values. It is due to the transducer array geometry effect.[19]

The wave velocity for a given medium is closely related to the density, modulus, Poisson's ratio, etc. Piche et al.[20,21] and Kourti et al.[22] has presented an ultrasonic technique to the characterization of polymers, rubber, and rubber blends. In this technique, a high-frequency sound wave (generated) travels through the test specimen, and its attenuation and velocity in the material are measured. From the mechanical measurement on SHRP asphalt, we see that the modulus may change, particularly after the applied load reaches the yield point. If the wave velocity can be predicted for all the events, we then have a better understanding of the properties of the specimen than from only the mechanical results. Wave speed determination can provide an in situ and independent method to monitor the progression of microdamages in asphalt specimens.

In our experience, the four-sensor system is so sensitive that small arrival time errors would cause tremendous errors in wave speed calculation. One possible solution is that a greater number of independent arrival times would result in better wave speed calculation by the least squares method. Some simulations have been done on six- and eight-sensor systems with different source locations. The sensor arrangement and the position of two simulated sources are shown in Figure 3.40. The sensor spacing for each pair of sensors (opposite each other, for example) was 4.6 in. The sensor arrangement for a four sensor system is the same as those in system calibration and AE measurements on SHRP asphalt. We introduced 1/4 microsecond to 1 μs errors from channel 1 to 4, and the corresponding errors in wave speed were estimated. The simulation results for six- and eight-sensor systems had much better wave speed prediction than the four-sensor system (Tables 3.4 and 3.5). Furthermore, the damage may not spread uniformly, and the material may no longer be isotropic and homogeneous. If more transducers are added to our testing system, we can get sufficient degrees of freedom in iteration and get the wave speed as a function of direction.

Based on the above findings, we upgraded the Locan-AT with more channels. The Locan-AT system was shipped back to the manufacturer, and an expansion chassis with four more channels was added to the main system. A pair of steel plates was modified to house eight AE sensors. The specimen with 0.5-mm thickness was prepared and tested in tension at 60°F. The wave speed determination in six- or eight-sensor systems cannot reach satisfactory results. Theoretically, the wave speed can be determined more accurately by introducing more channels with the arrival time error up to 1 μs. There are still several factors resulting in the unsatisfactory predictions: First, the arrival time error may be larger than 1 μs; especially for small AE signals, the choice of threshold voltage strongly affects the accuracy of arrival time. Second, the source location and wave determination program were based on a two-dimensional hypothesis. The thickness effect (the third dimension) may have little effect on the accuracy of source location: however, the thickness may result in a large error in wave speed determination. Third, owing to the plate geometry, the generated AE signal was highly dispersive. Ziola and Gorman[23] used the cross-correlation method to determine the source location in thin aluminum plate. This technique will be also applied to the determination of wave speed in poker chip specimens. The wave propagation in plates will be closely studied as well.

3.4 Conclusions

The AE technique was successfully applied to studying the microdamages in asphalt poker chip specimens. Some key conclusions are condensed, as follows:

- In the system calibration by a pulsed laser, the best way to mount the sensors to get better AE source location is to attach the sensors directly to the bound specimen rather than to the metal plates.

- The smaller asphalt-covered sphere shows better source location prediction than the larger one. The difference between the predicted location and actual source in a simulated specimen bound between two metal plates is not more than 10 mm.

- The Green's function of the testing system has been defined and is quite reproducible. The complete spectra from the four channels were recorded by hitting the source four times by laser beam.

- At the beginning loading of the specimen, there was a threshold load beyond which the AE events start to occur inside the specimen. The occurrence of AE signals indicated the damage in the specimen. Before the yield point, if the applying load does not reach the previous load level, there would be no significant AE signals in later loadings. The damage, which we attribute mainly to cavitation, takes time to heal.

- The failure surface has been compared with the mechanical history, AE source identification, and intensity. They show remarkable agreement. AE can trace the propagation of forming microcavitation.

- The large AE signals in the poker chip specimen occurred more frequently in the center than the edge. The cavities in the central region were larger and denser. This is consistent with the calculation of the stress analysis that the stress distribution is much higher in the center than the edge (Chapter 8).

- AE can give some early warning before the material fails. The onset of AE and AE rising rates in tension tests on specimens with thicknesses of 0.12 to 5.0 mm were studied. The thinner the specimen, the higher the proofing load and the lower the number of accumulated energy.

- From the cyclic compression test controlled by stroke, most of the observed AE signals happen in the first cycle, and far fewer in the following cycles. From the compression test controlled by load, most of the AE events have low energy counts and low amplitude. The AE accumulated energy was strongly affected by the loading rate.

- The AE measurements were very sensitive to the preparation conditions of asphalt cement. The specimens undergoing vacuum treatment result in cavities with smaller size and less density than the regular specimens. The AE events from vacuum-treated specimen showed lower amplitude distribution than the regular specimens.

- Asphalt possesses a special healing ability that can be evaluated by AE parameters. The AHI at different stress levels was proposed, and the location effects on healing process in poker chip specimens can also be monitored by AE. "Superhealing" of asphalt specimens was observed mechanically and acoustically.

- Most of the failures in poker chip specimens were due to cavitation. The source mechanism for cavitation can be defined by AE parameters. Some brittle (cohesive) and interfacial failures were observed in poker chip specimens. These happen suddenly and continuously near the rupture point and could not be discriminated by AE. The AE kept very "quiet" at very large strain range beyond the yield. This was tentatively explained by the "growing" of existing cavities inside the materials. The very weak signals from the "growing" could not be detected by AE because of the ductile behavior of asphalt cement.

- The wave speeds in the specimen could give us some key information about the materials, corresponding to the varying mechanical and temperature history. However, the accuracy of determination of wave speed was strongly dependent on the wave propagation in the thin-plate geometry. Some more careful studies on wave propagation in poker chip specimens are proposed for future works.

3.5 Recommendations

AE waves in asphalt poker chip specimens are highly modulated before they reach the AE transducers. Some studies on wave propagation theories, wave mode (speed) identification and finite element analysis are tentatively proposed for future works:

- **Wave propagation in plate-like materials. The traditional wave propagation theory defines several wave types that are pragmatically important in AE measurements. However, wave propagation in asphalt poker chip specimens is very complicated. The AE is transient, point source, and sometimes oriented. The specimen is finite, layered, and plate-like (the wave is highly dispersive). The asphalt itself is highly attenuative and nonelastic. Studies on modeling dilatation source inside a plate are also suggested.**
- **Wave mode and speed identification. The wave speed for a given material is closely related to the material properties. After studies on wave propagation in poker chip specimens have been achieved to some extent, wave mode and speed identification can provide an in situ method to monitor the properties of materials. The different modes of waves can be defined in poker chip specimens by six or eight AE transducers. Even the ultrasonic technique could be applied to characterizing the material properties.**
- **Finite element analysis of poker chip specimens with inner cavities. Studies of nonlinear finite element analysis of butt-joint specimens with inner cavities taking into account both the nonlinear elastic characteristics and the geometrical effects, should be taken. The stress field near the cavity should be carefully studied. If possible, calculation of the natural modes (resonances) of an enclosed cavity inside an elastic plate by an acoustic analysis with Abaqus" would be delivered.[24]**

3.6 Acknowledgments

The research reported here was financially supported by the National Science Foundation and (SHRP). We gratefully acknowledged the contributions made by a number of colleagues in the Center of Laser Studies at University of Southern California to the development of

the system calibration part of this work, in particular Dr. Alan Kost and Mr. Jose Angel Lopez.

Table 3.1: Proof testing on asphalt poker chip specimen 6in. in diameter at 60°F

Thickness (mm)	Proof Load range (lb)	AE Energy occuring (counts)	Loading Rate (psi/sec)
5	1,500–2,500	below 1,000	100
0.32–0.50	3,000–4,000	below 400	8
0.12–0.20	4,000–5,000	below 40	8

Note: Based on the data from Figures 3.21, 3.22, and 3.23

Table 3.2: Evaluation of the healing behaviors by AE energy counts for different tests with different healing times.

Sample	Test No.	Abs. Time (hr)	Healing Time (hr)	Stress (psi)													
				0	5	10	15	30	45	75	90	105	120	135	150	165	180
AK0103 (0.5mm)	AK010301	0.0	0.0	0	0	0	1,000	7,000	13,500								
	AK010302	309.8	309.8	0	0	0	0	1,000	2,500	14,000	23,000						
	AK010303	311.9	2.0	0	0	0	0	0									
AK04 (0.5mm)	AK040101	0.0	0.0	0	0	10,000	25,000	170,000	180,000								
	AK040102	59.9	59.9	0	0	0	1,000	1,800	2,000								
	AK040103	166.1	106.2	0	0	0	0	0	0	0	600	2,100	10,000	11,000	12,000	14,000	15,000
	AK040201	366.5	200.3	0	0	0	5,000	6,000	10,000								
AK05 (0.5mm)	AK050101	0.0	0.0	0	0	200	200	200	12,000								
	AK050102	50.2	50.2	0	0	0	0	0	0								
	AK050103	194.4	144.2	0	0	0	0	12	20	25	30	70	100	250	2,000	4,000	25,000
	AK050104	195.3	0.9	0	0	0	0	0	0	1,000	5,000						
	AK050105	196.1	0.8	0	0	0	0	80	200	2,000							
	AK050106	202.4	6.3	0	0	0	0	200	1,000								
	AK050107	216.8	14.4	0	20	200	200	210	250	1,500	2,000						
	AK050108	316.7	100.0	10	800	4,000	8,000	300,000	300,000								
AK30 (5mm)	AK300101	0.0	0.0	400	1,100	4,000	9,000	10,500									
	AK300102	169.2	169.2	0	400												
	AK300110	190.0	20.0	0	0	0	20	1,000	10,000	10,500	10,800	11,000					
	AK300111	389.1	199.1	0	0	105	300	400	1,000	3,000	4,000	7,000	10,500				
	AK300112	647.8	258.7	0	0	60	210	800	6,000								
	AK300113	647.9	0.1	0	0	0	0	200	4,000	5,600	6,000	8,000	9,000	10,000			
	AK300114	649.6	1.7	0	0	0	0	70	6,000	7,000	7,500	7,600	7,700	8,000			
	AK300115	649.9	0.3	0	0	70	70	1,000	1,000	7,000	7,000	7,000	7,100	7,300	10,500		
	AK300116	765.3	115.4	0	0	100	4,000	5,000	10,000	10,500	11,000	11,500	11,600				
	AK300117	766.0	0.6	0	0	0	80	8,000	9,000	10,000	10,500						
	AK300118	890.7	124.8	0	0	0	60	10,500									
	AK300119	935.1	44.4	0	200	210	280	4,000	10,500	10,500	10,500	10,500	10,500	10,600	11,000	11,500	
AD30 (5mm)	AD300110	0	0.0	0	0	15	300	1,050	3,000								
	AD300111	18.9	18.9	0	0	0	0	10	1,050								
	AD300112	1,244.9	1,226.0	10	1,050	1,500	1,800	1,900	2,000	2,100							
	AD300113	1,485.8	259.8	0	0	0	0	200	400	800	1,000	3,000					

Table 3.3: AHI for virgin and aged specimens.

Sample	Test	Healing Time (hr)	Stress Range (psi)					
			0–5	5–10	10–15	15–30	30-45	45–60
AK0103	AK010301	0						
	AK010302	310	0.00	0.00	0.00	0.00	0.17	0.23
AK04	AK040101	0						
	AK040102	60	0.00	0.00	0.00	0.07	0.01	0.02
AK05	AK050101	0						
	AK050102	50	0.00	0.00	0.00	0.00	0.00	0.00
AK30	AK300101	0						
	AK300102	169	0.00	0.57				
AD30	AD300110	0						
	AD300111	19	0.00	0.00	0.00	0.00	0.01	0.53

Table 3.4: Simulation of wave speed determination at 6- or 8-sensor system by introducing small arrival time error for case 1 (true wave speed is 63,700 in./sec).

	Applied Error (μsec)	4-sensor		6-sensor		8-sensor	
		Speed	Error	Speed	Error	Speed	Error
CH1	-1	div	100.00%	62,400	-2.04%	60,200	-5.49%
	-0.25	76,100	19.47%	63,300	-0.63%	61,400	-3.61%
	0	63,700	0.00%	63,700	0.00%	63,700	0.00%
	0.25	50,600	-20.57%	64,200	0.78%	71,000	11.46%
	1	0	-100.00%	65,800	3.30%	81,500	27.94%
CH2	-1	div	100.00%	61,000	-4.24%	83,600	31.24%
	-0.25	94,000	47.57%	62,800	-1.41%	72,200	13.34%
	0	63,700	0.00%	63,700	0.00%	63,700	0.00%
	0.25	43,000	-32.50%	64,700	1.57%	61,500	-3.45%
	1	0	-100.00%	68,600	7.69%	60,600	-4.87%
CH3	-1	0	-100.00%	63,200	-0.78%	82,900	30.14%
	-0.25	43,500	-31.71%	63,400	-0.47%	71,800	12.72%
	0	63,700	0.00%	63,700	0.00%	63,700	0.00%
	0.25	92,900	45.84%	64,100	0.63%	61,500	-3.45%
	1	div	100.00%	65,600	2.98%	60,800	-4.55%
ch4	-1	0	-100.00%	62,200	-2.35%	60,100	-5.65%
	-0.25	51,700	-18.84%	63,300	-0.63%	61,400	-3.61%
	0	63,700	0.00%	63,700	0.00%	63,700	0.00%
	0.25	76,900	20.72%	64,200	0.78%	70,900	11.30%
	1	117,000	83.67%	66,100	3.77%	81,400	27.79%

Table 3.5: Simulation of wave speed determination at 6- or 8-sensor system by introducing small arrival time error for case 2 (true wave speed is 51,300 in./sec.

	Applied Error (μsec)	4-sensor		6-sensor		8-sensor	
		Speed	Error	Speed	Error	Speed	Error
CH1	-1	44,700	-12.87%	45,500	-11.31%	51,400	0.19%
	-0.25	49,600	-3.31%	49,600	-3.31%	51,300	0.00%
	0	51,300	0.00%	51,300	0.00%	51,300	0.00%
	0.25	52,900	3.12%	53,000	3.31%	51,400	0.19%
	1	58,000	13.06%	59,700	16.37%	51,800	0.97%
CH2	-1	44,800	-12.67%	61,700	20.27%	51,400	0.19%
	-0.25	49,600	-3.31%	53,300	3.90%	51,300	0.00%
	0	51,300	0.00%	51,300	0.00%	51,300	0.00%
	0.25	52,900	3.12%	49,600	-3.31%	51,400	0.19%
	1	58,000	13.06%	45,500	-11.31%	51,800	0.97%
CH3	-1	61,200	19.30%	44,300	-13.65%	44,100	-14.04%
	-0.25	53,600	4.48%	49,200	-4.09%	49,300	-3.90%
	0	51,300	0.00%	51,300	0.00%	51,300	0.00%
	0.25	49,000	-4.48%	53,700	4.68%	53,500	4.29%
	1	42,500	-17.15%	63,700	24.17%	61,400	19.69%
CH4	-1	55,000	7.21%	55,900	8.97%	57,300	11.70%
	-0.25	52,300	1.95%	52,400	2.14%	52,700	2.73%
	0	51,300	0.00%	51,300	0.00%	51,300	0.00%
	0.25	50,300	-1.95%	50,300	-1.95%	50,000	-2.53%
	1	47,200	-7.99%	47,600	-7.21%	46,400	-9.55%

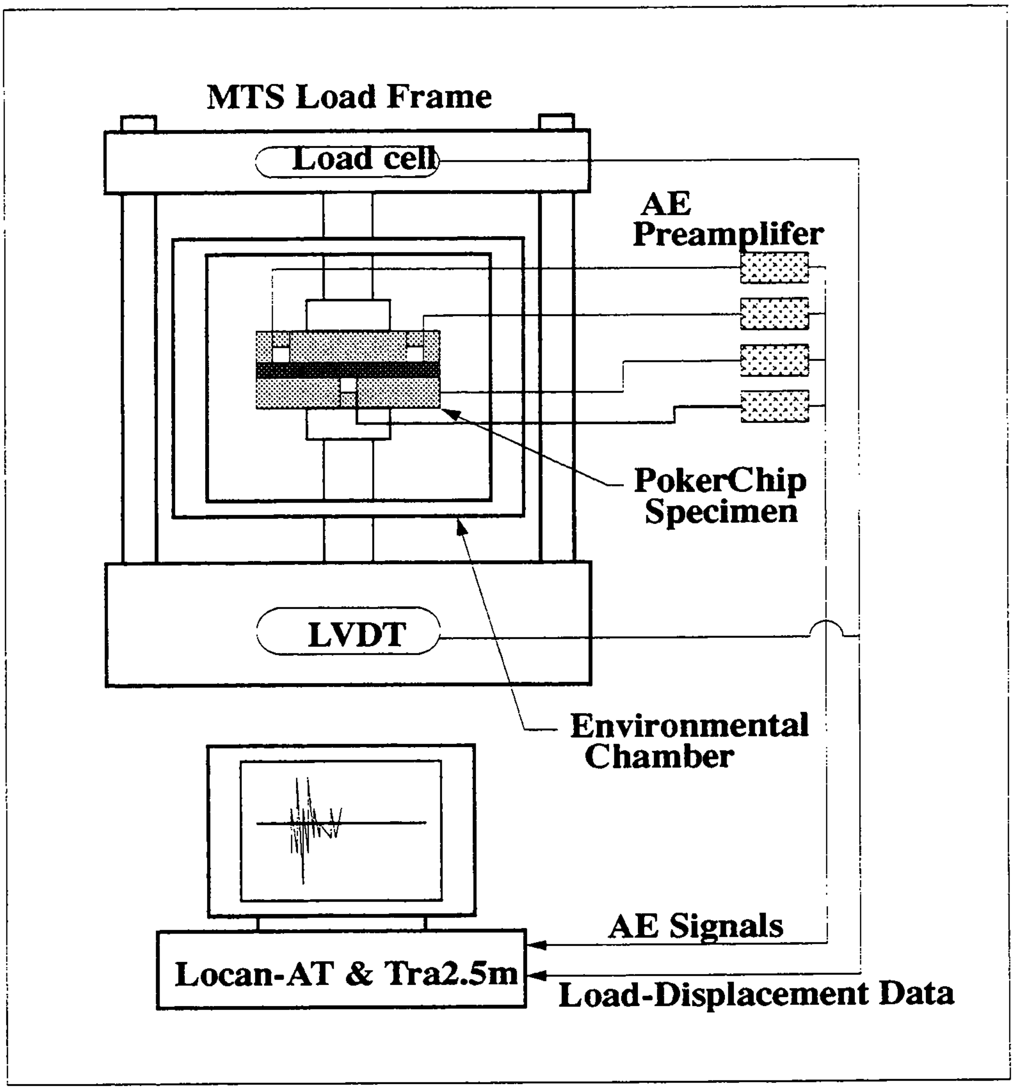

Figure 3.1: Schematic diagram of test setup and equipment.

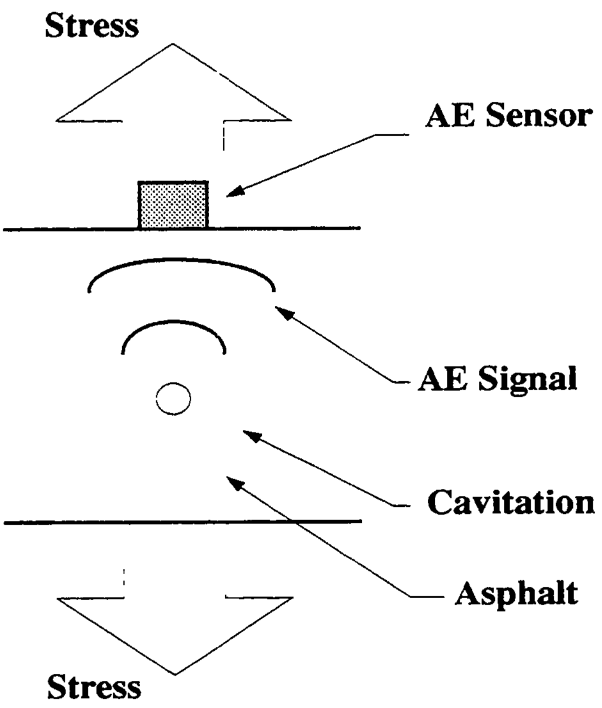

Figure 3.2: Schematic diagram to show AE signal from a cavitation in an asphalt poker chip specimen under a tension load.

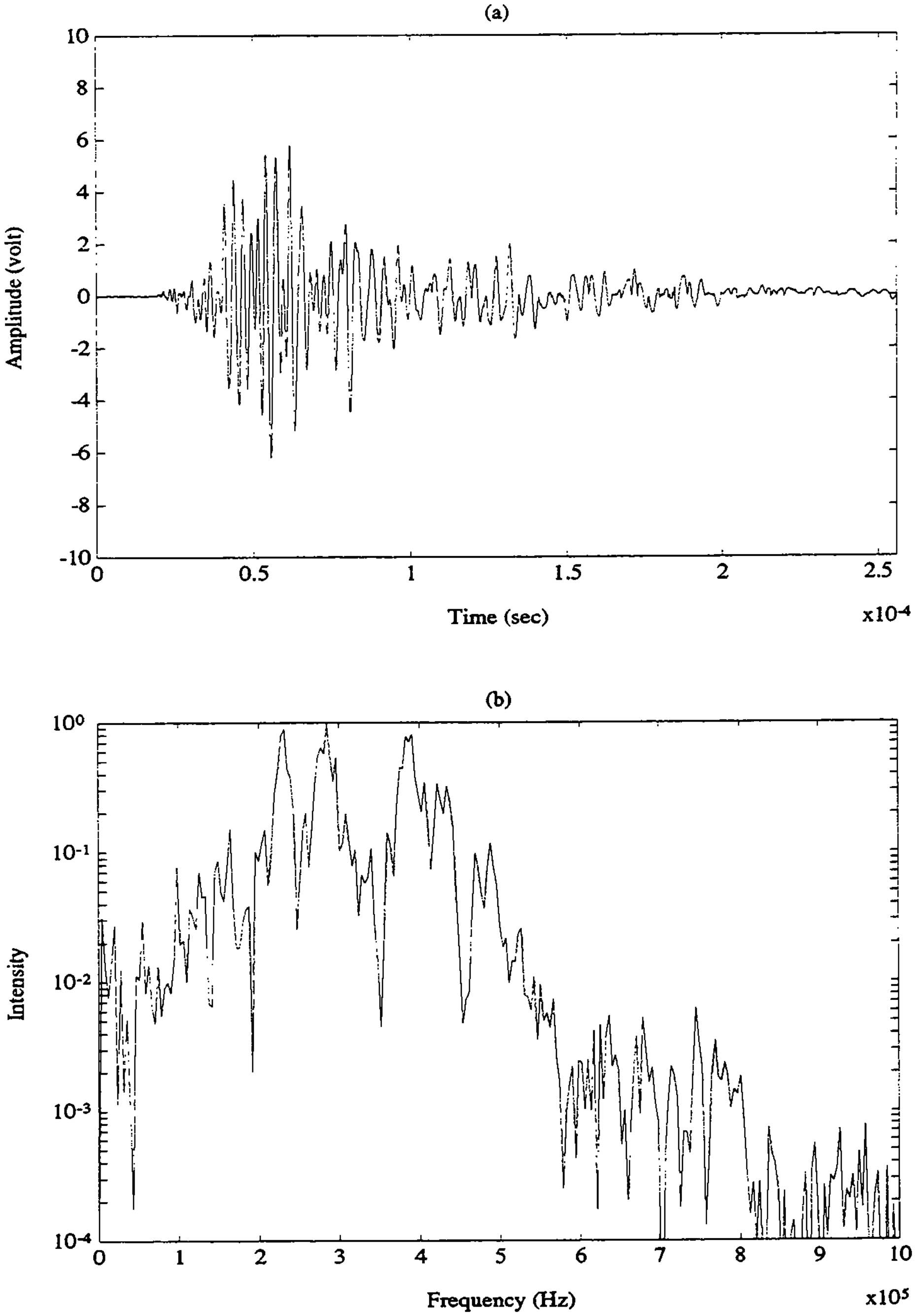

Figure 3.3: Typical AE signal waveform recorded by Tra2.5m (a transient wave recorder) in Locan-AT (graph [a]), and the FFT of the signal in graph (a) (graph [b]).

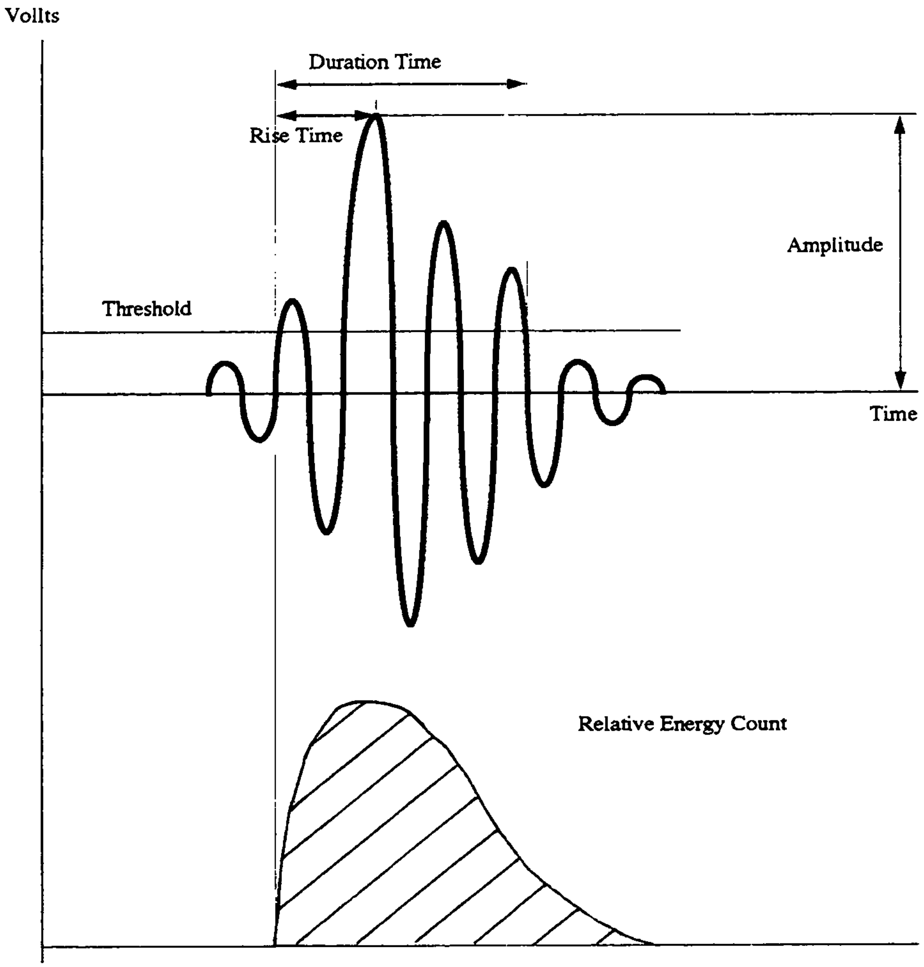

Figure 3.4: Parameters characterizing an AE signal.

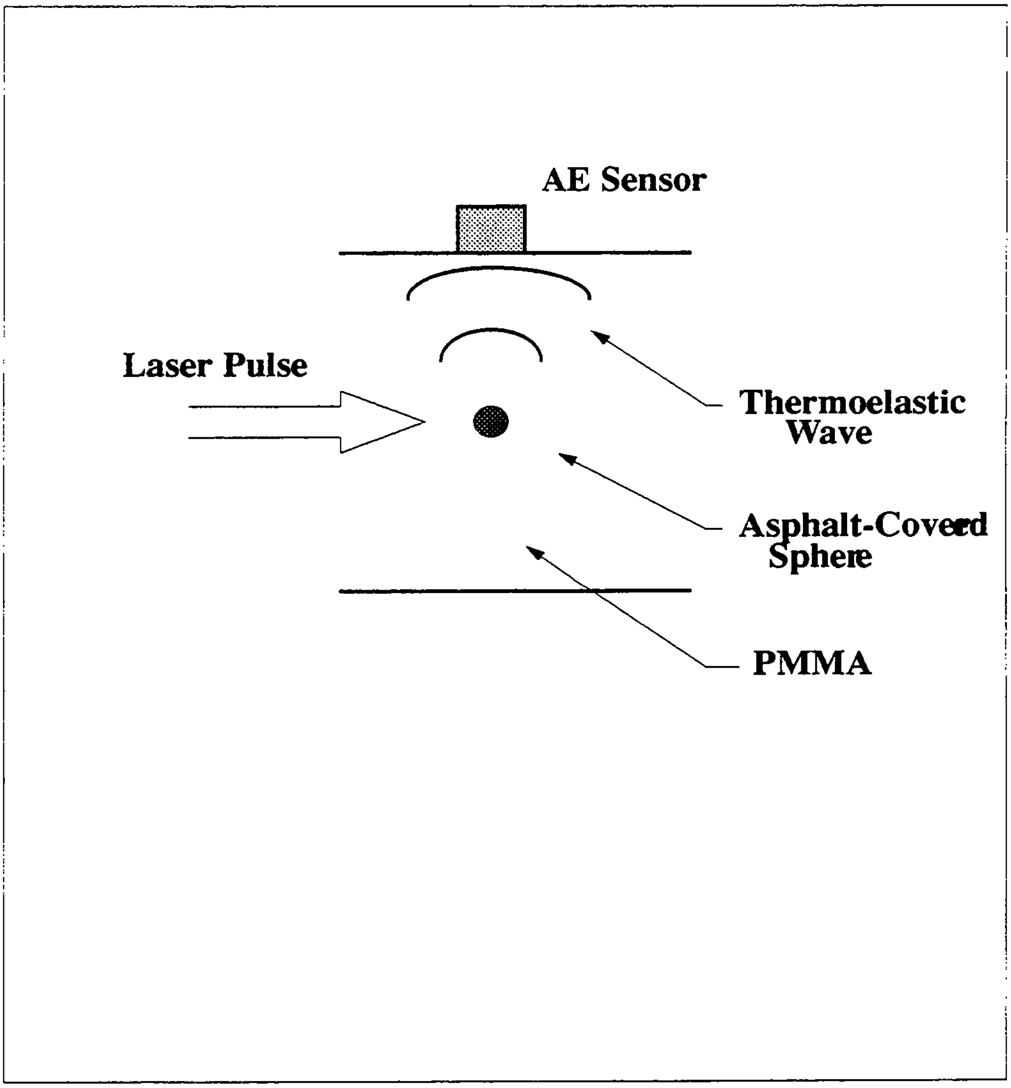

Figure 3.5: Schematic diagram to show AE signal from an asphalt-covered sphere in a PMMA plate by absorption of pulsed laser radiation and thermal expansion.

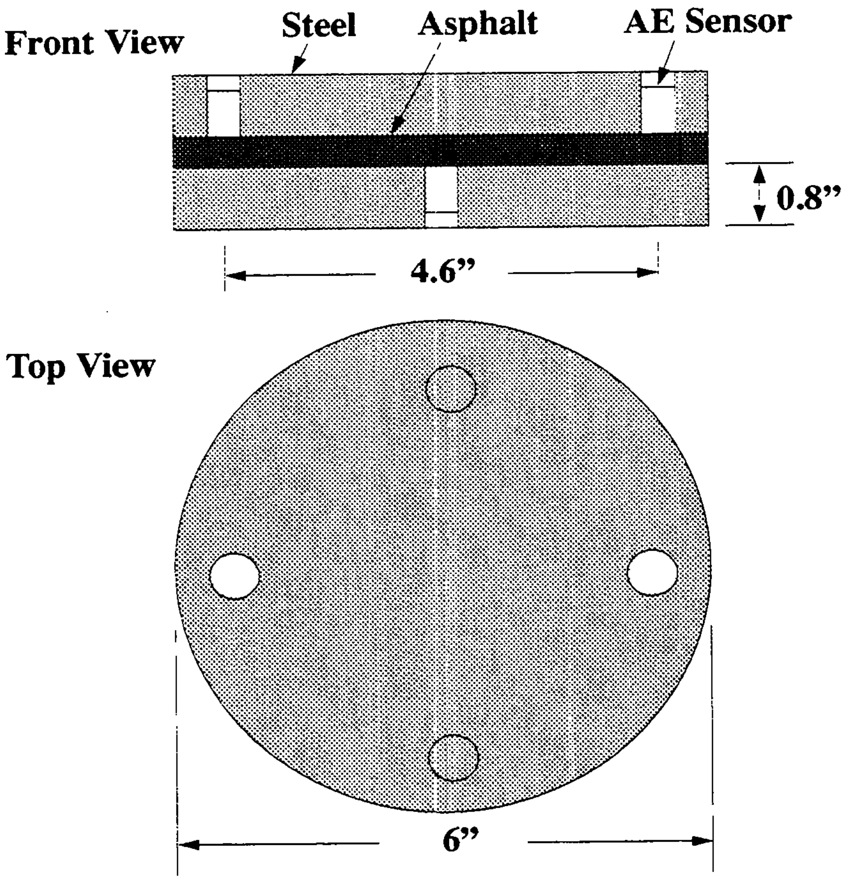

Figure 3.6: Schematic presentation showing modified grip with AE sensors. The AE sensors are in direct contact with the asphalt specimen.

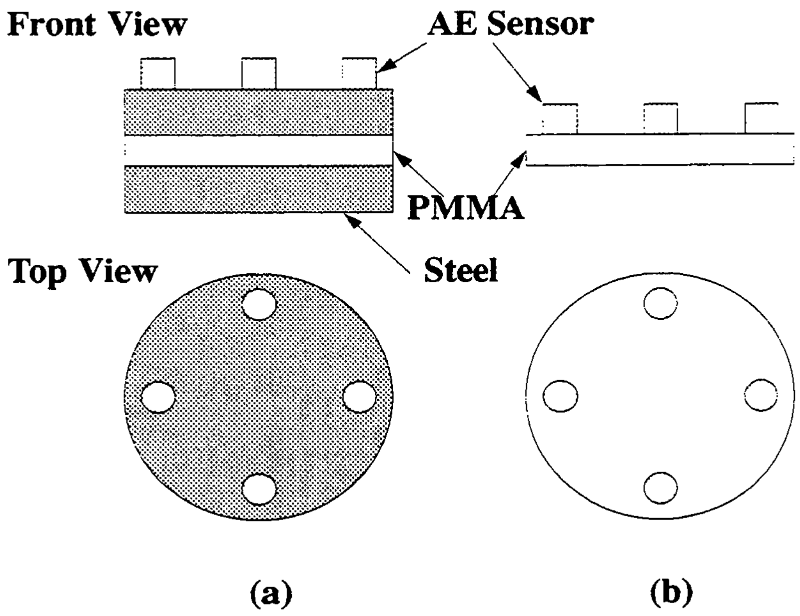

Figure 3.7: AE system calibration test schematic diagrams: AE sensors attached on the steel plate (a); AE sensors put on the PMMA disk (b).

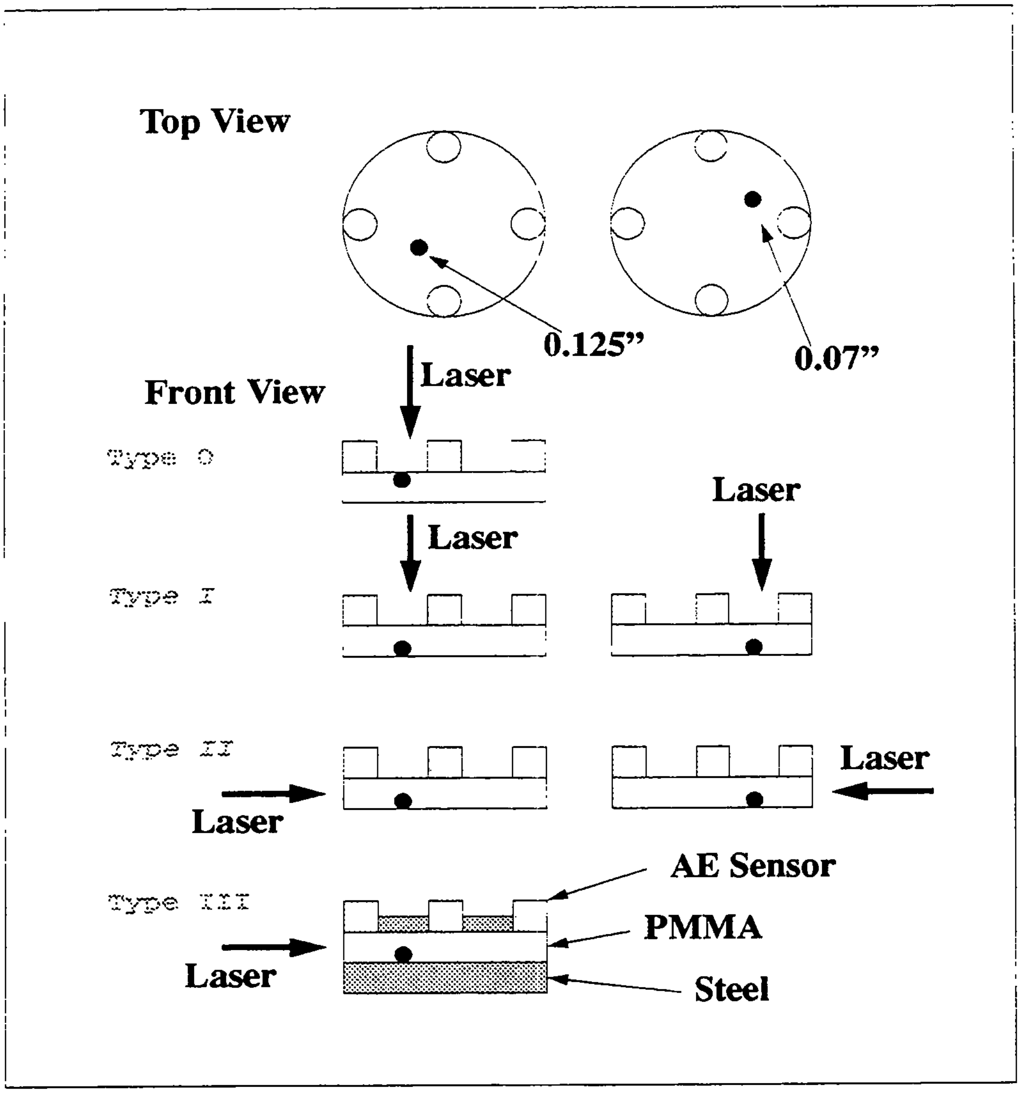

Figure 3.8: Test schematic diagram for system calibration.

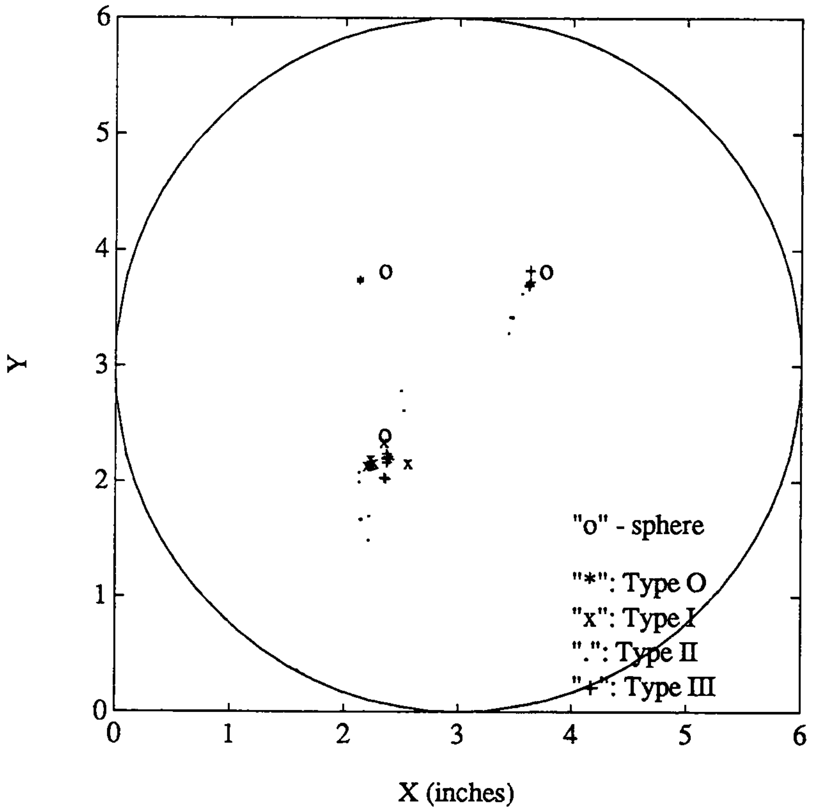

Figure 3.9: Sources located by Locan-AT for the hits with AE energy count greater than 10.

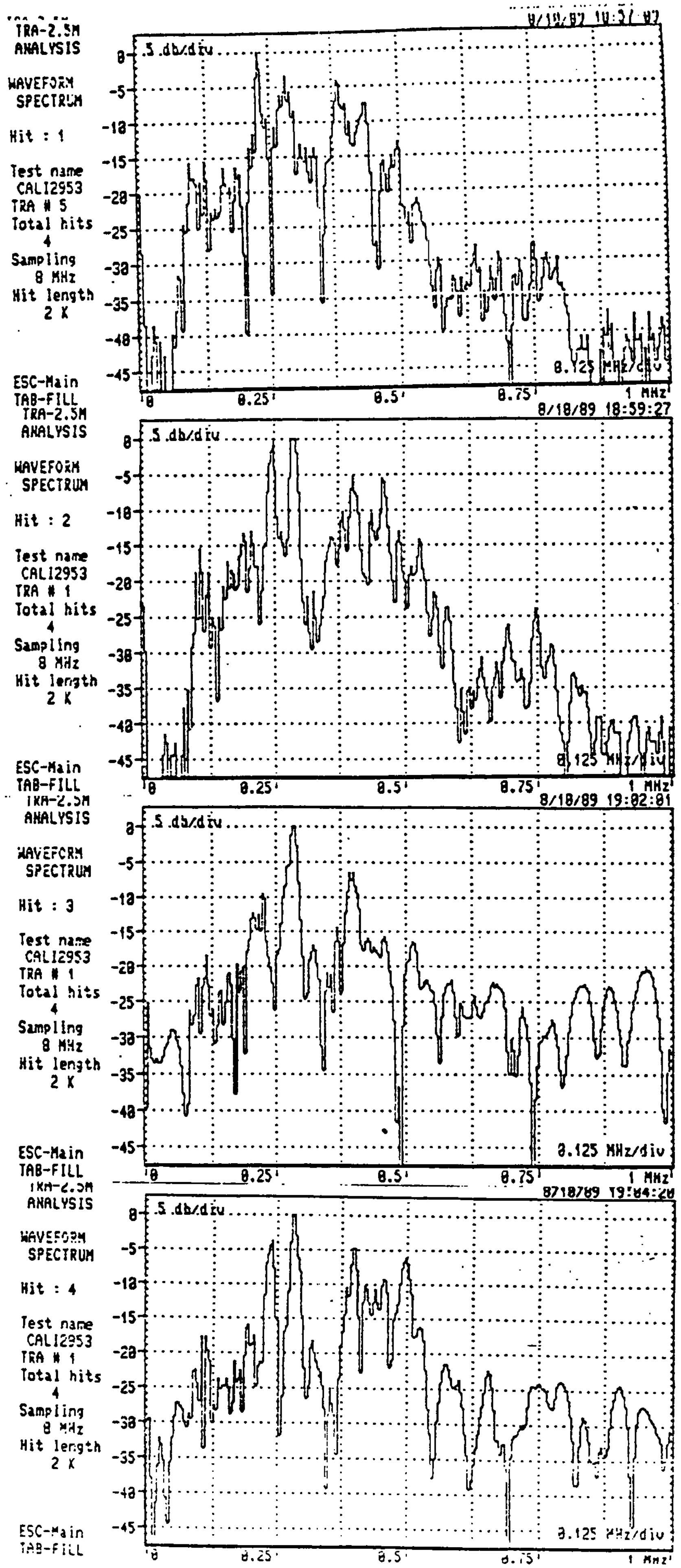

Figure 3.10: Spectra of the four channels for AE signal from small pure asphalt ball, using system calibration type I setup.

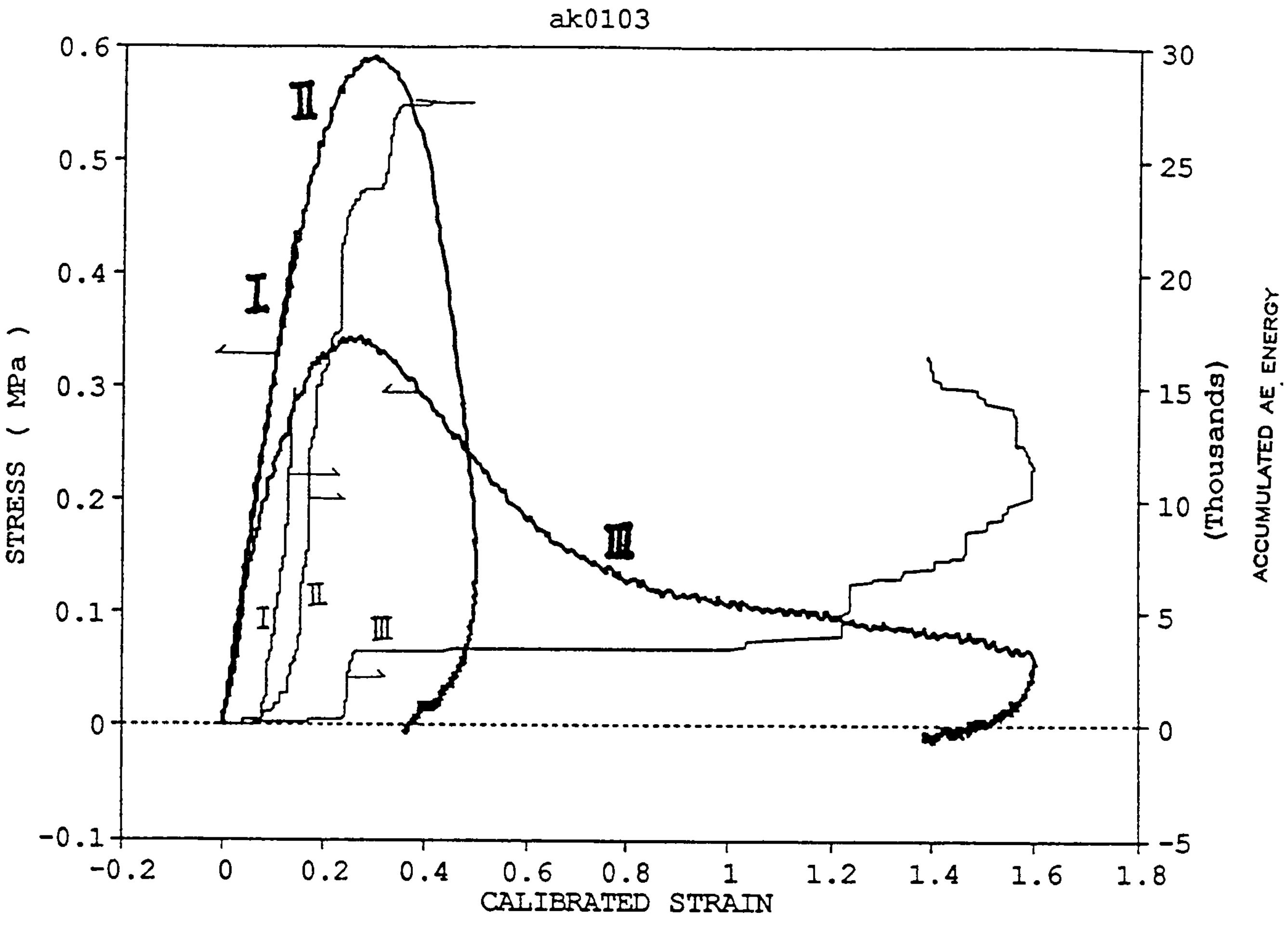

Figure 3.11: AE output signals corresponding to the mechanical behavior of AK0103 specimen

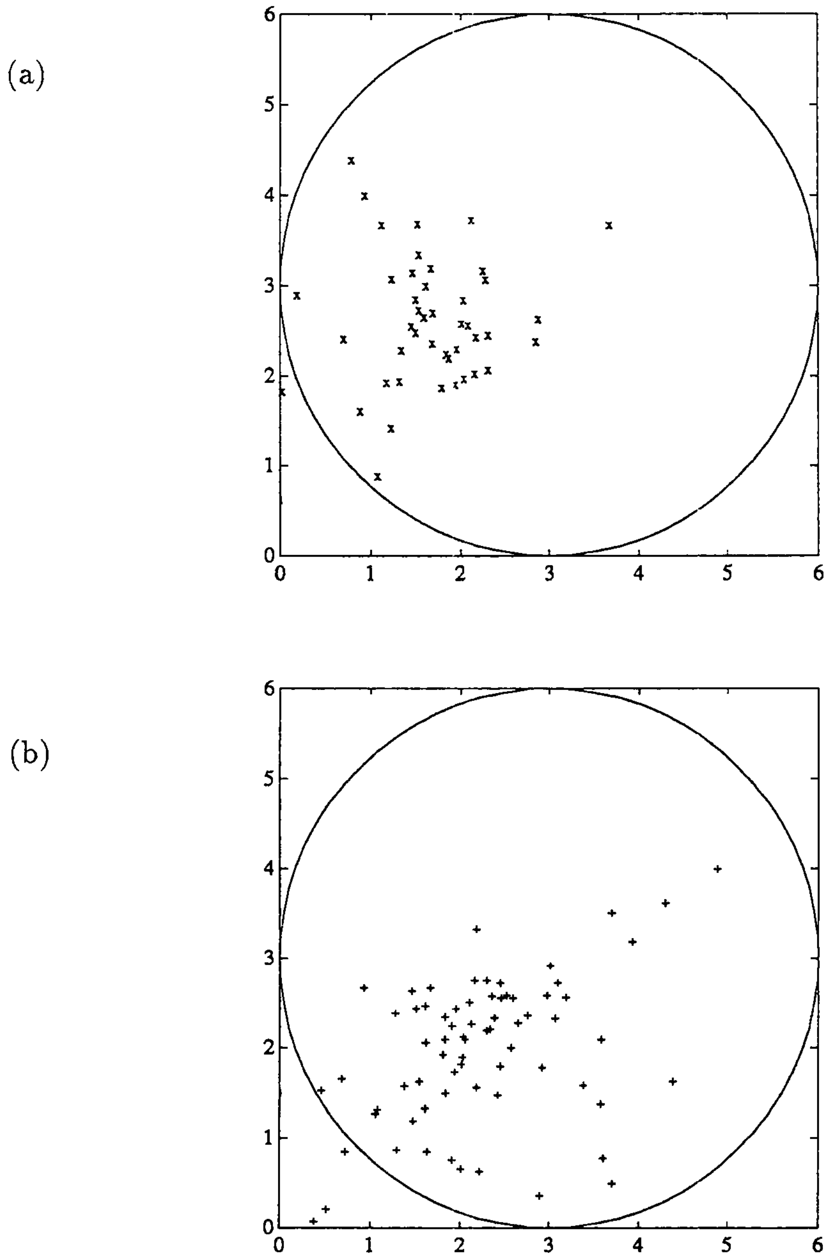

Figure 3.12: Detected AE sources for tests I (graph [a]) and II (graph [b]) on AK0103 specimen.

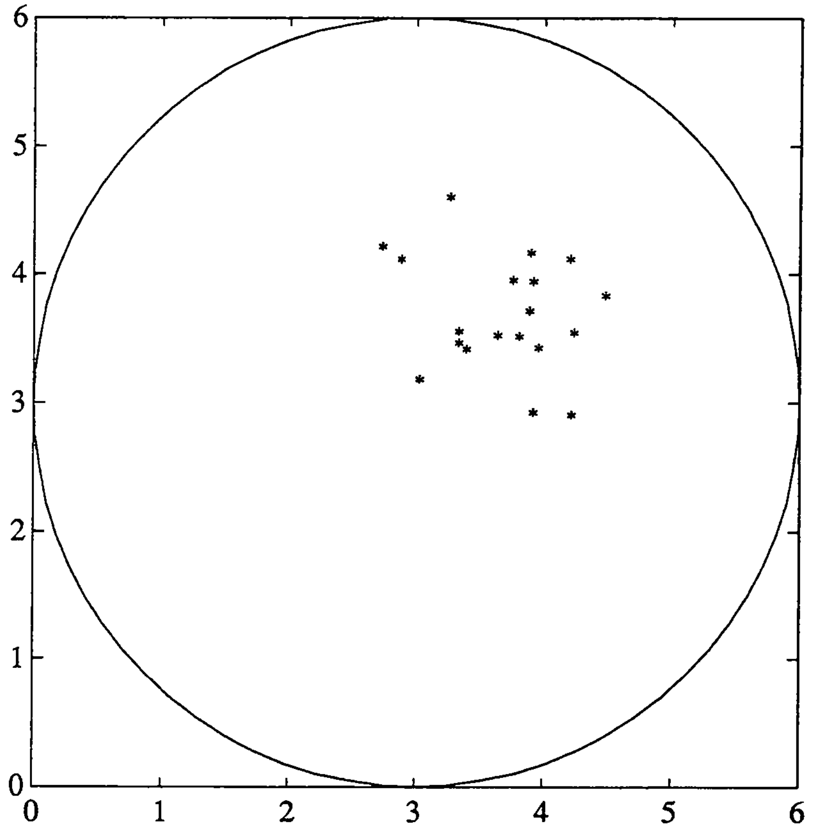

Figure 3.13: Detected AE sources for test III on AK0103 specimen.

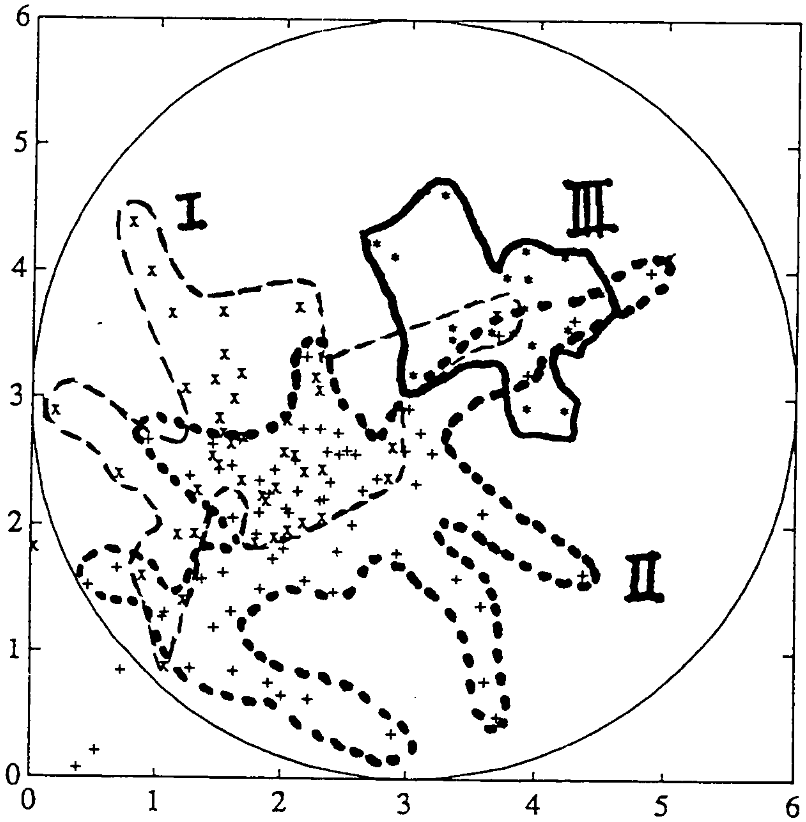

Figure 3.14: Healing behaviors and overall distribution of AE events on AK0103 specimen

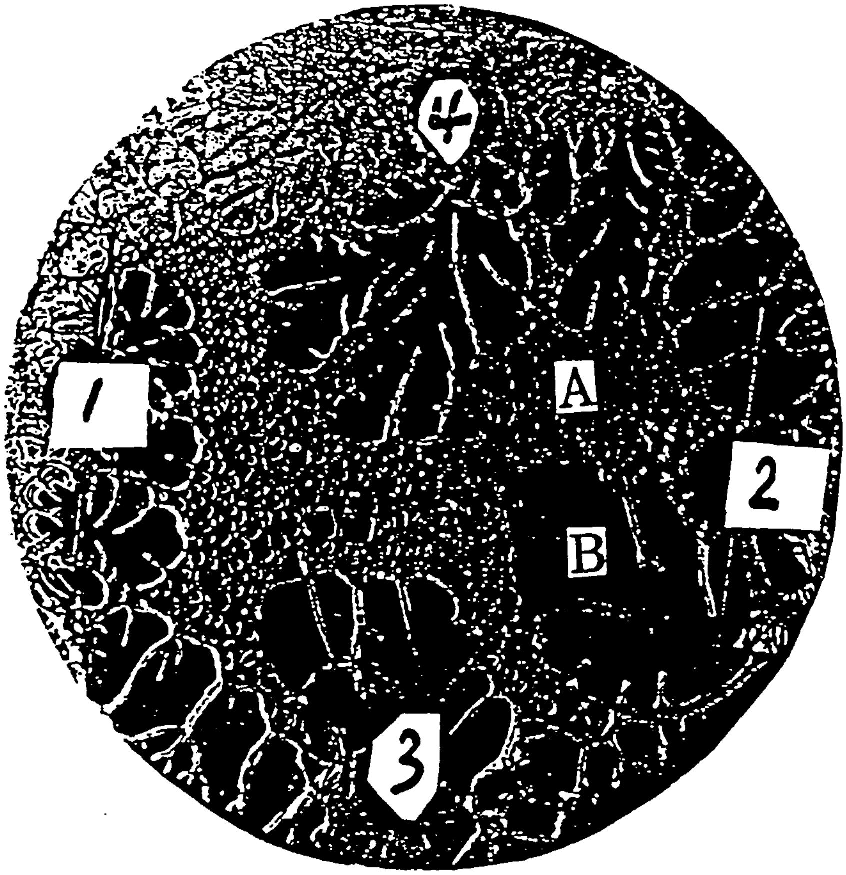

Figure 3.15: Picture of the rupture surface of AK0103 specimen: (A) cavities detected by AE; (B) fast failure large deformation with high strain rate after AK010303 test.

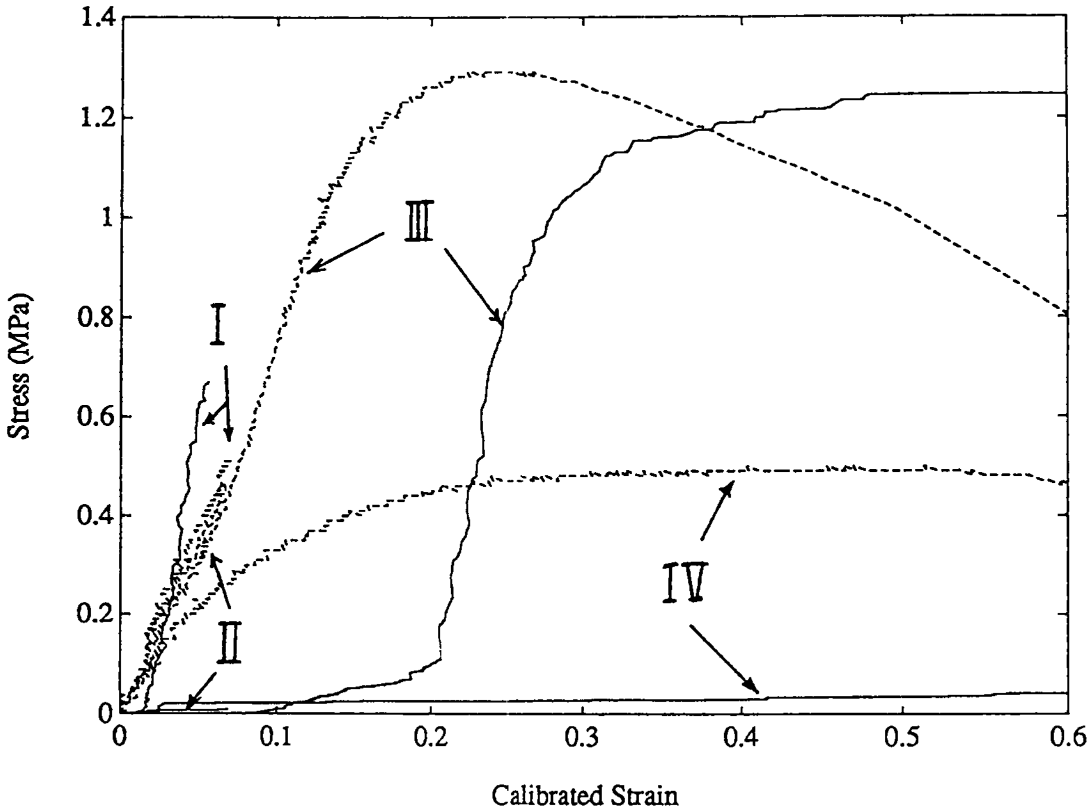

Figure 3.16: AE output signals corresponding to the mechanical behavior in the AK04 thin film specimen (0.5 mm in thickness). The dashed lines are the average uniaxial stress and the solid lines are the AE output as functions of strain. The test codes of Test I to IV are AK040101, AK040102, AK040103 and AK040201

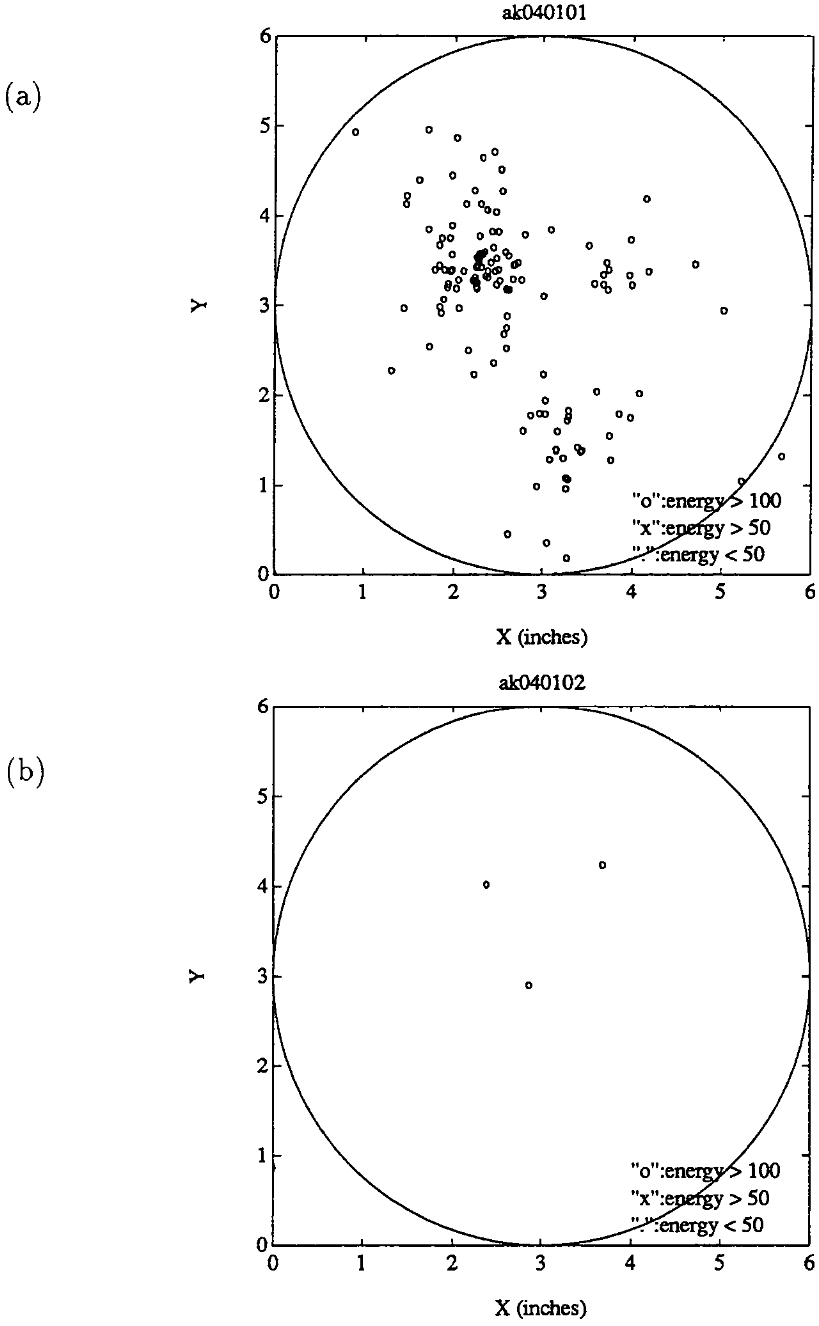

Figure 3.17: Detected AE sources with energy greater than 100 for tests of AK040101 (graph [a]) and AK040102 (graph [b]) on AK04 specimen.

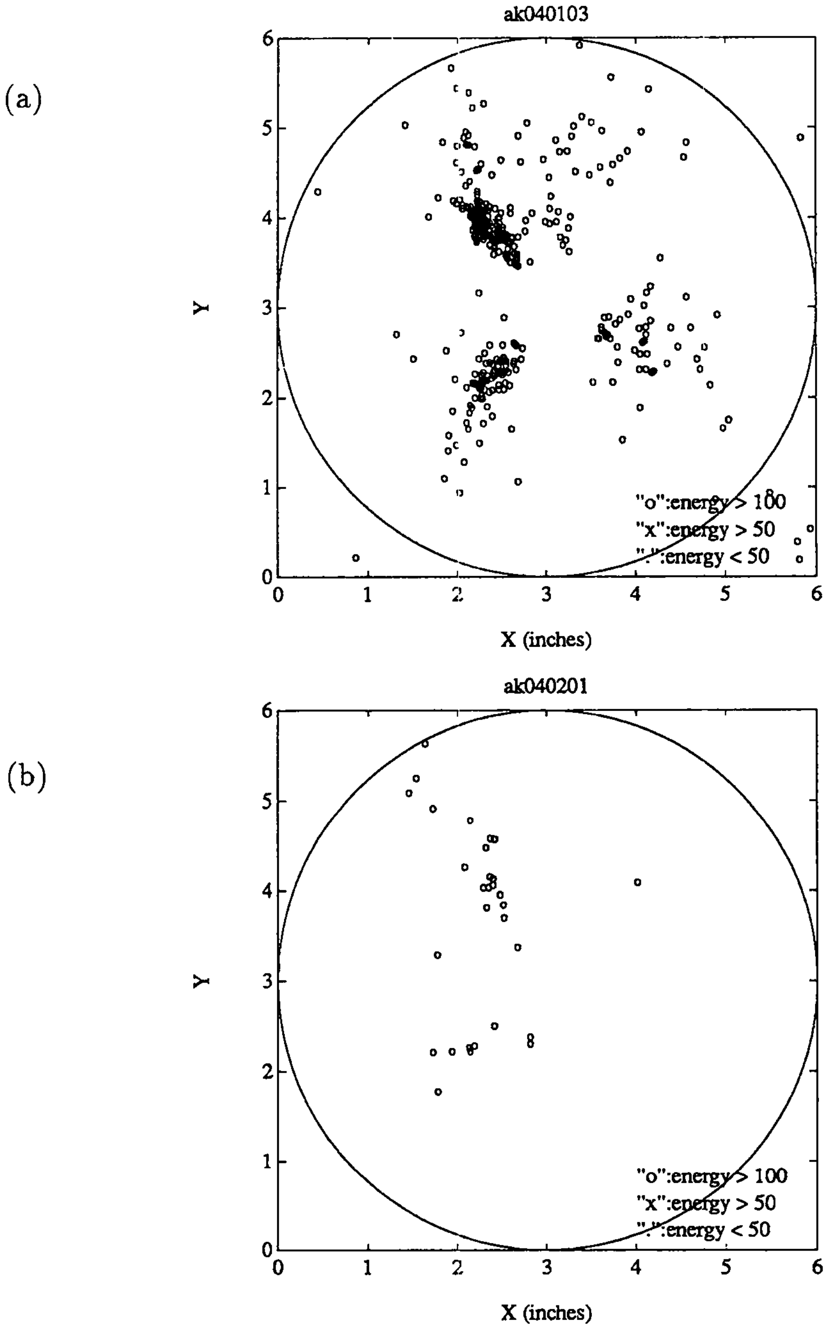

Figure 3.18: Detected AE sources with energy greater than 100 for tests of AK040101 (graph [a]) and AK040201 (graph [b]) on AK04 specimen.

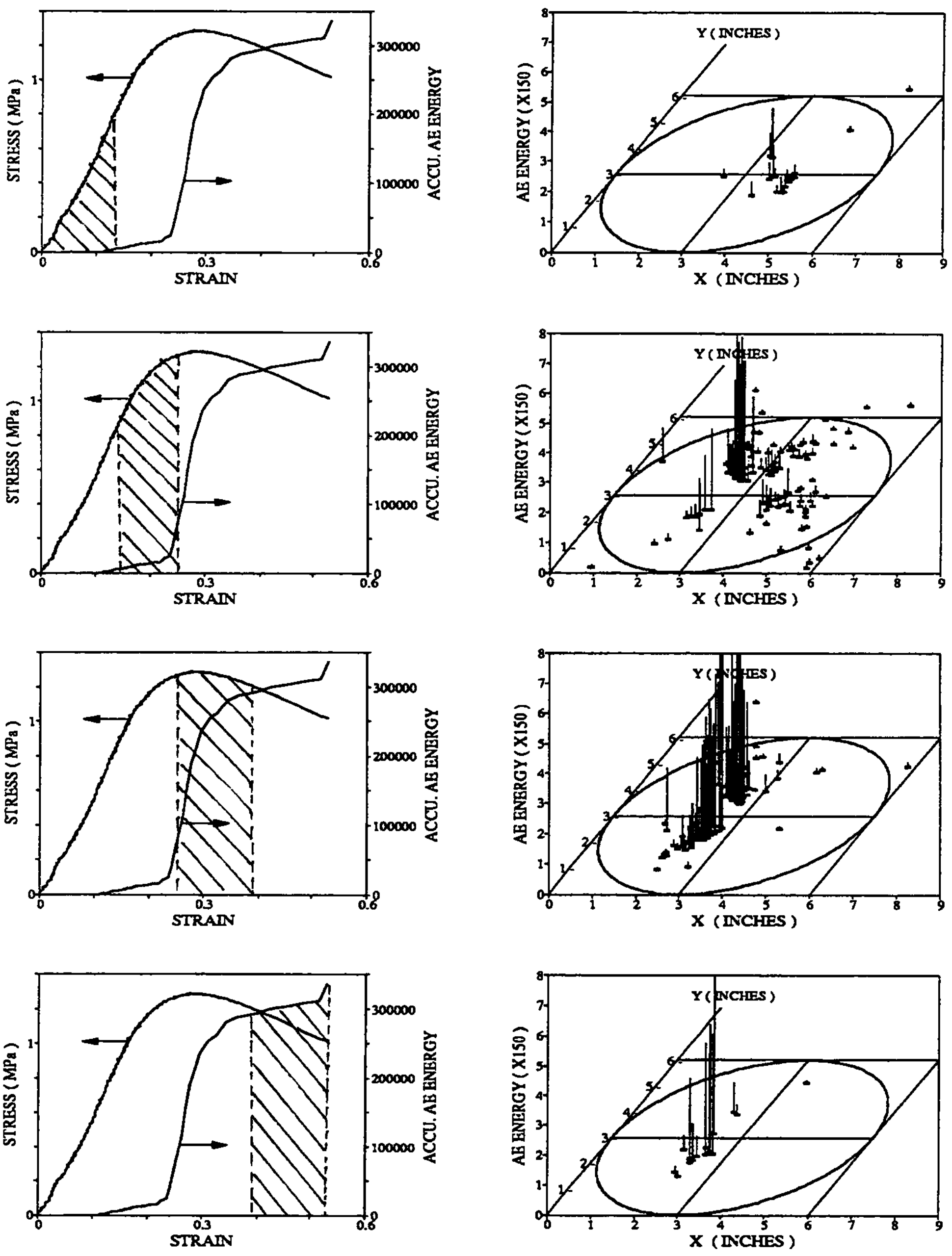

Figure 3.19: The plots on the left show the loading history and AE response for AK040103 test. Shaded areas indicate the intervals plotted on the 3-D diagrams to the right. Right-side 3-D plots show locations and AE signal intensities (vertical lines) of events occurring in the intervals indicated in the left-side plots.

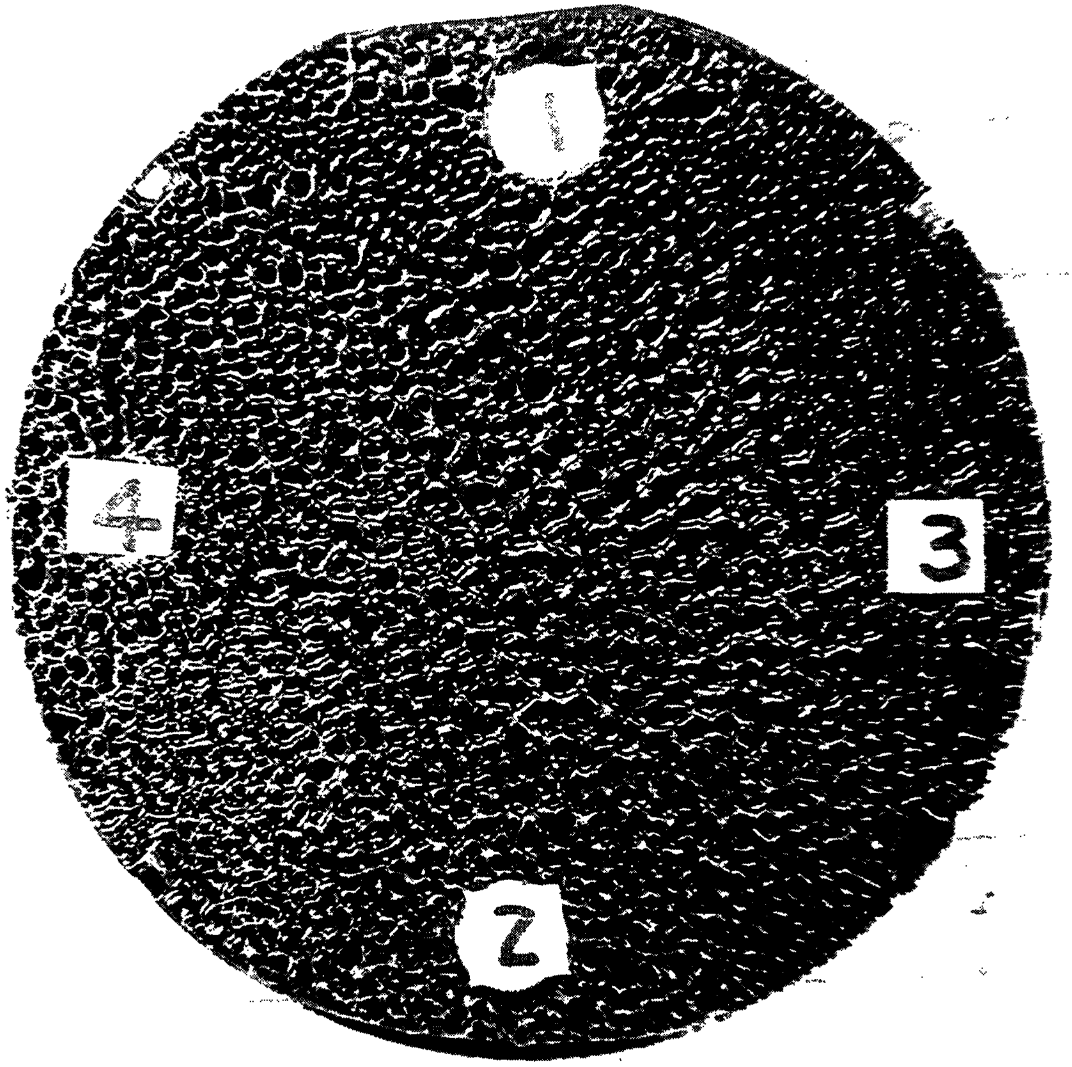

Figure 3.20: Picture of the rupture surface of AK04 specimen.

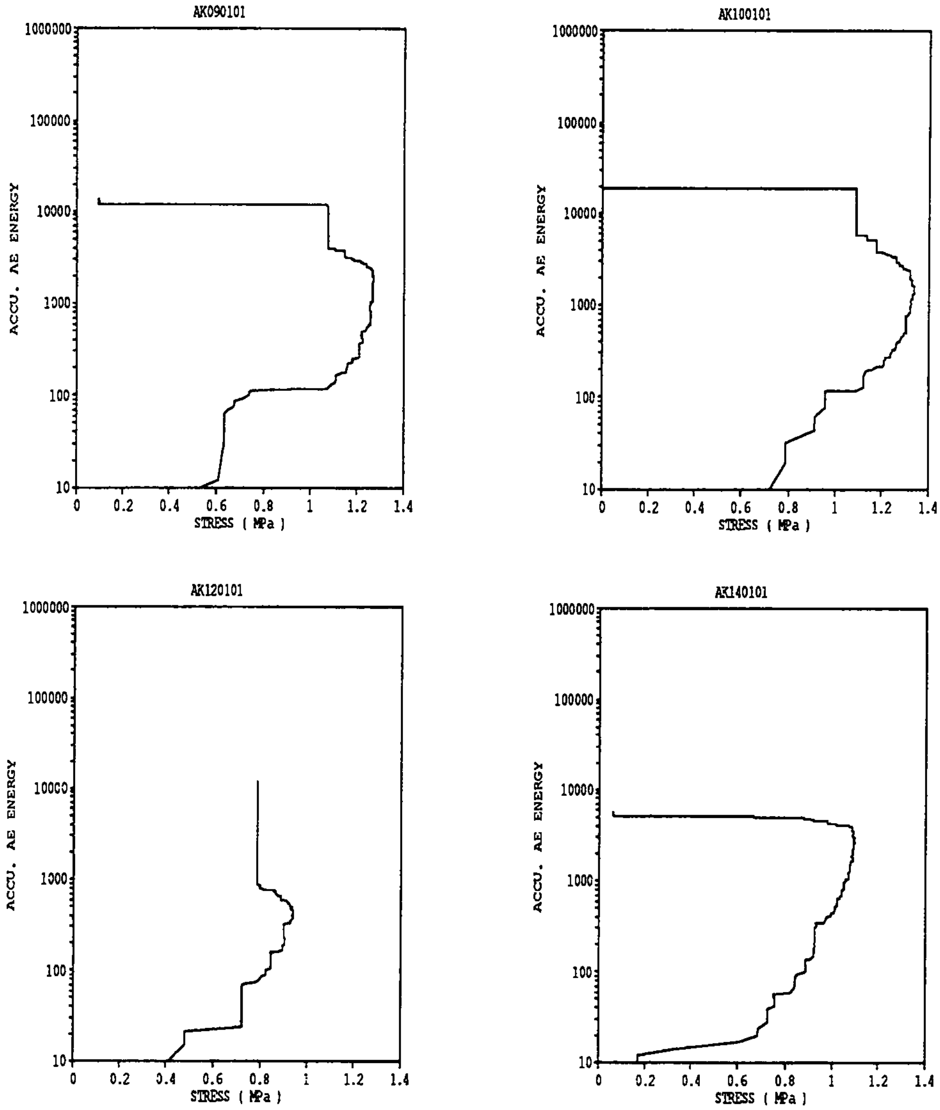

Figure 3.21: The accumulated AE energy corresponding with the applied load for AAK-1 specimen with thickness of 0.32 mm (AK10) to 0.5 mm (AK09 [vacuum treated], AK12, and AK14). MTS stroke control and loading rate in the linear range is 8 psi/sec.

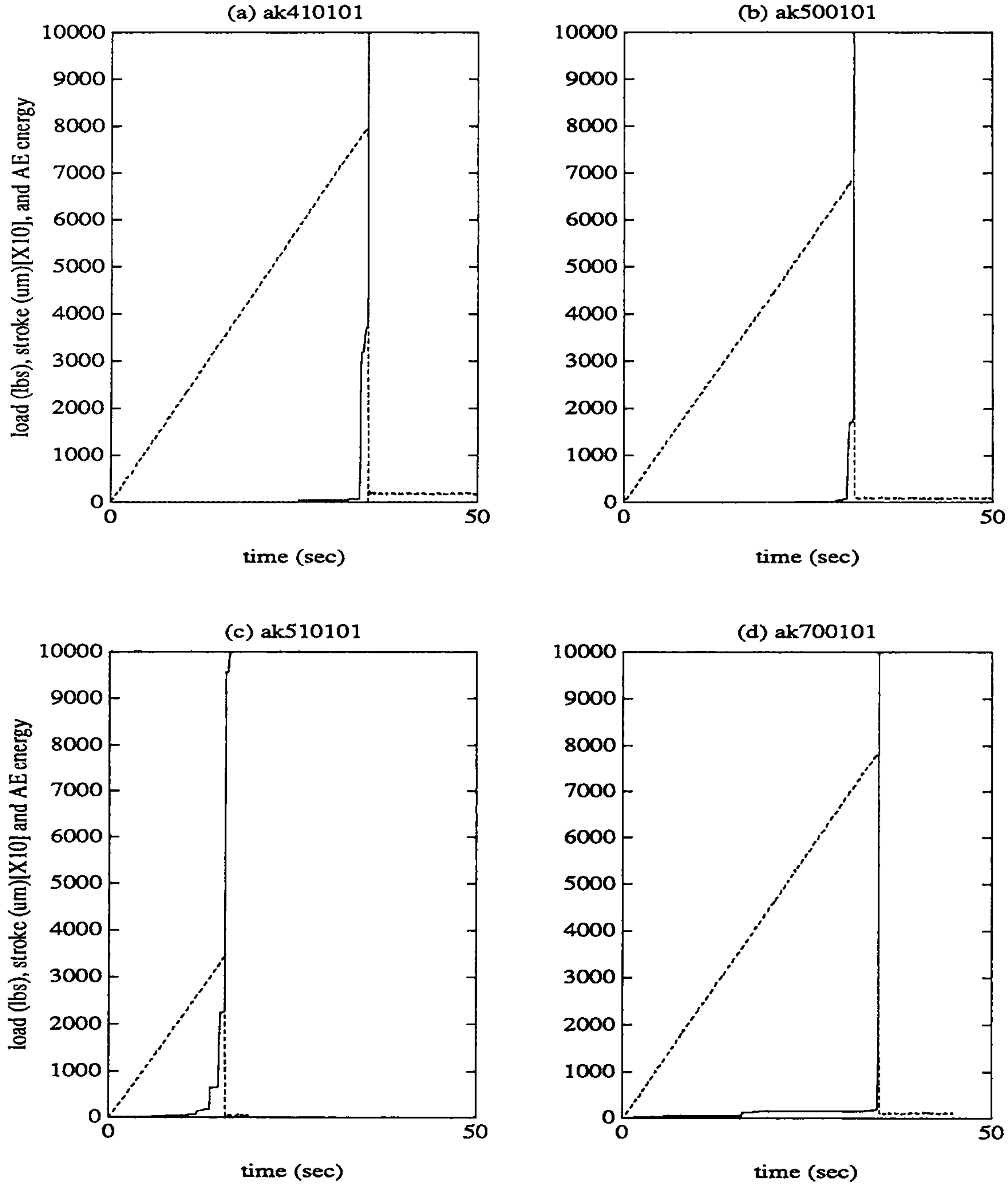

Figure 3.22: The AE output signals corresponding to the mechanical behavior of AAK-1 specimen with thickness of 0.12 mm (AK41, AK50, and AK51) to 0.2 mm (AK70) at loading rate of 8 psi/sec. The dashed lines are applied load, and the solid lines are accumulated AE energy versus time for each test.

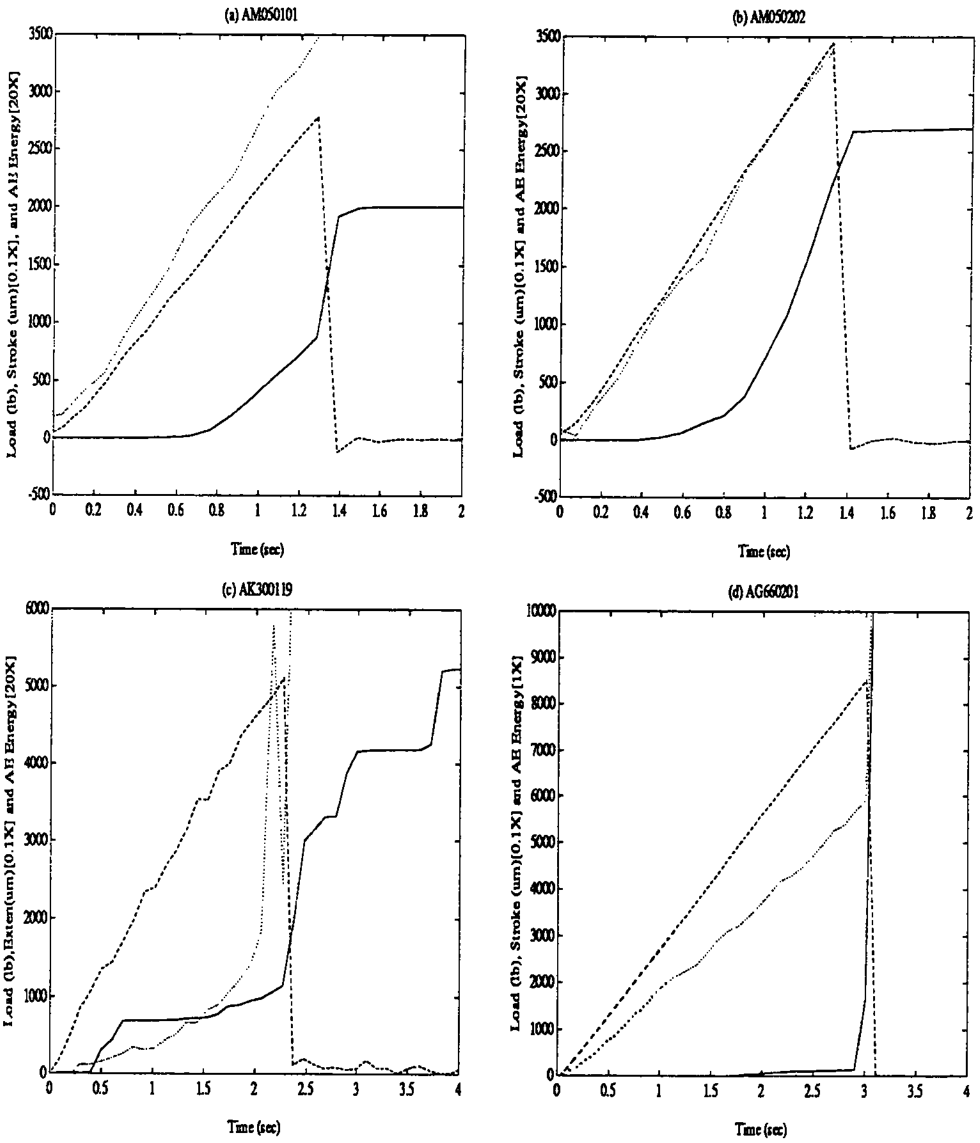

(a) AM050101

(b) AM050202

(c) AK300119

(d) AG660201

Figure 3.23: The AE output signals corresponding to the mechanical behavior of AAM-1 (graphs [a] and [b]), AAK-1(graph [c]) and AAG-1(graph [d]) asphalt specimens with 5-mm thickness. The dashed lines are applied load, and the solid lines are the corresponding accumulated AE energy as a function of time. The dotted lines are the displacement from stroke or extensometer for each test.

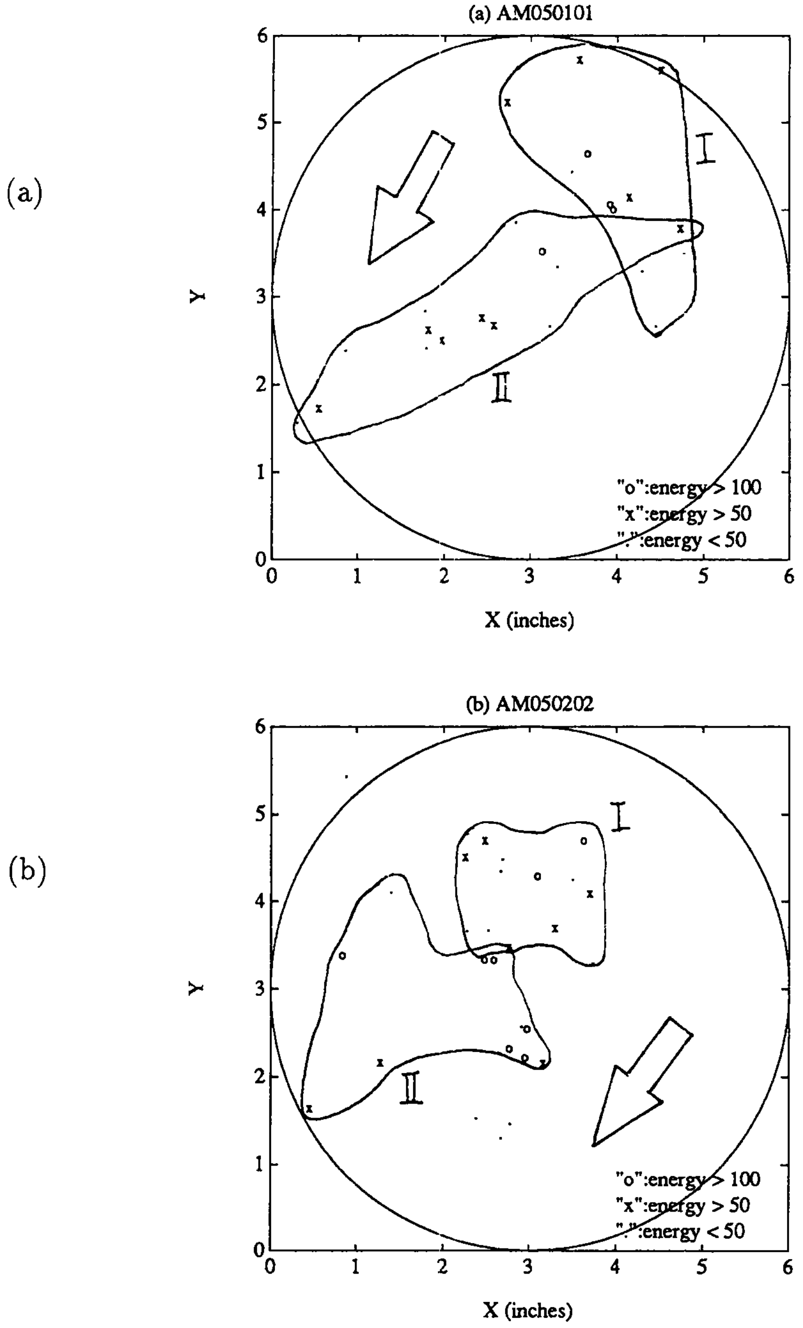

Figure 3.24: Detected AE sources for AAM-1 (graphs [a] and [b]) asphalt specimen with 5-mm thickness. The AE sources are grouped (region I and II) according to loading history. The arrows show the direction of AE signal propagation.

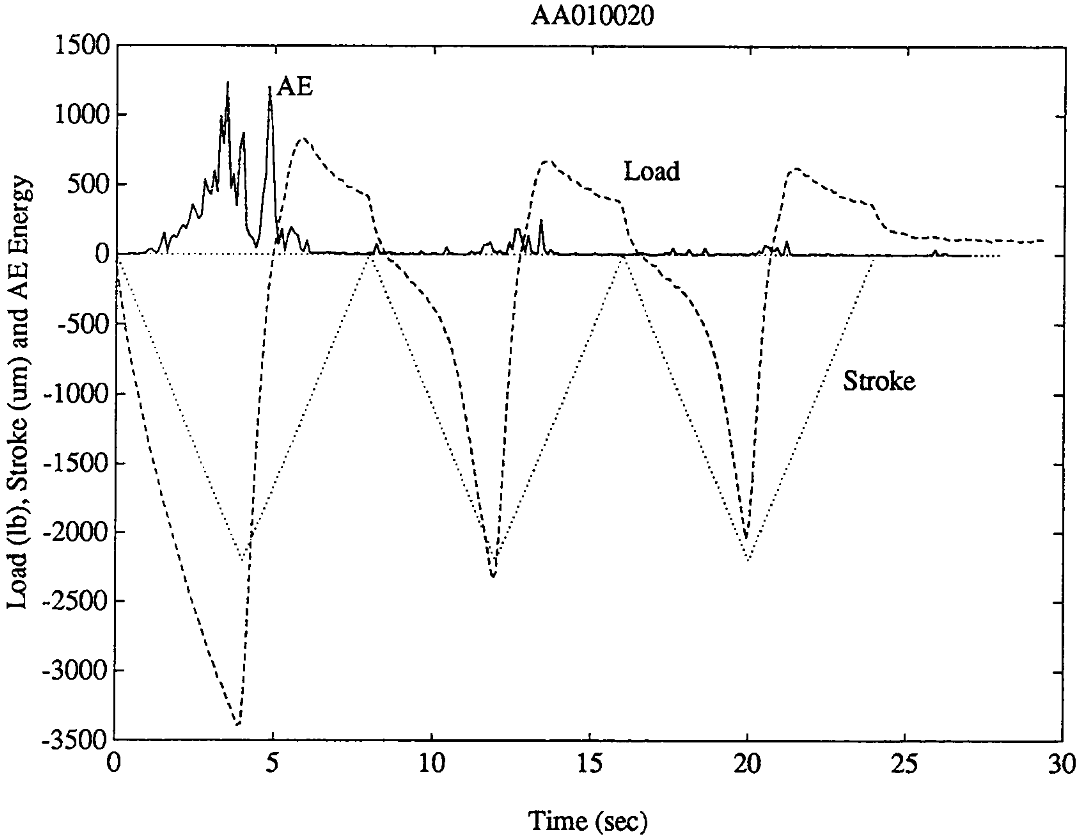

Figure 3.25: AE output signal energy for the cyclic compression test of aphalt AAA-1 with 5-mm thickness.

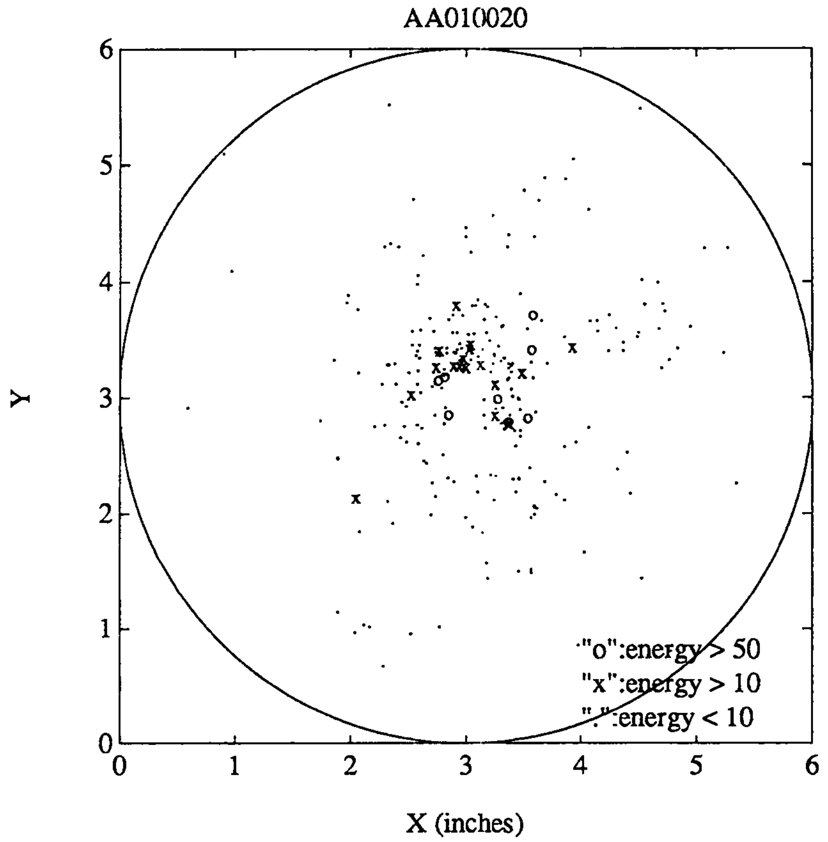

Figure 3.26: AE hits located in the cyclic test of asphalt AAA-1.

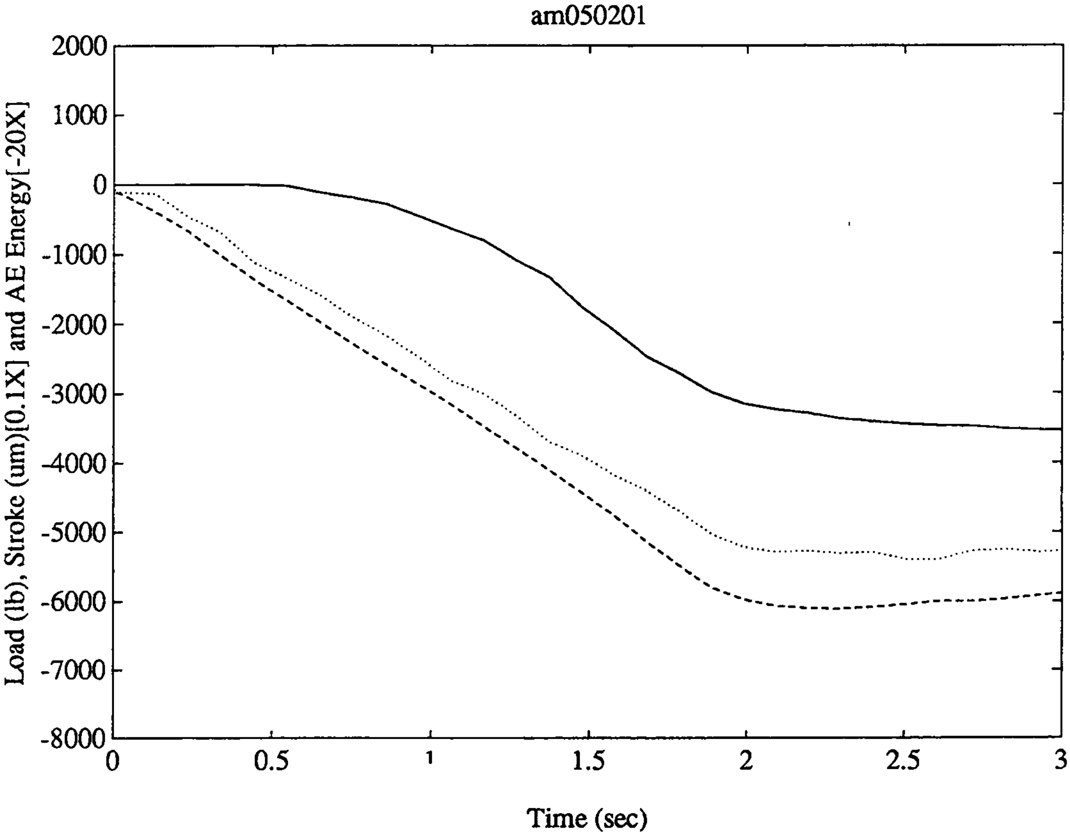

Figure 3.27: The AE output signals corresponding to the uniaxial compression tests on AAM-1 specimen with 5-mm thickness. The dashed, dotted, and solid lines represent the applied load, stroke displacement, and accumulated AE energy, respectively, as a function of time.

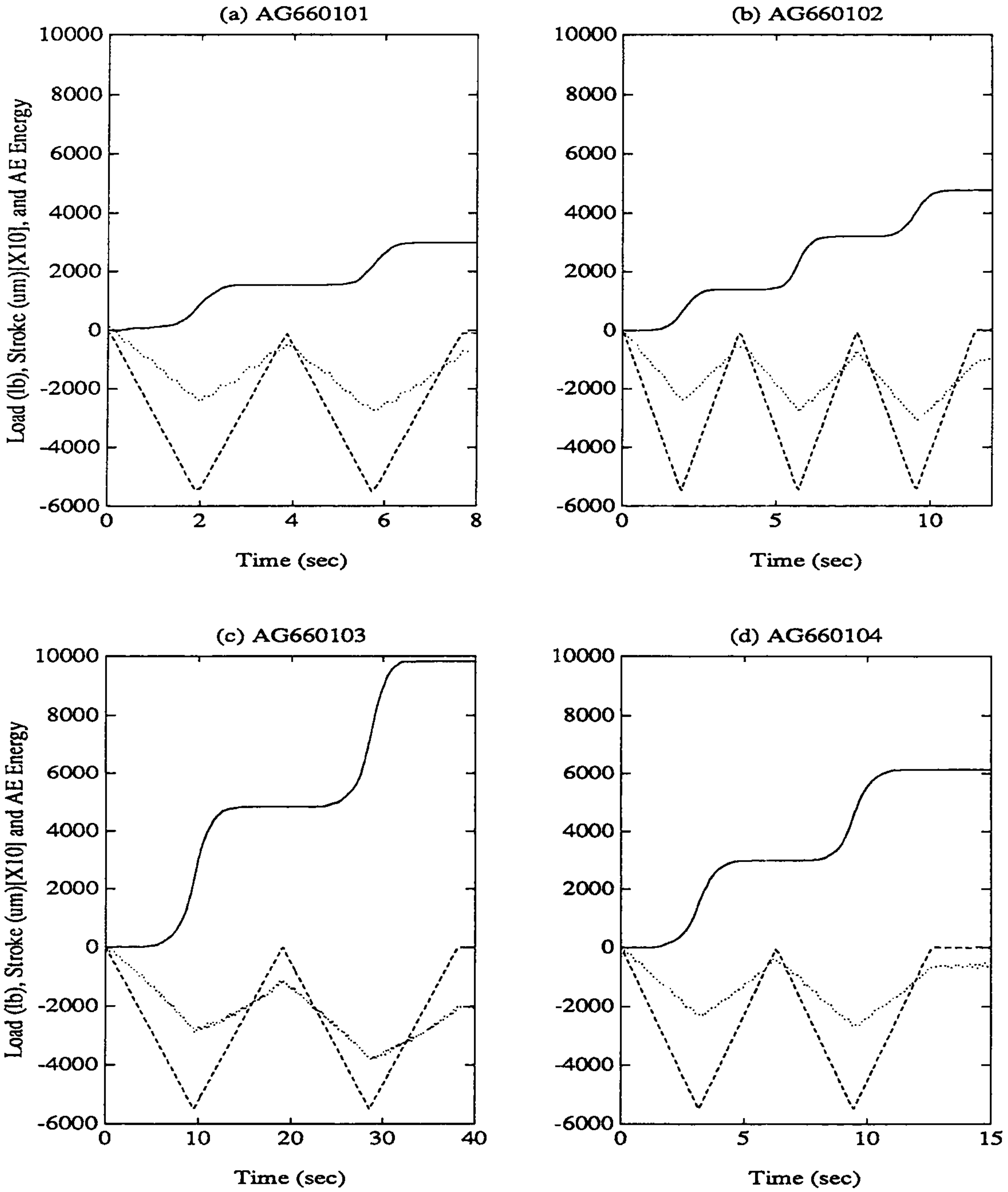

Figure 3.28: The AE output signals corresponding to the mechanical behavior of the uniaxial compression tests on AAG-1 specimen with 5-mm thickness. The dashed, dotted, and solid lines represent the applied load, stroke displacement, and accumulated AE energy, respectively, as a function of time.

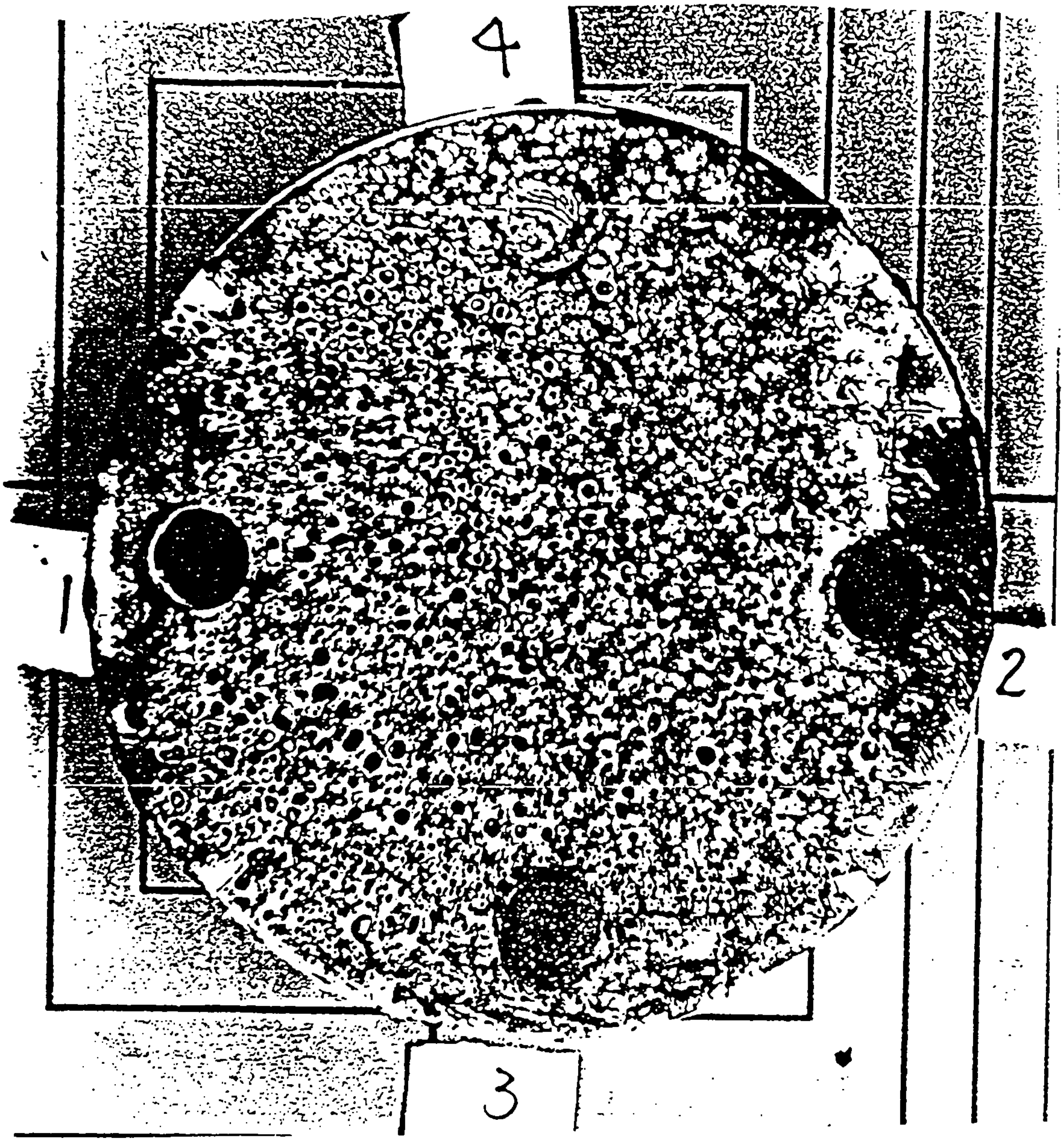

Figure 3.29: The rupture surface of a regular specimen.

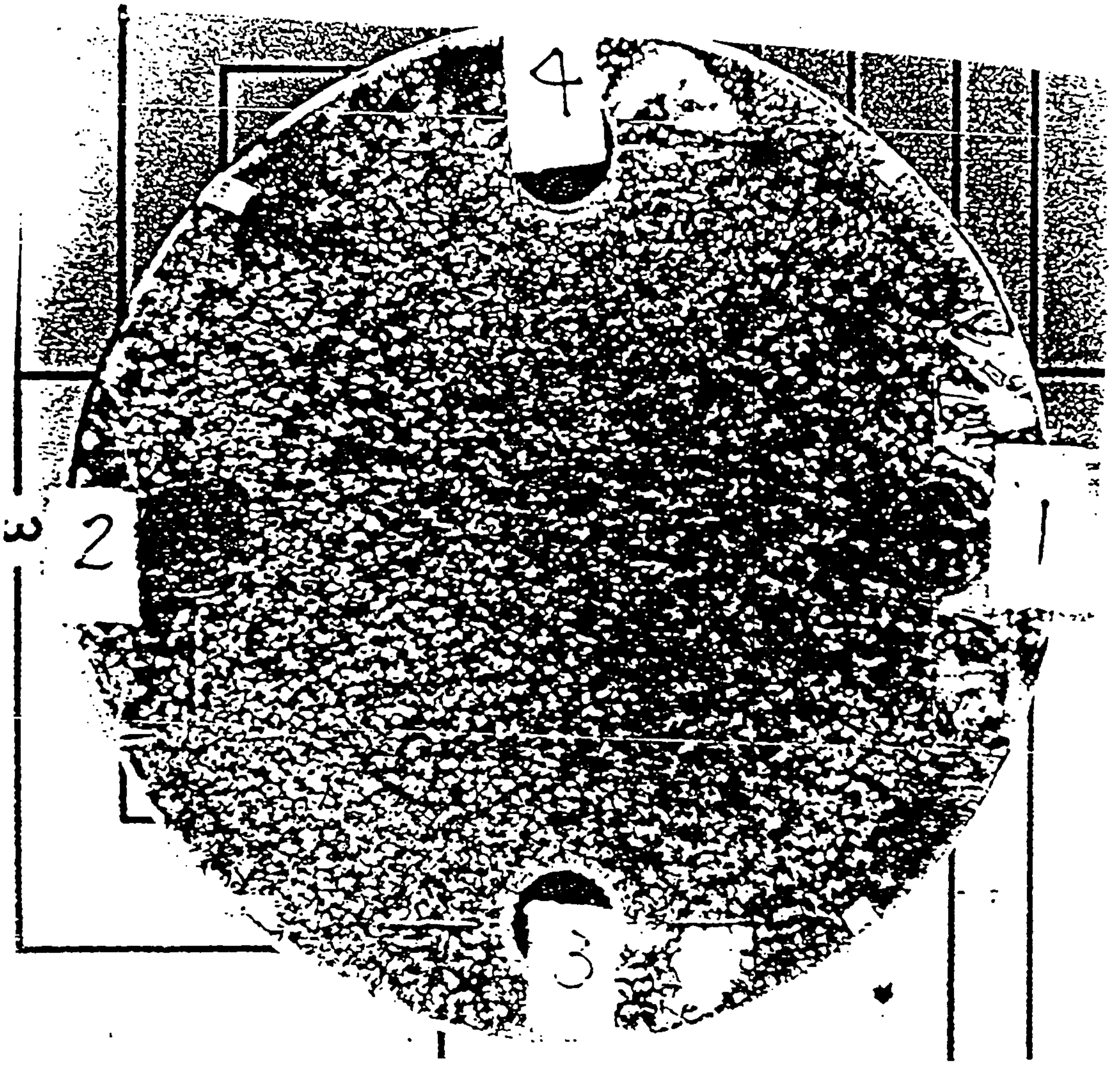

Figure 3.30: The rupture surface of a vacuum-treated specimen.

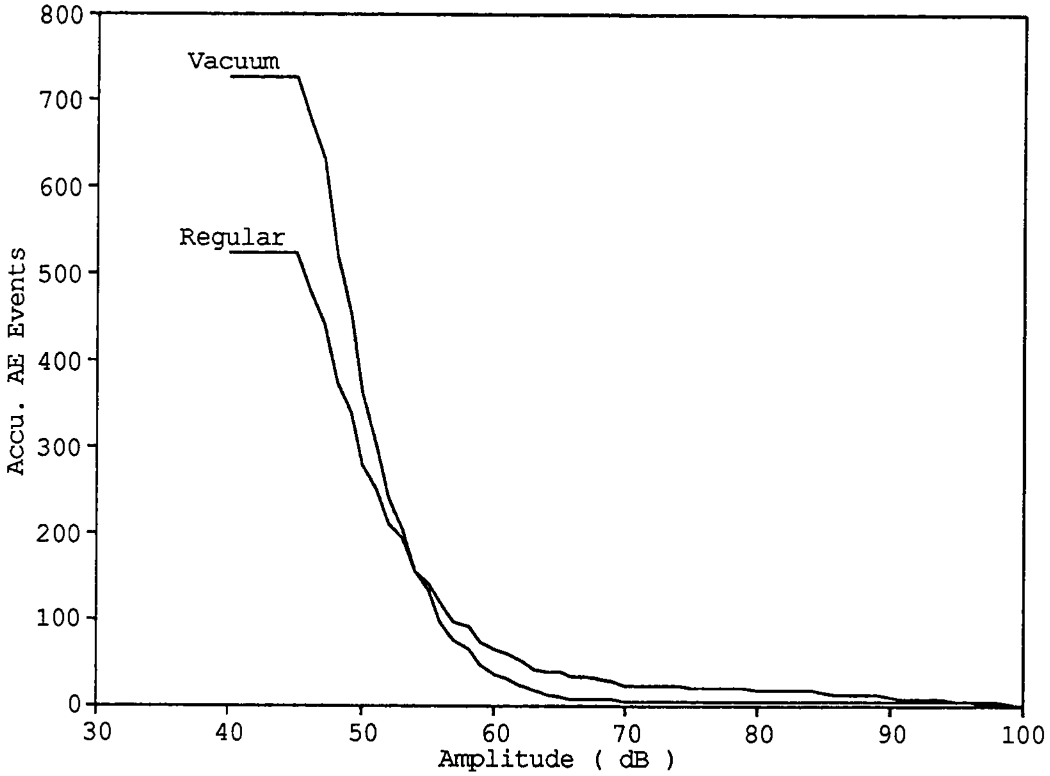

Figure 3.31: Comparison of AE amplitude distribution of a regular and a vacuum-treated specimen.

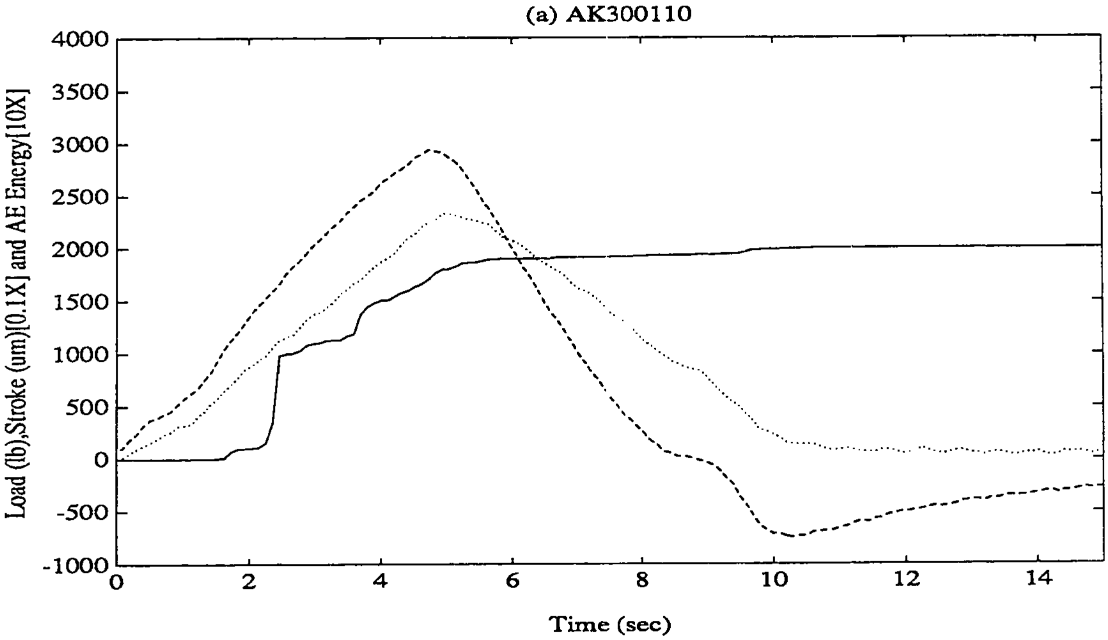

(a) AK300110

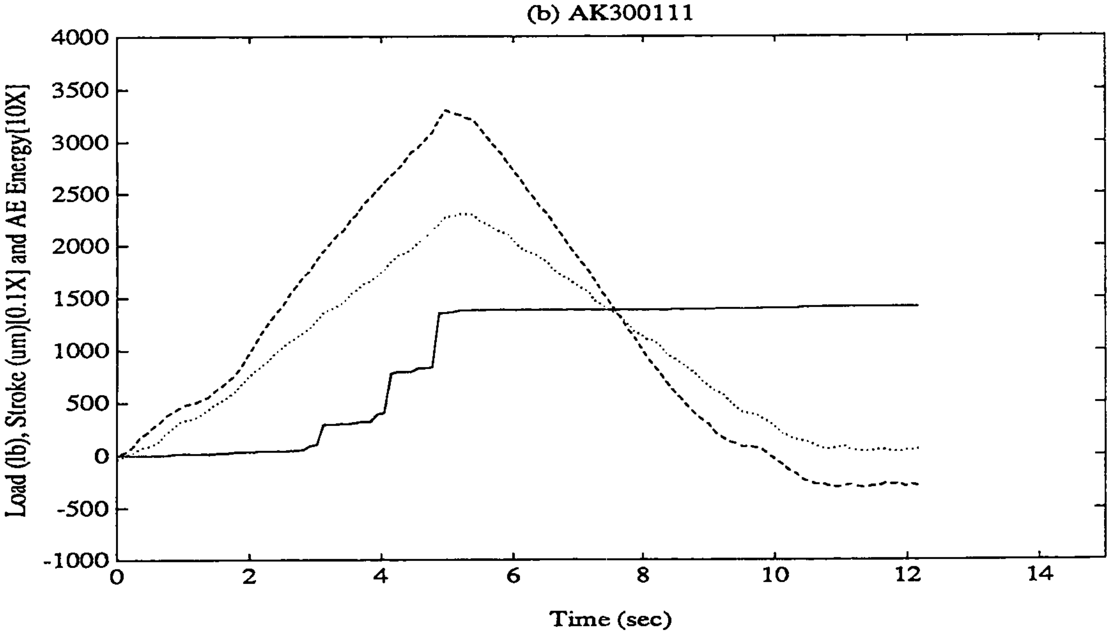

(b) AK300111

Figure 3.32: The AE output signals corresponding to the mechanical behavior in the AAK-1 specimen with 5 mm thickness at 60°F (graph (a)) and 50°F (graph (b)). The dashed, dotted and solid lines represent the applied load, stroke displacement and accumulated AE energy as a function of time.

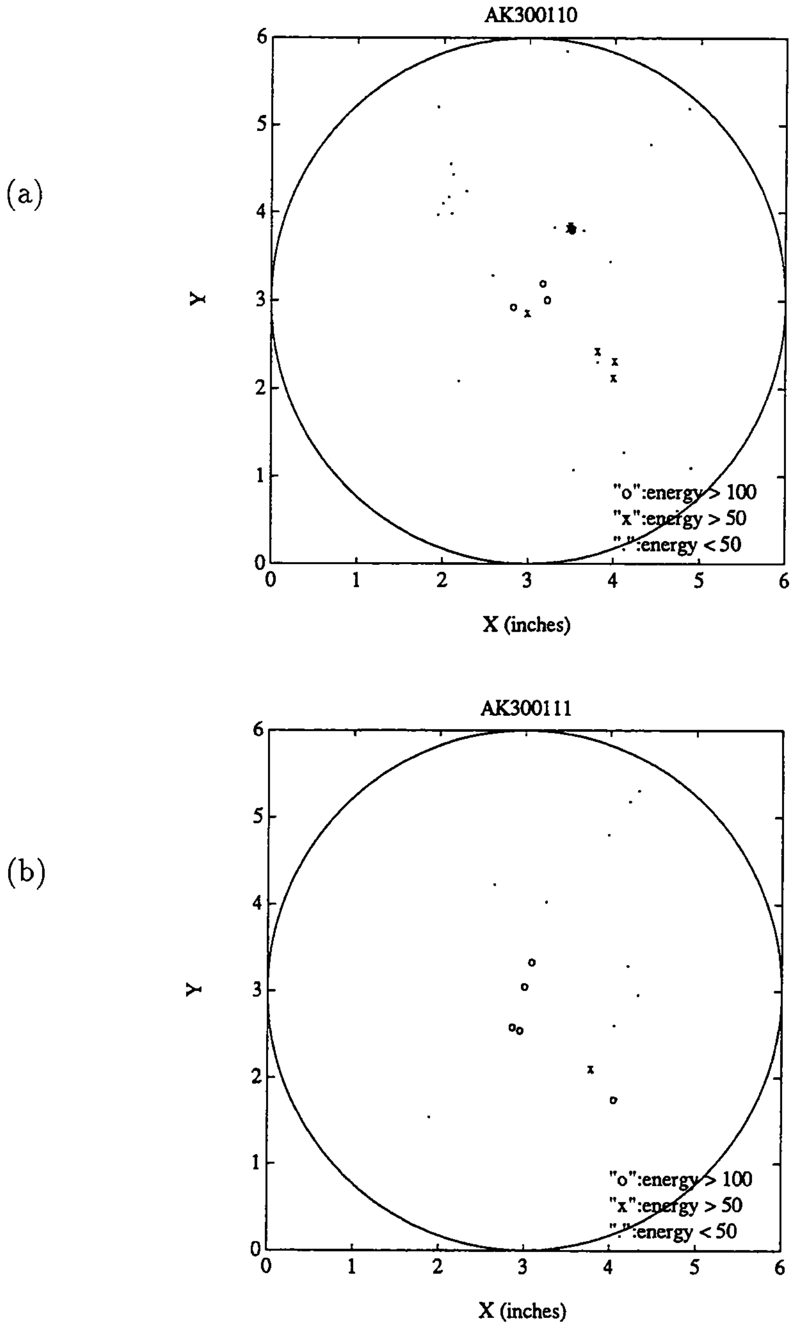

Figure 3.33: The detected AE sources in the AAK-1 specimen with 5-mm thickness at 60°F (graph [a]) and 50°F (graph [b]).

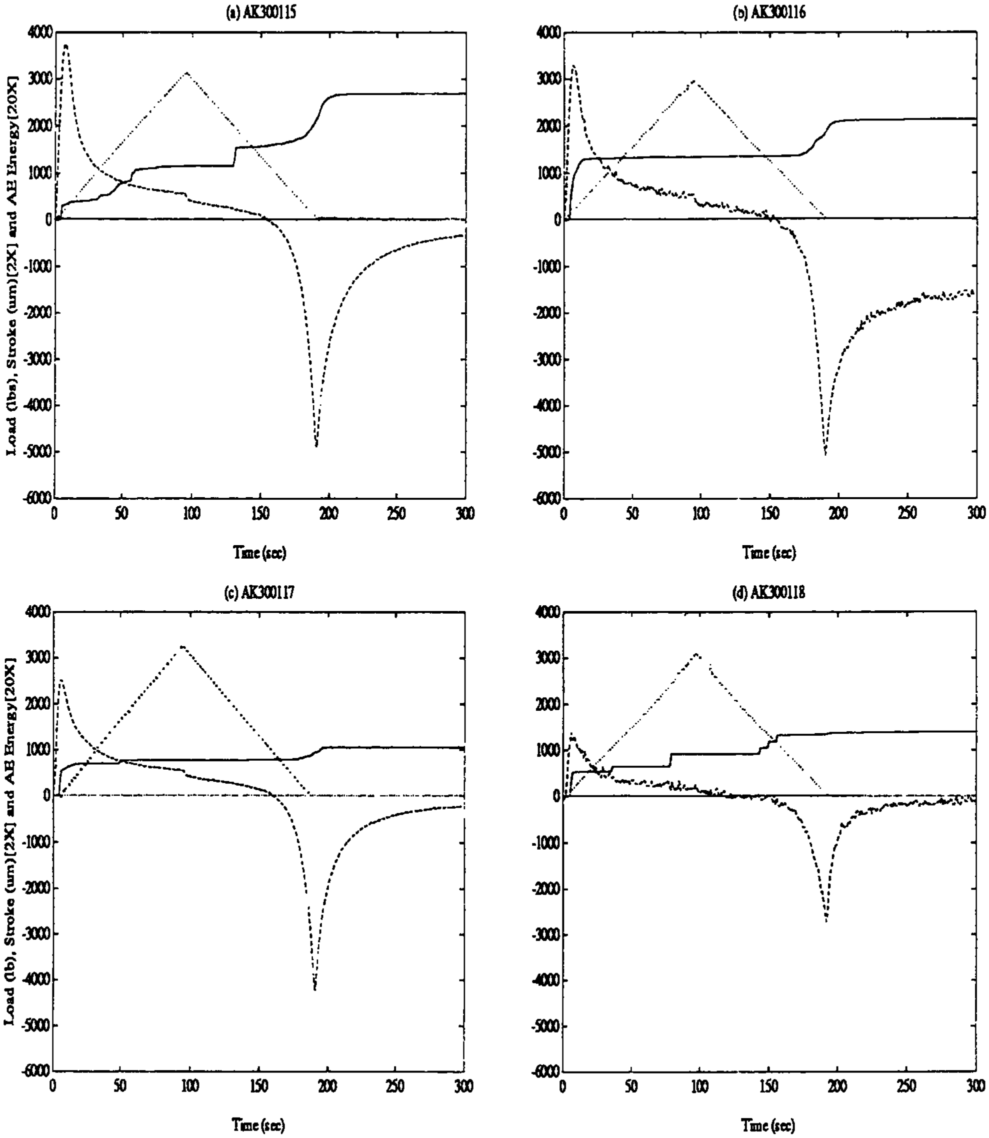

Figure 3.34: The AE output signals corresponding to the mechanical behavior (with very large deformation) in the AAK-1 specimen with 5-mm thickness.

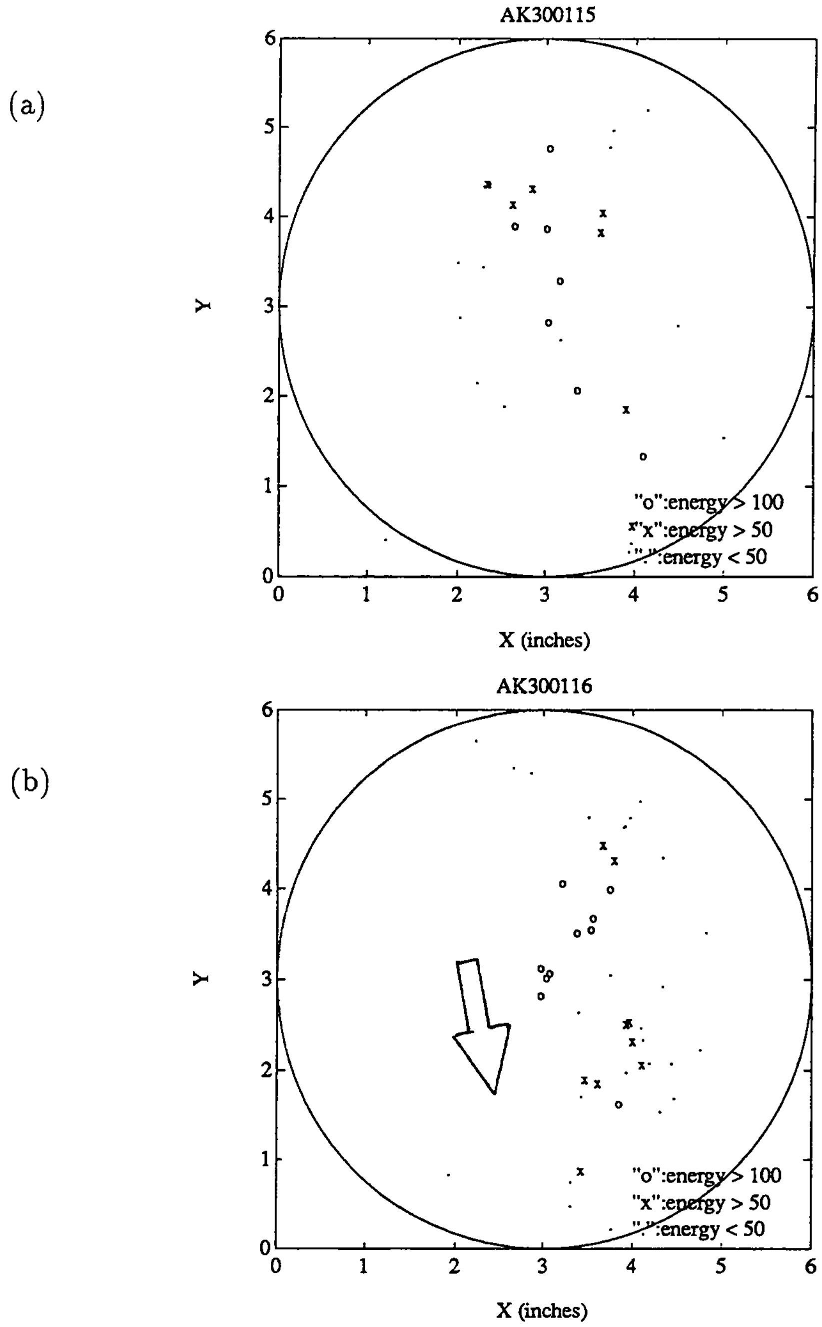

Figure 3.35: The detected AE sources in the AAK-1 specimen with 5-mm thickness. Graphs (a) and (b) show the AE source location of AK300115 and AK300116 tests, respectively.

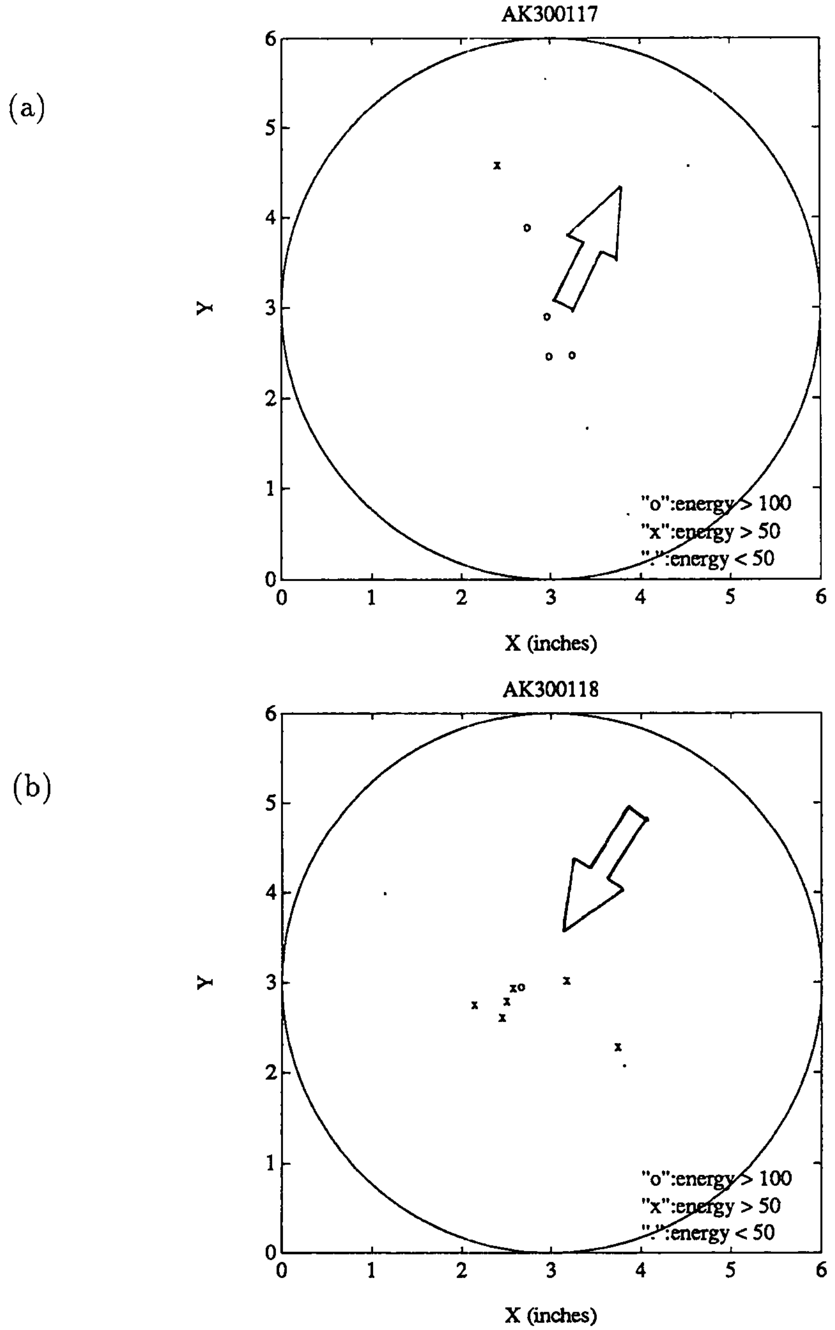

Figure 3.36: The detected AE sources in the AAK-1 specimen with 5-mm thickness. Graphs (a) and (b) show the AE source location of AK300117 and AK300118 tests, respectively.

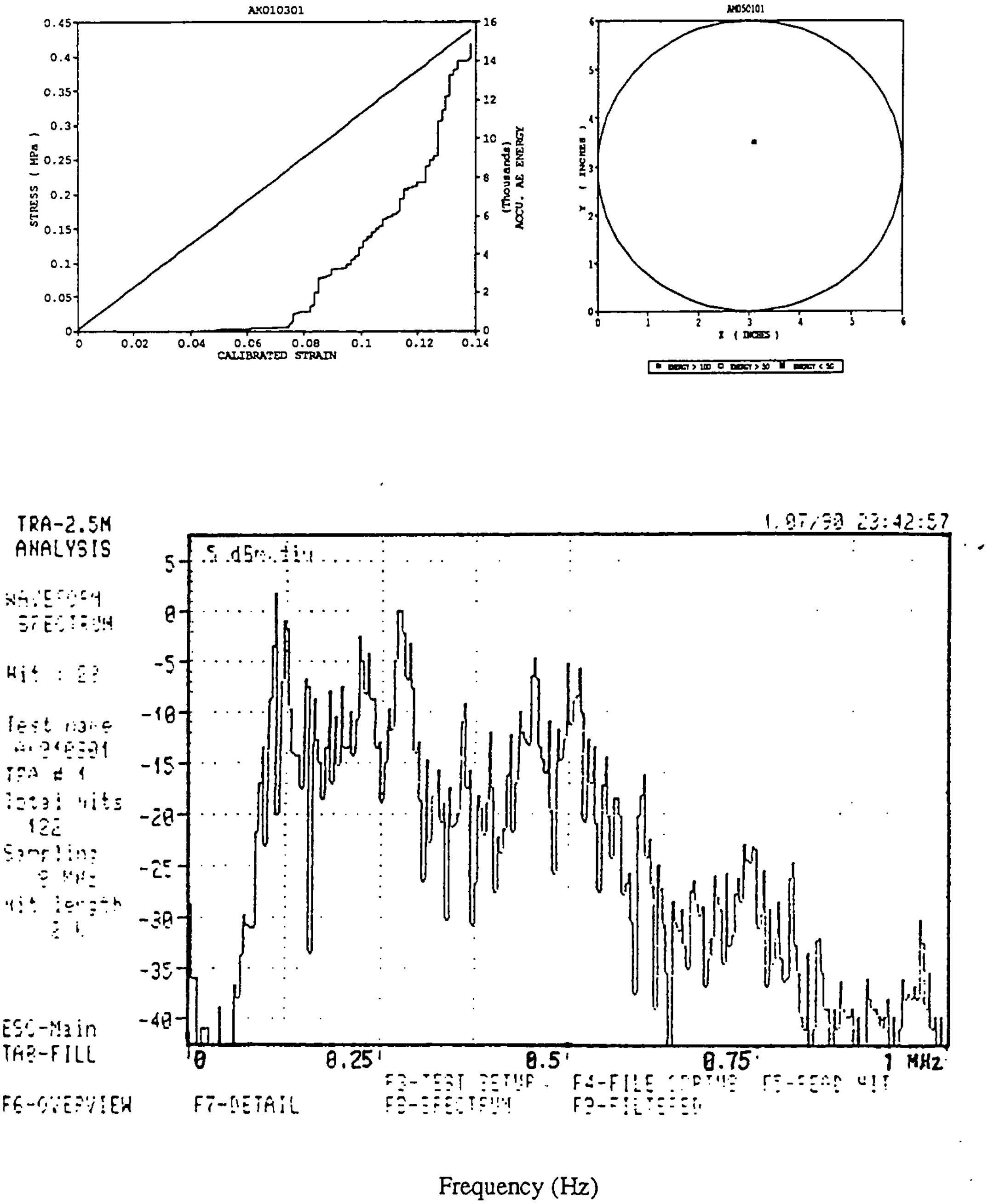

Figure 3.37: Spectrum (graph [c]) of an AE event for a specific loading condition (graph [a]) and location (graph [b]) in AK010301 test.

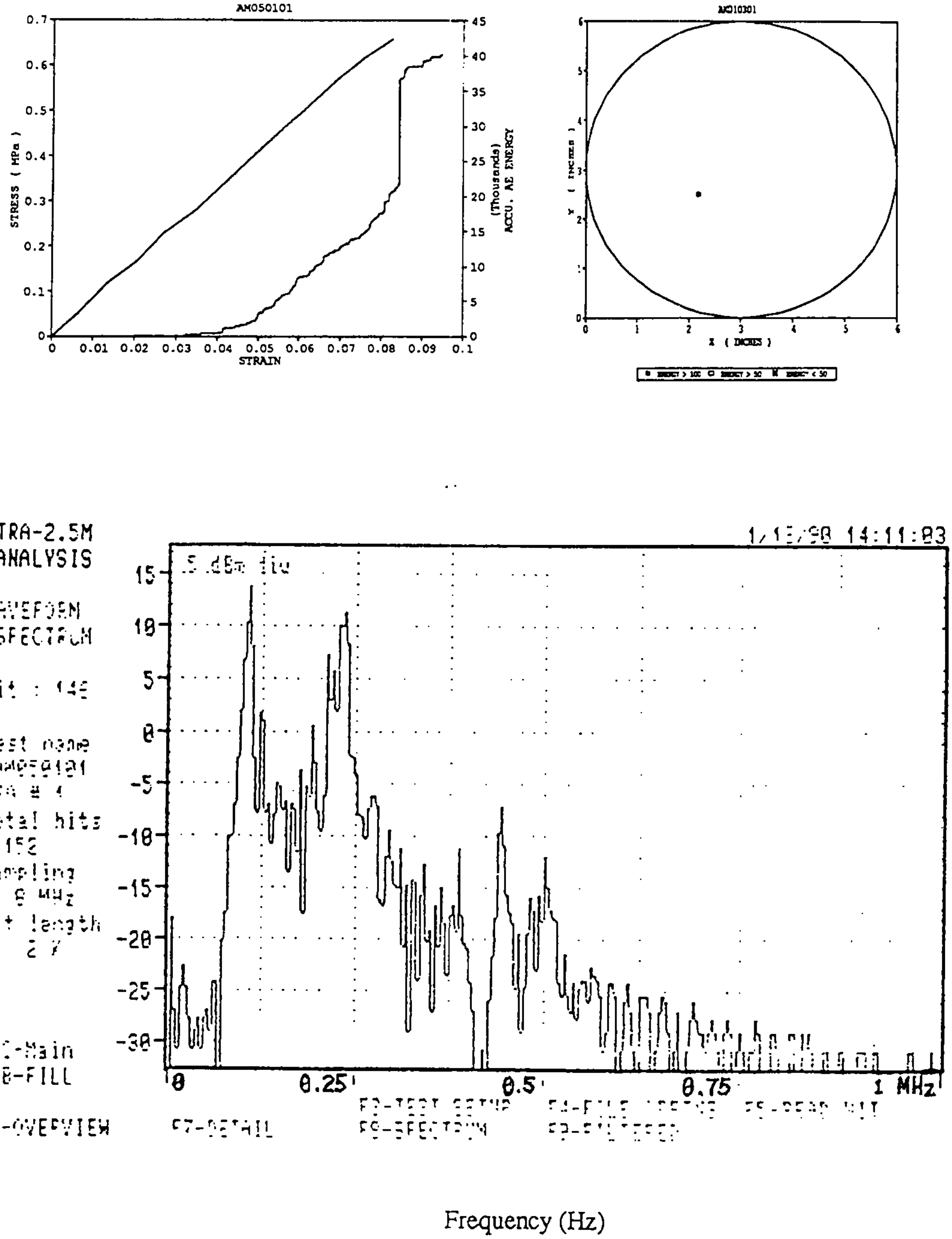

Figure 3.38: Spectrum (graph [c]) of an AE event for a specific loading condition (graph [a]) and location (graph [b]) in AM050101 test.

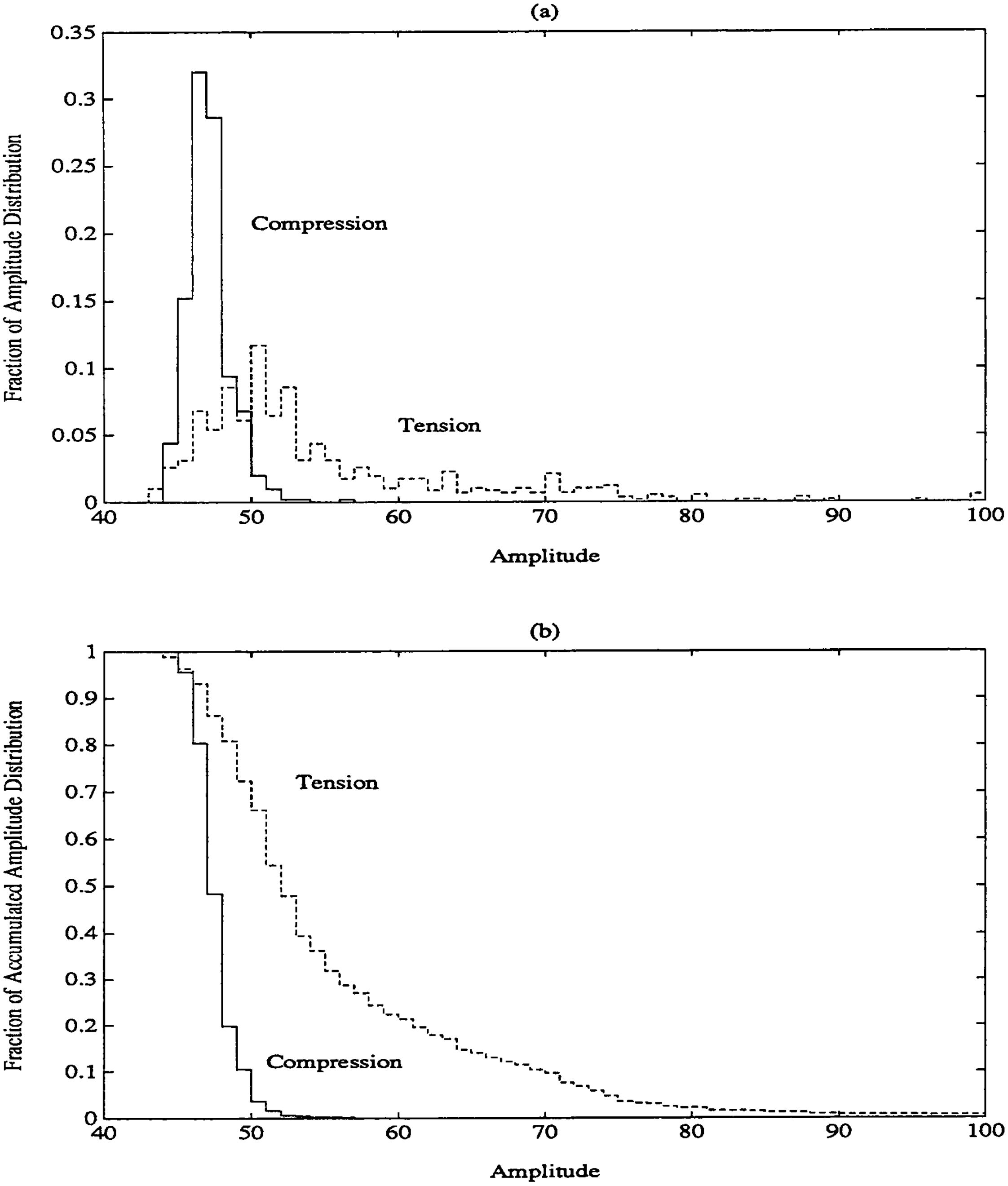

Figure 3.39: Comparison of AE amplitude distribution of tension and compression tests on AAG-1 specimen.

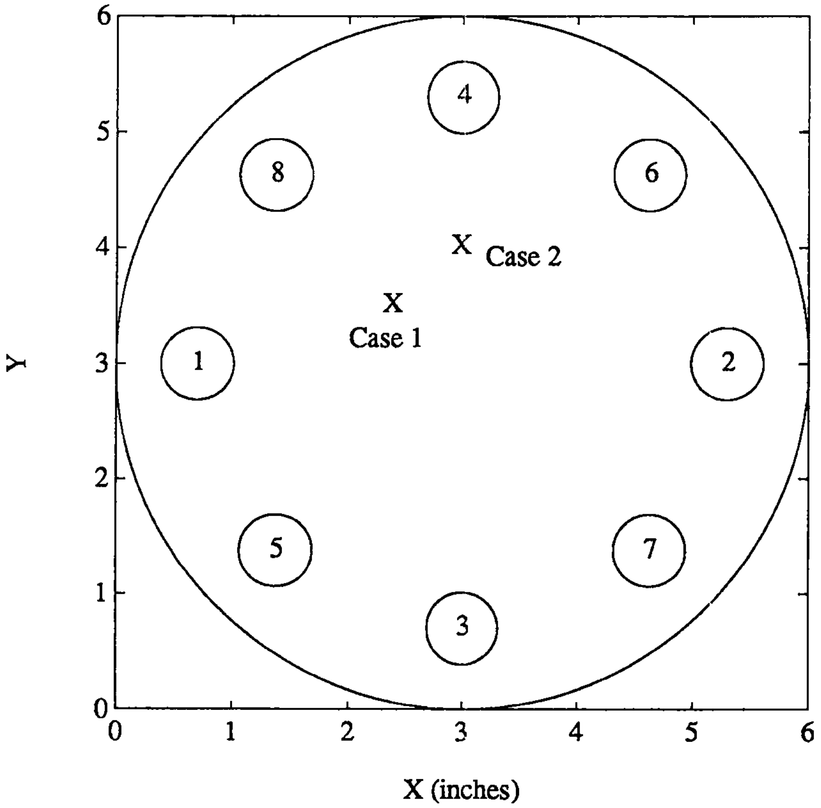

Figure 3.40: Schematic diagram of the simulation of the testing system for determining wave speed in four, (sensor No. 1 to No. 4), six, (sensor no. 1 to no. 6), and eight sensor (sensors no. 1 to no. 8) system. "X" denotes the location of the two cases studied.

References

1. ASME, *Elastic Waves and Non-Destructive Testing of Material* (American Society of Mechanical Engineers, 1978).
2. L. K. English, *Materials Engineering* **104**, 38 (1987).
3. H. V. Fuchs and R. Riehle, *WATER-Engineering & Management* **138**, 11 (1991).
4. W. V. Chang, B. Wijayarathna and R. Salovey, *Advances in Chemistry Series* **206**, 233 (1984).
5. P. Kakavas, Ph.D. thesis, Department of Chemical Engineering, University of Southern California, December 1987.
6. P. Kakavas and W.V. Chang, *Journal of Applied Polymer Science* **42**, 1997 (1991).
7. S. J. Vahaviolos, A. Pollock, and N. Lew, *Chemical Engineering Progress* **87**, 60 (1991).
8. ASTM, *E610–82, Standard Definition of Terms Relating to Acoustic Emission, Annual Book of ASTM Standards* (American Society for Testing and Materials (ASTM), 1982).
9. Physical Acoustics Corporation, *TRA–2.5M Transient Recorder Analyzer Operation Manual, version 1.03* (Physical Acoustics Corporation, New Jersey, 1988).
10. C. B. Scruby et al., *Material Evaluation* **39**, 1250 (1981).
11. J. Little and L. Shure, *Signal Processing Toolbox for Use with Matlab, Matlab User's Guide* (1988).
12. D. E. Bray and R. K. Stanley, Chapter 5 in *Nondestructive Evaluation*(McGraw-Hill, New York, 1989).
13. I. G. Scott, *Basic Acoustic Emission, Nondestructive Testing Monographs and Tracts, vol. 6* (Gordon and Breach Science Publishers, 1991).
14. C. B. Lin, S. Lee, and K. S. Liu, *Polymer Engineering and Science* **30**, 1399 (1990).
15. M. R. Gorman, *Journal of Composite Materials* **25**, 703 (1991).
16. S. Yuyame, "Several AE Sources Observed during Fracture of Repaired Reinforced Concrete Beams," *Proceedings of the 10th International Acoustic Emission Symposium*, Senday, Japan (1990).

17. Y. L. Chen and J. Israelachvili, *Science* **252**, 1157 (1991).

18. T. F. Yen. *Asphlatic Materials, Encyclopedia of Polymer Science and Engineering* Index Volume, 2nd Ed. (John Wiley and Sons, New York, 1990).

19. M. Ge, Ph.D. thesis, Department of Mineral Engineering, the Pennsylvania State University, 1988.

20. L. Piche, F. Massines, G. Lessard, and A. Hamel, *IEEE Ultrasonics Symposium*, 1125 (1987).

21. A. Hamel, L. Piche, F. Massines, and C. Neron, Ultrasonic characterization of polymers under simulated conditions, U.S. Patent No. 4,754,645, 1988.

22. "Application of Ultrasonic Techniques to the Characterization of Rubber and Rubber Blends," American Chemical Society, Rubber Division 139th Meeting, Toronto, Canada, May 21-24 1991.

23. S. M. Ziola and M. R. Gorman. *Journal of Acoustical Society of American*, 2551 (1991).

24. Hibbitt, Karlsson & Sorensen, Inc., *Abaqus Manual* (1991).

Chapter 4

Thermal Scanning Tests of SHRP Asphalts

4.1 Introduction

The thermal mechanical scanning test is a quick scanning method for evaluating different asphalts, modifiers, preparation conditions, thermal and mechanical histories on low temperature cracking resistance of asphalt thin films. Three SHRP asphalts and a rubber-modified SHRP asphalt specimen were tested in the thermal scanning tests. The poker chip specimen in thermal scan was tested by simultaneously stretching and cooling the specimen from a given high temperature (135° or 60°F) until the specimen failed.

The acoustic emission technique combined with the mechanical test is a powerful tool in the characterization of material properties and elucidation of fracture mechanisms. It is also a good index to assess the integrity of materials. The fracture surface of each specimen was recorded by camera for comparison of the failure process of different asphalts and different testing conditions. All this information is integrated and compiled to get a close understanding about the fracture process due to thermal effects.

4.2 Purpose of the Test

The purposes is to provide a very efficient and convenient way to evaluate the thermal response of different asphalts and modifiers and preparation conditions and to establish the complete test routine for thermal scanning of asphalt poker chip specimens.

4.3 Materials and Experimental

Asphalts used in the experiments were the SHRP asphalts: AAD-1, AAG-1, and AAK-1 (see Table 4.1 for the identification of asphalts).

The thermal mechanical scanning test was accomplished by subjecting the asphalt poker chip specimen to a fast cooling process (cooling rate ~ 2°F/min, see Figure 4.1). The temperature was dropped from 135° to --20°F, using liquid N_2 as the cooling medium. During the cooling process, the asphalt specimens were mounted on the loading system so that the thermal stress could be measured. The thermal strain consists of two parts: (1) the extra tension effect introduced by the contraction of the extension rods of the loading system, and (2) is the tension due to the contraction of asphalt itself. The extra tension effect will let the specimen eventually rupture when the system is cooled down to a certain low temperature. This rupture temperature for different asphalts will depend on their physical properties, such as the thermal expansion coefficient.

The basic routine for thermal mechanical scanning tests was as follows. First, a certain amount of asphalt was placed on the bottom plate of the grip. Diameter of the plate was 6 in. The environment temperature was then raised to the softening point of the specific asphalt. The temperature was kept for a certain period of time until the asphalt spreads on the plate. Second, the hydraulic system was used to compress the plates together to the desired thickness (controlled by four small metal spacers 0.5 mm thick). The specimen was allowed to cool under ambient conditions. Third, the AE sensors were mounted. The system was slowly heated again to the desired starting temperature, 135°F (this temperature is higher than the softening points of the SHRP asphalts). There was then a half-hour wait. For a test with a starting point lower than room temperature (e.g., 60°F), the specimen was cooled to the starting point, free of any axial loading or constraint, then allowed to equilibrize for 2 hrs. Lastly, the temperature control of the environmental chamber vessel to the desired point (−40°F). Liquid nitrogen was introduced to the system and the cooling process started. During the cooling process, the temperature history and the thermal load trace were recorded.

4.4 Results and Discussion

4.4.1 Thermal Scanning Tests of SHRP Asphalts

In order to develop a quick scan test for evaluating the thermal mechanical behavior (e.g., thermal cracks) of asphalts over a temperature range, thermal mechanical tests on three core SHRP asphalts, AAK-1, AAG-1, and AAD-1, were performed on our MTS machine with an environmental chamber. The results indicate that the sequence in terms of rupture equipped temperature is AAG-1 > AAK-1 > AAD-1, regardless of the starting point

(Figure 4.2). This ranking order is the same as the order obtained from thermal cracking resistance experiments conducted on asphalt aggregate mix by the 003A contractor, Dr. T. Vinson at Oregon State University.

The stress-temperature scans for AAK-1 are presented in Figure 4.3. As shown in this figure, utilizing the slightly different starting temperatures for three runs of AAK-1 asphalt ($\Delta T < 10$°F, nominal starting temperature 135°F) resulted in the thermal mechanical responses differing significantly. The higher the starting point, the softer the asphalt cement (the lower the thermal load). From pictures of the final rupture patterns, we observed different air bubble size and numbers. At the viscosity of 135°F, a small increase in temperature causes a great reduction of the stiffness (or the viscosity) of the asphalts[1]. A small extension of the poker chip specimen generates more bubbles at a higher starting temperature and causes asphalt to flow, enlarging the air bubbles. Therefore, the high temperature experienced by a pavement would be an important factor that affects the life of asphalt concrete. The AE signals corresponding to the stress-temperature trace for AAD-1, AAK-1, and AAG-1 asphalts are shown in Figure 4.4. From the stress–temperature curves, we can see that the stress first increases rapidly in the high-temperature range, then tends to change very slowly. In the low-temperature range, the stress increases until the specimen is ruptured.

To confirm the considerable effect of the starting point on asphalt properties, the cooling process was started at a much lower temperature (60°F) in the thermal scanning test, while keeping the cooling rate approximately the same ($2 \sim 3$°F/min). Figures 4.5 and 4.6 show the comparisons of thermal scanning for AAG-1, AAK-1, and AAG-1 at different starting points. In all cases, the apparent thermal load rises much more rapidly, and the final apparent load at rupture is much greater when the starting point is decreased from 135° to 60°F. The effect of the starting point can be reflected on the final rupture surface pattern more directly, as shown in Figure 4.7. At a higher starting temperature, a small thermal contraction of the system generates more bubbles and causes asphalt to flow. This would be the effect enlarging the bubbles (see Figure 4.7 [a]). In contrast, the higher viscosity of asphalt at a lower starting temperature causes asphalt to have larger resistance to flow, and hence the fracture pattern is like the one shown in Figure 4.7 (b).

4.4.2 Thermal Scanning Tests of Rubber-Modified Asphalt

Thermal mechanical scanning tests were also conducted to study the performance of rubber-modified asphalt. The primary consideration of using rubber to modify asphalt is (1) to increase the viscosity of the asphalt at high temperature; and (2) to decrease the cavitation in the asphalt material under mechanical and thermal loading conditions. By this means, we expect to improve the performance of asphalt.

The rubber modifier used in the modification is reclaimed tire rubber crumb provided by Manhole Ajusting, Inc., and the asphalt is SHRP AAG-1 asphalt. In our laboratory, a simple procedure has been developed to prepare the asphalt-modifier mixture. A predetermined amount (95 %) of AAG-1 asphalt was first heated to a temperature of around 170°C to cause it to flow, then a calculated amount of 5 % rubber modifier was added to the asphalt. After the fusing of the rubber modifier, a stirrer was turned on to stir the mixture. By mixing continuously for 3 hrs a macrohomogeneous liquid mixture was obtained. The mixture was then cooled at room temperature.

In order to compare the performance of modified and unmodified asphalt, the specimen preparation and test procedures were carefully controlled to ensure the same conditions. The thickness of the specimens was 0.5 mm. The thermal scanning tests were conducted with a starting temperature of 60°F.

Figure 4.8 shows the stress-temperature curves obtained from the tests. Comparing the two curves, we found that (1) at the initial stage of the cooling process, the stress of the unmodified AAG-1 asphalt rises more slowly than the modified specimen, indicating that the modification increased the stiffness of the asphalt; (2) the breaking stress of modified asphalt is much higher (more than 30% higher) than those of unmodified asphalt; and (3) the breaking temperature is greatly decreased for the modified asphalt compared to the unmodified asphalt. The cavities of the modified asphalt were observed to be much smaller than that in the unmodified asphalt. These results are agree with our prediction.

From the evidence of the thermal mechanical scanning tests, we conclude that rubber-modified asphalt showed improved performance over unmodified asphalt. The test results of our other mechanical tests also support this conclusion.

4.4.3 AE Measurement on Thermal Scanning Test

The thermal mechanical tests were conducted with AAD-1, AAK-1, and AAG-1 asphalt. The AE measurement with the thermal stress are shown in Figures 4.5 and 4.6. The AE signals of AAD-1 are less than the other two asphalts during the cooling process. A typical case of thermal failure on AAK-1 core asphalt is illustrated in Figure 4.7. The rupture surface resulting from thermal cooling is much different from that caused by tension. For different types of asphalt, the failure surface also provides us with some information. For example, AAG-1 core asphalt shows a strong tendency toward interfacial failure regardless of the test mode.

From the thermal scan tests, we found that damage detected by AE in the high-temperature region has a great effect on the mechanical behavior of asphalt. Thermal scan tests were conducted with asphalts AAD-1, AAK-1, and AAG-1 over a specific temperature range. This test can differentiate core asphalts in a poker chip specimen by simultaneously stretching and cooling the specimen from a given high temperature until the specimen fails. The starting temperature was later reduced from 140° to 60°F. Three types of SHRP asphalt, AAD-1, AAK-1, and AAG-1 were tested. Both the mechanical and the AE results showed that the specimens had the same tendency with regard to failure as at 140°F with the AAG-1 rupturing first, followed by AAK-1 and AAD-1. Interestingly, the AAG-1 showed a greater tendency toward interfacial failure than did the AAD-1. Furthermore, the responding AE signals increase much faster than they had previously. Figures 4.5 and 4.6 show the mechanical behavior and AE output in thermal scan tests at the same scale. We found that although the accumulated AE signals at rupture points are around the same magnitude (accumulated energy counts 200,000) for both sets of tests in these two quarters, the rupture stress is much higher for the tests at a lower starting temperature (60°F) than for those with a higher starting temperature (140°F). AE accumulated energy before fast rupture for AAD-1 asphalt has a greater value than those for AAK-1 and AAG-1. The rupture temperature of AAG-1 at an initial temperature of 140°F is higher than the test results conducted at an initial temperature of 60°F. We tentatively propose that the slight loading at the higher temperature could cause cavities that make the material softer and lead to lower fracture stress. The accumulated AE energy could be chosen as a criterion to evaluate the material conditions.

4.5 Conclusions and Recommendation

In the thermal mechanical scanning test, the lower the starting point (temperature), the more rapidly the apparent thermal load rises with specimen cooling, and the greater the final rupture load is. In comparing different asphalts, in terms of rupture temperature, a distinct sequence is observed on tested SHRP asphalts: AAG-1>AAK-1>AAD-1.

In the case of rubber-modified asphalts, the thermal scanning test indicates a significant improvement of low-temperature properties, reflected by lower rupture temperature, increasing stiffness at high temperature and rupture load, and fewer cavities on the rupture surface.

We found that the lower the starting temperature, the more rapidly the apparent thermal load rises with cooling and the greater the final rupture stress. This suggests that the permanent damage in asphalt might easily be caused by slight mechanical loading at high temperature and that it has a great effect on the mechanical behavior of asphalt.

AE is a good index to assess the damage in thermal mechanical scanning tests. The microfractures detected by AE in the high- temperature range have a great effect on the mechanical behavior of asphalt.

The test methods we used can provide a very efficient and convenient way to evaluate the thermal response of different asphalts and the application techniques of asphalt pavements. The complete test routine for thermal scanning of asphalt poker chip specimens has been well established in our laboratory. It would be easy to conduct the thermal mechanical test in regular transportation laboratories.

Table 4.1: Inspection of test asphalts.

Asphalt	Penetration (100g,5s,77°F,0.1mm)	Viscosity (140°F,Poises)	R&B Softening Point (°F)	Source
AAD-1	135	600	118	SHRP MRL
AAG-1	53	1862	120	
AAK-1	70	3256	121	

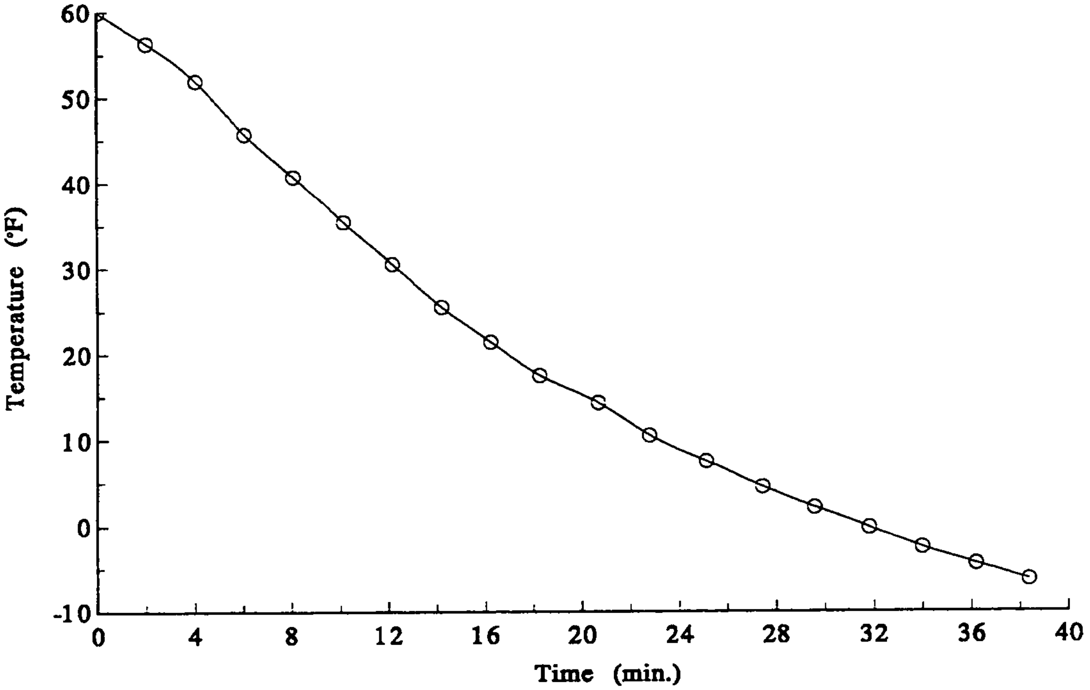

Figure 4.1: A typical cooling process in the thermal mechanical scanning test.

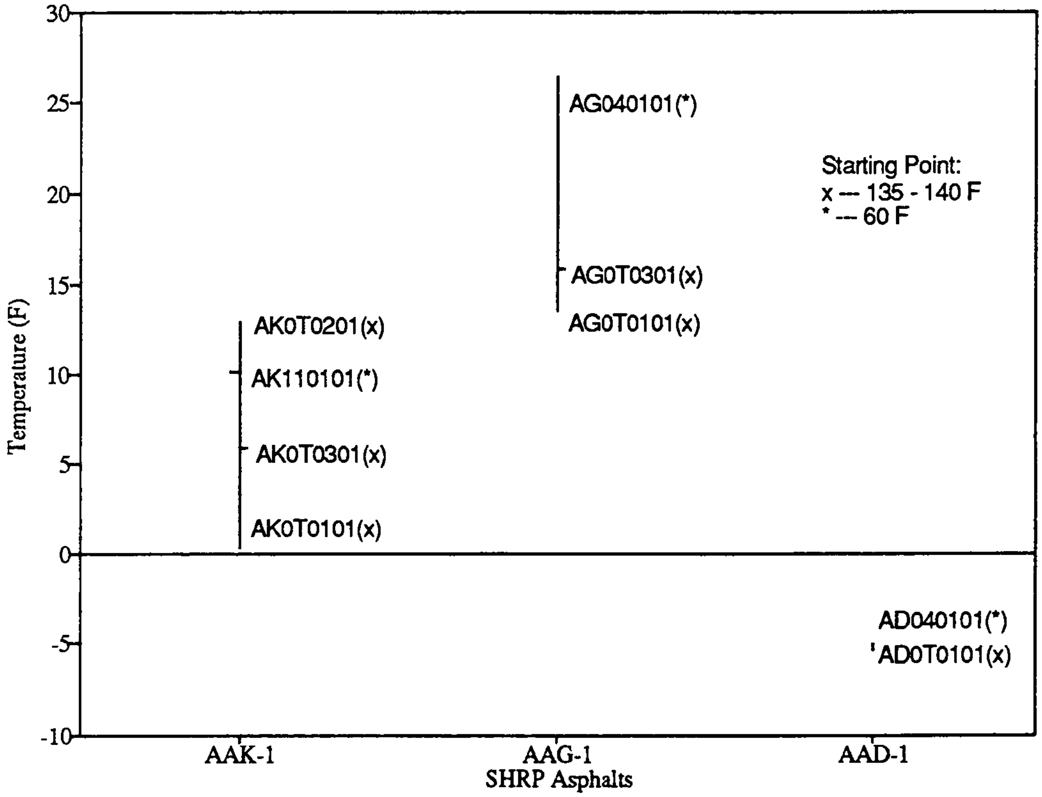

Figure 4.2: Rupture temperatures of Different kinds of SHRP asphalts in the thermal scanning tests.

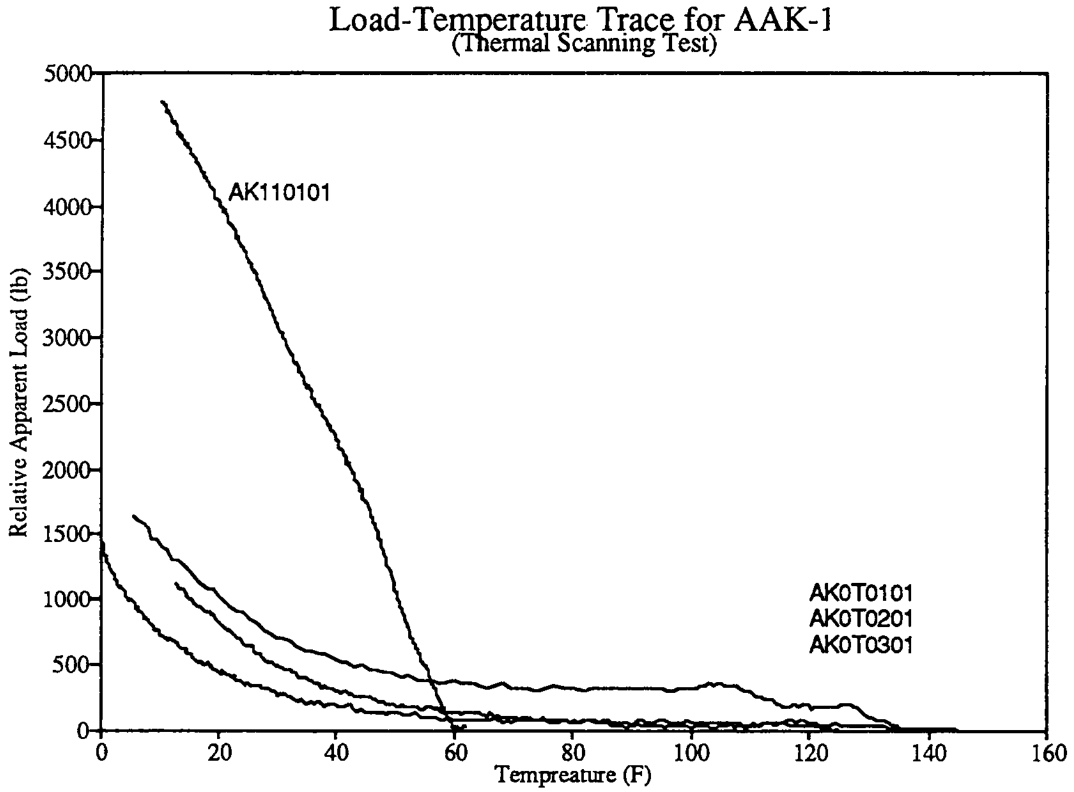

Figure 4.3: Load-Temperature trace for AAK-1 asphalt at different starting points in the thermal scanning tests.

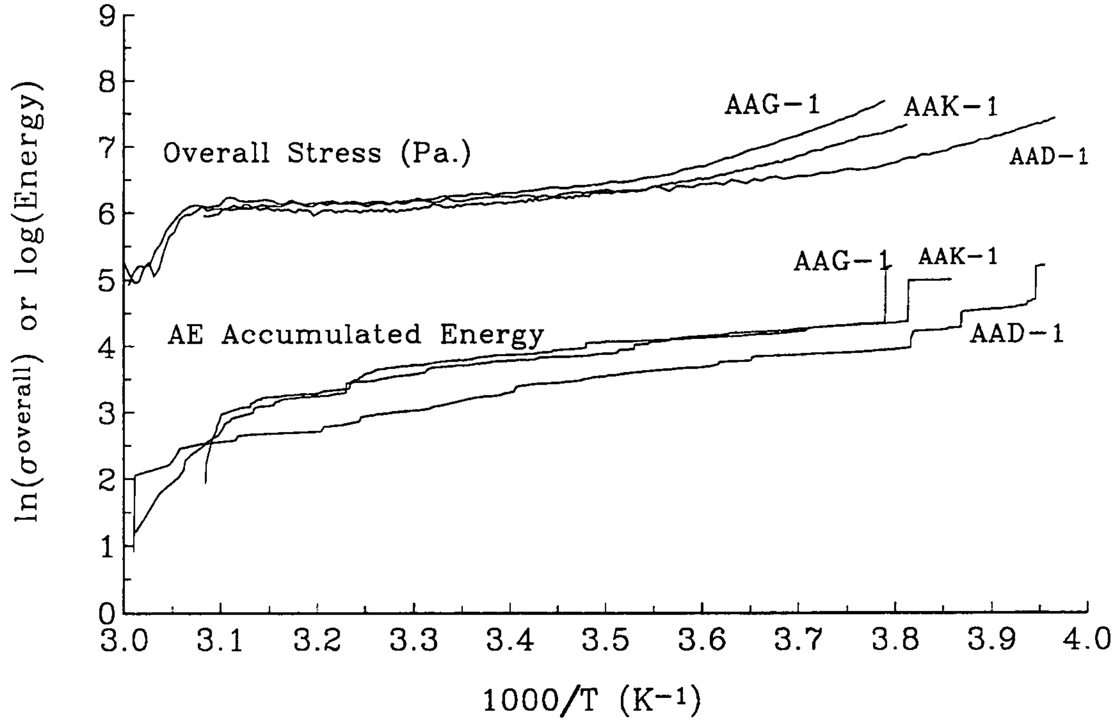

Figure 4.4: The AE output signals corresponding to the stresses for different kinds of SHRP asphalt.

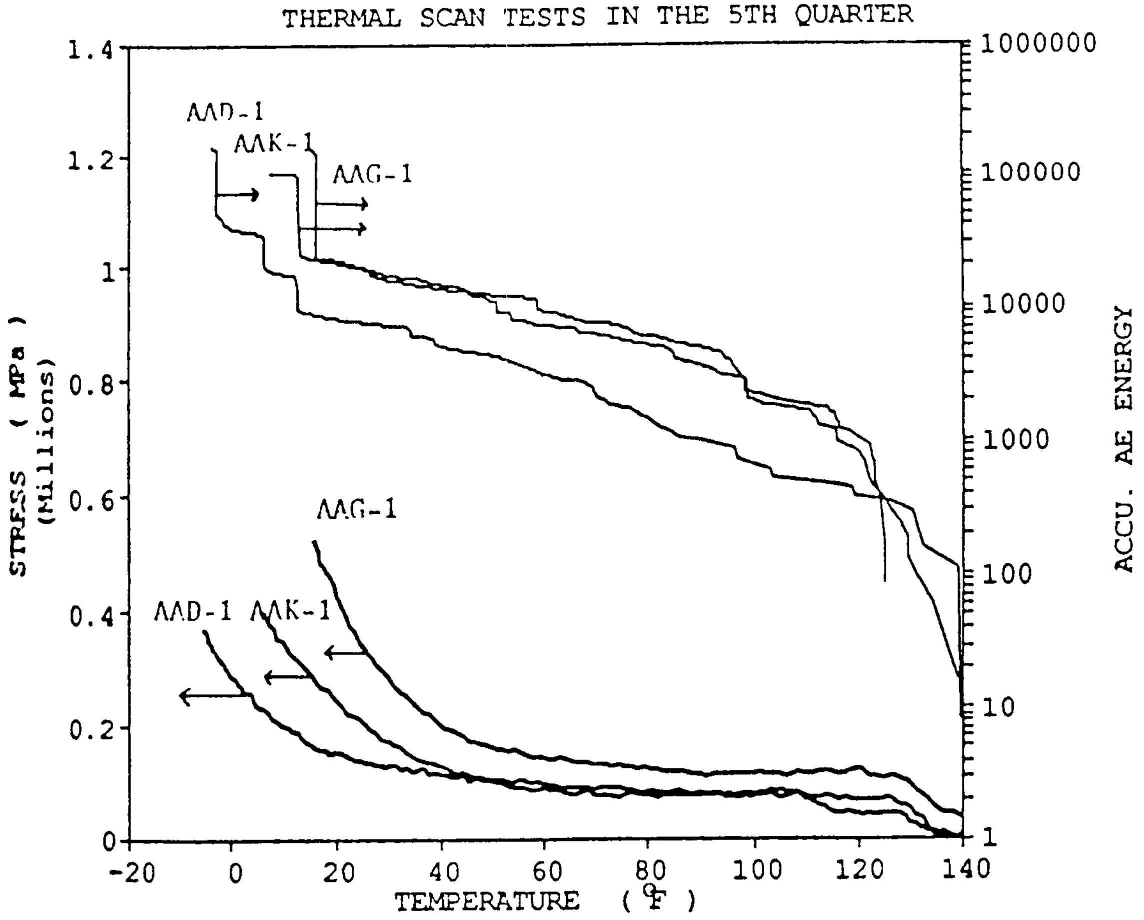

Figure 4.5: The AE output signals corresponding to the thermal scan tests for different SHRP asphalts initiated at 140°F.

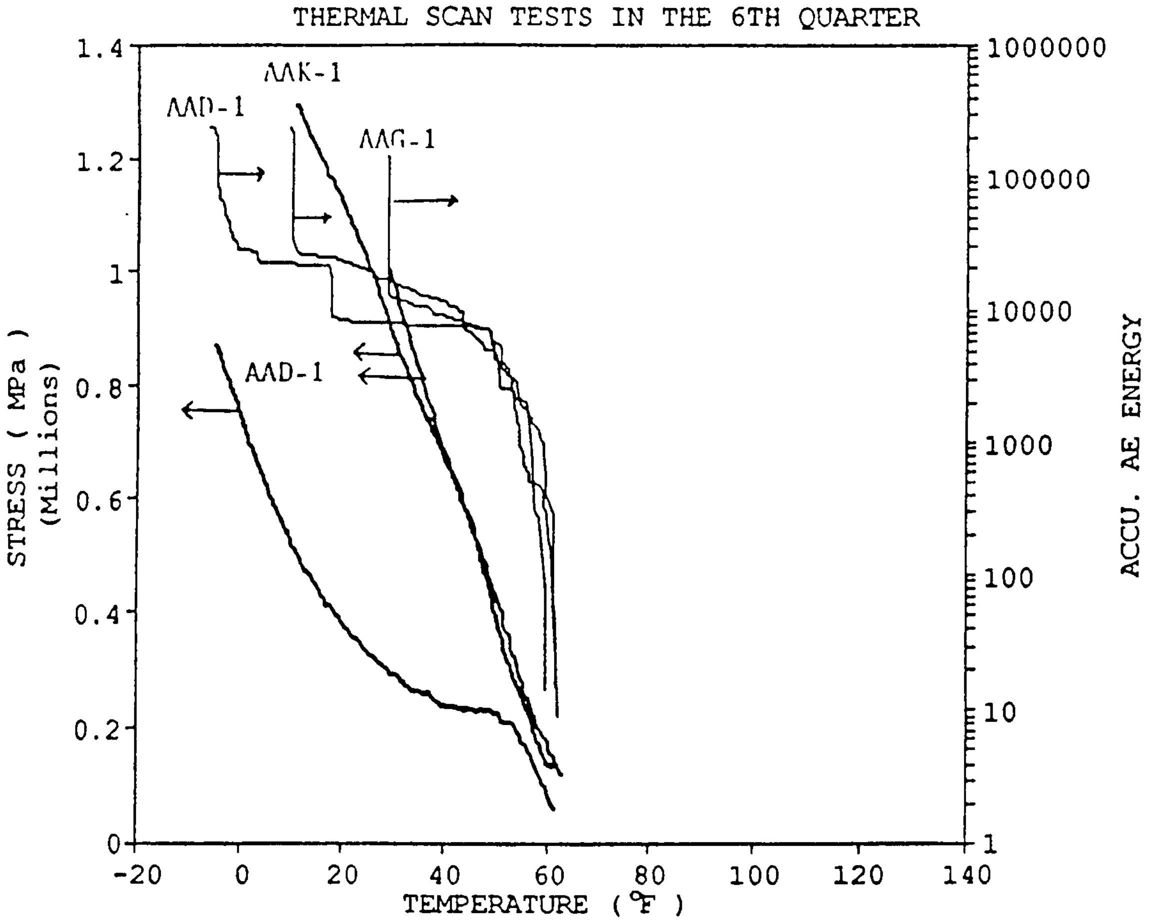

Figure 4.6: The AE output signals corresponding to the thermal scan tests for different SHRP asphalts in the initiated at 60°F.

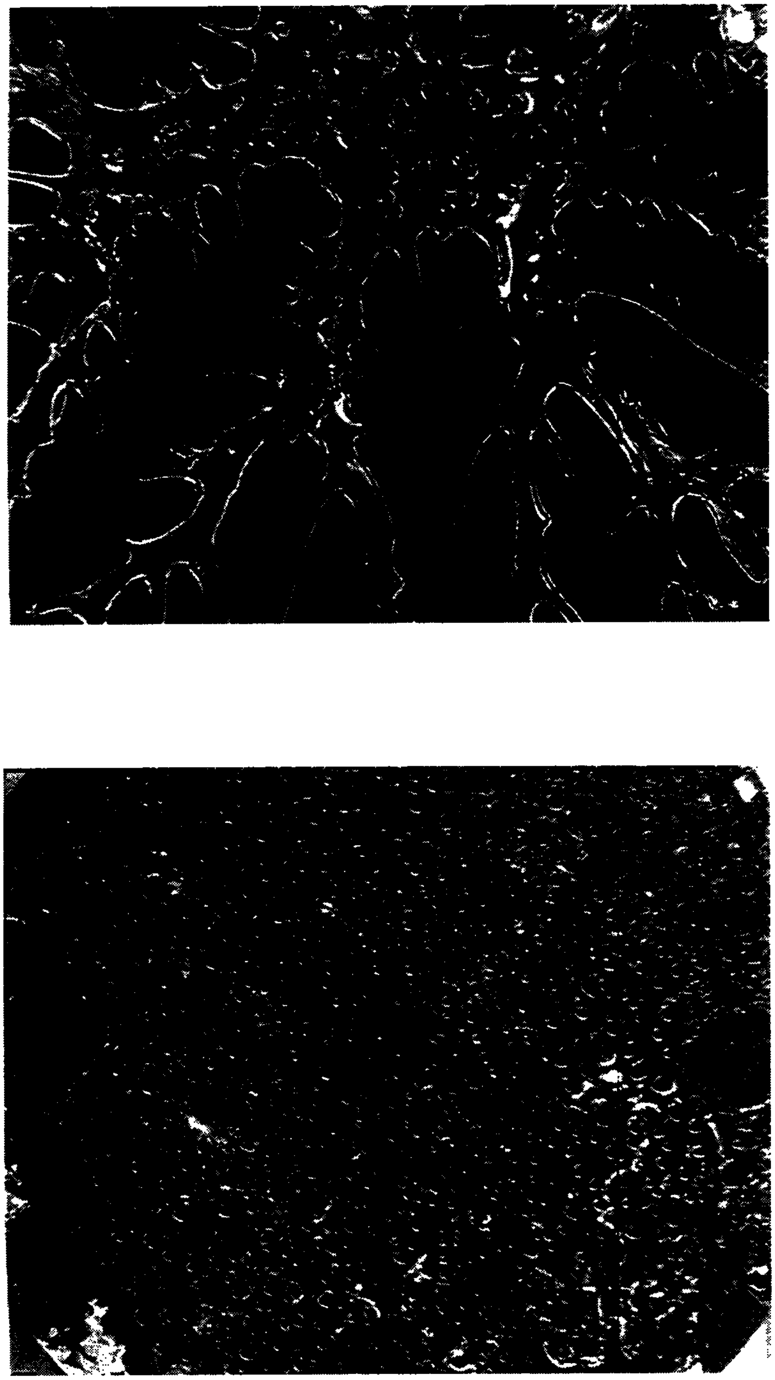

Figure 4.7: Fracture Patterns of AAD-1 asphalt in thermal scanning tests at different starting temperature: (a) 135°*F*; (b) 60°F.

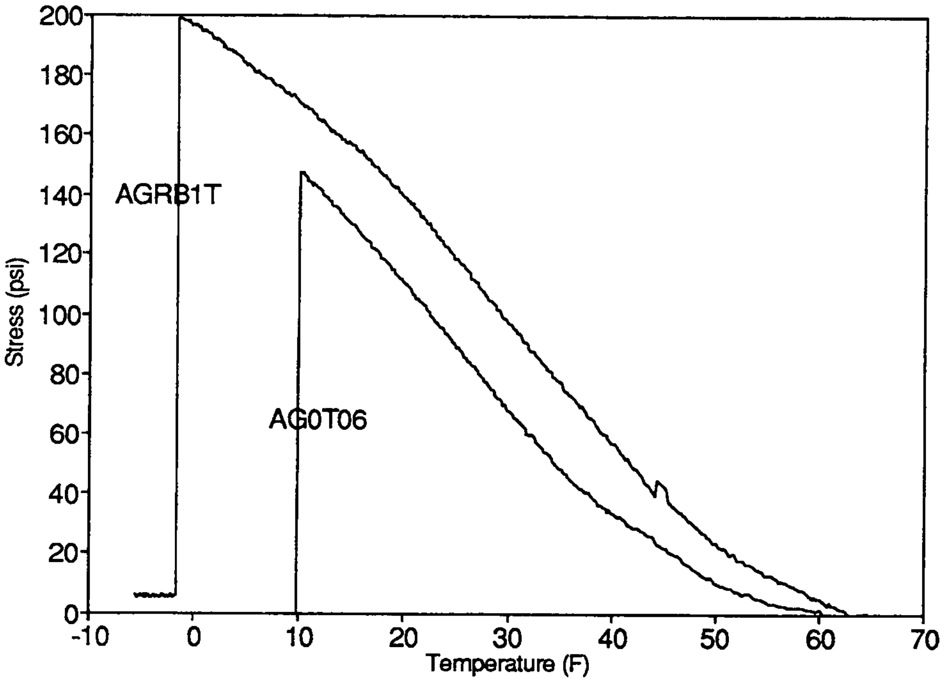

Figure 4.8: The corresponding stress of normal AAG-1 asphalt and rubber-modified AAG-1 asphalts in thermal mechanical tests.

Chapter 5

Acoustic Emission Measurement and Mechanical Test of Asphalt Concretes

5.1 Introduction

Asphalt concretes are composite materials consisting of air, aggregates and asphalt binders. One of the most important properties of an asphalt concrete in paving is its ability to resist permanent deformation under dynamic and/or static load. This behavior depends not only on the the composition of the concrete and the paving conditions, but also on the mechanical history it has experienced. Many test methods (such as creep[1] and shear dynamic loading[2]) have been employed for the characterization of asphalt concretes. In our laboratory, an effort has been made to combine acoustic emission (AE) measurements and material testing systems (MTS) mechanical tests to study the cohesive and adhesive properties of asphalt cements. It has been shown in the previous chapters, that this combination is a powerful tool for characterizing the mechanism of microdamage in asphalt thin films. In this chapter, AE technique is employed for monitoring the microfracture in the asphalt phase and/or between asphalt cement and aggregate when the asphalt concrete is subjected to mechanical loadings. Together, with mechanical results these give a comprehensive indication of the internal structure change of asphalt concrete during the loading process.

5.2 Purpose of the Test

Using our AE-MTS testing system, the purpose is to first demonstrate that the deformation behavior and microfracture of asphalt concrete under different loading conditions are similar to those of asphalt thin films; and secondly to show the utility of acoustic emission technique in assisting the researchers to monitor the microfracture in asphalt concretes.

5.3 Material and Experimental

In conducting the mechanical tests of asphalt concretes, four cylindrical specimens with different void contents were used. The specimens were supplied by Oregon State University (the A-003A subcontractor). The cores were 4 to 4.5 in. long and 4 in. in diameter. The specifications and test histories of the concrete specimens are given in Table 5.1.

The mechanical tests were carried out by uniaxial compression of the specimens in a radial direction and controlled by loading rate, loading range. and loading mode (single-cycle or multicycle loading). This is similar to the ASTM standard D4123-82 for measuring the resilient modulus of asphalt concretes. The loading level in the test is represented by the force per unit length of the specimen (lb/in.), and deformation is described by the nominal strain. The test temperature was 65°F.

The AE measurement has been applied to monitor the mechanical behavior of asphalt concretes. AE sensors were placed on the two circular faces of the concrete cylinder. Asphalt was used as the couplant to attach the sensors to the specimen.

5.4 Results and Discussion

5.4.1 Mechanical Tests of Asphalt Concretes

Figure 5.1 shows a typical result of the single cycle loading test. The compression force is controlled by a constant loading rate. Note that strain is still increasing after the maximal loading point, indicating a time delay between the maximal strain and the maximal load. Also, when load returns to zero, the deformation is not completely recovered and significant residual strain exists. This is similar to the findings from asphalt in our poker chip tests, as reported in Chapter 2.

Examining several load-strain curves (Figure 5.2), we find that in the loading region, the load-strain curves are concave upward, indicating that the stiffness of the specimens increases as the deformation progresses. We attribute this mainly to the increasing contact area of the concrete specimen as deformation proceeds. Comparing the load-strain curves in Figure 5.2, we see that this "hardening effect" is more significant for specimens with higher void contents (the void content is 8.7% for specimen II and 9.3% for specimen IV, compared with 6.9 and 5.8% for specimens III and V, respectively). From the test results of the two specimens of AC-30 asphalt, we see that the specimen with lower void content (specimen IV) has a lower initial stiffness than the specimen with the lower void content (specimen II). But this is not the case for specimens of AC-10 asphalt. The reason is not clear, but the difference is probably due to the inhomogeneous and anisotropic nature of the concrete specimens or to inaccurate measurement of the void content of the specimens.

Multicycle tests were conducted with specimen III (test number CC0303) and specimen IV (test numbers CC0402 and CC0403). The loading parameters (ramp frequency: 4 lb/in./sec and amplitude: 50 lb/in.) are the same for each test. The results obtained for specimen IV are shown in Figure 5.3. As we can see, the first cycle of each test exhibits the same characteristics as the single-cycle test. Initially, both the strain and the stress increase with time but the strain lags behind the stress. When the stress reaches its peak value, the strain still increases until it peaks at a later time, indicating a viscoelastic behavior or evidence of damage. As the stress returns to zero the strain does not go back to zero. The extent of hysteresis is significant and is consistent with what was observed in the poker-chip test for the pure asphalt (see, for example, Figure 2.14). As the cyclic loading proceeds, the mean strain increases but the strain increment for each cycle decreases with the loading cycles. The mean strain as a function of time is similar in shape to the creep compliance of asphalt at room temperature.

Another way to present the creep behavior of the mean strain is shown in Figure 5.4, where the ratio of the stress amplitude and the correspondence strain increment for each cycle is termed the apparent modulus and is plotted against number of loading cycles. In the first three cycles, the apparent modulus increases significantly, and, as the number of loading cycles increases, the apparent modulus tends to approach a certain constant value. Figure 5.5 shows the change of time delay between maximal strain and maximal load of each cycle as the test cycle increases. As we can see, the delay time decreases with an increasing number of cycles and approaches a constant volume of 0.255 which corresponds to a tan δ value of 0.325. An additional piece of information obtained from the multicycle tests is the change of the ratio of the strain increment to the maximal strain of each loading cycle. Here, both strain increment and maximal strain of each cycle are calculated using the residual strain of the previous loading cycle as a basis. The results are given in Figure 5.6. The trend of the change of this ratio is similar to the change of delay time.

Because of permanent deformation introduced in the compression test, the response of an asphalt concrete specimen in each individual test depends on its test history (i.e., it is affected by the previous tests on the specimen). For specimen IV after two multicycle tests (CC0402 and CC0403), two single cycle tests were conducted (CC0404 and CC0405). As shown in Figure 5.7 the stiffness of the specimen increases after each test.

We consider this to result from an increase in the contact area. When the specimen is subjected to compression load greater than a certain value, however, the stiffness of the specimen will decrease with increasing compression force (Figure 5.7), indicating that internal damage occurs.

Specimen IV was compressed in test CC0405 until it ruptured. The ruptured specimen is shown in Figure 5.8. The initial fracture occurred near the center of the specimen and the main crack propagated slowly from the center outward along the direction of the loading force. This is in agreement with the prediction of finite element simulation.

5.4.2 AE Measurement on Asphalt Concretes

Due to the intrinsic inhomogeneity of asphalt concrete material, optimization of proper test parameters and system settings is necessary for the acquisition of AE information. In our tests, attempts were made to achieve satisfactory signal acquisition by adjusting gain and threshold values of the Locan-AT system. Figure 5.9 shows a typical waveform and the corresponding spectrum obtained from a compression test of asphalt concrete. The spectra of most detected signals in the tests have peak of frequencies around 125 kHz. The spectrum shown in Figure 5.9 has a different tendency from the ones of the AE events from the poker chip specimen. This can be explained by the different geometry of the specimen.

As is well established in the asphalt poker chip test, AE energy is a good index to assess the damage in the material. AE is also an efficient method employed in the tests on asphalt concrete. Figure 5.10 shows the AE intensity together with the load-strain curve from a single compression cycle. The AE output is quiet at the initial loading stage. At a certain loading level, AE signals begin to occur, indicating the start of damage inside the specimen. The load level at the onset of AE is a widely used parameter to evaluate the integrity of materials. Table 5.2 lists the load, the time, and the corresponding strain of the specimen at the onset of AE obtained from single-cycle tests. After the onset of the first AE event, AE energy keeps increasing as the load increases. When the unloading starts, AE activity does not stop immediately until the maximal strain point is reached (Figure 5.10). After this point, no significant AE signals occur.

There are only two channels applied in the AE measurement on asphalt concrete. The AE source location can be obtained from the two absolute arrival times. This information can provide us with a one-dimensional source location. Figure 5.11 shows the AE signal intensity along the axial direction of the cylindrical asphalt concrete specimen. The distribution is not uniform. More AE sensors should be added in order to get a better understanding of the two- or three-dimensional source location.

AE response in multicycle dynamic tests is interesting and inspiring. As a result of cyclic loading, the AE activity also exhibits a cyclic feature (see Figure 5.12). In each loading cycle, AE starts at a certain load point, and there is a sharp rise in accumulated AE energy; then there follows a relatively quiet period until a certain load value in the next loading cycle is reached. This process repeats itself by cycle. Since the maximum load of each cycle is the same, obviously, the Kaiser effect does not hold for asphalt concrete in our test. Yuyama[3] used the ratio of the AE onset load to the maximal load the specimen experienced in the previous loading cycle to evaluate the structural integrity of the material. The validity of applying this method to asphalt concrete needs further investigation. In our test, the load at the onset of AE activity is plotted in Figure 5.13. The result suggests that the AE onset load tends to increase as the loading cycle increases, especially in the first several cycles.

More careful observation of the AE behavior during multicycle loading tests reveals that, in each cycle, AE events occur only when the strain reaches the previous maximum strain value in the last loading cycle. Before this point, there is no essential increase in accumulated AE energy (see Figure 5.14). The dominating factor for the generation of "new damage" in the asphalt concrete specimen is permanent deformation rather than the loading level. This is contrary to many engineering materials where damage extent is mainly determined by the maximum load force the specimen experienced. Since there is a "hardening" effect involved in the cyclic loading test, it is reasonable to find increasing AE onset load as the test cycle increases. To achieve a comprehensive understanding of the mechanical properties and damage mechanisms of asphalt concrete, further investigations of the AE characteristics need to be done. This will include the 3-D source location, the measurement of wave speed change in the specimen during mechanical test and the healing behavior of asphalt concrete.

5.5 Conclusion

The AE-MTS testing system can be effectively used in the characterization of asphalt concretes. From the concrete testing results, comprehensive understanding can be obtained both on the mechanical properties and material state (micro-damage, integrity, etc.).

In both single cycle and multicycle compression tests, the large permanent deformation always exits. The void content in an asphalt concrete will affect the initial stiffness of the concrete. For specimens with the same composition, the higher the void content, the lower the initial stiffness. In a multicycle compression, the stiffness of an asphalt concrete increases and hysteresis becomes less obvious with increasing number of compression cycles. The permanent deformation depends strongly on the mechanical history of the concrete specimen. It should be taken into account in the evaluation of its performance.

The micro-damage process in asphalt concretes can be reliably detected by AE. The results from both single cycle and multicycle tests indicate that the deformation of a specimen relates closely to AE event which is the measurement of damage state of the specimen. In further study of asphalt concretes, more sensors should be applied to obtain more accurate source location and, thus the wave velocity change during deformation of asphalt concretes.

5.6 Acknowledgements

The research reported here was financially supported by the SHRP. We wish to express our thanks to Professor T.S. Vinson of Oregon State University for preparing the asphalt

concrete specimens used in this study.

Table 5.1: Specification and test histories of asphalt concrete specimens.

Specimen Number	Run Number	Asphalt Type	Void Content	Shape: Cylinder†		Max. Load (lb/in)*	Loading Mode
				D (in)	h (in)		
II	CC0201	AC-30	8.7%	4	4.5	100	1 cycle
III	CC0301	AC-10	6.9%	4	4.5	50	1 cycle
	CC0302					50	1 cycle
	CC0303					50	9 cycles
IV	CC0401	AC-30	9.3%	4	4.25	50	1 cycle
	CC0402					50	15 cycles
	CC0403					50	15 cycles
	CC0404					500	1 cycle
	CC0405					700	1 cycle
V	CC0501	AC-10	5.8%	4	4	52	1 cycle

* Loading rate: 20 lb/in/sec (Load control).

† D: diameter; h: height.

Table 5.2: Strain and load values at AE onsets in concrete tests.

Test number	AE onset time	Load	Strain
CC0201	2.3	46	2.32e-3
CC0301	0.4	8.4	2.70e-4
CC0501	1.5	31	1.94e-3

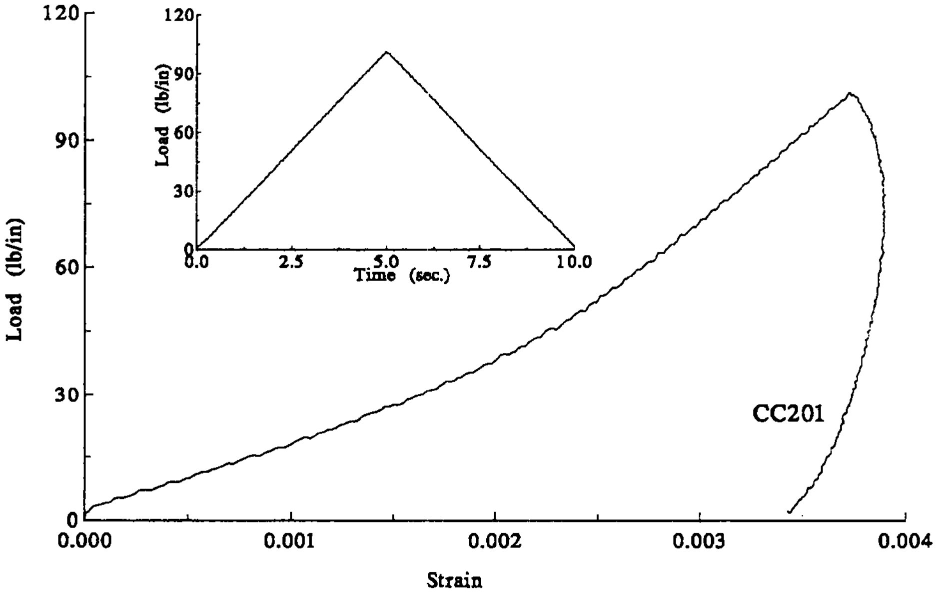

Figure 5.1: Typical single cycle compression test of asphalt concrete. (Specimen: II/CC0201, cf. Table 5.1).

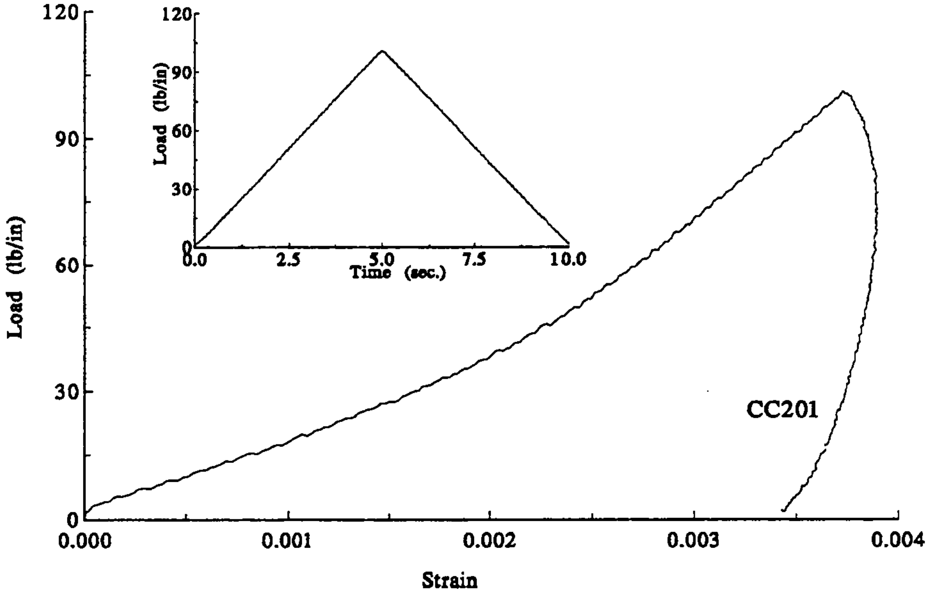

Figure 5.2: Response of the specimens in the single compression tests.

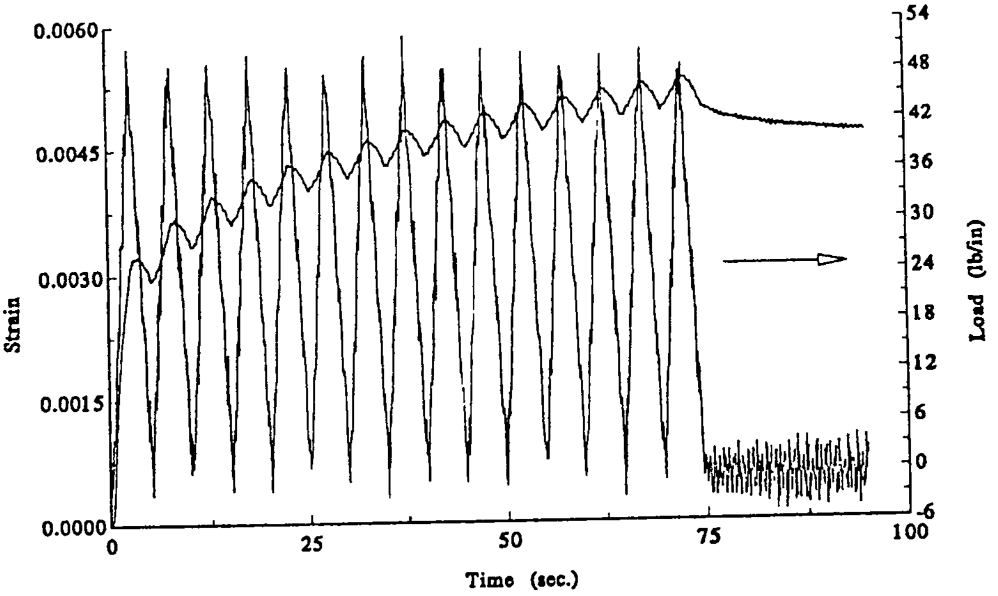

Figure 5.3: Multi-cycle compression of asphalt concrete (Specimen: IV/cc0402, cf. Table 5.1).

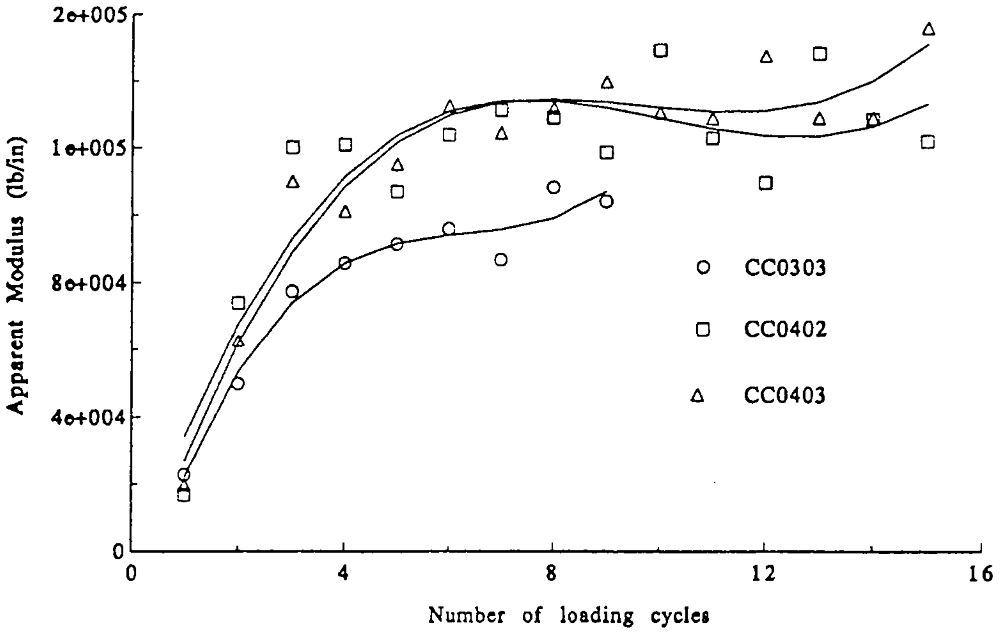

Figure 5.4: Change of apparent modulus in multi-cycle compression.

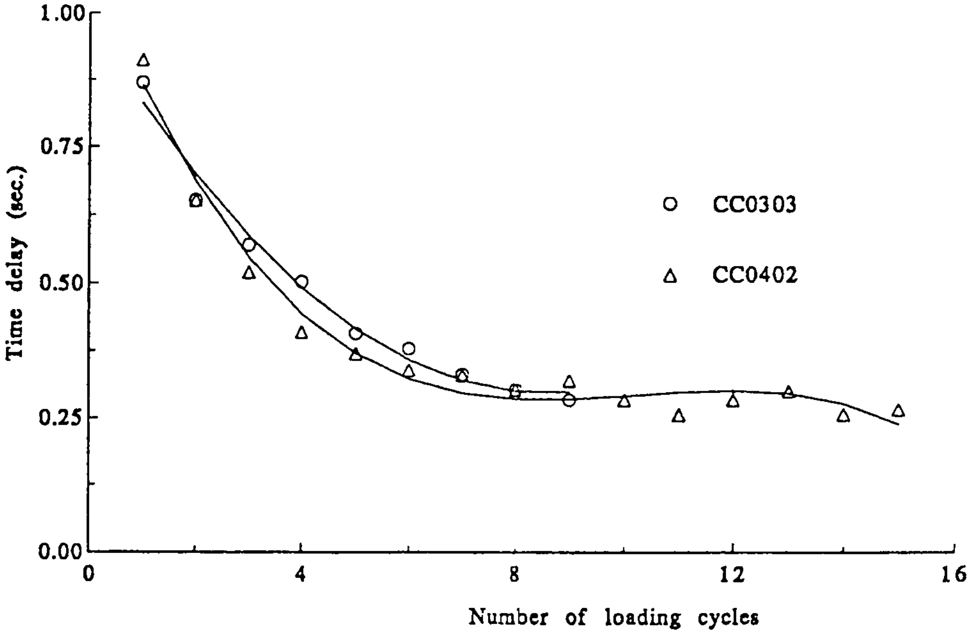

Figure 5.5: Change of time delay between maximum strain and load in multi-cycle compression.

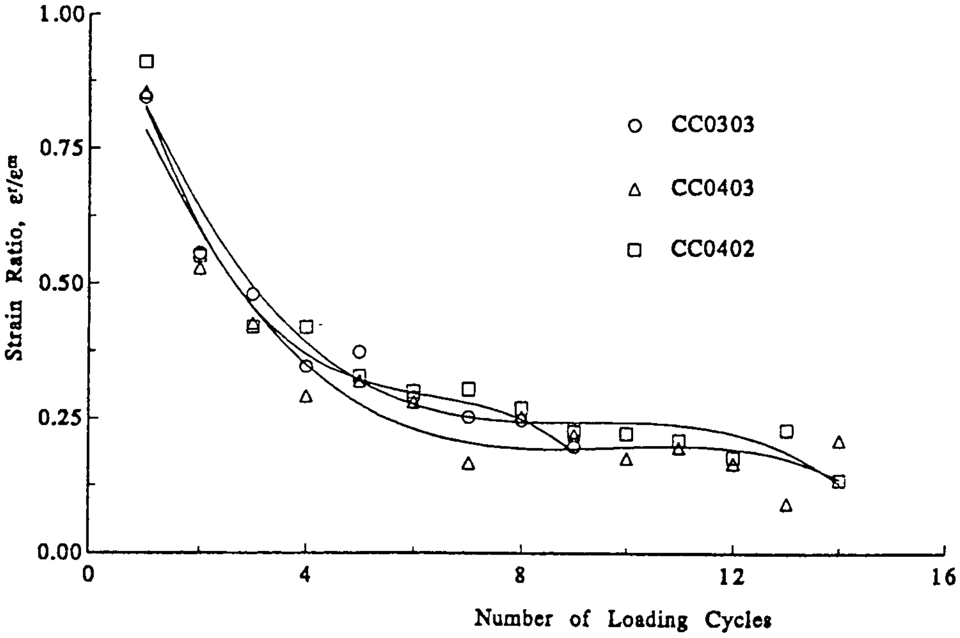

Figure 5.6: Change of the ratio of residual strain to maximum strain in each cycle.

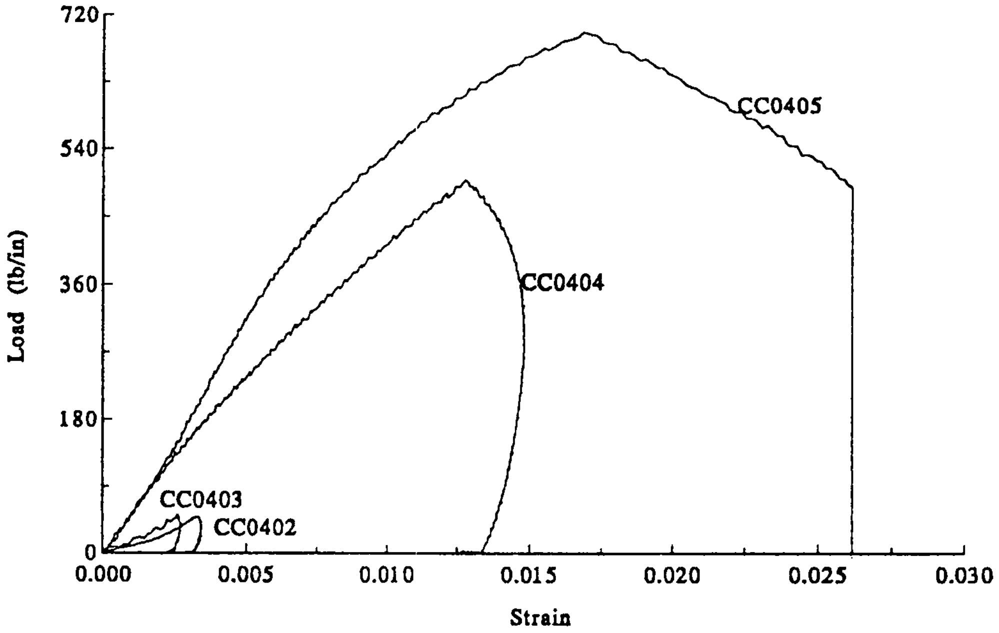

Figure 5.7: Comparation of mechanical response of specimen IV in single cycle compressions.

Figure 5.8: Fracture pattern of asphalt concrete.

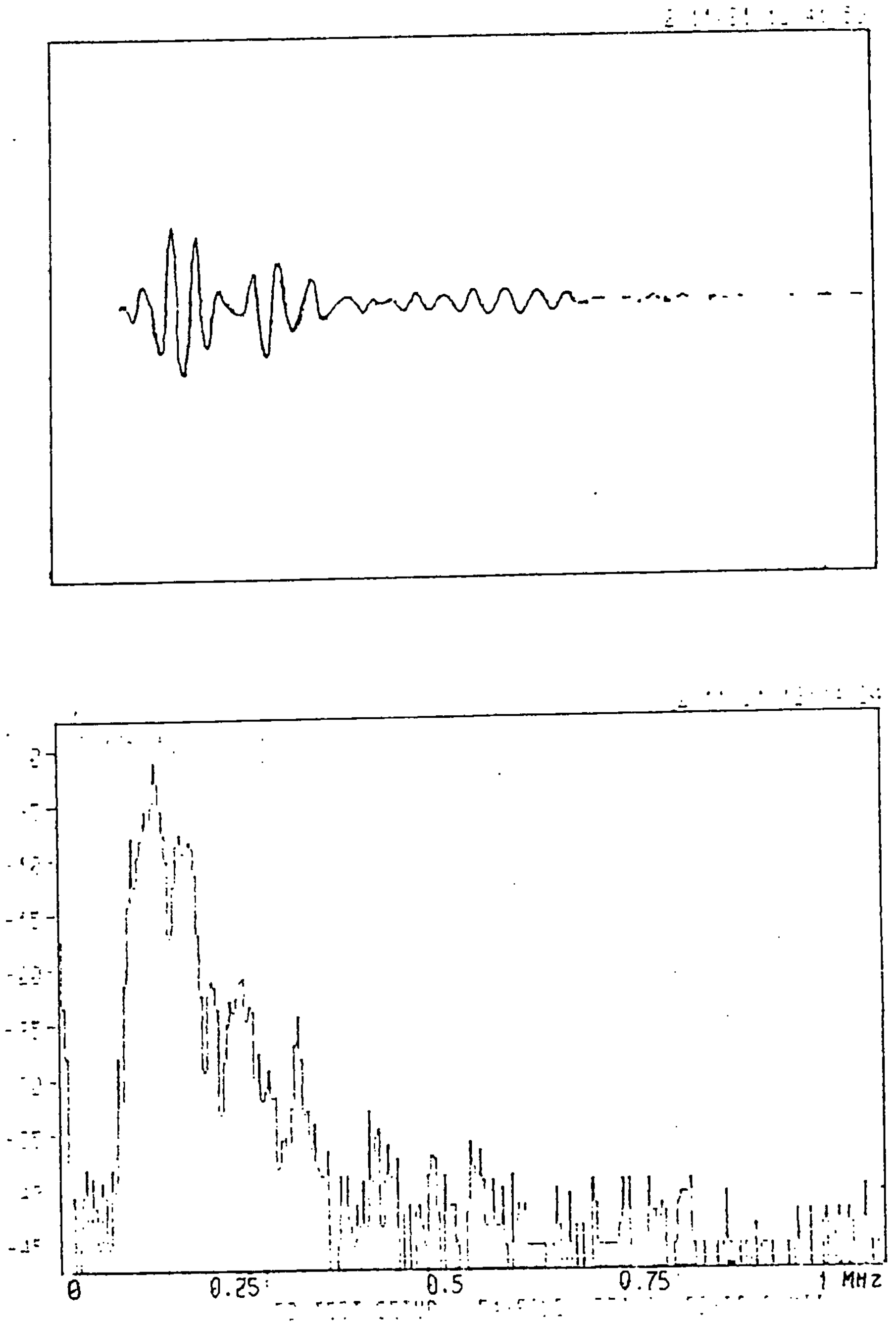

Figure 5.9: Typical wave form and spectrum of asphalt concrete.

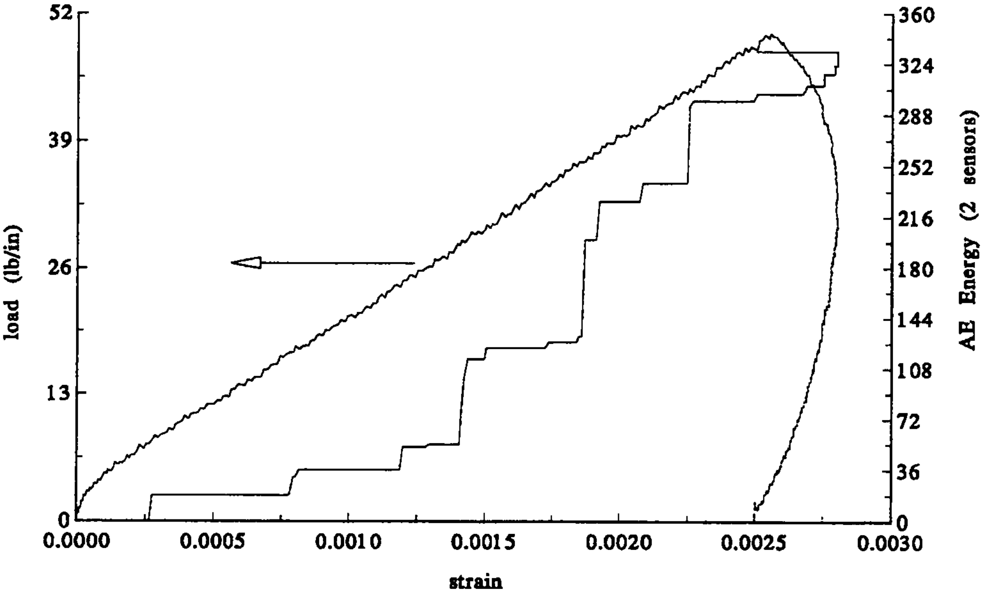

Figure 5.10: AE activity in a single cycle compression.

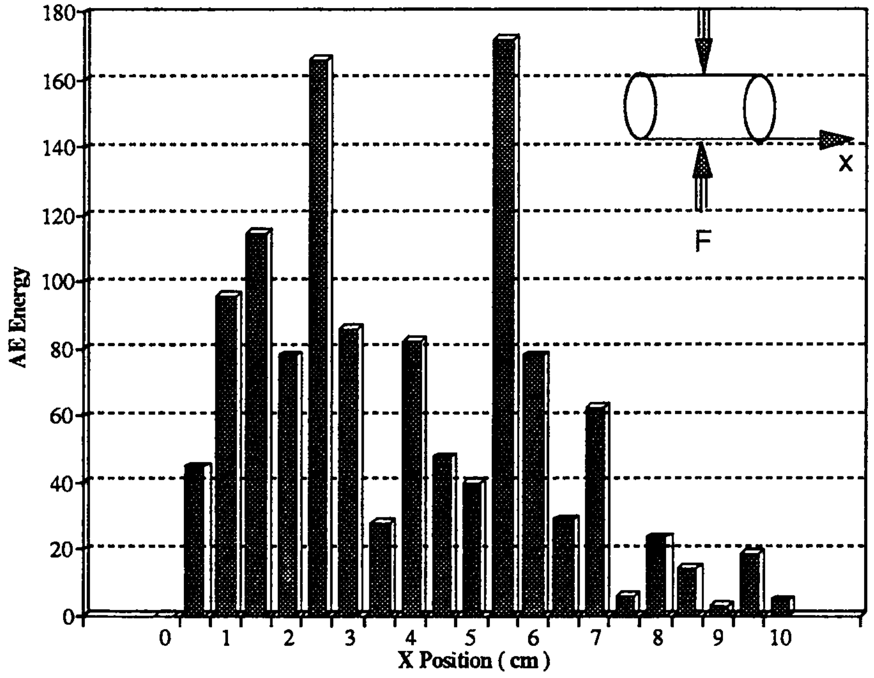

Figure 5.11: AE intensity distribution along the axial direction of asphalt specimen.

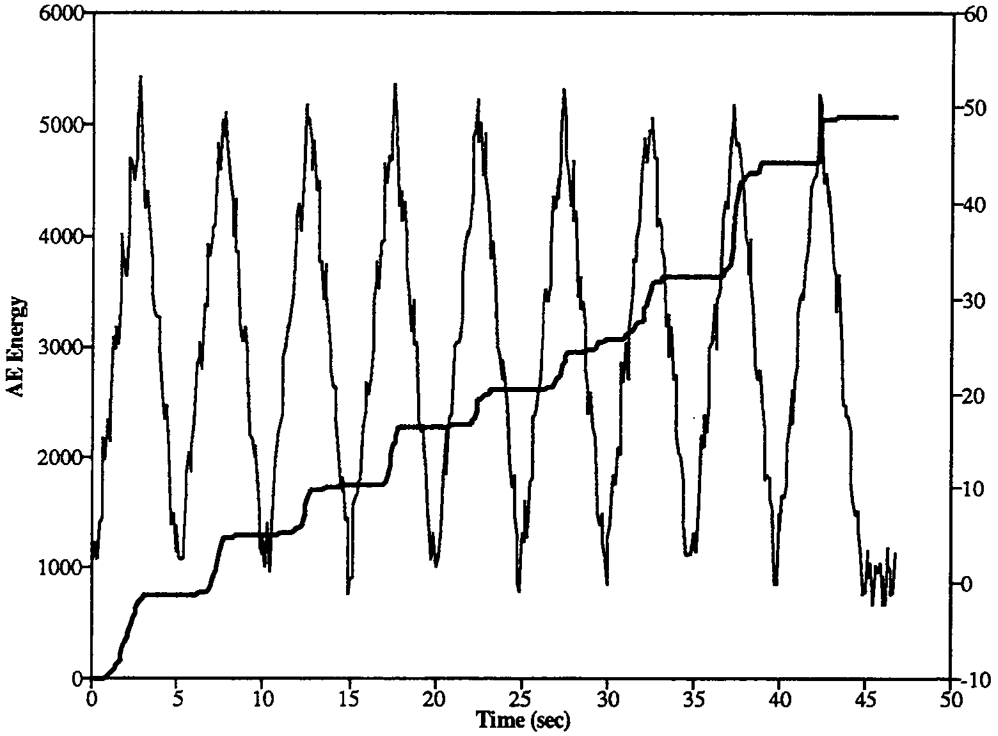

Figure 5.12: Cyclic feature of AE event in multi-cycle compression.

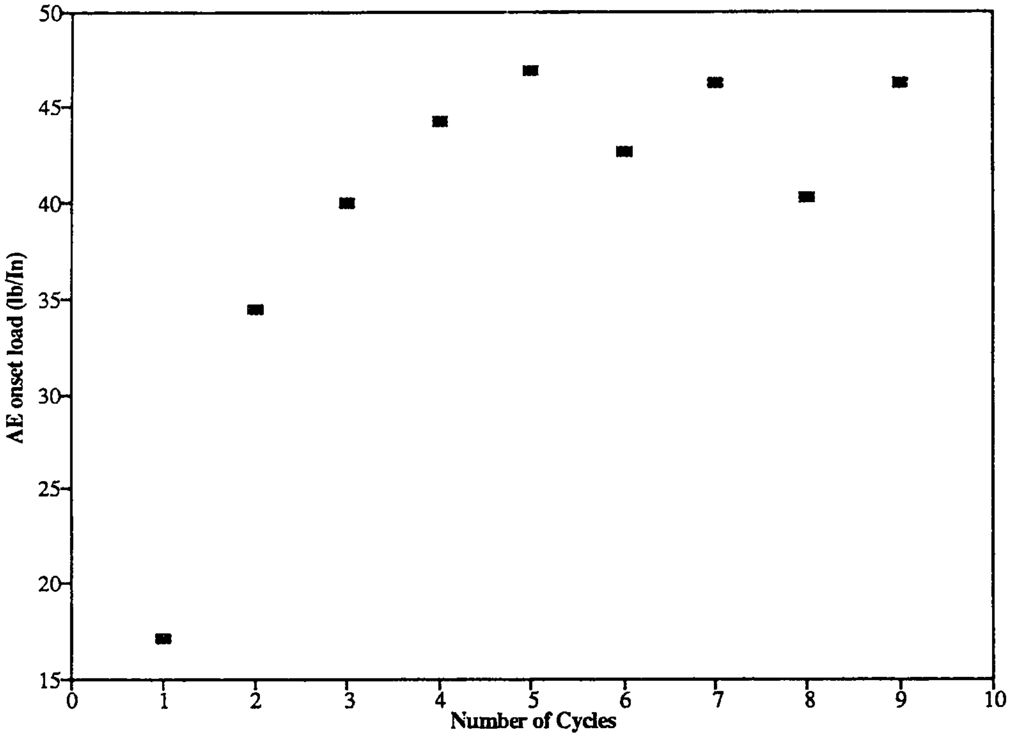

Figure 5.13: AE onset load in multi-cycle compression.

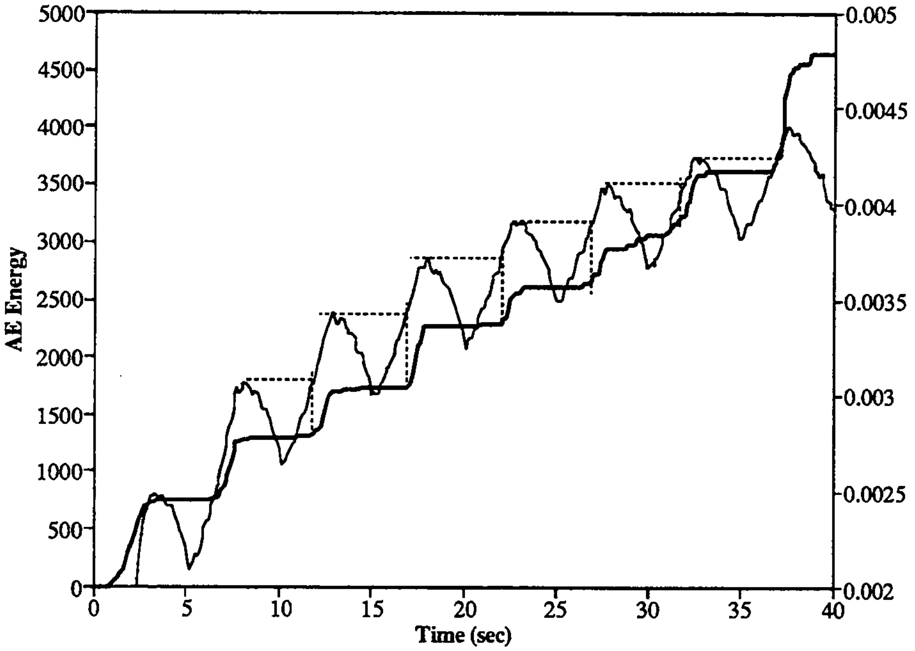

Figure 5.14: AE activity is controlled by the strain state of asphalt concrete.

References

1. J. F. Hills, "The Creep of Asphalt Mixes", in *Journal of the Institute of Petroleum*, **59**, 570 (1973).
2. J. Sousa and C. L. Monismith, "Dynamic Properties of Asphalt Concrete", in *Journal of Testing and Evaluation*, **16**(4), 350 (1988)
3. S. Yuyama, "Several AE Sources Observed During Fracture of Repaired Reinforced Concrete Beams", 10th *International Acoustic Emission Symposium*, October 22-25, 1990, Senday, Japan.

Chapter 6

Characterization of Asphalt Surface by Contact Angle Measurements

6.1 Introduction

The practical strength of adhesive joints is known to be directly proportional to the thermodynamic work of adhesion at the interface. The work of adhesion W_a is the change in the Gibbs free energy per unit area of interface and is equal to

$$W_a = \gamma_1 + \gamma_2 - \gamma_{12}, \tag{6.1}$$

where γ_1 is the surface tension of phase i, and γ_{12} is the interfacial tension.

In a liquid-liquid system, all the surface tension terms in equation 6.1 can be independently measured and hence W_a can be determined. However, in a solid-solid system, neither the surface energy of the solid nor the interfacial tension can be directly measured. Many techniques were developed to characterize the surface energies of solids[1] and a number of models have been proposed to predict the thermodynamic work of adhesion from the surface energy parameters of the two component phases.[2,3]

Contact angle measurement is perhaps the most widely used technique for investigating the surface interactions between two phases such as liquid-liquid and solid-liquid interfaces. By measuring the contact angles between asphalts and different liquids, surface energies of an asphalt surface can be characterized. The contact angle ($\angle c$) of a sessile liquid drop on a horizontal surface can be obtained directly by measurement of the slope of a tangent to the profile at a point where the liquid and solid meet. The distinct advantage of contact angle measurement is that this method is sensitive to only the surface molecular layer. This is not true of other, more sophisticated, surface characterization techniques. Conventional goniometry methods for contact angle measurement have a number of limitations. Chief among these is that the operator must position the two tangents visually. Thus, angle determination is highly subjective. Agreement among different operators and different laboratories is not always good. A typically standard deviation is more than 2°.

In 1982, Israel first observed that when a laser beam was projected at a solid-liquid-air or solid-liquid-liquid interface two beams resulted.[4] It was observed that these two beams were related to the contact angle between the liquid and the solid. From their observations, a new method of contact angle measurement termed laser contact angle goniometry (LCAG) was developed.[5] This new method does not require visual determination of tangents to curve surfaces and is, thus, less subjective. It allows for the measurement of contact angles on all types of surfaces, utilizing very small liquid drops on samples of minimal surface area. The technique is particularly useful for curved surfaces that since the quality of the data obtained for curved surfaces is usually better than that obtained for flat surfaces. This is because diffraction lines are thinner if the laser beam touches a smaller portion of the test surface.

6.2 Purpose

The objective of this work is to demonstrate the utilities of LCAG for the characterization of asphalt binder.

6.3 Apparatus

The apparatus we used to measure contact angles follows that of Huff.[6] A 1-mW helium-neon laser (Newport product model U-1321p) was mounted to a three-axis translator in an optical bench to serve as the source of a beam of coherent light. The beam essentially has a divergence less than 1.0 mra. The laser beam was passed through a filter to absorb heat and through three optical planoconvex lenses to focus the beam and reduce its diameter. The sample stage was placed in the position where the focal point of the optical lenses was such that the narrowest beam width passed the solid-liquid-air interface. An environmental chamber was made by our machine shop for investigation. In the chamber, the solid substrate examined was placed on a platform above the humidifying solvent, which was the same with the liquid phase in order to keep the chamber saturated with liquid vapor. After passing through the chamber, which was placed on an X-Y-Z stage, the beam was directed at a flat, rigid screen perpendicular to the beam, approximately 33 cm from the substrate. The precise distances between the laser, the substrate, and the screen are relatively unimportant, but brighter images are obtained if the distances are kept as short as possible and the measurements are made in a dark environment.

6.4 Experimental

The asphalt substrates were prepared by the following procedures. First, a small amount of asphalt was placed on a clean microslide, and the slide was kept in an oven with temperatures in the range of 70° to 80°C for five hrs. Then the asphalt material was melted and spread along the surface of microslide. Finally, it was allowed to rest at room temperature until the surface was even and smooth. The asphalts examined were for AAK, AAG, AAM and AAD.

The wetting liquids used in our measurements were distilled water, formamide, and glycerol. It is very important not to use oily liquids because they have the tendency to interact with the asphalt surfaces and change the chemical properties of the asphalts. For example, tricresyl phosphate, a hydrophobic liquid, was used to measure the contact angle on asphalts. It was found that the angle decreased within a few minutes and the color changed, indicating that some components were extracted from asphalts to liquid. Therefore, the hydrophilic liquids were preferred in the study on asphalt surfaces.

For each liquid type, three different volumes 2, 4 and $6 \mu L$ were used on contact lenses and three 2, 5 and 10 μL were used on asphalts to investigate the volume-dependence property. In order to avoid vaporization of the liquids during the measurements, we placed the sample (substrate and liquid) into a presaturated environmental chamber. Measurements were taken over 6 min to observe the time-course phenomena.

In order to measure the contact angle of a liquid drop on a solid surface, the solid substrate was first placed on the platform inside the environmental chamber that contained the liquid in its base container. Then we covered the chamber and waited for at least 10 min until the saturated vapor filled the chamber. During this period, the solid substrate was able to reach the energy equilibrium with the liquid vapor. Next, we placed the chamber on an X-Y-Z translational stage with micrometer resolution, and a liquid drop was placed on the solid substrate. The stage was first adjusted vertically until the laser beam impinged on the sample, and then was adjusted horizontally until the beam impinged on the solid-liquid-air interface. When the laser beam was precisely aimed at the solid-liquid-air interface of the liquid on a solid sample, it produced two scattering lines on screen that are theoretically normal to the profile of the liquid and solid surfaces at the point of contact. The stage was further adjusted so that the angle formed between the two scattering lines on screen was maximized. After placement of a drop on the substrate surfaces, the contact angle was measured at 1, 2, 3, 4, 5, and 6 min. A sheet of polar graph paper with circles of 360°, with 1° gradations, was pinned to the screen in order to read the data directly. In every case, measurements were made on two opposite sides of each liquid drop and were averaged to balance any differences in contact angle due to imperfect drops and/or surfaces.

6.5 Observations and Suggestions

1. It was noted that if too much of the beam touched either the droplet or the asphalt surfaces, broad, wedge-shaped lines appeared due to the width of the beam touching the surfaces. Narrow and straight patterns could be produced and measured reliably only if the beam grazed the solid or droplet surfaces. Only when the beam grazed the solid-air-liquid interface could both scattering lines be produced simultaneously.

2. It was found that after measurement, if the drop was removed, a circle was left by the drop on the surface of the asphalt. The larger the drop size, the more obvious the circle.

3. It was found that if the angle was taken to the different positions by rotating the drop, the contact angle might be different. It is believed that this could be due to the improper delivery of the drop or the surface imperfection of the asphalt. The data were excluded from the report when this situation occurred.

6.6 Results and Discussion

There are several results obtained in our experiments. First, the value of the contact angles are relatively insensitive to the size of the drop for all types of asphlats (Figures 6.1, 6.2, 6.3). That is, there is not significant relation between the droplet volume and the contact angle. In our figures, bars show the zero-time contact angle, which were obtained by the extrapolation of the finite time data points, using the linear regression method; and the brackets represent the standard errors of each measurement. Second, it is found that for distilled water the order of the magnitude of contact angle is AAD > AAK > AAM > AAG; for formamide AAD > AAK > AAM > AAG and for glycerol AAK > AAD > AAM > AAG (Tables 6.1-6.3). The data suggested that AAD and AAK contain fewer polar components than AAM and AAG. The result is consistent with the finding of A-002A. It was not known if the softness of asphalts affected the angle measurements or not, because it was observed that the AAD asphalt was the softest one in all types of asphalts and the STD of its contact angles was the largest. Third, the time-course observations have shown that the contact angles do not changes significantly over time if the drops stay stable with asphalt and the measurements are taken in an environmental chamber. For example, in the measurements of distilled water on AAK, the contact angle changes approximately 1° over 6 min (Figure 6.4), whereas in the measurements of tricresyl phosphate on AAK, the angle decreases rapidly in first 3 min and continue decreasing thereafter (Figure 6.5). Fourth, for temperature dependency of contact angles on asphalts, we have not found significant relationship between temperature and contact angles due to the lack of temperature control in our laboratory (Figure 6.6). Last, because of laser beam produces scattering lines normal to the profile of the surface on which it impinges, observers can measure the contact angles objectively and repeatably.

6.7 Conclusions and Recommendations

1. It has been demonstrated that LCAG is a simple and cost-effective test for surface characterization of asphalt binders. The test as it is and by itself, is a useful specification tool for qualifying asphalt binders.
2. The test, when combined with the modified blister test discussed in Chapter 5 offers a rational scheme to evaluate and to predict the effect of water immersion, PH, etc. on the adhesive strength of asphalt/aggregate systems. However a further research is needed (1) to develop a consistent and quantitative procedure to separate the dispersive and acid-base contributions of asphalt to the molecular interactions between asphalt and aggregate, and (2) to establish a quantitative model for characterizing acid-base interactions. A recent model proposed by the author is a good starting point.[2,7]

Table 6.1: Contact angle measurement of asphalts-distilled water.

Volume (μl)	AAK ∠c (°)	AAK STD (°)	AAG ∠c (°)	AAG STD (°)	AAM ∠c (°)	AAM STD (°)	AAD ∠c (°)	AAD STD (°)
2	96.2	1.3	86.1	1.5	88.7	1.4	99.2	2.9
5	95.2	1.7	85.4	1.9	90.9	1.4	99.1	2.6
10	97.9	2.6	86.7	1.4	90.7	1.6	99.7	2.9

Table 6.2: Contact angle measurement of asphalts-formamide.

Volume (μl)	AAK ∠c (°)	AAK STD (°)	AAG ∠c (°)	AAG STD (°)	AAM ∠c (°)	AAM STD (°)	AAD ∠c (°)	AAD STD (°)
2	88.3	2.3	76.0	1.5	81.4	1.5	90.3	2.7
5	89.1	2.6	77.6	1.0	81.2	1.6	89.2	2.9
10	86.4	2.4	76.4	1.2	80.1	1.5	89.5	2.3

Table 6.3: Contact angle measurement of asphalts-glycerol.

Volume (μl)	AAK ∠c (°)	AAK STD (°)	AAG ∠c (°)	AAG STD (°)	AAM ∠c (°)	AAM STD (°)	AAD ∠c (°)	AAD STD (°)
2	93.6	1.6	81.4	1.6	85.0	1.0	88.8	2.4
5	95.0	1.1	83.1	1.4	85.2	1.0	92.5	2.6
10	94.1	1.5	82.0	1.4	86.7	1.2	93.5	2.5

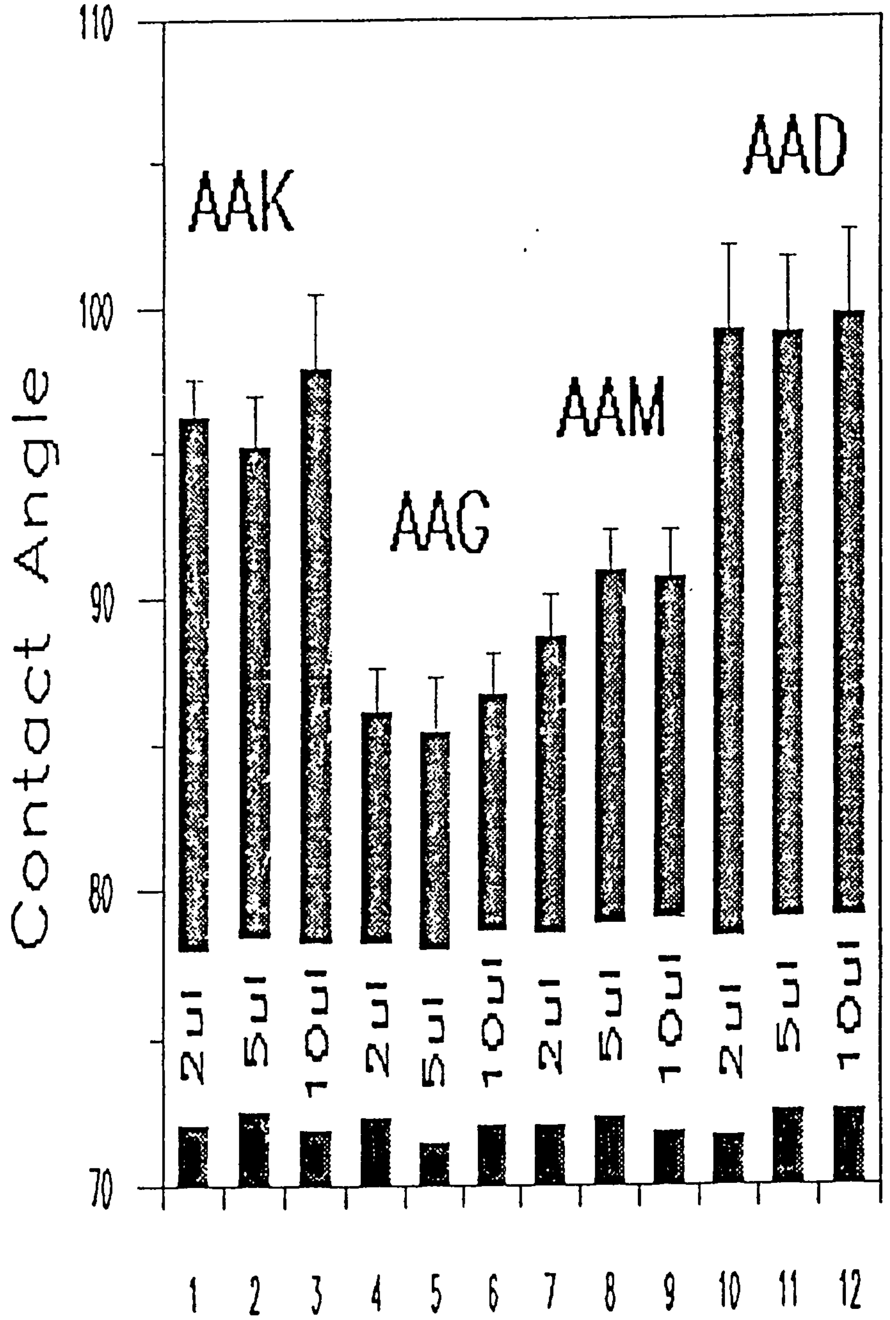

Figure 6.1: Contact angle versus drop volume for 4 asphalt materials with 5 observations per point; brackets represents SDs.

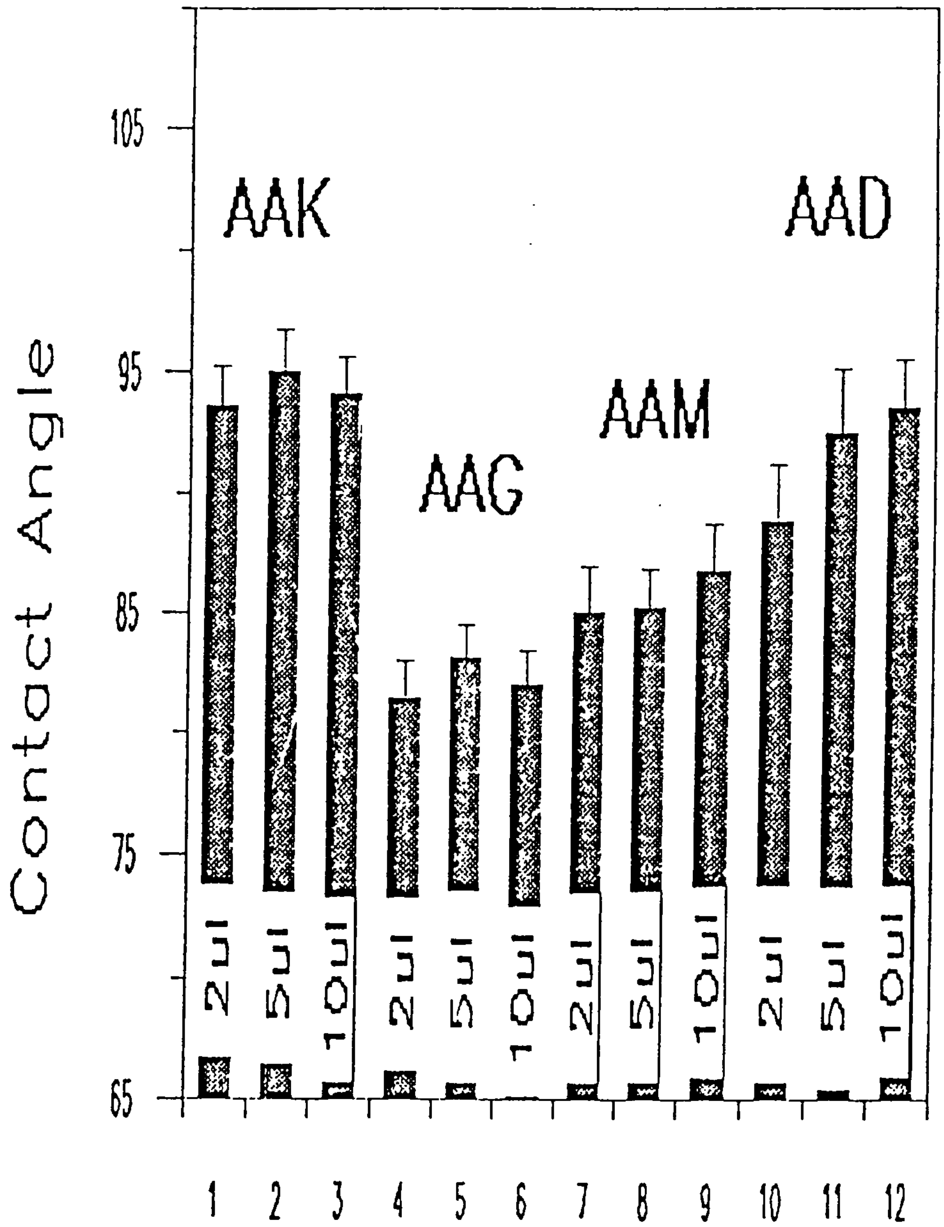

Figure 6.2: Contact angle versus drop volume for 4 asphalt materials with 5 observations per point; brackets represents SDs.

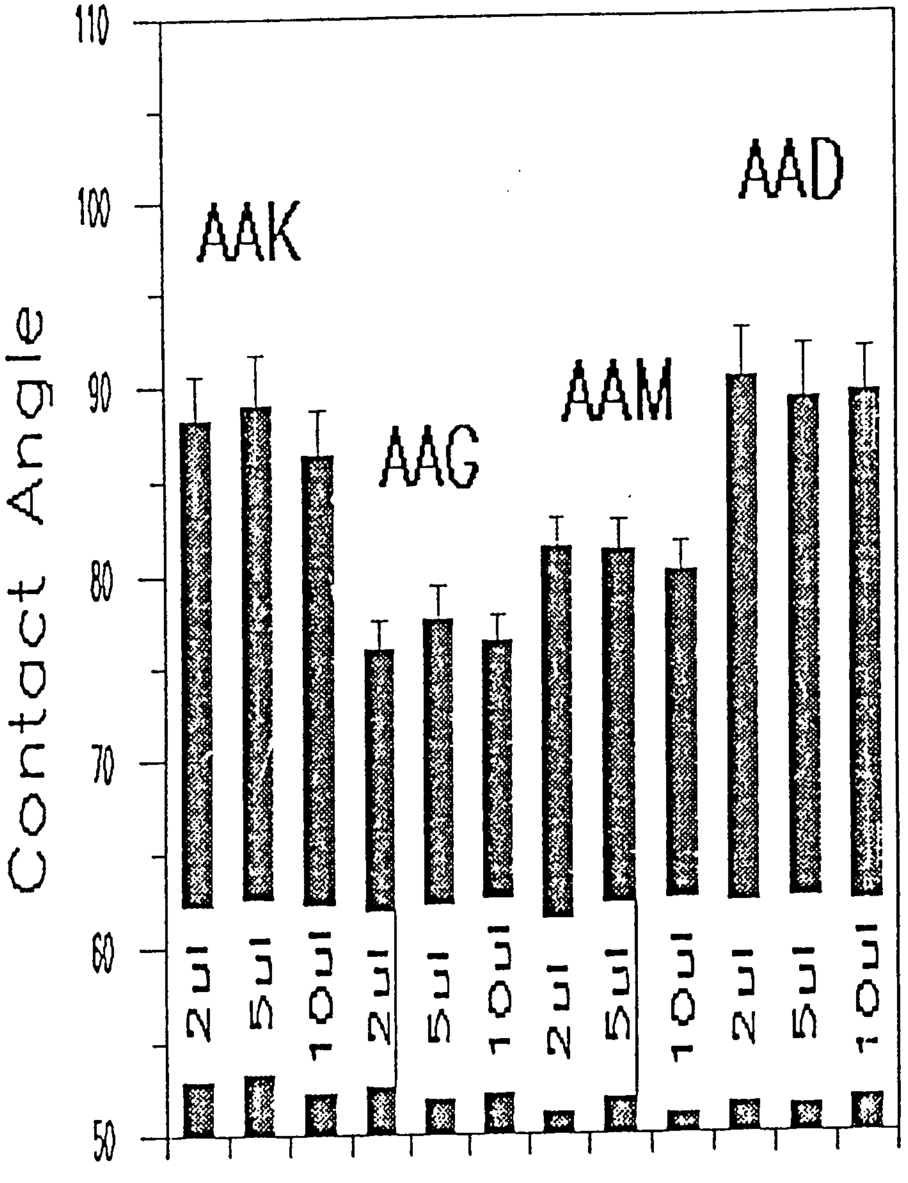

Figure 6.3: Contact angle versus drop volume for 4 asphalt materials with 5 observations per point; brackets represents SDs.

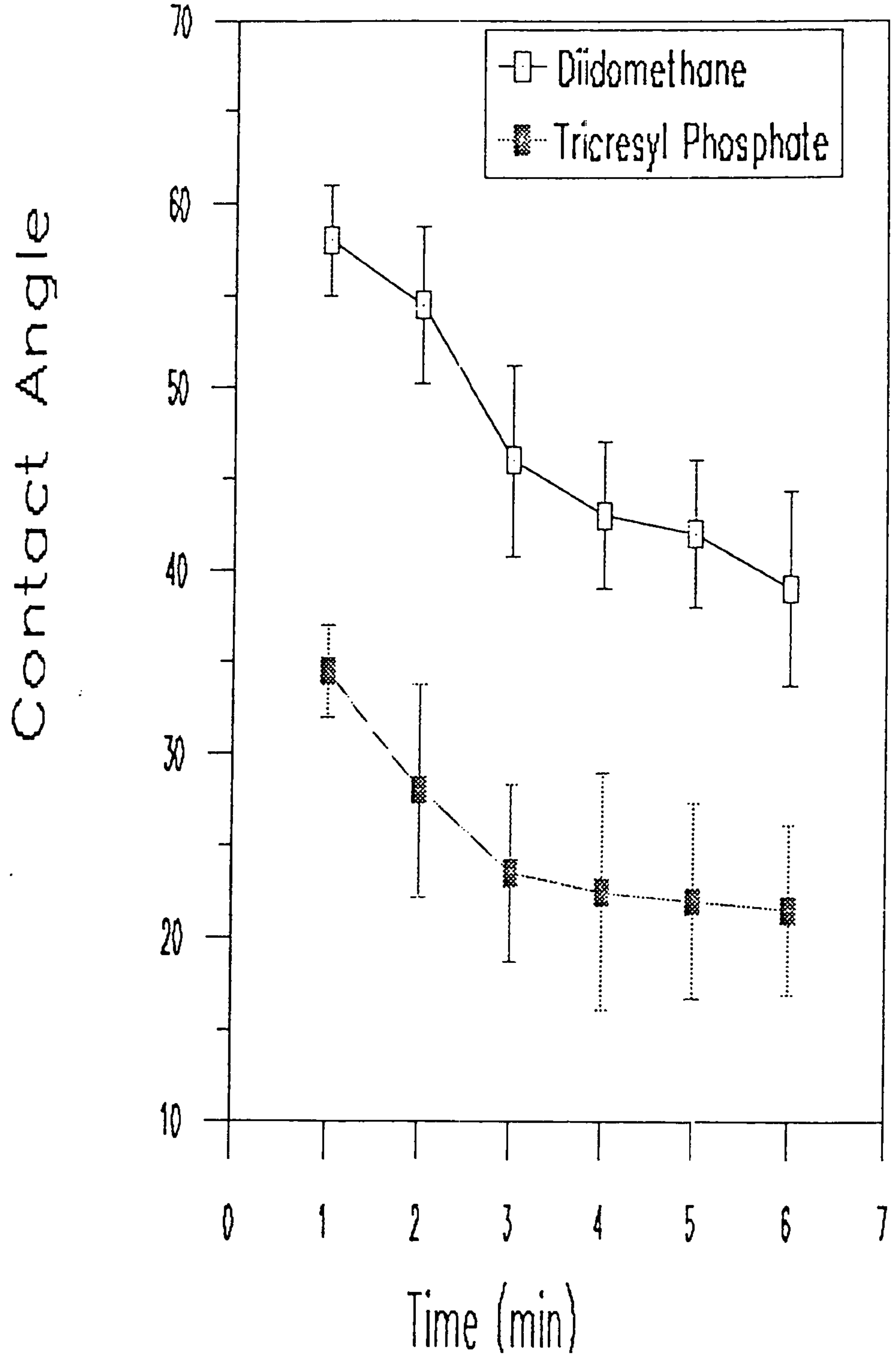

Figure 6.4: Contact angle as a function of time for liquid interaction with asphalt AAK.

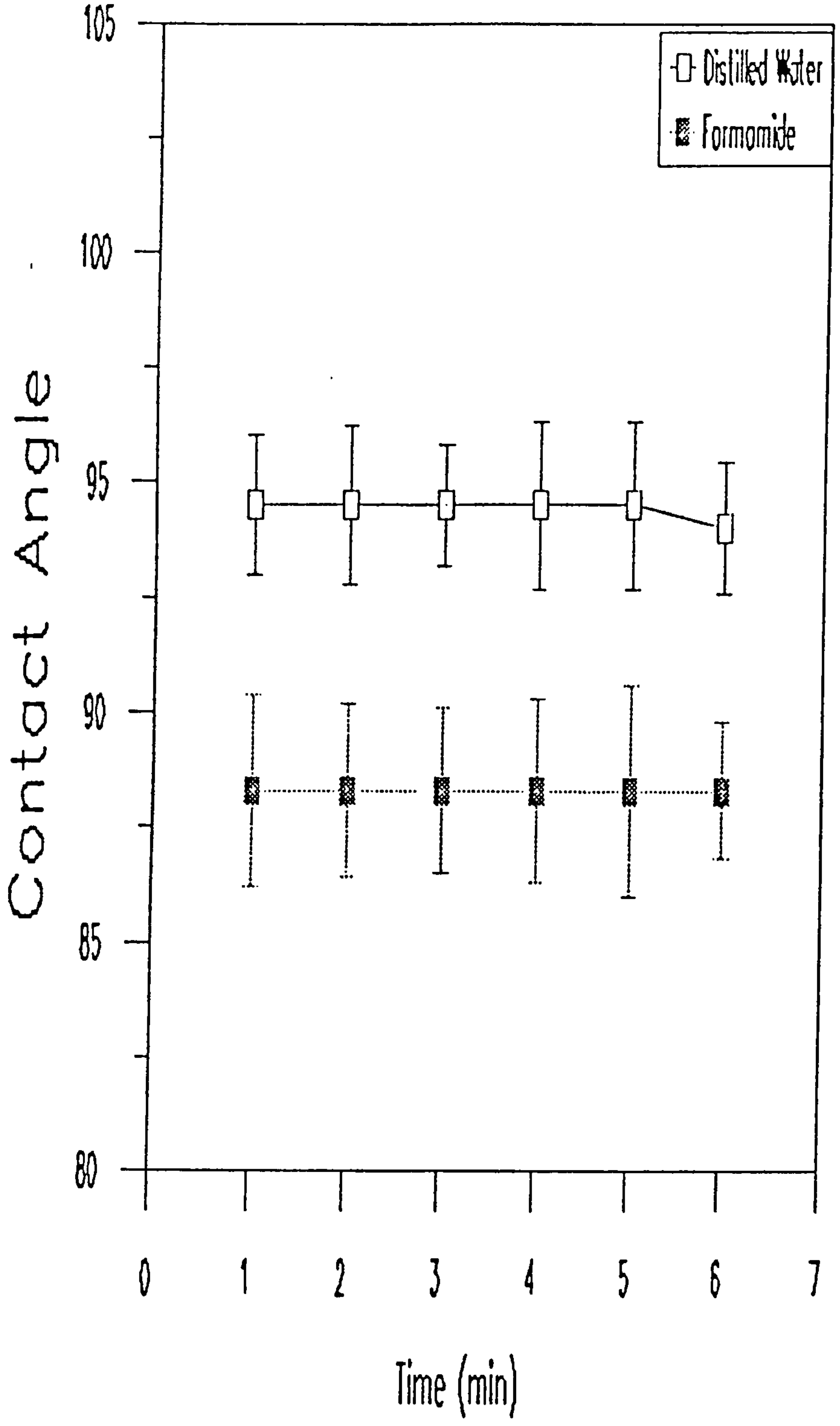

Figure 6.5: Contact angle as a function of time for liquid interaction with asphalt AAK.

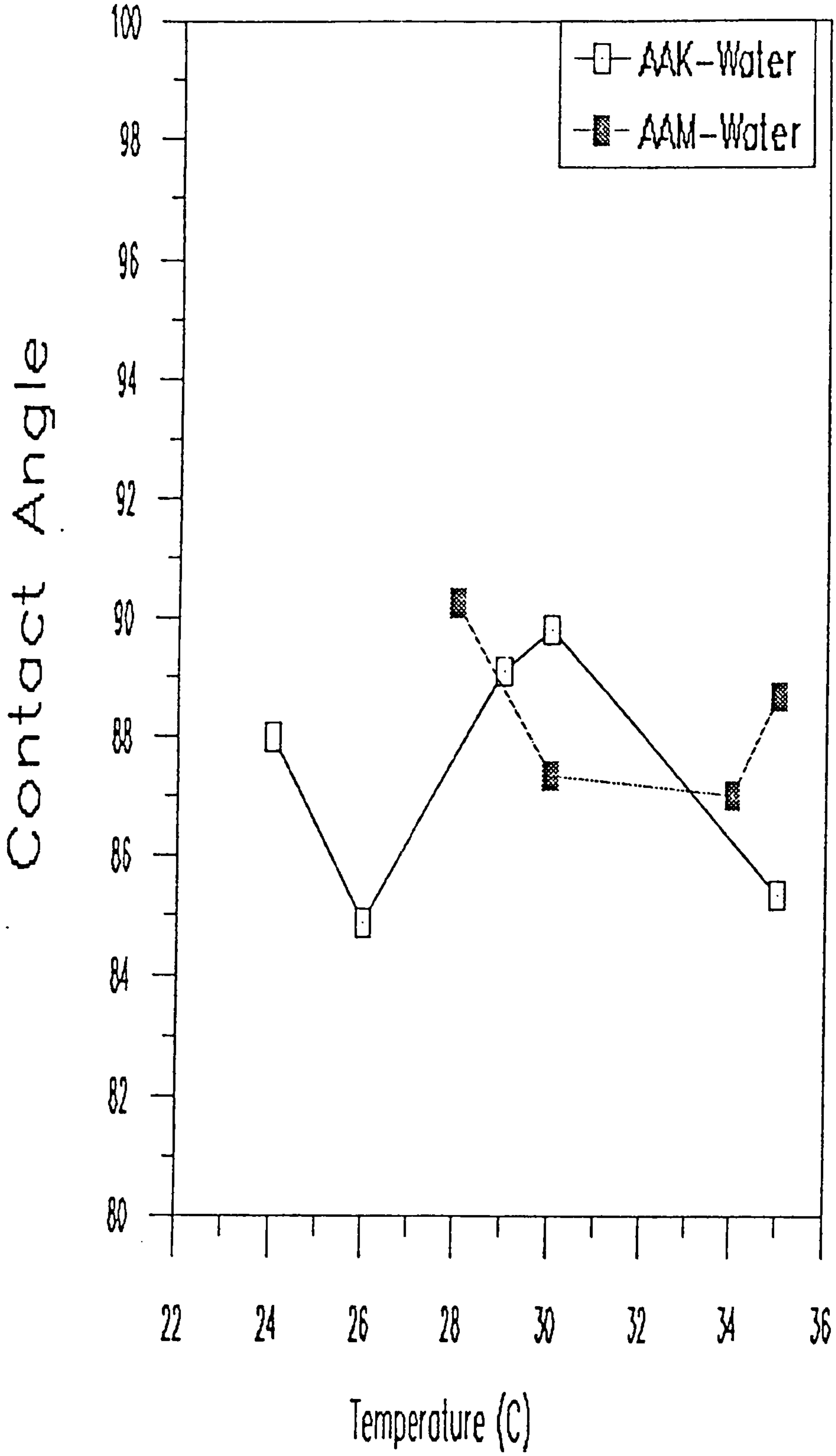

Figure 6.6: Temperature dependence of contact angle versus temperature.

References

1. Adamson, *Physical Chemistry of Surfaces*, 4th Ed., J. Wiley, New York (1982).
2. W. V. Chang and F. Chen, *Polym. Materials Sc. & Eng.* **61** 607 (1989).
3. W. V. Chang and F. Chen, "Role of Acid-Base Interactions in Wetting, Spreading and Adhension" (submitted to *Journal of Adhesion Science & Technology*).
4. S. C. Israel, W. C. Yang and C. H. Chae, "Characterization of Polymer Surfaces by Laser Contact Angle Goniometry" ACS, Division of Polymer Chemistry Meeting, Dallas, Texas, *Polymer Reprints* **30**(1) 328 (1989).
5. S. C. Israel, "Contact Angle Measurement by Laser Beam Projection", U.S. Patent Application Ser. No. 718865 (1984).
6. J. F. Bush, J. W. Huff and D. L. Mackeen, "Laster-Assisted Contact Angle Measurements," *American Journal of Optometry & Physiology Optics* **65**(9) 722 (1989).
7. F. Chen and W. V. Chang, "An Applicability Study of a New Acid-Base Interaction Model to Polypeptides and Polyamides," *Langumuir* (in press).

Chapter 7

A Modified Adhesive Blister Test for Asphalt-Aggregate Systems

7.1 Introduction

The concept of fracture in materials may be divided into two general classifications: (1) the separation of a material from itself (cohesive fracture), and (2) the separation of a material from a dissimilar material at the bond line between the two materials (adhesive fracture). In the case of adhesive fracture, the specific adhesive fracture energy, Γ_a, is defined as the energy released per unit of new surface created on separation of dissimilar materials. Within the fracture mechanics interpretation, Γ_a is viewed as a fundamental property of the adhesive system. The adhesive fracture energy is typically several orders of magnitude higher than the corresponding thermodynamic work of adhesion. However, an adequate thermodynamic work of adhesion is a necessary condition for a good adhesive joint. Γ_a can be written as a product of the thermodynamic work of adhesion and a factor whereof the magnitude depends on the extensibility of the adhesive, as well as the contributions due to plastic and viscoelastic effects. Water and its solutions may greatly reduce the thermodynamic work of adhesion of the asphalt-aggregate system and may cause the pavement to disintegrate.

Various specimens and data analysis methods have been employed for evaluating the adhesive fracture energy. Several of these are included in two references.[1,2] For the adhesion study on asphalt concrete pavements, the blister test seems most appropriate for both experimental and analytical fracture analysis of adhesive debonding. It also provides a convenient way to study the effect of water immersion, pH, salt concentration, etc. on the adhesive strength. This test, together with the contact angle measurement of asphalt surface, offers a rational basis for the evaluation and selection of asphalt-aggregate systems for pavement applications.

The blister test method is defined in Figure 7.1. The specimen is an asphalt disk, which is bonded to a rigid substrate except for a central portion of the radius, a. When the unbonded region is pressurized, as by the injection of compressed fluid, the disk lifts off the substrate and forms a "blister" whose radius stays fixed until a critical pressure, P_{cr}, is reached. At this value the radius of the blister increases in size, signifying an adhesive failure along the interface. For linear elastic and LVE materials, simple procedures whereby Γ_a can be uniquely determined from P_{cr} are well established.[2]. A nonlinear elastic analysis of the blister test was recently completed by Chang and Peng, whereby procedures for determining Γ_a from P_{cr} were discussed.[3] If the behavior of asphalt is characterized, procedures for determining Γ_a from P_{cr} can be developed by nonlinear finite element analysis. Hence, the key problem involved in this phase of study is the development of test procedures for determining the critical pressure, P_{cr}.

7.2 Purpose

The purpose of this work element is to develop a modified blister test for evaluating the adhesive strength of asphalt-aggregate systems in the presence of water.

7.3 Experimental

The purpose of the experimental work is to determine values of fracture parameters. It is expected that adhesive failure will occur along the aggregate/asphalt interface under certain experimental variables and testing conditions.

7.3.1 Materials

The substrates used in our blister test research were aluminum, PMMA, Teflon, and aggregate (granite). Before specimens with aggregate substrates were available, three types of substrate materials, aluminum, PMMA and teflon, were used in the initial phase of the research. These materials provided very different surface characteristics.

The adhesive cements in all tests were asphalts AAG-1 and AAK-1. To determine the precise load, P_{cr}, at which debond starts to extend, an AE technique was developed to monitor the tendency of failing in the specimen and to determine the position of the initial disbonding.

7.3.2 Apparatus

In the laboratory, a prototype of the blister test device was assembled. A schematic of the device is shown in Figure 7.1. In the blister test, the loading is pressure. The pressure medium was water, which was controlled through a pressure regulator.

7.3.3 Description of Specimens

Two types of specimens, conventional specimens (without physical constraint) (see Figures 7.2, Diagrams 1 and 2) and modified specimens (with physical constraint) (see Figure 7.2, Diagrams 3 and 4), were prepared. We started with the conventional specimens. It was found that when asphalt materials were tested in the blister configuration of conventional specimens, the specimens always failed in a mode beginning at the periphery of the disbonding area and extending into the bulk asphalt. No apparent adhesive failure was observed. However, disbonding does occur in pavement applications. We realized that conventional specimens did not simulate asphalt's configuration in an asphalt-aggregate mix, whereof the thin film of asphalt is physically constrained by the neighboring aggregate particles. As discussed in the last two chapters, adhesive failures were observed in some poker chip tests. The success of poker chip test in simulating the behavior of the asphalt-aggregate mix motivated us to modify the conventional specimens by placing on top of the asphalt layer a PMMA plate of the same diameter as the asphalt layer (see Figure 7.2, Diagrams 3, 4). With this additional physical constraint, we were successful to induce the adhesive failure along the interface. Both asphalt AAK-1 and asphalt AAG-1 were used in this study.

7.3.4 Description of the Experimental Procedures

The experiments were carried out in the following sequence.

1. The surface of the substrate was cleaned with kerosene, but not roughened.
2. To initiate disbonding, a predisbond area of radius a was made by applying a Teflon tape sprayed with RAM GS-3 dry lubricant.
3. The bulk asphalt was heated at 80°C for 1 hr and cooled at room temperature for a certain time, then poured onto the substrate to the desired thickness.
4. In the case of modified specimens, a PMMA plate with the same size as that of the asphalt specimen was placed on the asphalt specimen.
5. The specimens were cooled at the testing temperatures for at least 3 hrs.
6. The specimens were placed in water at room temperature for a specified time of immersion.
7. A pressure fitting with a pipe nipple was screwed into the substrate through the pressure hole.
8. The AE sensors were attached on the substrate surface around the asphalt specimen.

9. The specimen was mounted at the bottom of a transparent plastic tank filled with water.
10. The pressure was introduced and increased in the initially disbonded cavity by the injection of pressurized water at a constant pressurization rate.
11. The pressure was slowly increased until the specimen ruptured.
12. Measurements were made of the AE events and the imposed pressure at failure.
13. The fracture surface was assessed and pictures were taken of the fracture surfaces.

7.4 Results and Discussion

Based on the above experimental procedures, the typical test results are summarized in Table 1.

7.4.1 Description of the Experimental Variables

The experimental variables in our blister test are the testing temperature (T), the pressurization rate, the radius of the predisbond area (a), asphalt layer thickness (h), asphalt layer radius (L), the radius of the pressure hole for water access (r), and the water immersion time (TW).

It was found that in the case of the conventional specimens, at temperatures of 0°C or below, the asphalt film shattered into pieces upon the application of pressure. (Figure 7.2, Diagram 5 and Figure 7.3). At temperatures higher than 10°C, a blister was formed and ruptured immediately. In the intermediate temperature range between 0° and 10°C, a stable blister was formed and grew considerably before rupturing (Figure 7.2, Diagrams 1 and 2 and Figure 7.4). In the research, we concentrated our investigation at low temperatures from −3° to 5°C. In our opinion, it is in this temperature range that water causes most disbonding problems.

Since asphalt is a viscoelastic material, we expect that P_{cr} depends on the pressurization rate. A moderately slow pressurization rate of 0.5 to 1.5 psi/min was used in our experiment because disbonding takes place slowly in pavement applications. A predisbond area was deliberately made in order to initiate debonding along the interface. For a nonlinear material such as asphalt, the predisbonding radius should not be selected independently of the asphalt thickness, h, and the radius of the specimen, L.[3,4] In consideration of these factors, we selected values of a between 0.25 and 0.85 in. with h/a values changing from 0.26 to 1.00. After a specimen was prepared, it was subsequently immersed in water for a period between 0 to 40 hrs. It was reported that in asphalt concrete pavements, water could cause loss of the adhesive strength between the aggregate and asphalt, as well as loss of cohesive strength and stiffness in asphalt film.[5]

7.4.2 Fracture Analysis

The failure mode was assessed and pictures were taken of the fracture surfaces. In the case of the conventional specimens, it was found that at low testing temperatures such as 0°C or below, as the pressure was increased, the asphalt layer obviously "pouched out" to some extent, followed by a brittle failure taking place in a certain direction in the bulk asphalt as was shown in Figure 7.2, Diagram 5 and Figure 7.3. In the intermediate temperature range, such as 2° to 5°C, a stable blister was formed and grew as the pressure was increased. It was observed that failure often occurred beginning at the tip of the predisbonded area, then propagated into the bulk asphalt near the bondline. Eventually the specimen ruptured at the periphery of the blister when the crack extended across the thickness of the asphalt layer (see Figure 7.2, Diagram 2 and Figure 7.4). However, in some cases (usually at higher testing temperatures such as 5° or 6°C) when the blister grew big enough, it ruptured somewhere on the bulb away from the crack tip region (Figure 7.2, Diagram 1). In both cases, a thin layer of asphalt coated on the fracture surfaces of the substrate was observed (Figure 7.2, Diagrams 1 and 2 and Figure 7.4).

The location of the fracture initiation site, as well as the path of crack propagation of the above experimental results, can be qualitatively explained with the help of the nonlinear elastic, finite element analysis of blister test.[3] When deformation in a blister is infinitesimal, the maximal value of the greatest one of the three principal stresses, namely σ_{max1}, as well as the mean stress (not shown), occurs at the tip of the predisbond area (Figure 7.7). As the pressure increases, the blister is further deformed but the stress concentration is still at the crack tip (Figure 7.8). If the adhesive or the cohesive fracture energy of the system is small, the predisbonding will extend starting from the crack tip, such as in the cases of temperatures below zero for asphalt AAK. Since the shear strength of asphalt is relatively low, the crack extends along a roughly 40° surface across the thickness of the asphalt film. As temperature slightly increases, the fracture strength of the system increases such that the predisbond remains stable until the blister is significantly inflated. As shown in Figure 7.9, the stress concentration moves away from the tip of the crack, which corresponds to the case of Figure 7.2, diagram 1.

In the case of modified specimens, for the aggregate-AAK-1 system in which the radius of the predisbonded area was larger than that of the pressure hole, when the pressure reached a critical value failure occurred in a mode beginning at the tip of the predisbonded area and propagating along the asphalt-aggregate interface. No crack was found either in the bulk asphalt or at the asphalt-PMMA interface. No asphalt residue was observed on the disbonding surface of aggregate (see Figure 7.2, Diagram 3 and Figure 7.5). For the Teflon-AAK-1 system, with the initial disbond area being the size of the pressure hole, cohesive failure first occurred in the bulk asphalt at the periphery of the pressure hole. The crack then propagated upward into the area close to the bondline of PMMA plate and asphalt until the PMMA plate was lifted off. Layers of asphalt coated both on the fracture surface of PMMA and on the surface of Teflon were observed. (Figure 7.2, Diagram 4 and Figure 7.6).

7.4.3 Determination of P_{cr}

One of the novel features of this test is the adoption of the AE measurement. AE provides a sensitive way to determine P_{cr} and to predict the path of crack propagation. Figure 7.10 plots the acumulative AE energy and pressure as functions of time for a modified aggregate specimen. The history of AE events for the test is given in Table 7.2. The first significant AE event happened at 706 second after pressurization, when the pressure reached 17 psi. The crack grew stably as pressure increased until pressure reaches 42 psi at about 28 min. Based on this information, the adhesive fracture energy can be calculated by a viscoelastic finite element analysis with a realistic constitutive model.

We have developed software to process AE data that provides physical pictures of the fracture process. Figure 7.11 shows the spatial distribution of AE events with different energy content prior to the unstable growth of the crack. Figure 7.12 is a similar plot for the events associated with fast crack growth. Figure 7.13 combines information given in Figures 7.11 and 7.12. These figures, together with Figure 7.5, show clearly that the AE signals concentrated in the region where the interfacial debonding occurred and propagated.

In the case of the aggregate-AAG-1 system, the fast crack propagation happened when the pressure reached 18 psi under the similar testing conditions and experimental variables with those of aggregate-AAK-1 system.

7.5 Conclusions and Recommendations

It has been shown that the blister test technique developed in our laboratory is an useful method to evaluate the resistance of asphalt-aggregate joints to environment-assisted disbonding failure, as well as to evaluate the adhesive strength of asphalt-aggregate system. The testing apparatus has been set up. We have developed an easy-to-use and low-cost sample preparation procedure. The experimental variables and testing conditions were defined. AE technique has achieved good success in identifying P_{cr} as well as in determining the initiation site and propagation route of the debonding process.

It is recommended that follow-up test programs should be conducted on different asphalts and different aggregate substrates. A viscoelastic finite element analysis should be conducted to relate experimentally determined P_{cr}, the adhesive fracture energy, and the rheological properties of asphalt.

In addition to being a valuable tool for fundamental study, the modified blister test and the LCAG (Chapter 6) will be simple, direct, and relevant enough to be seriously considered as specification tests for state and county highway agencies.

Table 7.1: Typical results of blister test

System	P (psi)	T (°C)	h (in.)	L (in.)	TW (hr)	r (in.)	Failure	Note	Figure Number
Aggr./AAG	10.5	5	0.21	2.43	0	0.625	Cohesive	$a = 0.81 > r$	2, Diagram 1
Aggr./AAG	50.0	2	0.30	2.43	12	0.625	cohesive	$a = 0.85 > r$	2, Diagram 2 Figure 7.4.
Aggr./AAK	42.0	-3	0.25	2.35	30	0.625	adhesive	$a = 0.85 > r$ Modified	2, Diagram 3 Figure 7.5.
Teflon/AAK	30.5	-3	0.25	2.35	12	0.250	Cohesive	$a = r = 0.25$ Modified	2, Diagram 4 Figure 7.6.
Al/AAG	40.0	0	0.12	3.00	0	0.400	Cohesive	$a = r = 0.40$	2, Diagram 5 Figure 7.3.
PMMA/AAG	15.0	3	0.18	2.35	0	0.25	Cohesive	$a = 0.50 > r$	2, Diagram 2
Aggr./AAG	18	-3	0.25	2.35	40	0.625	Cohesive	$a = 0.85 > r$ Modified	-

Note: *Aggr. = aggregate; Al = aluminium

Table 7.2: AE output of the blister test

Event	Time	x	y	AE Energy
1	654.39398125	7.80	-0.02	36
2	692.72345700	3.15	6.35	57
3	703.76546375	0.76	5.11	31
4	703.76705600	0.76	5.11	33
5	704.77862350	1.34	5.92	46
6	706.67504900	7.01	2.77	24
7	706.88923700	3.33	3.39	375
8	707.03538625	5.23	3.33	35
9	719.59344150	1.68	2.32	80
10	739.02719225	1.43	6.62	30
11	740.52062500	2.84	5.78	46
12	807.59917450	3.35	7.69	26
13	809.19427750	1.62	3.00	83
14	852.91370500	1.34	4.90	83
15	912.03875275	3.47	4.48	109
16	926.85632675	4.09	1.90	39
17	926.88312575	3.60	3.00	181
18	1016.71983275	1.39	5.02	68
19	1045.09240600	3.90	-0.12	27
20	1314.95740525	7.40	-2.42	60
21	1316.80844150	4.26	1.89	34
22	1332.26079525	4.95	-1.58	113
23	1397.60754875	1.32	5.03	75
24	1412.83845525	3.08	1.05	42
25	1461.23595075	1.73	2.15	25
26	1462.59461600	3.50	1.37	170
27	1518.93121150	3.32	0.84	82
28	1676.69906825	5.74	6.46	172
29	1676.75689225	5.02	3.84	182
30	1676.80842175	4.66	3.77	93
31	1676.85953450	4.59	3.84	80
32	1677.17039725	4.73	3.19	84
33	1677.18590425	5.30	5.64	129
34	1677.18934650	4.29	4.36	142
35	1677.65579800	0.15	3.81	68

Table 7.2: (continued)

36	1677.73871325	4.07	4.27	324
37	1678.06974375	4.77	3.30	40
38	1678.08134325	4.08	3.49	90
39	1678.13576325	4.87	4.38	147
40	1678.16164650	4.49	3.97	63
41	1678.28348100	7.63	3.76	89
42	1678.43931175	5.44	4.33	61
43	1678.54184075	3.27	4.27	29
44	1678.75953600	6.32	5.41	70
45	1678.79038350	3.82	3.55	47
46	1679.05620300	5.73	4.89	81
47	1679.09619625	6.47	5.20	59
48	1679.11313800	3.52	4.85	61
49	1679.32247025	4.15	4.15	61
50	1679.35046600	4.26	3.85	49
51	1679.46455850	3.15	5.31	38
52	1679.52168675	3.48	6.62	87
53	1679.62266125	3.82	4.12	37

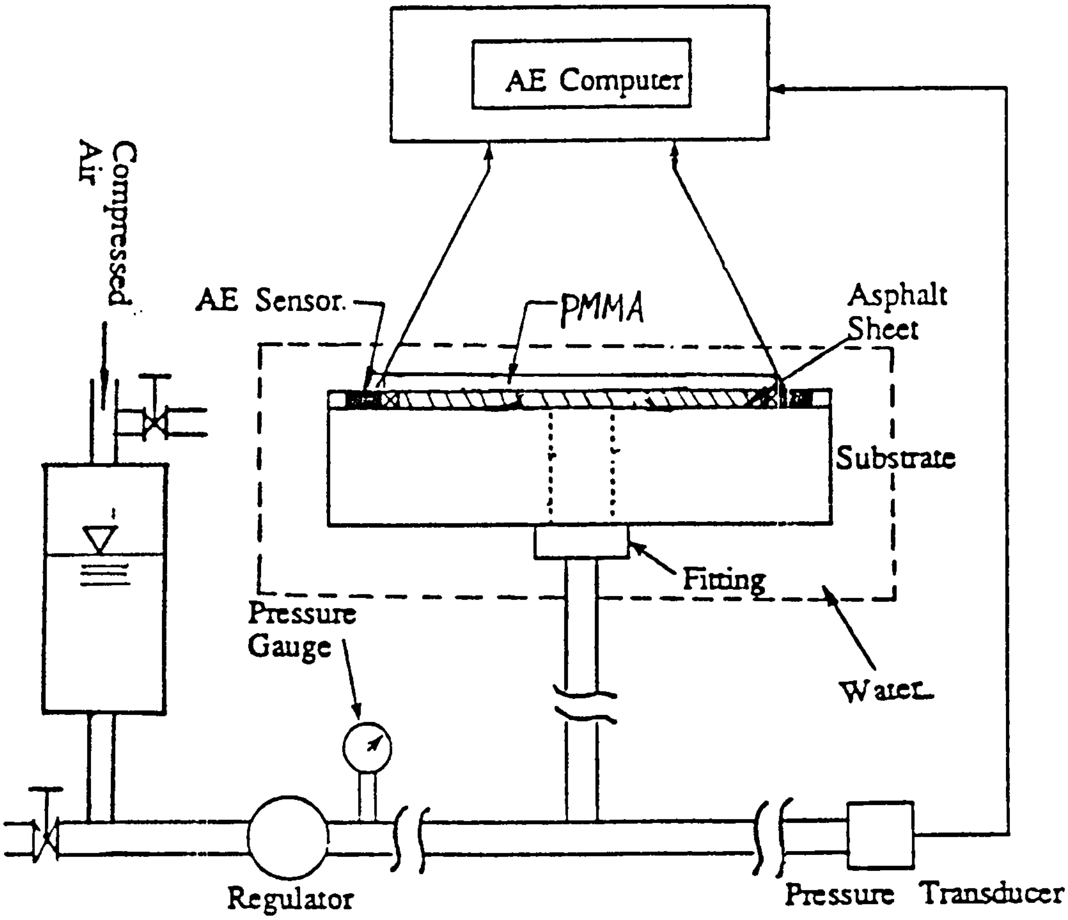

Figure 7.1: Blister test system.

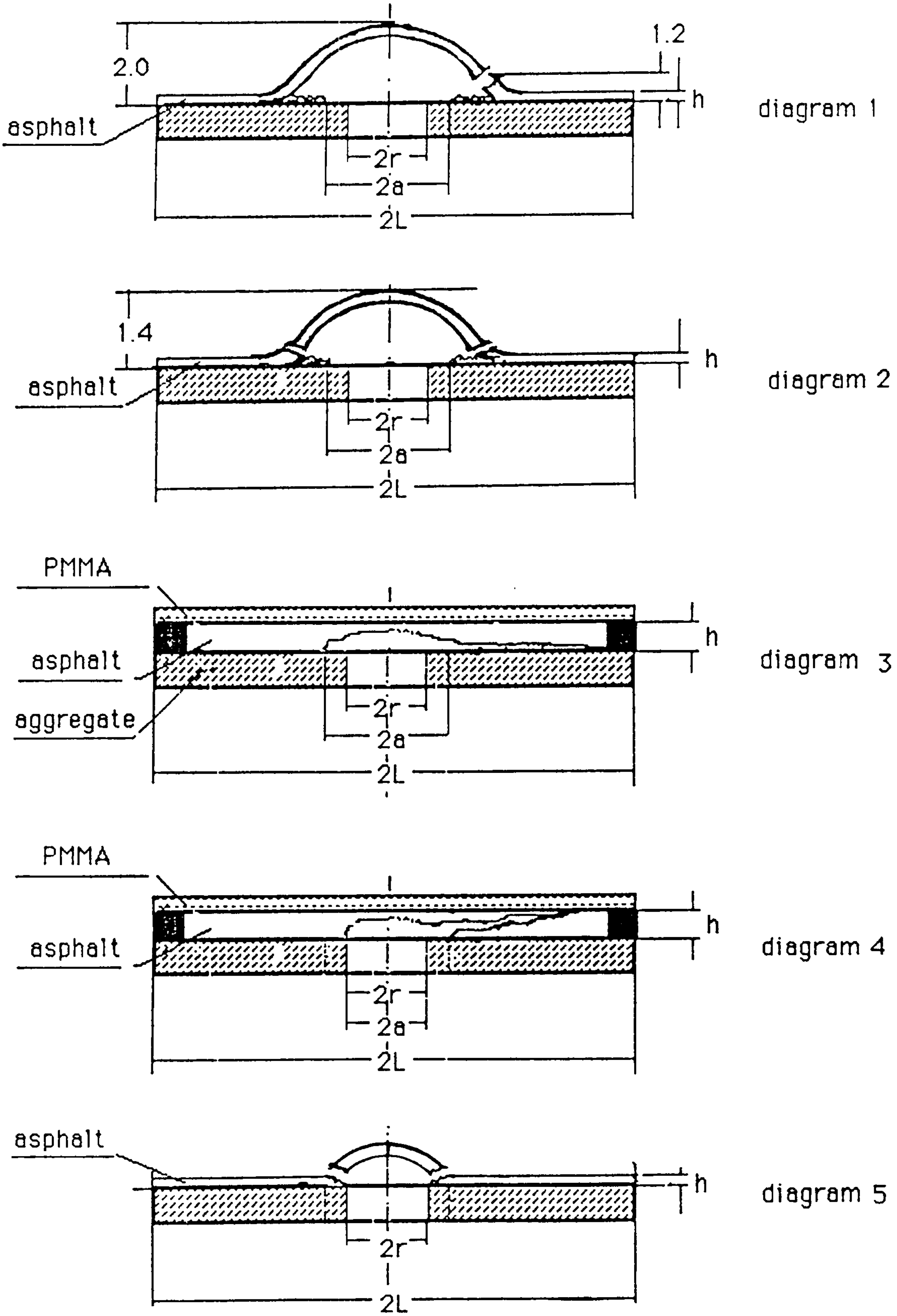

Figure 7.2: Diagram 1 - 5 for fracture analysis.

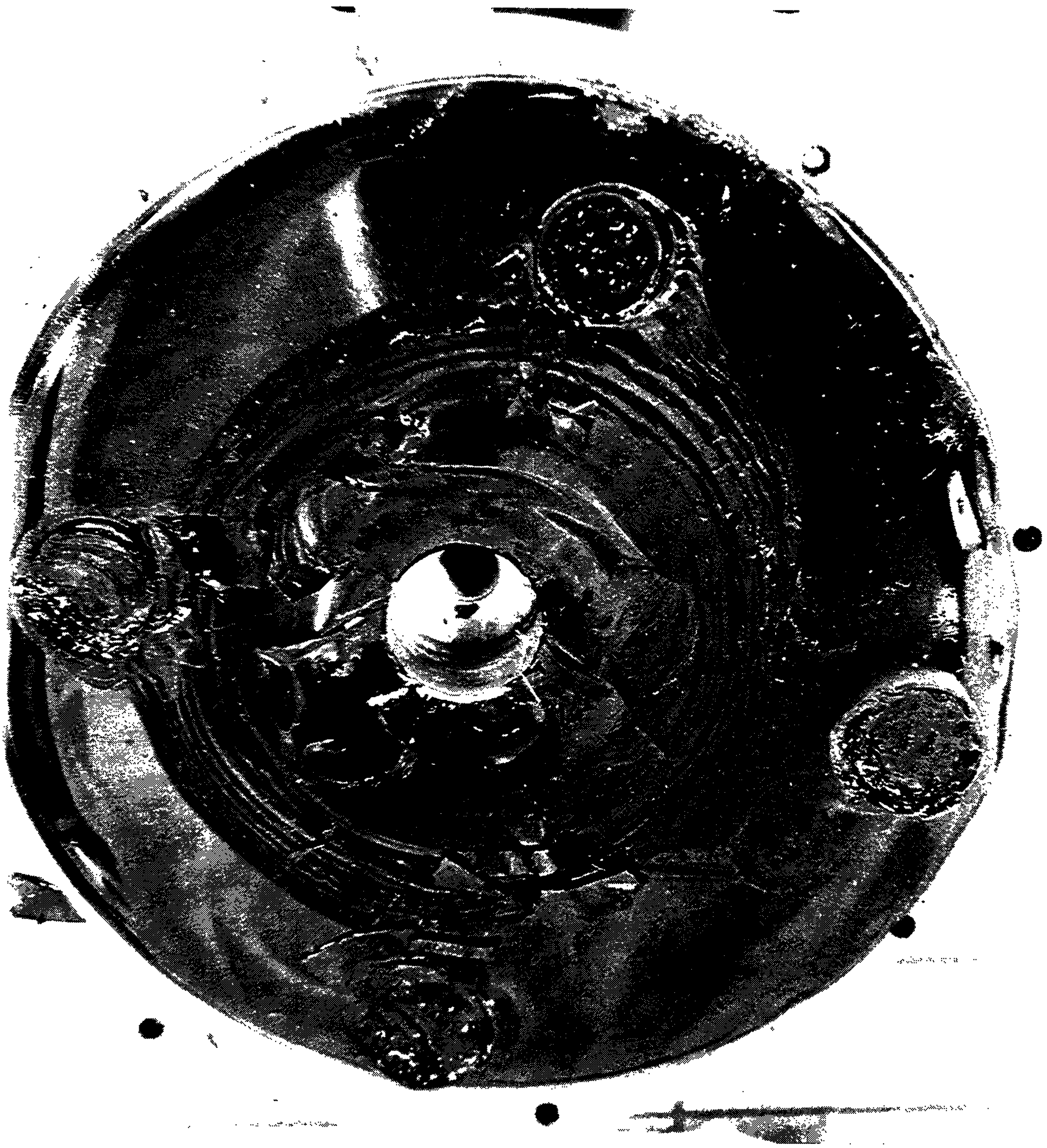

Figure 7.3: The blister test fracture surface of aluminum-AAG system, with failure taking place in the bulk asphalt at the tip of predebonded area.

Figure 7.4: The blister test fracture surface of granite-AAG system, with failure first propagating near the bondline in the asphalt phase and eventual rupture in the bulk asphalt.

Figure 7.5: The blister test fracture surface of a modified specimen of aggregate-AAK system, with adhesive failure taking place along the interface.

Figure 7.6: The blister test fracture surface of modified specimen of Teflon-AAK system, with failure taking place in the bulk asphalt.

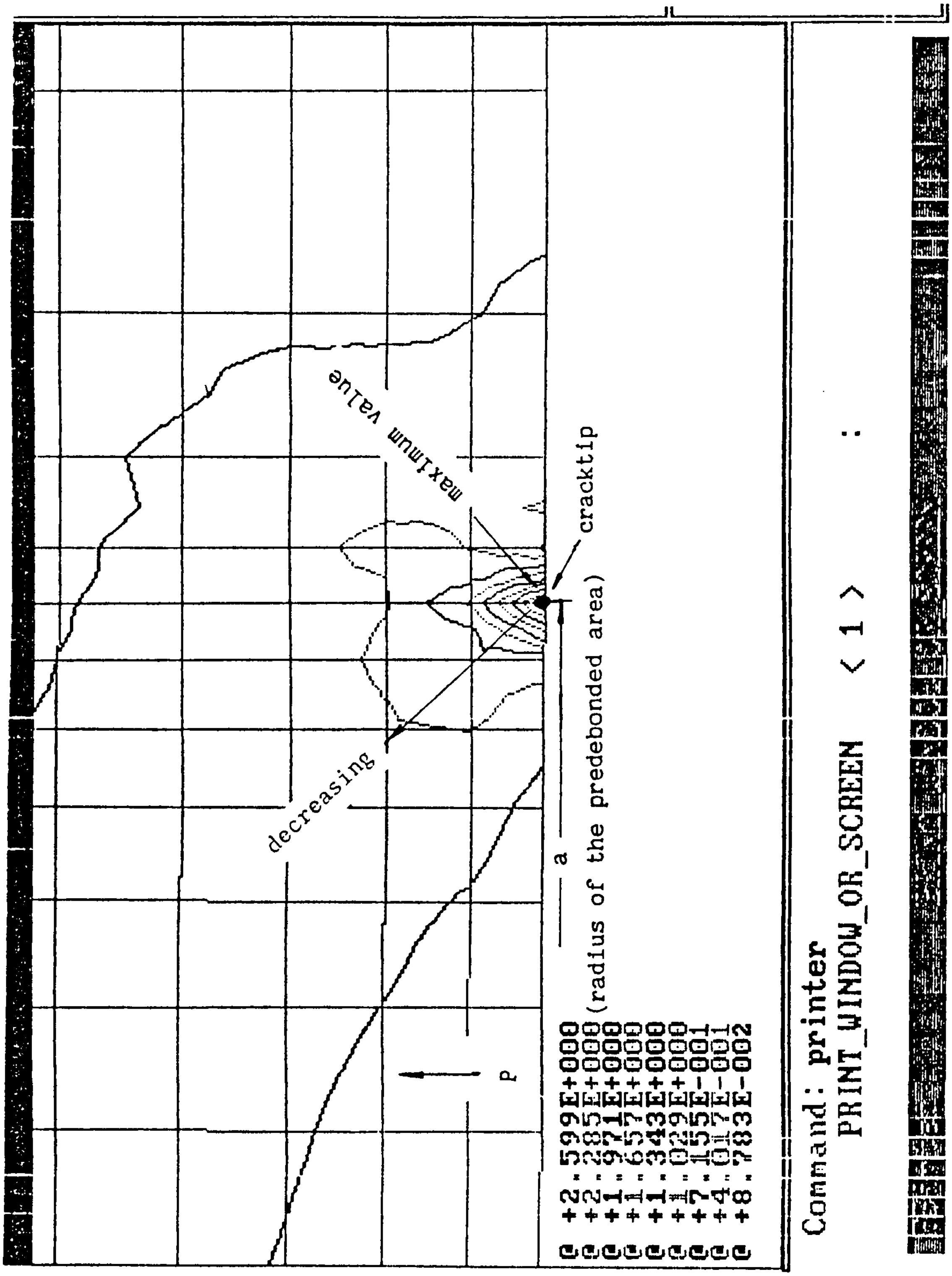

```
Command: printer
  PRINT_WINDOW_OR_SCREEN   < 1 >   :
```

Figure 7.7: Stress distribution for the blister test at the onset of pressure loading.

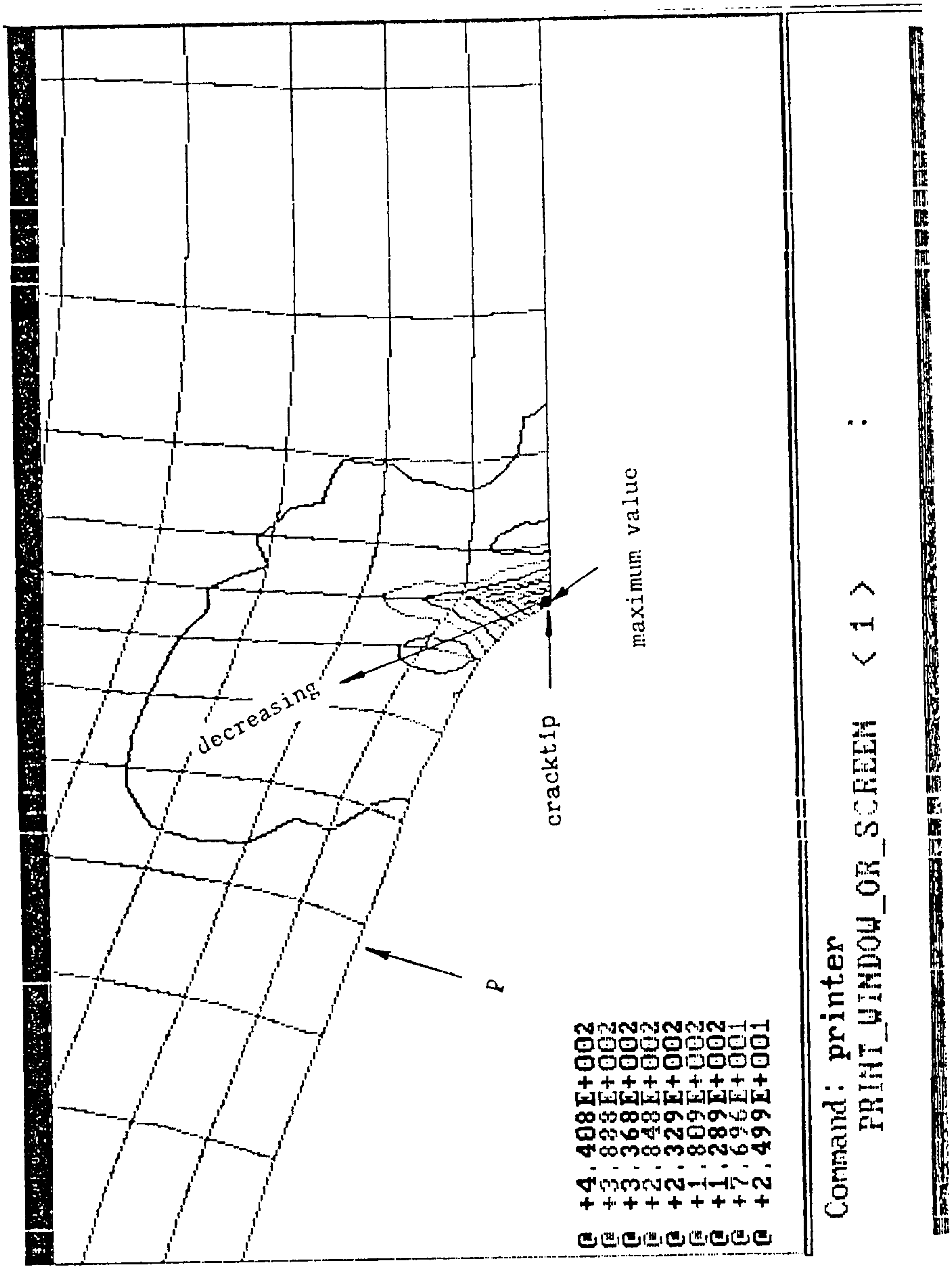

```
Command: printer
PRINT_WINDOW_OR_SCREEN < 1 > :
```

Figure 7.8: Stress distribution for the blister test during pressure loading failure occurring at the cracktip.

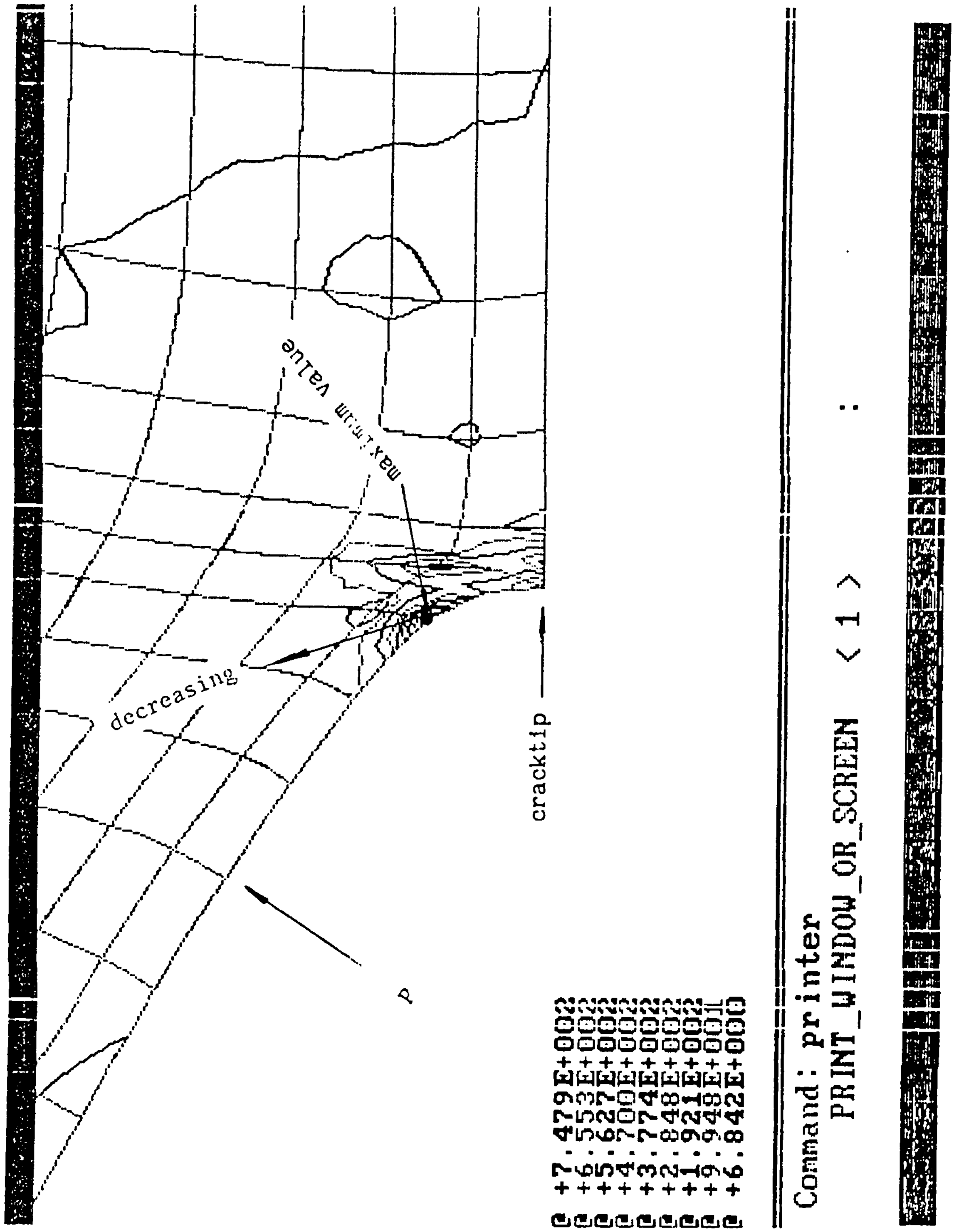

```
Command: printer
   PRINT_WINDOW_OR_SCREEN  < 1 >  :
```

Figure 7.9: Stress distribution for the blister test during pressure loading failure occurring at a certain position on the blister.

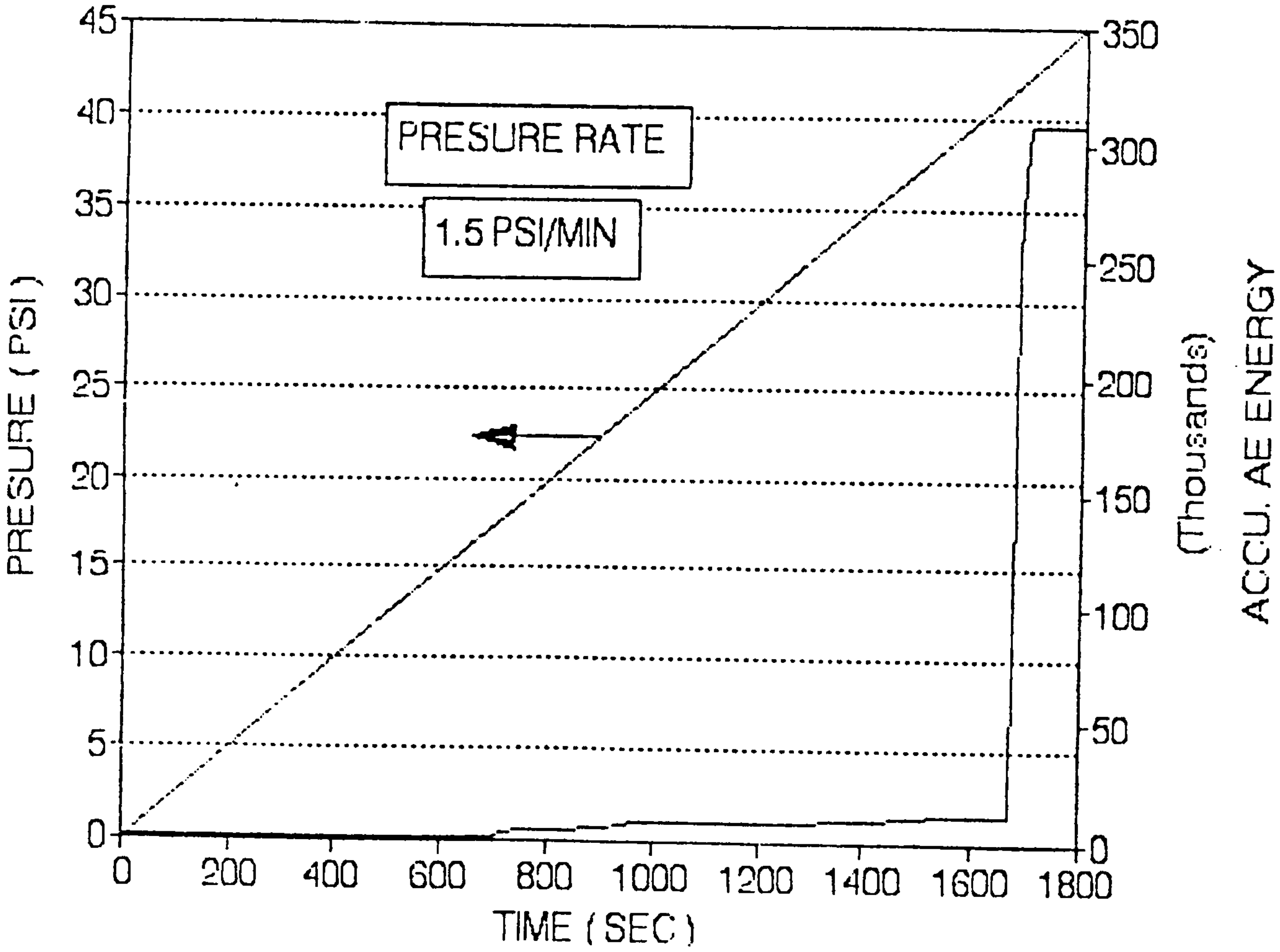

Figure 7.10: The AE output signals corresponding to the pressure imposed in blister test.

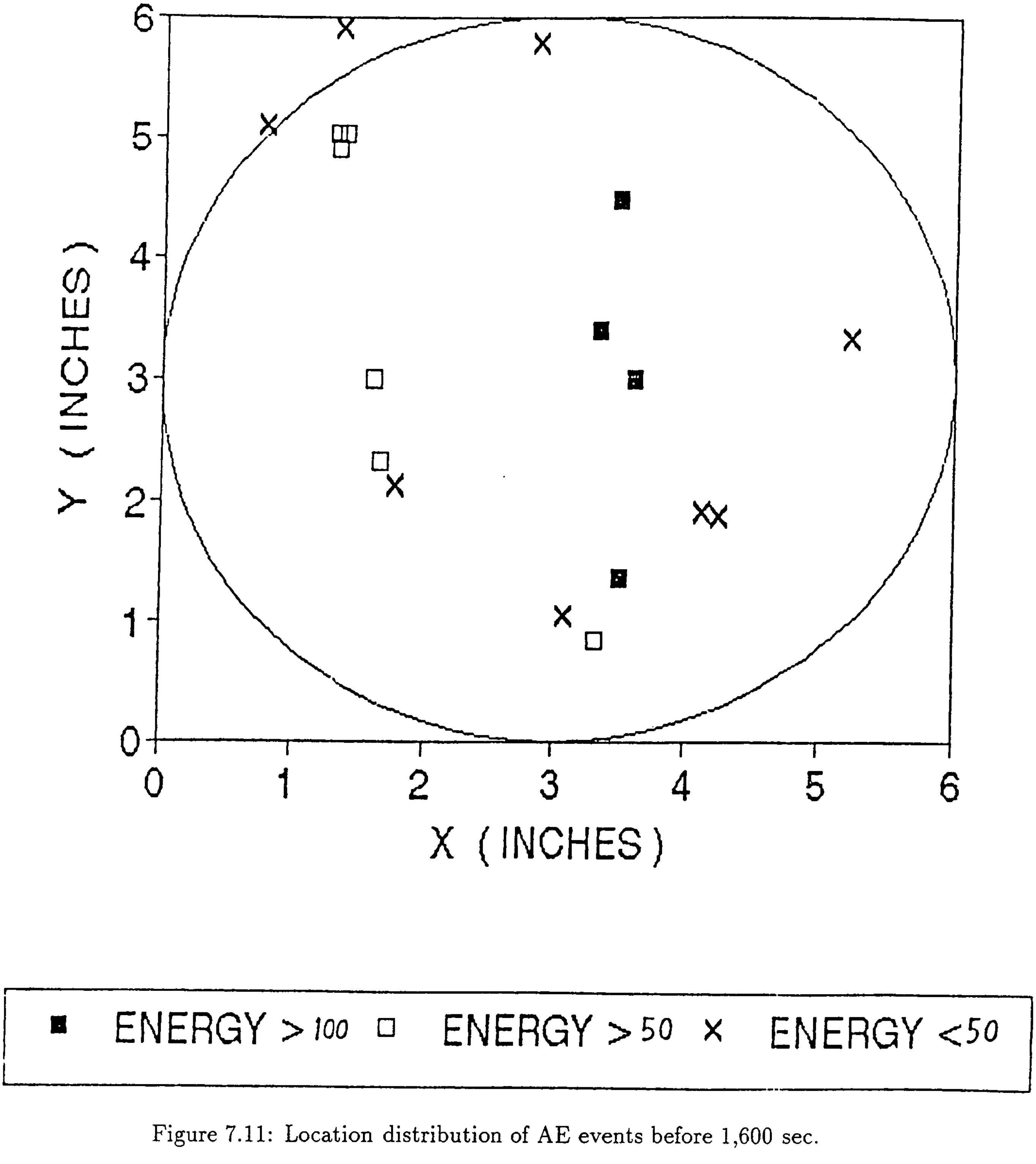

Figure 7.11: Location distribution of AE events before 1,600 sec.

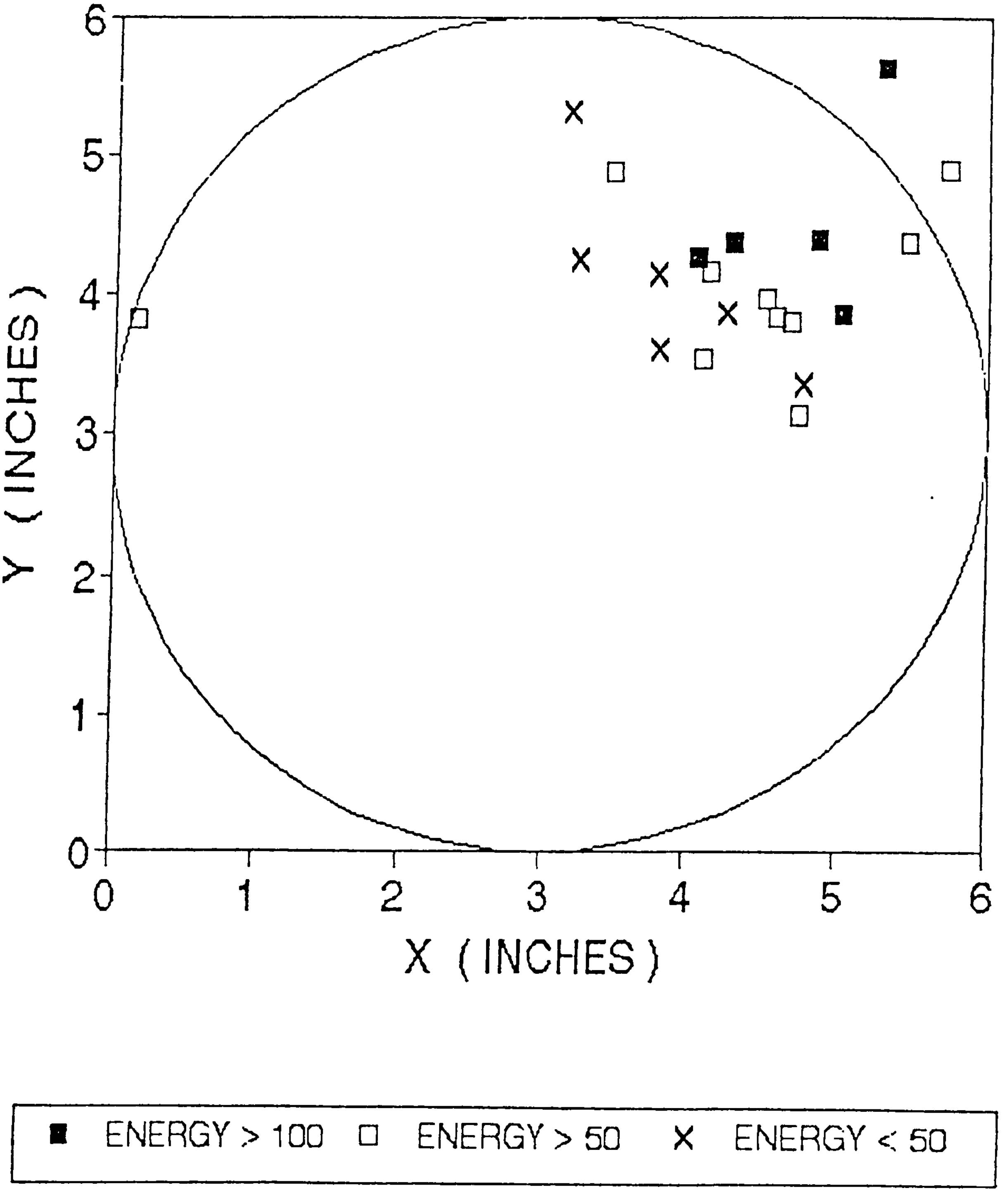

Figure 7.12: Location distribution of AE events aftere 1,600 sec.

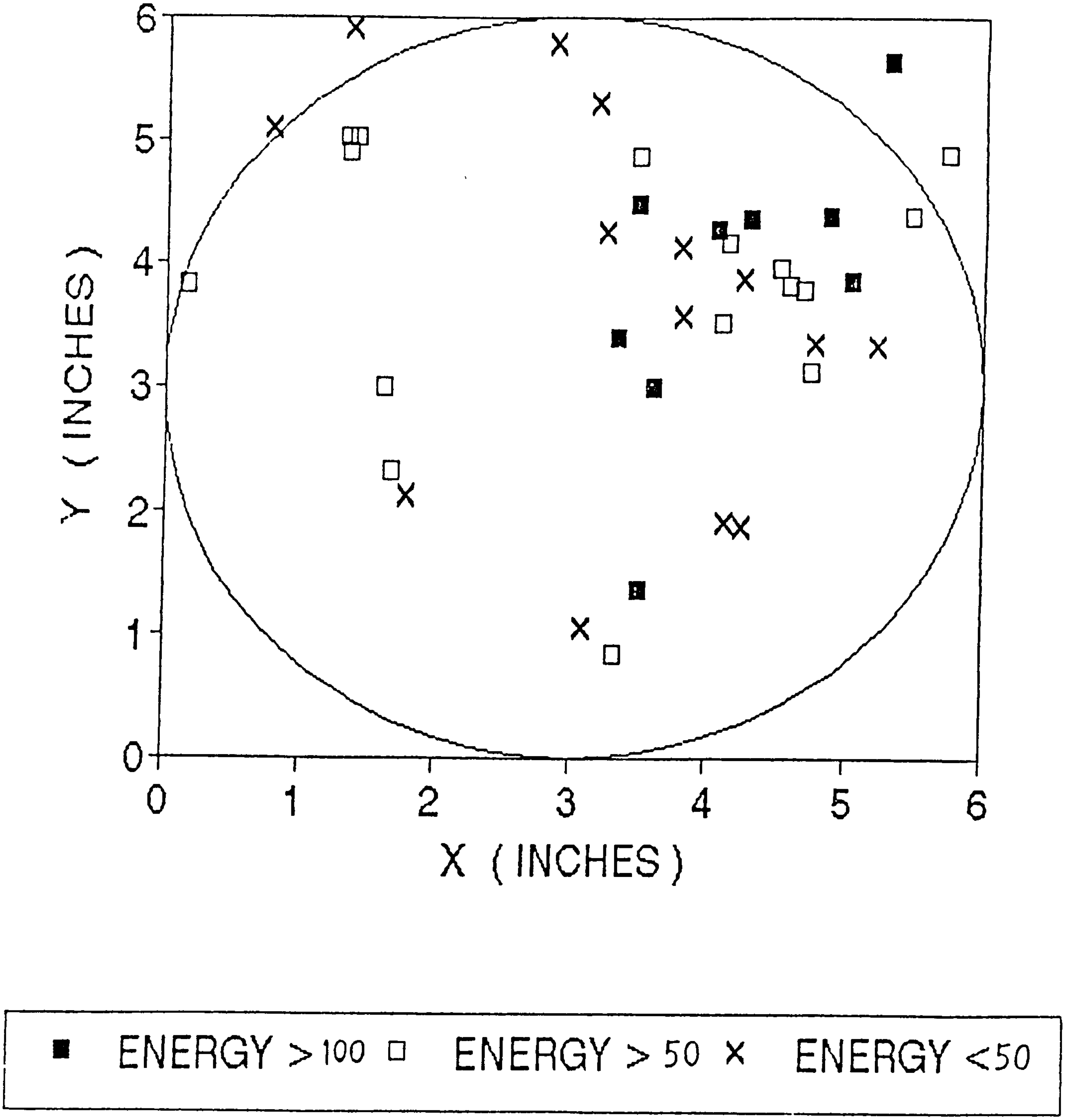

Figure 7.13: The overall location distribution of AE events in blister test.

References

1. R. L. Patrick. ed. *A Treatise on Adhesion and Adhesives. 1 and 2* Marcel Dekker, New York, 1969.
2. G. P. Anderson, S. J. Bennett and K L. DeVries, *Analysis & Testing of Adhesive Bonds*, Academic Press, New York, 1977.
3. W. V. Chang and S. Peng "Nonlinear Elastic Analysis of Adhesive Blister Test", *International Journal of Fracture* **53** 77 (1992); also Chapter 9 of this report.
4. S. J. Bennett, K. L. Devries and M. L. Williams "Adhesive Fracture Mechnics", *International Journal of Fracture* **10**(1) (1974).
5. R. L. Terrel and J. W. Shute, *Summary Report on Water Sensitivity*, SHRP-A-304, Oregon State University, 1989.

Chapter 8

Nonlinear Finite Element Analysis of the Poker Chip Testing

8.1 Introduction

Adhesives exist mainly in thin-film form in practical applications. Frequently, the joints are subjected to tensile loadings, even though an experienced design engineer would prefer to avoid it.

Butt-joint tests are designed to evaluate the tensile and compressive behavior of an adhesive joint. The mechanical behavior of a butt-joint specimen is also of great importance to many industrial applications, such as elastomer mountings, cushioning, and flexible couplings. A butt-joint specimen could fail either cohesively or adhesively, depending on the strengths of the material and the stress distribution in the specimen.

The butt-joint specimen analyzed in this paper is an elastomer layer bonded between two rigid circular plates (Figure 8.1). A specimen of this type was called "poker chip" by Williams and his associates at Caltech.[1] They employed the test to study the effect of triaxial stress states on solid propellants. They reported cavitation in elastomers when specimens are subjected to tensile loadings.[1,2] Similar observations were reported earlier by Yerzley[3], and Gent and Lindley[4] on elastomers, and by Mack[5] on asphalt. The load-extension curve for butt-joint specimens of rubber-like materials usually shows a distinct yield stress before rupture. Gent[4,6] investigated the internal rupture of bonded rubber specimens and pointed out that a critical value of hydrostatic pressure exists at which the failure of the rubber layer takes place. Chang and his associates[7,8] used the poker chip test to simulate highly filled vulcanizates. Both systems show similar characteristics of distinct yield point, stress softening, and cavitation when subjected to uniaxial tension. They suggested that the mechanical behavior of both the poker chip specimen and filled vulcanizates are strongly related to the cavitation process. An elaborate testing system measuring both acoustic emission in and mechanical response of butt joint specimens was established to monitor the cavitation process in elastomer[9-13] and asphalts.[14-17]

To predict the performance of a butt joint, such as its stiffness, strength, fatigue strength, healing ability, and the dependence of all these properties on bondline thickness, void content, etc., requires in-depth understanding of stress distributions and microfracture processes. Most of the previous analyses of butt-joint tests were restricted to linear elastic analysis.[18-31]

Klingbeil and Shield[32] conducted a theoretical nonlinear analysis assuming the material to be incompressible and to have the neo-Hookean or Mooney type strain energy density function. Two postulates were made in their analysis: (1) Material planes initially normal to the direction of loading remain plane in the deformed state, (2) the boundary condition of zero surface traction on the free surface is replaceable by the approximate boundary condition of vanishing force and moment resultants on every portion of the free surface. The effects of these postulates on the large-deformation behavior of a thin joint have not been thoroughly examined. Recently, Dymnikov[33] and his associates presented a nonlinear analysis based on the minimization of the additional work during loading. They modified the isotropic Hookean equation by allowing both the shear and the bulk moduli to be functions of volume dilatation. However, their model did not take into proper account the nonlinear stress-strain behavior typical of elastomers.

No elastomer is truly incompressible, although many are nearly incompressible with Poisson's ratios between 0.49 to 0.4998.[34] The assumption of incompressibility significantly simplifies the theoretical analysis and gives good approximate solutions to many problems. However, for the poker chip geometry, this assumption may result in significant errors. This chapter presents a computer analysis that takes into account both the nonlinear elastic characteristics and the compressibility of materials.

8.2 Finite Element Analysis

The material was assumed to be nonlinear elastic and described by the Ogden-Tschoegl strain energy function,[35-37] which can be expressed as

$$W = \sum_{k=1}^{m} \mu_k(\lambda_1^{n_k} + \lambda_2^{n_k} + \lambda_3^{n_k} - 3)/n_k, \tag{8.1}$$

where the λ_j's define the principal stretches and μ_k, n_k are material constants.

The 3-term Ogden-Tschoegl strain energy function was proven successful in describing the large-deformation behavior up to rupture for natural rubber vulcanizates.[37] A one-term Ogden-Tschoegl equation is adequate if the maximal stretch ratio is less than 3.[35,36] Introduction of the Ogden-Tschoegl strain energy function into the Boltzmann superposition integral allows accurate prediction of the viscoelastic behavior of rubberlike materials.[38-42] The exponent n_k is a measure of the strain-hardening effect. Taking a simple tension experiment as an example, the stiffness of the material decreases with increasing stretch ratio, λ, if n_k is between 0 and 1. For a material with n_k larger than 1, there is a well defined stretch ratio, before which the stiffness increases with elongation and beyond which the stiffness decreases with elongation. The dependence of n_k on the nature of the material, crosslink density, temperature, and crosslinking conditions was examined by Chang et al.[40,42] In uncrosslinked materials, n_k was found to be small (typically about 0.5) and sensibily independent of temperature if the temperature is above the glass transition temperature.

The above strain energy function assumes that the material is incompressible. The mixed finite element method[47,48] is frequently used to analyze the stress distribution in incompressible materials. The method treats the displacements and the hydrostatic degrees of freedom as the unknown variables. Hence, it greatly increases the number of equations. Moreover, no material is truly incompressible. Therefore, we use the penalty finite element method in this study. This method treats the material as nearly incompressible and uses only the displacements as the independent variables. In fact, the introduction of the penalty function is equivalent to modifying the strain energy function from absolutely incompressible type to nearly incompressible type. In this chapter, the strain energy function is modified by adding another term to the above function to describe the bulk modulus of the material. The bulk term W_b can take the form

$$W_b = -\int_1^J P dJ, \tag{8.2}$$

where J is the ratio of the deformed volume over the original undeformed volume and P is an arbitrary pressure function. The following pressure function is chosen based on both theoretical considerations and experimental results:[37]

$$P = -\lambda(J^{-1} - J^{-10})/9, \tag{8.3}$$

where λ is Lame's constant.

The modified Ogden-Tschoegl strain functions can then be expressed by

$$W = \sum_{k=1}^{m} \mu_k[(\lambda_1^{n_k} + \lambda_2^{n_k} + \lambda_3^{n_k} - 3)/n_k - \ln J] + \lambda(9 \ln J + J^{-9} - 1)/81, \tag{8.4}$$

where the first $\ln J$ is introduced to ensure that the stresses calculated from the strain energy function are zero at the undeformed state.

Both one-term and three-term functions are used in this study. Values of n_k ranging from 0.2 to 8 were used in the one-term study to investigate the effect of the strain-hardening parameter on the stress distribution in a poker chip specimen. A three-term function is used with the following material constants[36] to simulate the behavior of a typical vulcanized natural rubber

$$\mu_{1,2,3} = 0.618, \quad 0.001245, \quad -0.00982 \text{ MPa};$$
$$\mathrm{n}_{1,2,3} = 1.3, \quad 5.0, \quad -2.0.$$

In the case of infinitesimal strains, the material defined above can be treated as linear elastic with the shear modulus $G = 0.4146$ MPa. The μ_i values in equation (8.4) were assumed to be constants. Lame's constant λ was determined based on the different incompressibility assumed. The following equation was used to relate Poisson's ratio ν and Lame's constant λ:

$$\lambda = 2G\nu/(1-2\nu). \tag{8.5}$$

The relation between the λ and the bulk modulus K is

$$\lambda = 3K\nu/(1+\nu). \tag{8.6}$$

The assumed Poisson's ratio ranges from 0.45 to 0.49932.

The finite element axisymmetric formulation for each material is based on the total Lagrangian procedure.[13,43] The deduction of stresses and elastic moduli as a function of the principal stretches were referred to in Ogden's book.[37] The regular Newton-Raphson method[43] was used in the nonlinear iteration. The axisymmetric element codes for this kind of hyperelastic material is linked with a commercial finite element package, AFEM.[44]

8.3 Numerical Experiments and Discussion

8.3.1 Finite Element Model

Figure 8.1 shows the cross-section of the poker chip geometry. The shadowed area is the section studied. Figure 8.2 (a) shows the discretization and the boundary condition of the finite element model. The loading on the elastomer specimen was a prescribed boundary condition, (PBC), that is, a prescribed boundary displacement $w_z = \Delta h$ at $y = h$. An axisymmetric state was assumed. In effect, we assume that the plates to which the elastomer disk is bonded are rigid.

The nominal stress, σ_n, in Figure 8.1 is simply defined as the applied load, F, divided by the interface area. The nominal strain, ϵ_n, is defined as

$$\epsilon_n = \Delta h/h, \tag{8.7}$$

where h is half of the rubber layer thickness. The apparent modulus, E_a, is used to relate the nominal stress and the nominal strain:

$$\sigma_n = E_a\,\epsilon_n. \tag{8.8}$$

The finite element discretization of the problem is also shown in Figure 8.2 (a). Figure 8.2 (b) is an example of the deformed shape. The elements are nine-node axisymmetric elements. In order to get the accurate stress and strain distributions, the effect of the mesh size on the results was carefully checked. The stresses at the interesting locations, the apparent modulus, and the lateral contraction, calculated for a certain number of elements, were compared with the results calculated for double that number of elements until the relative deviation between them was less than 1%. The effect of the arrangement of elements was also checked. The mesh near the lateral is finer than the mesh near the axis (Figure 8.2). This is because the stress is quite stable near the center and varies a lot near the edge.

8.3.2 Stress Distribution

8.3.2.1 Three-term Ogden-Tschoegl Model

The stress distributions were obtained for the three-term Ogden-Tschoegl material with a shear modulus of 0.4146 MPa and different Poisson's ratios and different aspect ratios. The aspect ratio is defined as $R/4h$, where R and h are the radius and half of the thickness of the specimen, respectively. The apparent modulus of the specimen was calculated as a function of both the nominal strain and the aspect ratio. The lateral contraction was also obtained and discussed.

When the bonded end-plates of poker chip specimens are separated, the free surface at the edge will contract. The extent of this lateral contraction depends on the effective Poisson's ratio of the material. Edge distortions produce a significant alteration of the stress distribution for a distance of up to a few elastomer layer thicknesses from the edge if the deformation is infinitesimal. Volume changes, which depend on Poisson's ratios of materials and aspect ratios of specimens, affect the stress throughout the whole specimen. The stress distributions in incompressible poker chip specimens of high aspect ratios can be estimated by lubrication theory.[19,21] Equations based on lubrication theory are given in Table 8.1.

Figure 8.3 shows the stress distribution along the interface, that is, the upper boundary ($z = h$) in Figure 8.2 (a). The nominal strain ϵ_n is 0.005, and the aspect ratio S is 15. All the stresses are expressed as the dimensionless ratio over the Young's modulus E. The nominal strain is so small that the same results can also be obtained by linear calculation. The three normal stresses, σ_{zz}, σ_{rr}, and $\sigma_{\theta\theta}$, have almost the same values and the same distributions. The three normal stresses peak at the center and decrease almost parabolically towards the edge. The shear stress τ_{rz} is relatively small. Except for the shear stress, all the other stresses on the middle plane are almost the same as the corresponding stresses at $r = h$ (Figure 8.4). The shear stress τ_{rz} at $z = 0$ theoretically should be zero. The stresses calculated near the edge ($r = R$) are not as accurate as the stresses in other portions of the specimen because of the singularity near the edge of the interface ($r = R$ and $z = h$). The consistency of the three normal stresses and the negligible shear stress demonstrate that a highly hydrostatic state is generated. The hydrostatic pressure (the negative mean stress) varies over radius r and the thickness $2h$.

Although the stress distribution as shown in Figure 8.3 agrees qualitatively with the prediction of lubrication theory,[19,21], they differ in quantitative prediction. For example, the calculated values for $\sigma_{zz}(0,h)/E\epsilon$ and $\sigma_{zz}(0,h)/\tau_{rz}(R,h)$ are, respectively, 2.16 and 16.3, but the corresponding values based on the lubrication theory are 9.00 and 30. This suggests that at S=15, a material with a Poisson's ratio as high as 0.49932 cannot even be considered as incompressible. In fact, as is discussed in a separate paper[45] the applicability of lubrication theory to the design of elastomeric butt joints is very limited.

The stress distribution in a specimen with aspect ratio $S = 1$ is shown in Figure 8.5. Now σ_{zz} is about 50% higher than σ_{rr} and $\sigma_{\theta\theta}$. When $S = 15$ and Poisson's ratio $\nu = 0.45$, the σ_{zz} is about 20% higher than the two other normal stresses (Figure 6). It demonstrates that the smaller the aspect ratio or the larger the Poisson's ratio, the closer the system is to the hydrostatic pressure state.

The octahedral stress τ_0 was proposed to determine the extent of how close the system is to the pure hydrostatic state. By the definition[46], τ_0 can be evaluated by

$$\tau_0{}^2 = 2/3\, J_2 = 1/9\,[(\sigma_{zz} - \sigma_{rr})^2 + (\sigma_{zz} - \sigma_{\theta\theta})^2 + (\sigma_{rr} - \sigma_{\theta\theta})^2] + \sigma_{rz}{}^2 + \sigma_{r\theta}{}^2 + \sigma_{z\theta}{}^2, \quad (8.9)$$

where J_2 is the second invariant of the stress deviation.

The octahedral stress τ_0 is equal to zero in a state of pure hydrostatic pressure. The more the extent of the system deviates from a pure hydrostatic state, the larger is the octahedral stress. It is more appropriate to use the ratio of the octahedral stress over the mean stress, τ_0/σ_0, as a quantitative parameter, where the mean stress σ_0 is defined as

$$\sigma_0 = -P = (\sigma_{zz} + \sigma_{rr} + \sigma_{\theta\theta})/3, \quad (8.10)$$

where P is the hydrostatic pressure.

Figures 8.7 and 8.8 show τ_0/σ_0 distributions for various aspect ratios and various Poisson's ratios, where the mean stress is evaulated at the center ($r = 0, z = 0$). The distributions of the relative octahedral stresses are almost uniform in most ranges of radius r, except near the edge. Furthermore, the results suggest that the stresses in the poker chip specimen approach a hydrostatic state as the aspect ratio or Poisson's ratio increases. Figure 8.9 shows the axial stress distribution on the middle plane for specimens with S=15 and different Poisson's ratios. Figure 8.10 is a similar plot showing the effect of aspect ratios.

The stress distributions discussed so far are all obtained from a case of using very small strain, $\epsilon_n = 0.005$, where nonlinear effects are negligible. The stress distribution along the middle plane ($r = 0$) for a larger nominal strain, $\epsilon_n = 0.29$, is plotted in Figure 8.11.

The values and the distribution of three normal stresses are almost the same, and the shear stress is small, still showing a near hydrostatic state. Figure 8.12 shows the axial stress distribution over the middle plane for various nominal strains. The load-bearing capability of this material increases as the strain increases. The shear stresses not shown are negligibly small.

Figures 8.9, 8.10 and 8.12 show that the normal stresses in the center become progressively flatter as Poisson's ratio decreases, the aspect ratio increases, and the nominal strain increases. This suggests that the effective Poisson's ratio of this material decreases with increasing strain. This is probably due to the strain-hardening nature of this material, meaning that the incremental shear modulus increases with strain. Since the bulk modulus is practically constant, the effective Poisson's ratio decreases with the strain.

8.3.2.2 Effect of the Strain-Hardening Parameter

To further investigate this hypothesis, we conducted a numerical analysis on materials of the same shear modulus but with different strain-hardening parameters. To clearly show the effect of the strain-hardening parameter, the one-parameter Ogden-Tschoegl equation was used. Figure 8.13 presents the effect of nominal strain on the bond-plane axial stress distribution for a nearly incompressible (Poisson's ratio of 0.49932) uncrosslinked elastomer (with the stress-hardening parameter; $n_k = 0.4$). The vertical axis is the axial stress normalized by the corresponding maximal stress that appears at the center of the disk. The horizontal axis is a normalized radius (radial coordinate divided by joint radius). The maximal stress first increases with the apparent strain and then decreases after reaching the maximum. Furthermore, the stress distributions at different strains are very different; the stress decays more rapidly with the radius as the strain increases. It suggests that the effective Poisson's ratio of the material increases with the nominal strain because the incremental shear modulus decreases with the strain for this strain-softening material.

Similar plots for materials with higher strain hardening parameters are given in Figures 8.14 ($n_k = 1.3$) and 8.15 ($n_k = 8$). The case of $n_k = 1.3$ represents a moderately cured elastomer and the case of $n_k = 8$ is a hypothetical, highly stretched or highly oriented material. As shown in Figure 8.14, the maximal stresses increase with strain over the strain range analyzed (up to a strain of 0.29). Contrary to the uncrosslinked elastomer, the stress decays more slowly with the radius as the strain increases. Figure 8.15 shows that the peak stresses for $n_k = 8$ are only slightly higher than those for $n_k = 1.3$; however, the axial stress distribution is more uniform than that for $n_k = 1.3$. The effect of Poisson's ratio is illustrated in Figure 8.16, where the stress distribution in a high- density foam of uncrosslinked elastomer (Poisson's ratio = 0.495) is given. The stress distribution is more uniform than that in Figure 8.13. In light of the result shown in Figure 8.16, Figure 8.15 may be interpreted as if the effective Poisson's ratio of this material decreases from 0.49932 at infinitesimal deformation to about 0.495 at a nominal strain of 0.15. Numerical results for materials of small n_k at large deformations are sensitive to mesh size. Therefore, more elements are used for the case of $n_k = 0.4$ than for the other cases.

8.3.3 Nominal Stress and Apparent Modulus

8.3.3.1 Three-term Ogden-Tschoegl Model

In the adhesive butt-joint test, the applied load F is the most important quantity to be measured. The nominal stress σ_n, which is defined as applied load divided by the interface area, can be easily obtained in experiments. In the finite element analysis, the applied load F is calculated by integrating the σ_z distribution over the interface ($z = h$).

Figures 8.17 and 8.18 show the dimensionless nominal stress σ_n/E and dimensionless apparent modulus E_a/E as a function of the nominal strain for various Poisson's ratios. The dimensionless apparent modulus E_a/E decreases as the nominal strain increases due to the nonlinear effects. The dependence of the apparent modulus on the Poisson's ratio is due to the difference in bulk moduli. Because of the build-up of the triaxial stress within the poker chip specimen, the apparent modulus depends on the bulk modulus.

The geometric effect on the apparent modulus has been studied by Gent et al.[21] for incompressible materials under small extension. They obtained the relation

$$E_a/E = 1 + 2S^2, \tag{8.11}$$

where S is the aspect ratio defined by $R/4h$.

The relations between the relative apparent moduli and the aspect ratio at different strains are illustrated in Figure 8.19. The relative apparent moduli for larger nominal strains are lower than those for smaller nominal strain, due to the nonlinearity involved in the large deformation.

The curve for the small strain ($\epsilon_n = 0.005$) approaches the relation described by equation 8.11 when the aspect ratio decreases. There are significant deviations for large aspect ratios, say, $S > 3.75$. These deviations are due to the difference in bulk moduli between two cases. The bulk modulus in equation 7.11 is theoretically infinite because of the assumption of incompressibility. However, for any real material the bulk modulus is finite, and its value is related to its Poisson's ratio. As the aspect ratio increases, the extent of the hydrostatic state increases and so does the contribution of the bulk modulus to the apparent modulus. Therefore, the deviation from equation 8.11 becomes more pronounced. The effect of finite bulk modulus on the apparent stiffness of a butt-joint subjected to an infinitesimal deformation has been well studied.[1,21,22,29] Our results agree well with the theoretical analysis of Lindsay et al. for cases of $S > 5$. For $S < 3$, our calculations agree better with the approximate equations of Gent and Lindley.[21]

The lateral contraction on the middle plane ($z = 0, r = R$) is another important quantity that is measureable in the test. Figure 20 shows the lateral contraction U_0 as a function of the nominal strain. Compared to the relative apparent modulus in Figure 8.16, there is little nonlinear effect on the lateral contraction. The almost linear relation in Figure 8.20 may be used as an additional means to estimate nominal strain. This relation can also be used to estimate the Possion's ratio if the nominal strain is independently measured in the experiment.

Some numerical experiments were conducted to find the stress distribution and apparent modulus for specimens of nonuniform thickness caused by either the nonparallel rigid plates or the eccentric extension rods. This is no longer an axisymmetric problem. The plane strain state is assumed to conduct the analysis. The nominal strain is calculated at the center of the specimen. The stress distribution is different from what is calculated under the normal axisymmetrical conditions. Higher than normal stresses are observed in thinner locations and lower than normal stresses in thicker locations. However, they compensate each other; consequently, there was a very small change in the apparent modulus (less than 1%) when the $\Delta h/h$ varies from zero (parallel) to as much as 45% through the nominal strain up to 0.30, where Δh is the difference of thicknesses of the two edges in this case.

8.3.3.2 One-term Ogden-Tschoegl Model

A distinctly different nominal stress-strain behavior was observed for stress-softening materials. Figure 8.21 summarizes simulation results for materials, with $n_k = 0.4$ and different Poisson's ratios. Notice that for nearly incompressible stress-softening materials there exists a well-defined peak load beyond which a joint will fail. The strain where the peak load (or the instability) occurs, increases with the value of n_k. This instability was also observed by Klingbeil and Shield[31] in the neo-Hookean and the Mooney materials, but their peaks happen at nominal strains about 0.3 to 0.4, much higher than what is observed here.

The existence of the peak load is a direct consequence of the stress distribution in such materials, which has been discussed in section 8.3.2.2. The load-bearing capability of a joint increases with the shape factor of the joint (Figure 8.22). The strain, where the peak load locates, first decreases and then increases with increasing S. For example, the peak strains increase from 0.065 for S=15 to 0.011 for S=75. This is qualitatively consistent with our recent experimental results on asphalts,[14] even though the asphalts are viscoelastic liquids at the test conditions. Does a joint in tension behave similar as to one in compression? Yes, according to linear analysis, but no, according to the more accurate nonlinear analysis (Figure 8.23).

Computer simulation also allows monitoring of deformed profiles. As shown in Figures 8.24 and 8.25, the lateral surface contracts as the joint is stretched. A material with a low Poisson's ratio contracts less than one with a Poisson's ratio close to 0.5 (incompressible). When the lateral surface contracts radially, the longitudinal material segment in the surface is subjected to a large extension. What prevents the material from contraction is the resistivity to tension of the material segment. For a material with a small n_k, the resistivity to further extension may decrease with the strain of the segment. When it reaches a critical value, the material element yields (or plastically deforms), which usually occurs near the bond plane. For a nearly incompressible material with a large shape factor, plastic deformation starts at very low nominal strain. As shown in Figure 8.24, it happens at a macroscopic strain between 0.06 and 0.08. When this plastic deformation happens, the lateral surface shows a Bingham-flow type of profile. This profile was observed in poker chip specimens of asphalts when they was subjected to a constant rate of displacement.[15]. As the Poisson's ratio decreases, the nominal strain of the joint at which flow starts increases (Figure 8.25). Figure 8.26 presents volume dilatation as a function of nominal strain for materials with different values of Poisson's ratio. The strains where the peak load, the peak dilatation, and the plastic deformation occur are almost identical, reflecting the fact that these phenomena all result from the same fundamental mechanism.

8.4 Conclusions

A nonlinear finite element analysis of butt joints that takes into account both the nonlinear elastic characteristics and compressibility of materials has been successfully carried out and the key conclusions are summarized here.

- A large hydrostatic stress state is generated in a butt-joint specimen. The magnitude depends on the shape factor, Poisson's ratio, and the nominal strain of the joint.
- Our calculations of the stiffness at infinitesimal deformations as a function of Poisson's ratio and the shape factor agree well with the theoretical analysis by Lindsey, Schappery, and Williams if the shape factor, S, is larger than 5. For cases of $S < 3$, our results agree better with the approximate equations by Gent and Lindley.
- The stiffness decreases with the nominal tensile strain, and this dependence is sensitive to the strain-softening characteristics of the material, which can be measured in terms of the one-term Ogden-Tschoegel equation.
- When a high-aspect-ratio such specimen of strain-softening materials as uncrosslinked elastomers is deformed, a well-defined peak load occurred at a critical strain, beyond which a seemly plastic deformation occurs near the junction of the free and fixed surfaces. Volume dilatation of the specimen decreases with further extension.
- The apparent higher stiffness in compression than in tension is explained by our nonlinear analysis.

ACKNOWLEDGMENTS

We would like to thank the Parker-Hannifin Foundation, Parker Seals Group, and the National Research Council-Strategic Highway Research Program for financially supporting this project. Dr. Ali Sarhangnezhad's assistance in linking our programs with FEM Engineering's finite element package (AFEM) is highly appreciated.

Table 8.1: Stress distributions are predicted by the lubrication theory.

$\sigma_{rr} = \sigma_{\theta\theta} = A - B/2$,	$\sigma_{zz} = A + B$
$A = 4S^2 E\epsilon[1 - (r/R)^2]$,	$B = E\epsilon[1 - (z/h)^2]$
$\tau_{rz} = 2E\epsilon S(r/R)(z/h)$,	$S = R/4h$
$\sigma_{zz}(O,h)/\tau_{rz}(R,h) = 2S$	

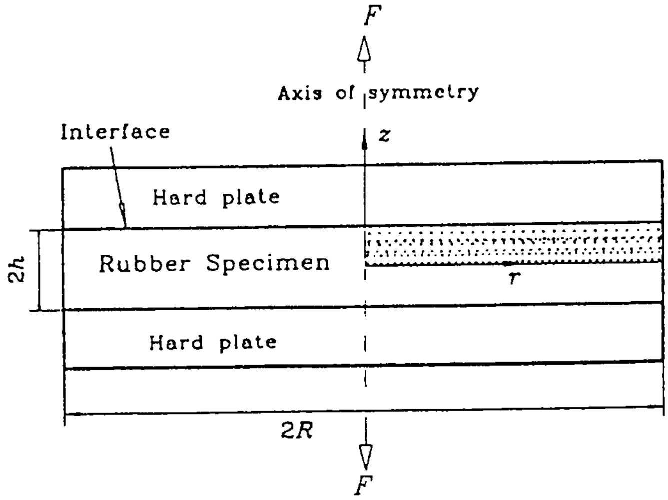

Figure 8.1: A sketch of poker chip geometry. The shadowed area represents the section studied.

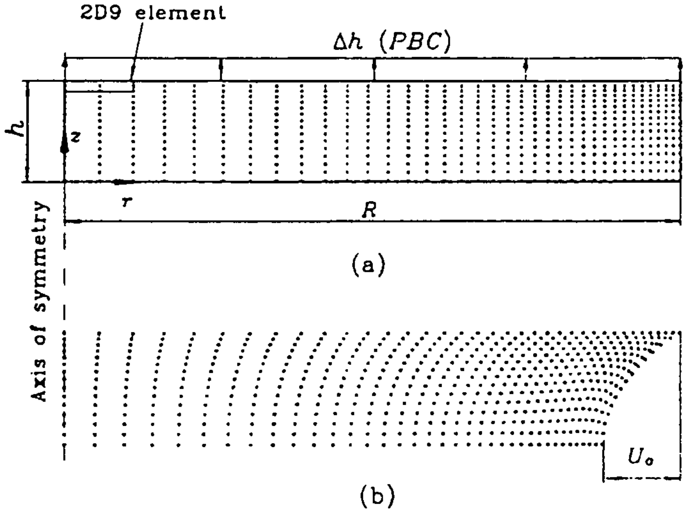

Figure 8.2: (a) Finite element model. (b) The deformed shape of a poker chip specimen.

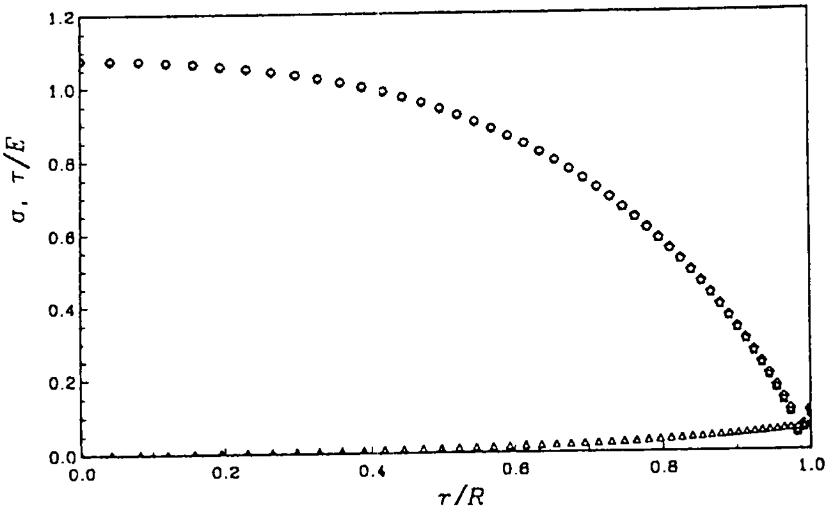

Figure 8.3: Stress distribution on the interface ($z = h$); $\circ, \sigma_z$; $\diamond, \sigma_r$; $\Box, \sigma_\theta$, $\triangle, \tau_{rz}$; $\nu = 0.49932$, $\epsilon_n = 0.005$, the aspect ratio $S = 15$.

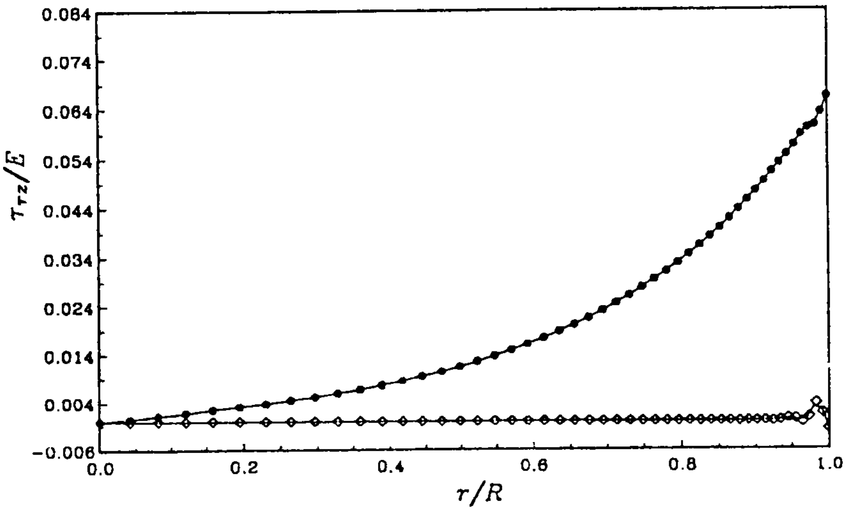

Figure 8.4: A comparison of shear stress distributions. $\circ$, on the interface; $\diamond$, on the middle plane, $\nu = 0.49932$, $\epsilon_n = 0.005$, $S = 15$.

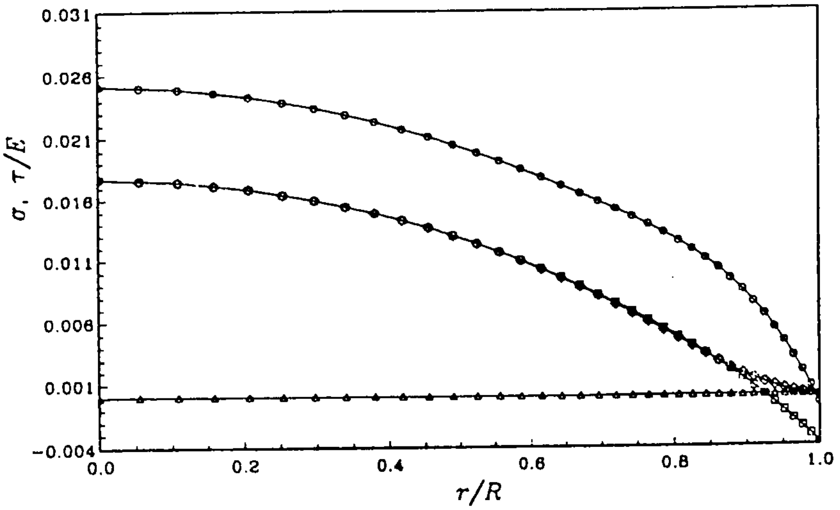

Figure 8.5: Stress distribution on the middle plane ($z = 0$). $\circ, \sigma_z$; $\diamond, \sigma_r$; $\square, \sigma_\theta$; $\triangle, \tau_{rz}$; $\nu = 0.49932$, $\epsilon_n = 0.005$, $S = 1$.

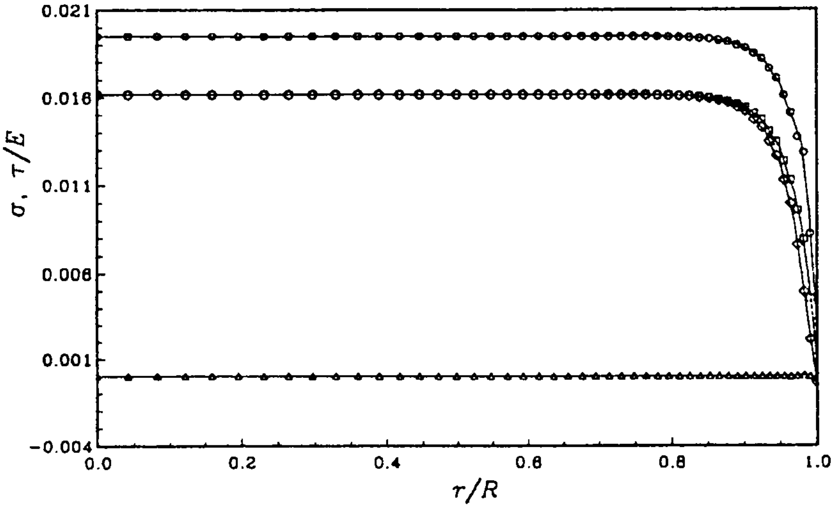

Figure 8.6: Stress distribution on the middle plane. $\circ, \sigma_z$; $\diamond, \sigma_r$; $\square, \sigma_\theta$; $\triangle, \tau_{rz}$; $\nu = 0.45$, $\epsilon_n = 0.005$, $S = 15$.

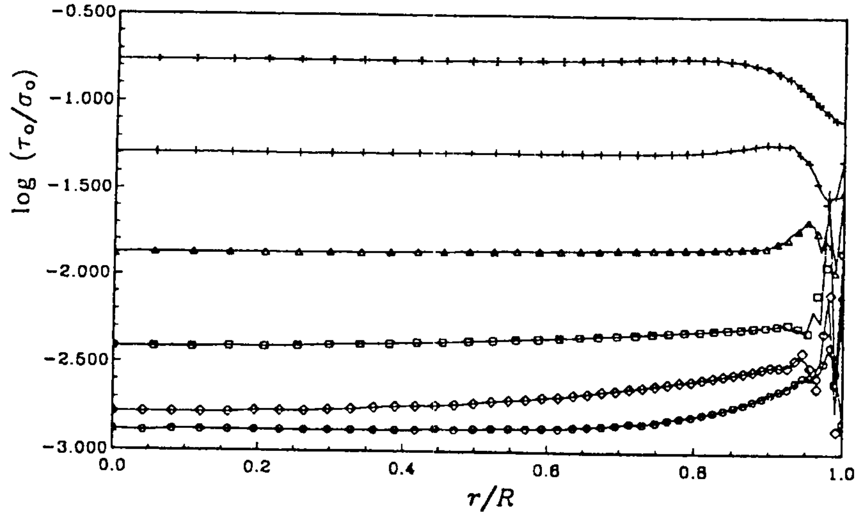

Figure 8.7: The (relative) octahedral stress distributions on the middle plane for different aspect ratios S, where σ_o is evaluated at the center ($r = 0, z = 0$). $S = 37.5(\circ)$, $15.0\text{in}(\diamond)$, $7.5(\square)$, $3.75(\triangle)$, $1.875(+)$, $1.0(\oplus)$; $\nu = 0.49932$, $\epsilon_n = 0.005$.

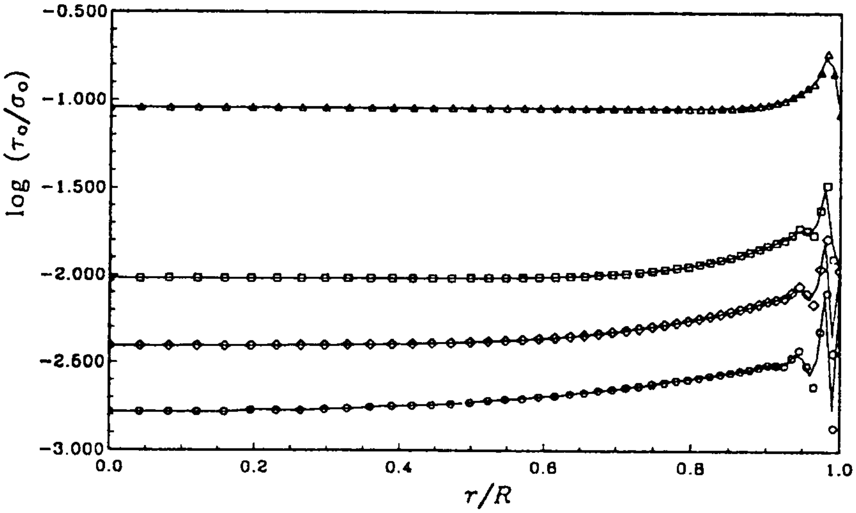

Figure 8.8: The (relative) octahedral stress distributions on the middle plane for different Poisson's ratios, where σ_o is evaluated at the center ($r = 0, z = 0$); $\nu = 0.49932(\circ)$, $0.498(\diamond)$, $0.495(\square)$, $0.45(\triangle)$; $\epsilon_n = 0.005$; $S = 15$.

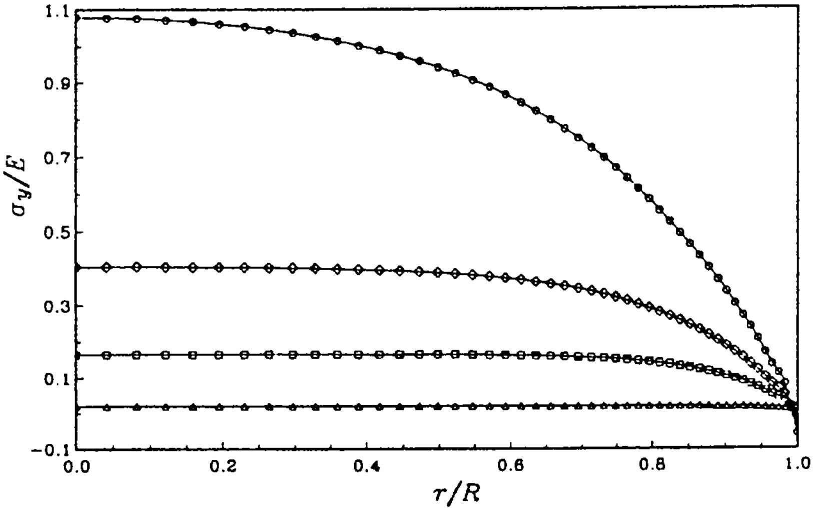

Figure 8.9: Axial stress distribution on the middle plane for different Poisson's ratios. $\nu = 0.49932(\circ)$, $0.498(\diamond)$, $0.495(\square)$, $0.45(\triangle)$; $\epsilon_n = 0.005$, $S = 15$.

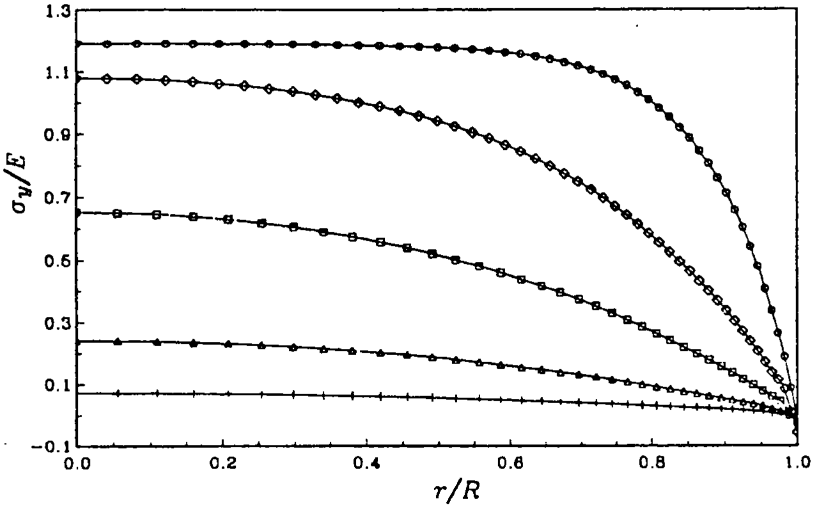

Figure 8.10: Axial stress distribution on the middle plane for different aspect ratios. $S = 37.5(\circ)$, $15.0\text{in}(\diamond)$, $7.5(\square)$, $3.75(\triangle)$, $1.875(+)$; $\nu = 0.49932$, $\epsilon_n = 0.005$.

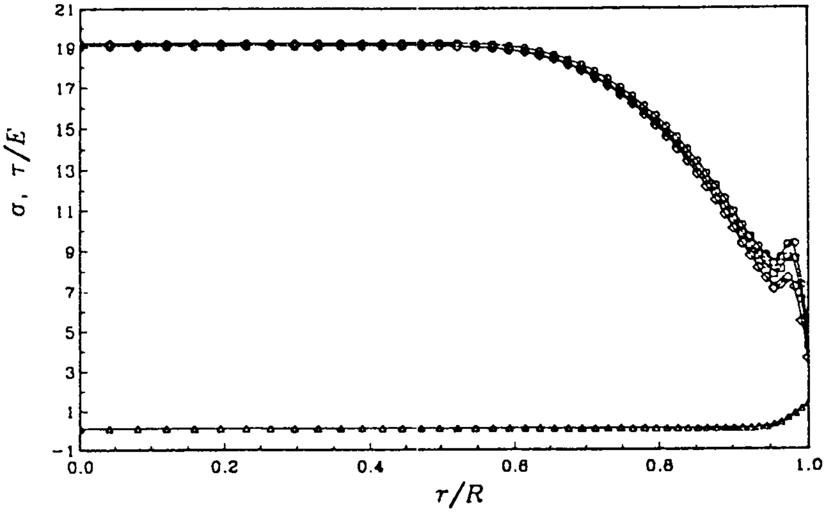

Figure 8.11: Stress distribution on the middle plane for large strain. $\circ, \sigma_z$; $\diamond, \sigma_r$; $\square, \sigma_\theta$; $\triangle, \tau_{rz}$; $\nu = 0.49932$, $\epsilon_n = 0.29$, $S = 15$.

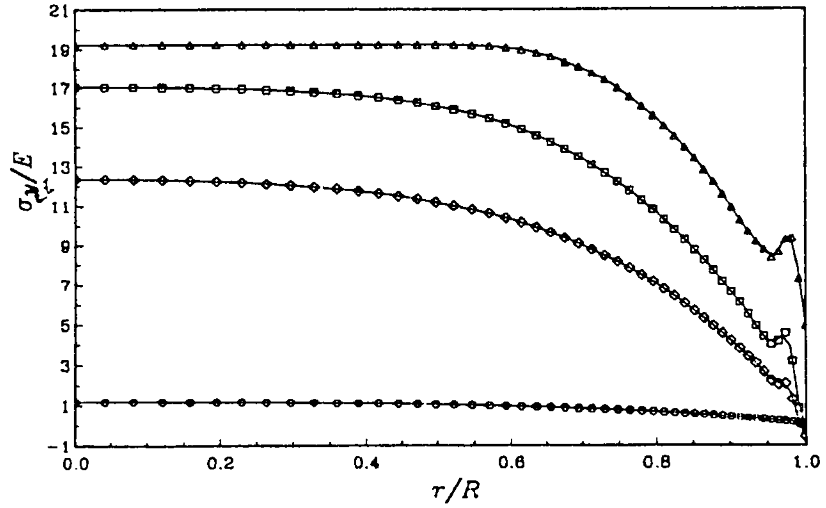

Figure 8.12: Axial stress distribution on the middle plane for different deformations. $\epsilon_n = 0.005(\circ), 0.08(\diamond), 0.15(\square), 0.29(\triangle)$; $\nu = 0.49932$, $S = 15$.

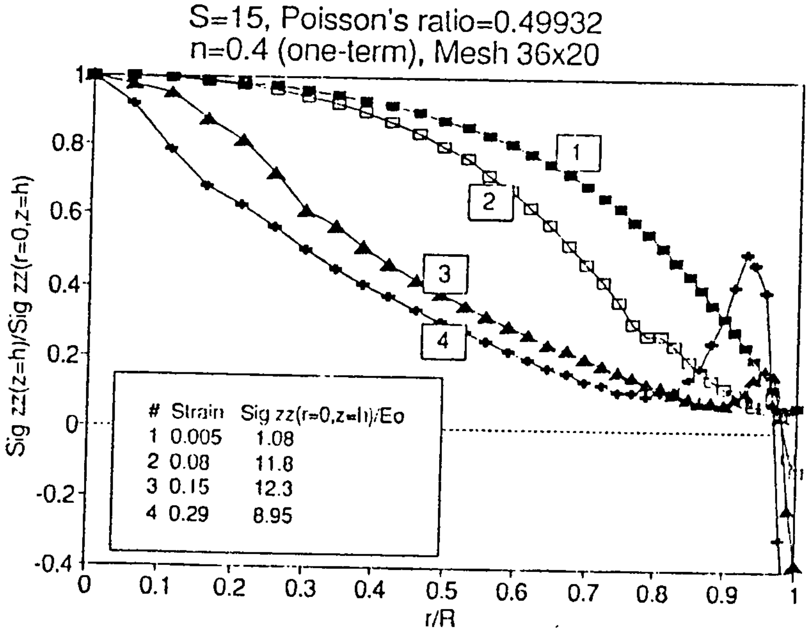

Figure 8.13: Axial stress distribution at the bond plane for a butt-joint specimen with n = 0.4 and Poisson's ratio of 0.49932, subjected to different apparent axial strains.

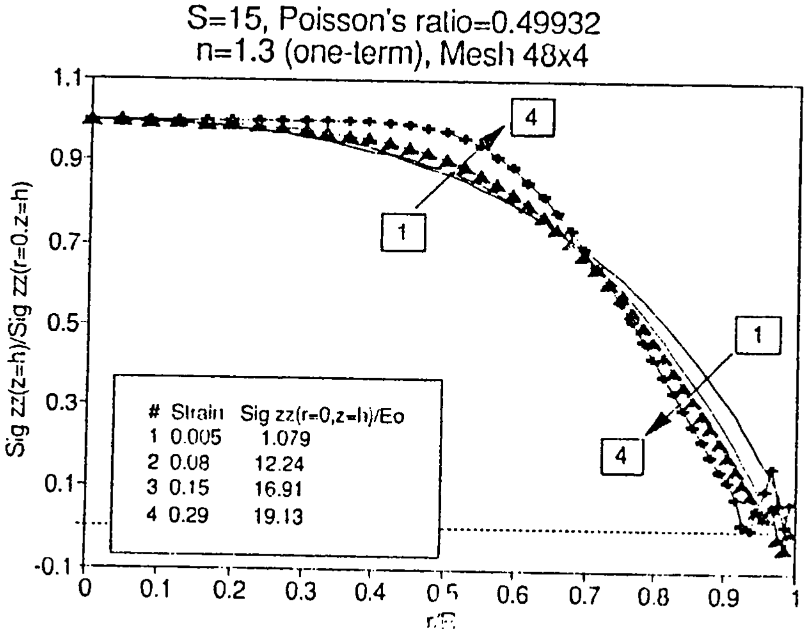

Figure 8.14: Axial stress distribution at the bond plane for a butt-joint specimen with n = 1.3 and Poisson's ratio of 0.49932, subjected to different apparent axial strains.

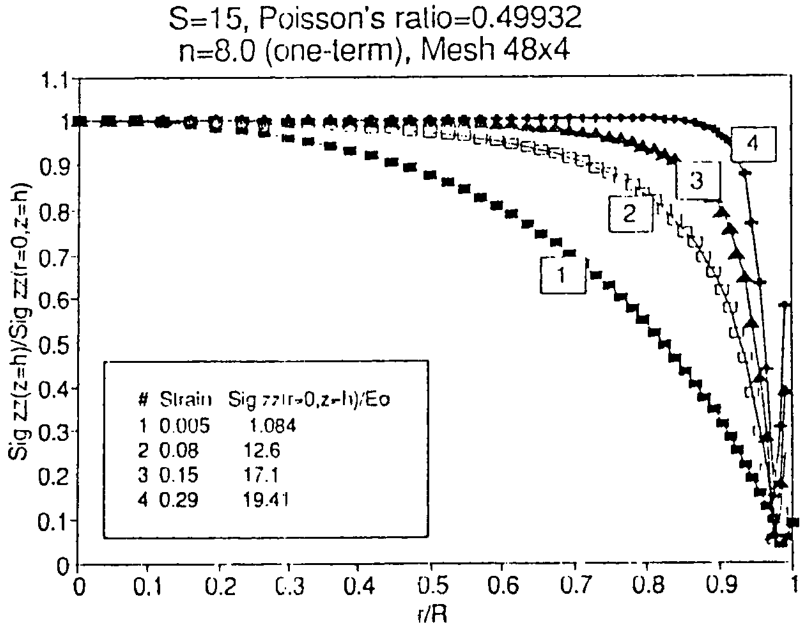

Figure 8.15: Axial stress distribution at the bond plane for a butt-joint specimen with n = 0.8 and Poisson's ratio of 0.49932, subjected to different apparent axial strains.

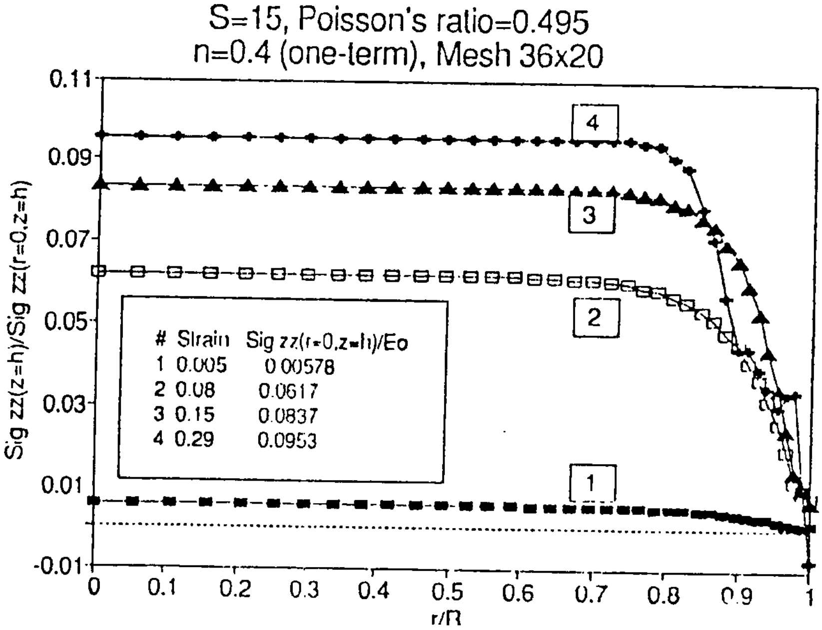

Figure 8.16: Axial stress distribution at the bond plane for a butt-joint specimen with n = 0.4 and Poisson's ratio of 0.495, subjected to different apparent axial strains. E_0 is the Young's modulus of the material.

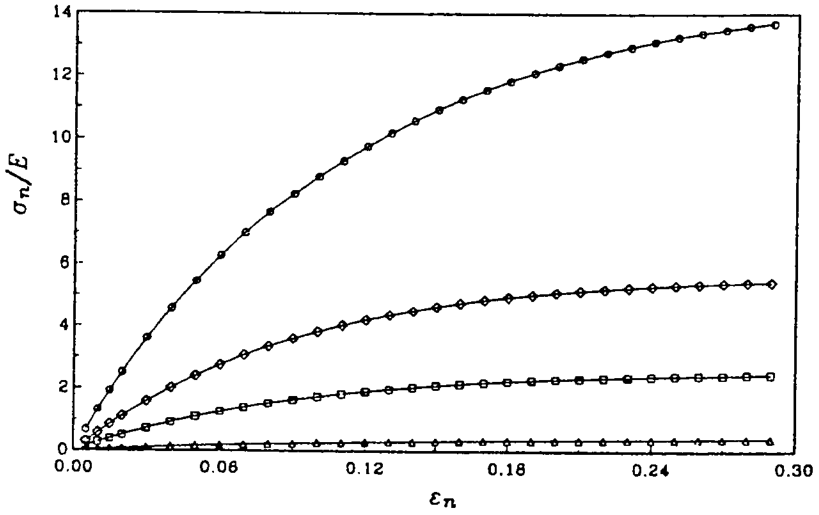

Figure 8.17: Nominal stress versus nominal strain. ν = 0.49932(○), 0.498(◇), 0.495(□), 0.45(△); $S = 15$.

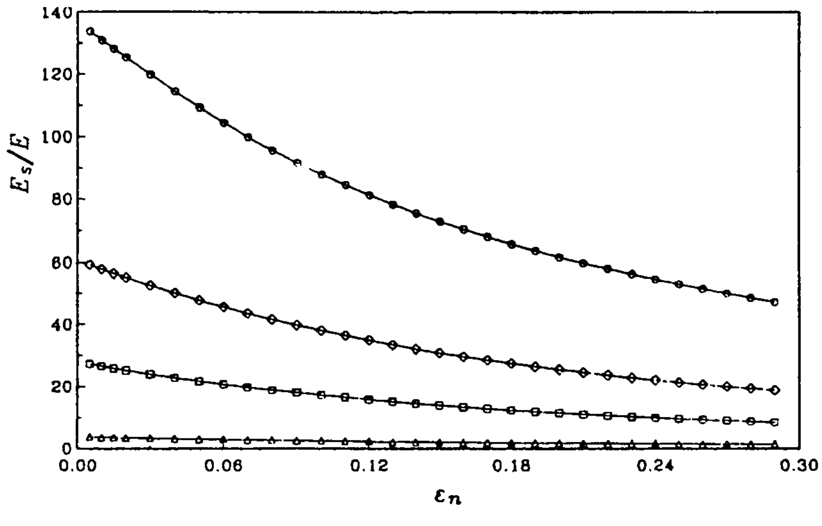

Figure 8.18: Apparent modulus (relative) versus nominal strain. ν = 0.49932(○), 0.498(◇), 0.495(□), 0.45(△); $S = 15$.

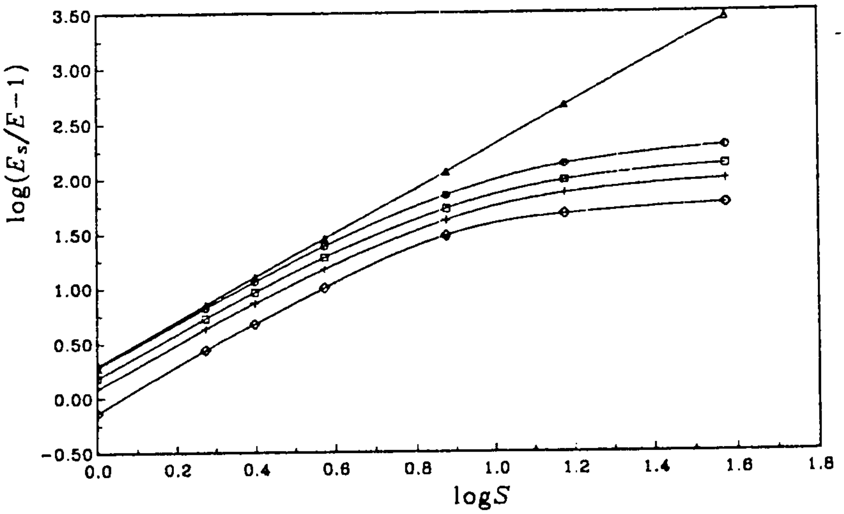

Figure 8.19: Apparent modulus versus nominal strain. $\epsilon_n = 0.005(\circ)$, $0.08(\Box)$, $0.15(+)$, $0.29(\diamond)$; $S = 15$, $\nu = 0.49932$. The straight line ($\triangle$) is defined by $E_s/E = 1 + 2S^2$.

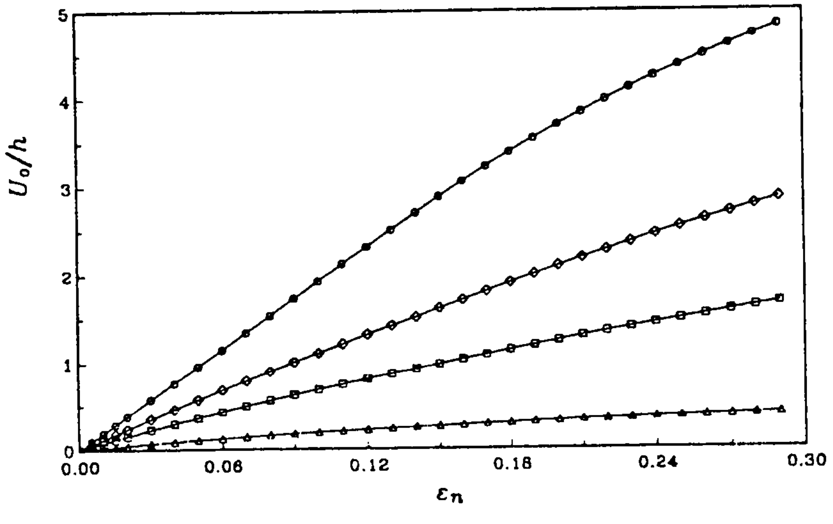

Figure 8.20: The center contraction as a function of nominal strain. $\nu = 0.49932(\circ)$, $0.498(\diamond)$, $0.495(\Box)$, $0.45(\triangle)$; $S = 15$.

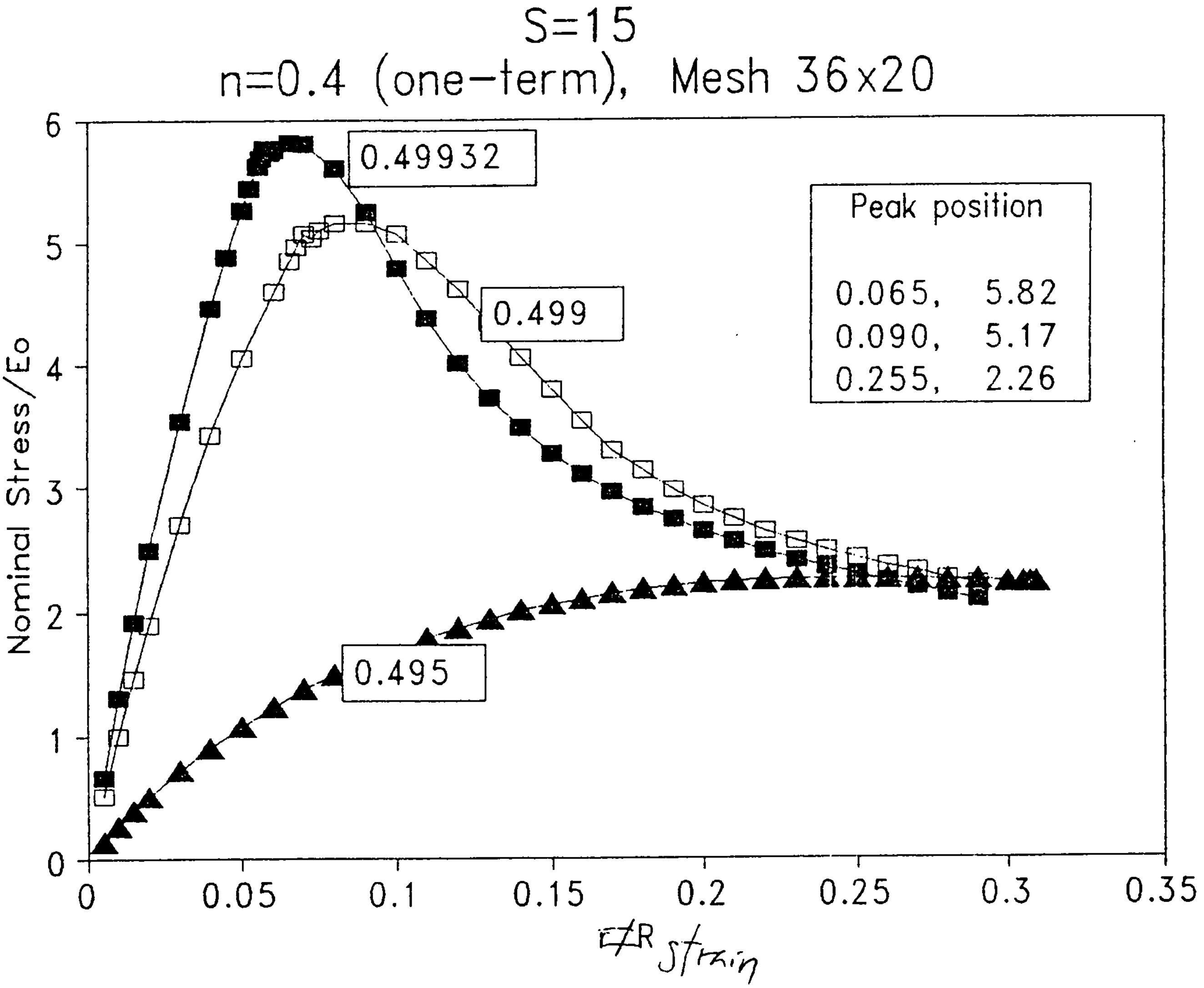

Figure 8.21: Effect of Poisson's ratio on the nominal stress-strain (or load-deformation) relations of butt joint. Nominal stress = $\frac{Load}{Area}$, strain = $\frac{Elongation}{Original\ Thickness}$.

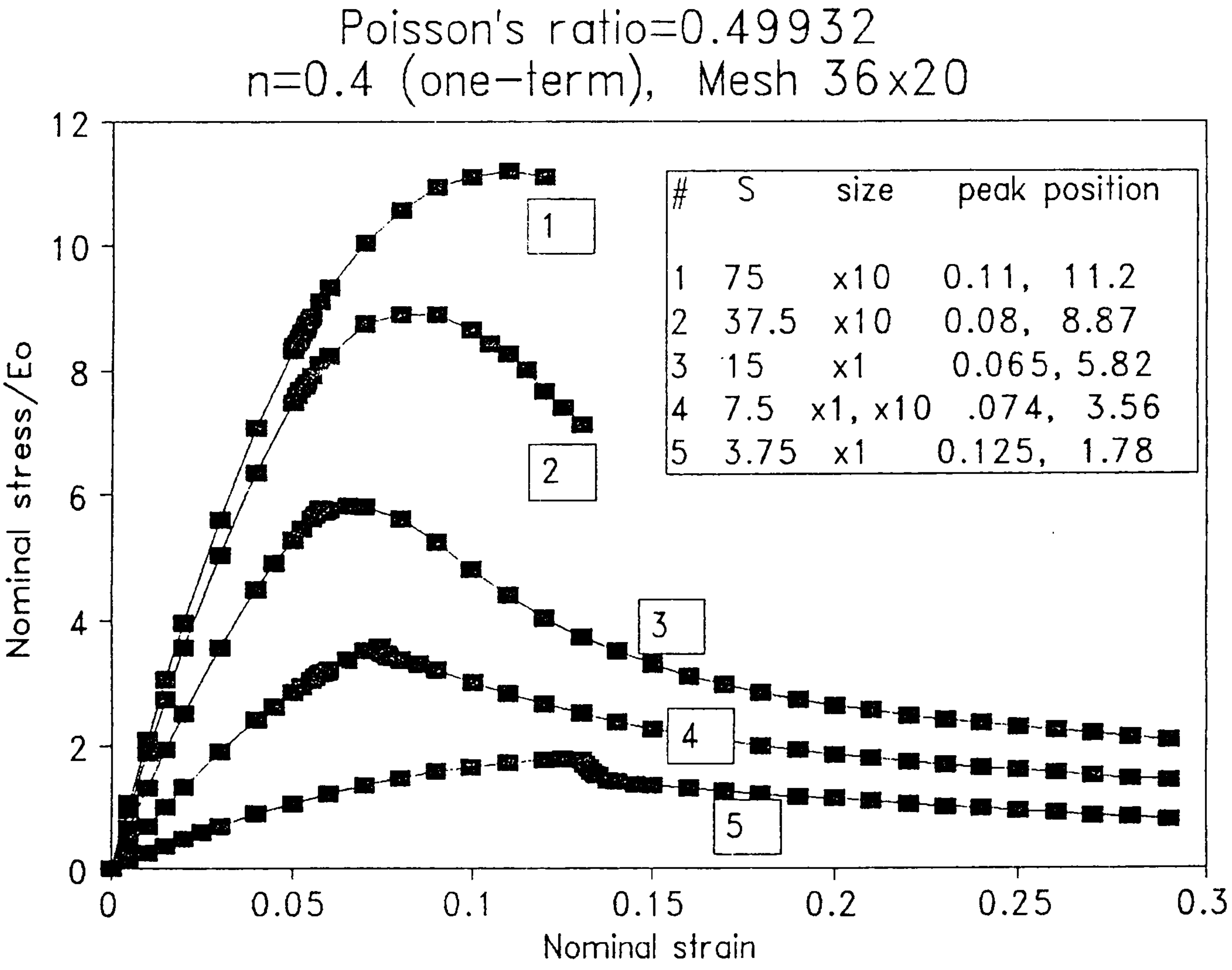

Figure 8.22: Effect of shape factor on the load-deformation relations of butt joints.

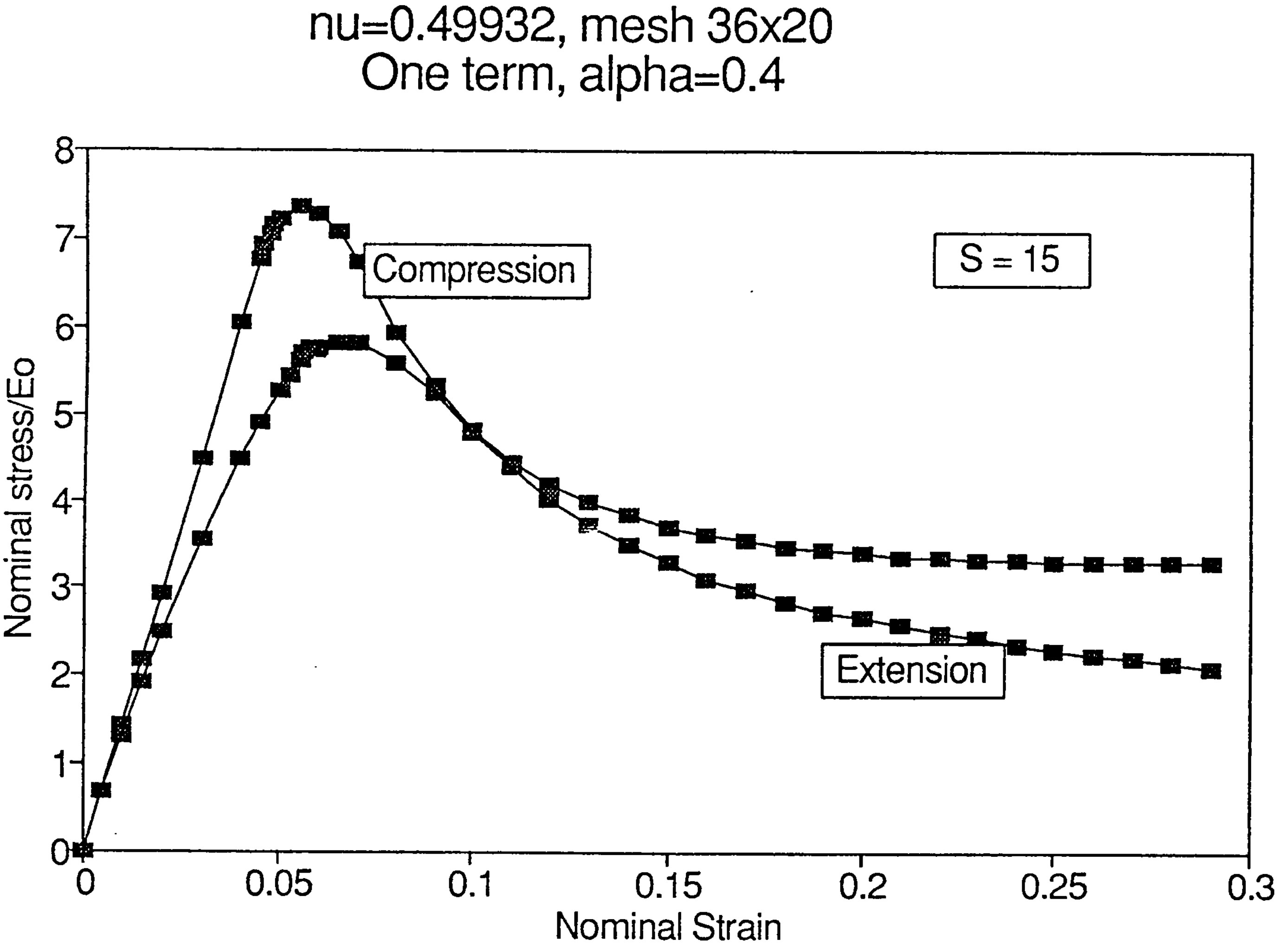

Figure 8.23: Load-deformation relations for a butt joint in extension and in compression.

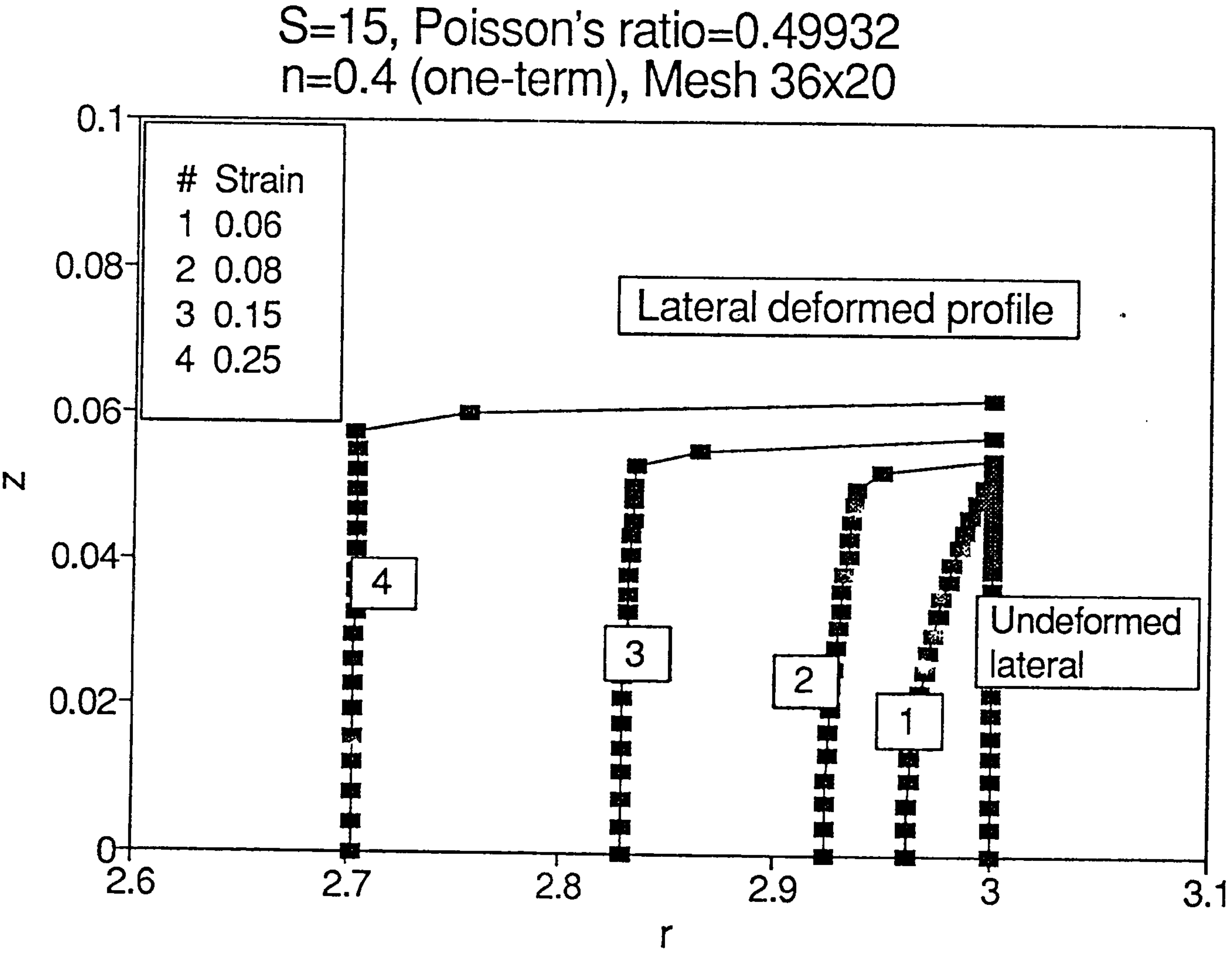

Figure 8.24: Lateral deformed profiles of a butt joint specimen of Poisson's ratio = 0.49932 at different nominal strains.

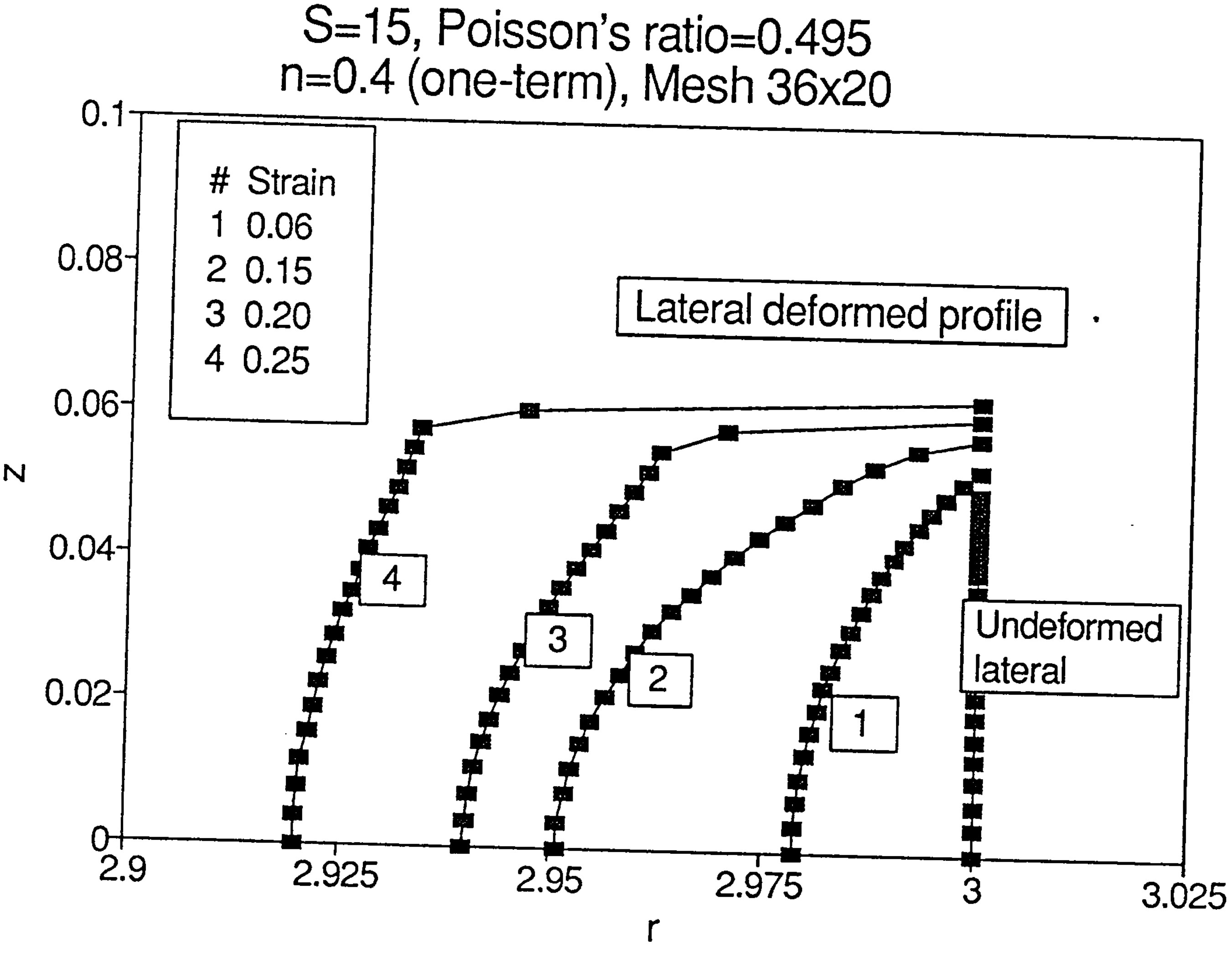

Figure 8.25: Lateral deformed profiles of a butt joint specimen of Poisson's ratio = 0.495 at different nominal strains.

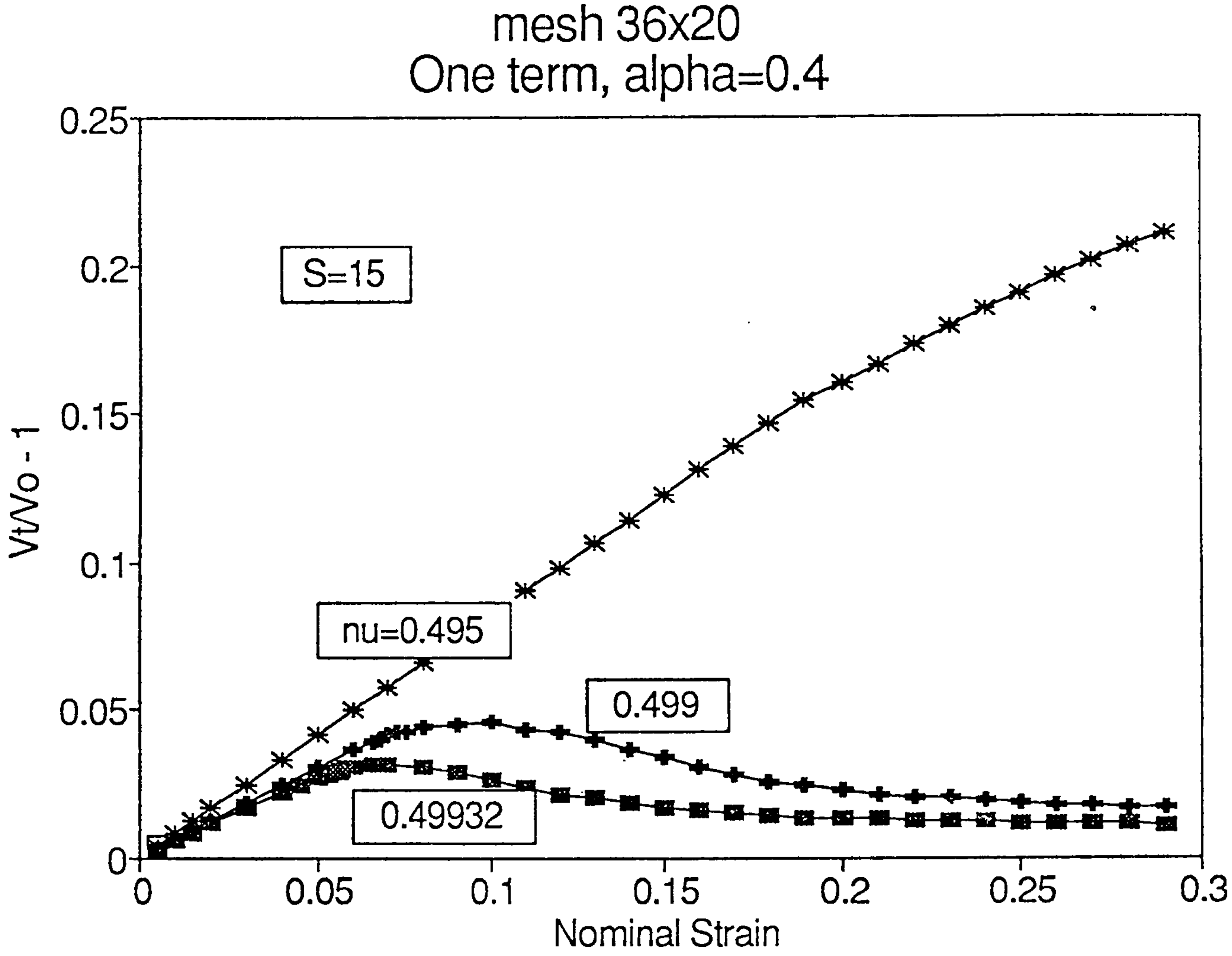

W.V.Chang

Figure 8.26: Volume dilation of nominal strain relationships of butt joint specimens of different Poisson's ratio values.

REFERENCES

1. G. H. Lindsey, R. A. Schapery, M. L. Williams, and A. R. Zak, *GALCIT Report SM 63-6* (Caltech 1963).
2. G. H. Lindsey, *Journal of Applied Physics* **38** 4843 (1967).
3. F. L. Yerzley, *Industrial Engineering Chemistry* **31** 950 (1939).
4. A. N. Gent and P.B. Lindley, *Proceedings of the Royal Society of London* Series A, **249**, 195 (1958).
5. C. Mack, *Industrial and Engineering Chemistry* **49**, 422 (1957).
6. A. N. Gent, *Rubber Chemical Technology* **63**, G50 (1990).
7. B. Wijayarathna and W. V. Chang, "Cavitation in Filled Elastomers and Bonded Rubber Disks", Proceedings 1979 U.S. - Japan Society of Rheology Joint Meeting, Hawaii, April 1979.
8. B. Wijayarathna, Ph.D. thesis, Chemical Engineering Department, University of Southern California, 1979.
9. W. V. Chang, B. Wijayarathna, and R. Salovey, *Advances in Chemistry Series* **206** 233 (1984).
10. W. V. Chang, *Acoustic Emission in Bonded Rubber Disks*, (Annual report to Hydril Co., Los Angeles, December 1979).
11. W. V. Chang, "Detection of Cavitation in Bonded Rubber Disks", Proceedings IUPAC 28th Macromol Symposium, p. 545, 1982.
12. P. Kakavas and W. V. Chang, "Detection and Spectrum Analysis of Microcavitation in Bonded Elastomer Disc" (129th Rubber Division Meeting, ACS, New York, 1986).
13. P. A. Kakavas, Ph.D. thesis, Chemical Engineering Department, University of Southern California, 1987.
14. W. V. Chang, "The Application of Acoustic Emission to Study Asphalt Cohesive and Adhesive Strength," (Position paper, SHRP Rheology Meeting, State College, Pennsylvania, May 7-9, 1990).
15. W. V. Chang, "The Application of Acoustic Emission to Study Asphalt Cohesive and Adhesive Strength," (Final Report, SHRP Project A-002B, Part 3, 1991).

16. W. V. Chang, X. Qin, and W. Ma, " Thin Film Mechanical Properties of Polymer-modified Asphalts," (Best poster paper) 139th ACS Rubber Division Meeting, Toronto, Ontario, Canada, May 21, 1991; submitted to *Rubber Chemistry Technology.*

17. W. V. Chang, H. Wang, and J. Tsai, "Acoustic Emission in Thin Film of Polymer-Modified Asphalt," (Poster paper, 139th ACS Rubber Division Meeting, Toronto, Ontario, Canada, May 21, 1991).

18. G. Pickett, *Journal of Applied Mechanics* **11**, pA-176 (1944).

19. G. J. Dienes and H. F. Klemm, *Journal Applied Physics* **17**, 458 (1946).

20. Y. Kobatake and Y. Inoue, *Applied Science Research*, **A7** 53 (1958); ibid **A7**, 100 (1958).

21. A. N. Gent and P. B. Lindley, *Journal of the British Rubber Producers' Association* **173**, 111 (1959).

22. A. M. Messner, "Stress Distributions in poker chip Tensile Specimens," (Bulletin of Working Group on Mechanical Behavior, CPIA Publ. No. 27, p109 1963).

23. K. T. Sundara Raja Iyengar and R. S. Alwar, *ZAMM* **43**, 17 (1963).

24. J. P. Benthem, *Quarterly Journal of Mechanics and Applied Mathematics* **16**, 413 (1963).

25. P. B. Lindley, *Journal of Strain Analysis* **3**, 142 (1963).

26. A. N. Gent and E. A. Meinecke, *Polymer Engineering and Science* **10**, 48 (1970).

27. B. P. Holownia, *Journal of Stain Analysis* **6**, 121 (1971).

28. S. R. Moghe and H. F. Neff, *Journal of Applied Mechanics* **38**, 393 (1971).

29. B. P. Holownia, *Journal of Strain Analysis*, **7**, 236 (1972).

30. A. N. Gent, R. L. Henry and M. L. Roxbury, *J. Appl. Mech.* **41**, 855 (1974).

31. T. Sawa, K. Temma, and Y. Tsunoda, *International Journal of Adhesion and Adhesives* **9**, 161 (1989).

32. W. W. Klingbeil and R. T. Shield, *ZAMP* **17**, 281 (1966).

33. S. Y. Dymnikov, *Soviet Applied Mechanics* **24**, 912 (1989).

34. Y. Obata, Ph.D. thesis, School of Engineering, Kyoto University, Japan 1974.

35. P. J. Blatz, S. C. Sharda, and N.W. Tschoegl, *Transactions of the Society of Rheology* **18**, 145 (1973).

36. S. C. Sharda, P.J. Blatz, and N.W. Tschoegl, *Letters to Applied Engineering Science* **2**, 53 (1974).

37. R. W. Ogden, *Non-linear Elastic Deformation*, Ellis Horwood Limited, New York (1984).

38. W. V. Chang, R. Bloch, and N. W. Tschoegl, *Proceedings of the National Academy of Science, USA*, **73**, 981 (1976).

39. W. V. Chang, R. Bloch, and N. W. Tschoegl, *Rheological Acta.* **15**, 367 (1976).

40. W. V. Chang, R. Bloch, and N. W. Tschoegl, *Journal of Polymer Science, Polymer Physics Edition*, **15**, 923 (1977).

41. W. V. Chang, R. Bloch, and N. W. Tschoegl, *Macromolecules*, **9**, 917 (1976).

42. R. Bloch, W. V. Chang, and N. W. Tschoegl, *Journal of Rheology*, **22**, 1 (1978).

43. K. J. Bathe, *Finite Element Procedures in Engineering Analysis*, Prentice-Hall, Englewood Cliffs, New Jersey (1982).

44. *AFEM–Manual*, FEM Engineering, Inglewood, California, (1989).

45. W. V. Chang and S. H. Peng, "Design of Nonlinear Elastomer Mountings" (to be submitted to *Rubber Chemistry and Technology*).

46. Y. C. Fung, *Foundations of Solid Mechanics*, Prentice-Hall, Engelwood Cliffs, New Jersey (1965).

Chapter 9

Nonlinear Elastic Analysis of Adhesive Blister Test

9.1 Introduction

The increasing use of blister testing in the adhesive strength measurements makes the blister test a standard method of testing adhesive bonds. For a review of the blister test analysis, see Liechti's paper.[1] For more recent applications, check references.[2–5]

All the previous work seems restricted to linear conditions. The analysis results can only be used for small deflection cases. Some results are even restricted to very thin specimens because the linear plate theory is used.[6] The linear analysis cannot provide adequate information to guide the blister test experiment on such nonlinear materials, as elastomers. The deflection involved in such an experiment can be quite large, especially for thin blister specimens. The nonlinearity may be significant, depending on the material used and the adhesive strength of the system.

This chapter develops a nonlinear numerical procedure to analyze the blister test based on the linear method used by Bennett et al.[7] This method is a numerical procedure for performing an energy balance analysis. Our analysis is formulated based on the total Lagrangian description.

This chapter considers the pressurized penny-shaped specimen proposed by Williams.[8] For convenience of discussion, here is a brief description taken from Anderson et al.[9] A blister test in the simplest form consists of a disk or plate that has been bonded to a rigid material, except for a central portion of radius a. When the unbonded region (Figure 9.1) is pressurized, as by the injection of compressed fluid, the plate lifts off the substrate and forms a "blister" whose radius stays fixed until a critical pressure, p_{cr}, is reached. At this value, the radius of the blister increases in size, signifying an adhesive failure along the interface.

For complicated cases, the substrate may not be a rigid plate comparing to the blister specimen,[1,10] and the adhesive layer on the interface may need to be considered.6, 11. Also, the loading may not be of uniform pressure, etc.

The aim of numerical analysis of a blister test is to obtain the relation between the specific adhesive fracture energy γ_a and the critical pressure p_{cr}. Depending on the linear condition, one can find[9]

$$\gamma_a = k\frac{p_{cr}^2}{E}, \tag{9.1}$$

where E is Young's modulus and k depends on the geometry of the test piece but is independent of the pressure. From plate theory, the energy balance yields a linear solution,[8]

$$k = \frac{32a}{3(1-\nu^2)}\left(\frac{h}{a}\right)^3, \tag{9.2}$$

where h and a are the thickness and the unbonded radius of the specimen, respectively (Figure 9.1), and ν is Poisson's ratio.

For the case of an infinite linear isotropic, incompressible continuum bonded to a rigid substrate with a small penny-shaped debond,[9]

$$k = \frac{3a}{2\pi}. \tag{9.3}$$

For the nonlinear case, k is generally not a constant, it is a function of deformation and needs to be estimated numerically.

In finite element analysis, the loading is usually assumed to be independent of deformation.[12] This assumption present no problem with linear analysis, but would introduce gross errors in nonlinear blister analysis. The blister specimen is generally subjected to pressure loading (a few cases are subjected to concentrated load.[8,13] The pressure is converted to the equivalent node forces in finite element treatment. This conversion depends on the normal direction and the area of the surface that is pressurized. Both the normal direction and the area of the surface change during the deformation. In our program, the equivalent node forces are recalculated from pressure, based on the new direction and new area after each numerical iteration.

9.2 Nonlinear Analysis Procedures

In the blister test, the elastic strain energy stored in the disk can be determined from input work. In linear conditions, the elastic strain energy U can be expressed as[9]

$$U = \frac{1}{2}pV = \pi p\int_0^a w(r)r\,dr, \tag{9.4}$$

where p is the pressure applied, a is the debonded radius, $w(r)$ is the vertical displacement as a function of radius r (Figure 9.1), and V is the volume of the blister.

For the nonlinear cases, the dependence of vertical displacement w on pressure p is a complex function. At the current time, t, the total work input can be determined from the following equation

$$W(a,t) = \int_0^t p(u)\frac{\partial V(a,u)}{\partial u}du = 2\pi \int_0^a \left(\int_0^t p(u)\frac{\partial w(r,u)}{\partial u}du \right) rdr, \tag{9.5}$$

where the volume of the blister $V(a,t)$ is defined by

$$V(a,t) = 2\pi \int_0^a w(r,t)rdr. \tag{9.6}$$

If the material is elastic and fracture does not occur, the total work input is equal to the total elastic energy stored in the material. Therefore, the equation 9.5 allows us to calculate $U(a,t)$, the total elastic strain energy stored.

Suppose that at time t, the pressure load reaches the critical value, p_{cr}, and debonding starts to propagate. The unbonded radius a changes to $a + \delta a$. By utilizing the energy balance and neglecting the energy dissipation, we can set the criterion of crack instability as

$$\delta W - \delta U \geq \gamma_a \delta A, \tag{9.7}$$

where $\delta A = \pi(a+\delta a)^2 - \pi a^2$ is an assumed small increment in crack area; δW and δU are the work done by the pressure and the strain energy change of the system during the crack propagation, respectively. In its mathematical form, δU is

$$\delta U = U(a+\delta a, t) - U(a,t) = W(a+\delta a, t) - W(a,t). \tag{9.8}$$

By assuming that the pressure is constant during the fracture, δW can be evaluated from the increment in blister volume, δV

$$\delta W = p_{cr}\delta V = p_{cr}[V(a+\delta a, t) - V(a,t)]. \tag{9.9}$$

Then the specific adhesive fracture energy can be estimated as

$$\gamma_a = \frac{\delta W}{\delta A} - \frac{\delta U}{\delta A}, \tag{9.10}$$

where the right hand side is defined as the potential energy release rate[9] (or simply the strain energy release rate.[14]

The specific adhesive fracture energy γ_a expressed in equation 9.10 depends on time t, or in other words, is a function of critical pressure p_{cr}. It should be noted that p_{cr} has a unique value for a specific system. The nonlinear analysis in this chapter gives a relation between γ_a and p_{cr}. Once the critical pressure is measured in the real experiment, then the specific adhesive fracture energy can be determined from the relation.

The nonlinear finite element analysis of a blister test follows the procedures listed below:

1. Create a mesh model of the blister test (as shown in Figure 9.2).
2. Apply pressure uniformly over the surface of the unbond surface, increase it step by step, and calculate the volume and the total strain energy U as a function of pressure by equations 9.5 and 9.6.
3. Remove the constraints on additional nodal points along the bottom of the specimen, simulating an increase in the debond radius (a to $a + \delta a$), and then repeat step 2.
4. Calculate the δU by equation 9.8 the δW by equation 9.9, then the γ_a by equation 9.10.
5. Change the analysis parameter, that is, the thickness h of the specimen (the mesh model may need to be changed correspondingly), or the material constants etc. Repeat steps 1 through 4.

Material Model The rubber-like material defined by the Ogden-Tschoegl strain energy function is introduced as our test specimen.[15,16,17,18] The strain energy function can be expressed as

$$W = \sum_{k=1}^{m} \mu_k(\lambda_1^{\alpha_k} + \lambda_2^{\alpha_k} + \lambda_3^{\alpha_k} - 3)/\alpha_k, \tag{9.11}$$

where λ_j defines the principal values of the stretch tensor.

The finite element formulation for such a material is based on the total Lagrangian procedure.[15,19] The above strain energy function is modified with another bulk term by assuming near incompressibility:[19]

$$W = \sum_{k=1}^{m} \mu_k[(\lambda_1^{\alpha_k} + \lambda_2^{\alpha_k} + \lambda_3^{\alpha_k} - 3)/\alpha_k - \ln J] + \lambda(9\ln J + J^{-9} - 1)/81 \tag{9.12}$$

where λ is Lame's constant and J is the ratio of the deformed volume over the original one. Both one-term and three-term functions are used. Without additional specification, the model we used is the three-term model with the following material constants:[18]

$$\begin{array}{rcllll} \mu_{1,2,3} & = & 89.60, & 0.1806, & -1.424 & \text{(psi)}; \\ \alpha_{1,2,3} & = & 1.3, & 5.0, & -2.0; & \\ K & = & 44092.4 & \text{(psi)}, & & \end{array}$$

where K is the bulk modulus that has nearly the same value as Lame's constant λ for nearly incompressible materials.[19]

In case of infinitesimal strains, the material defined above can be treated as linear elastic with the following constants

$$E = 180.21 \text{ (psi)}, \quad \nu = .49932.$$

9.3 Results and Discussion

9.3.1 On the Finite Element Analysis

In our analysis, the mesh model (Figure 9.2) consists of two parts; the unbonded part and the bonded part for the convenience of adjusting the mesh size near the crack tip. We use a nine-node, axisymmetric, isoparametric element. The plate radius R equals 3.0 in., the unbond radius a is 0.4 in. which remains unchanged, and the thickness h is taken as a variable. The analysis is nonlinear, both kinematically and materially. The loading is deformation-dependent.

During the analysis, we usually need 50 to 120 load (pressure) intervals to reach final configuration before the elements near the crack tip are severely distorted and the convergence is difficult to reach. One example of deformed shape of a final state is illustrated in Figure 9.2. At least one of the local principal stretches near the crack tip is very large, say, 3 to 4.

To get accurate results, the effects of the mesh size should be taken into account. Generally speaking, finer mesh has better results but is more expensive in computation. The numerical results depend not only on the total number of elements in a mesh model, but also on the arrangements of these elements. The arrangement here means the non-uniform mesh sizes for different locations. Some other modeling factors will also have effects on numerical analysis of a blister test, for example, the ratio $\delta a/a$. We have checked the effects of such factors. The deviation of our results caused by mesh modeling factors is within 1% for the low pressure part. For the higher pressure part, the deviation may be as high as 2.5%. The deviation estimation here is obtained from a comparison between different arrangements. Take the mesh size factor as an example. We analyze one FEM model first, double the element number, and calculate again. If the difference between the results is within 1% for the low pressure part, we then consider the other factors. If some arrangements are changed due to the requirements of the other factors, the effect of mesh size will be checked again. Sometimes, this process will need to be repeated several times to obtain the final results.

9.3.2 On the Dimensionless Representation $p_{cr}^2 a/E\gamma_a$

The dimensionless representation $p_{cr}^2 a/E\gamma_a$ is usually used in the blister test. This parameter depends on the geometry of a blister test under the linear conditions. Table 9.1 is a comparison of our results with the results from other papers. In consideration of that, only the linear results are available from the previous work; the results of this nonlinear analysis listed in Table 9.1 are calculated for very low pressure to avoid the nonlinearity. The result in the first column of Table 9.1 is obtained from linear finite element calculation by Bennett et al.[7] Their results obtained from standard mesh and fine mesh differ by as much as 10%. Farris and Keer[10] constructed a linear model to analyze the energy release rate of a blister test. Their analysis included the stress singularities at the crack tips. Their numerical results by assuming a rigid substrate are listed in column 2 of Table 9.1. Both Bennett and Farris use as their specimen material ($E = 500$ psi, $\nu = 0.499$) the Solithane 113 adhesive, whose Poisson's ratio is near ours ($\nu = 0.49932$). This means that the comparability between their results and ours is adequate. For this analysis, no results for finer mesh are listed because we checked different mesh sizes, and the best and most reasonable results are picked. Our results are a little larger than Bennett's and Farris's. The experimental data shown in Figure 9.6 in Bennett et al. are a little larger than Benett's results obtained from linear finite element calculation, but no digital experimental data are provided.

To obtain the specific adhesive fracture energy γ_a by equation 9.10, the new fracture surface area δA should, theoretically be infinitely small. This requirement cannot be satisfied in numerical analysis unless other methods are used (e.g., the extrapolation based on results calculated from a variety of δa values). For this reason, we calculated the results for different values of a and δa that are listed in Table 9.2. We suggest that it is better to replace a in the dimensionless parameter $p_{cr}^2 a/E\gamma_a$ with $\bar{a}$ for the numerical analysis. The advantage of doing so is that the results are more consistent when $\bar{a}$ is used ($\bar{a}$ is an average of a and $a + \delta a$). The geometric average has proved more adequate than the arithmetic average. This may be due to the geometric average $\bar{a}$ being the radius that divides the new fracture area into two equal parts, and the area is the basis of this analysis. Then the formula for $\bar{a}$ is

$$\bar{a} = \sqrt{\frac{1}{2}\,[a^2 + (\delta a + a)^2]}, \tag{9.13}$$

where the higher-order term containing $(\delta a)^2$ cannot always be neglected to provide a sense of accuracy.

9.3.3 On the Nonlinear Results

The specific adhesive fracture energy γ_a and the dimensionless representation $p_{cr}^2 a/E\gamma_a$ as a function of the critical pressure p_{cr} are obtained for various values of h/a (see Figures 9.3 and 9.4). The lines labeled ∞ in Figure 9.4 are not nonlinear results. These lines are defined by equation 9.3 and are plotted only as a reference. For higher h/a values, the dimensionless representation $p_{cr}^2 \bar{a}/E\gamma_a$ is almost constant when the critical pressure is small. For very small h/a values, $p_{cr}^2 \bar{a}/E\gamma_a$ changes drastically and shows significant nonlinearity. Note that under a linear condition, $p_{cr}^2 a/E\gamma_a$ is a pressure-independent constant.

Clapeyron's theorem states that for a linear elastic body, the strain energy stored is equal to one-half of the work input done by the external forces of the equilibrium state.[20] Based on this theorem, on can easily obtain the following relation for linear analysis of a blister test:

$$\delta W = 2\delta U. \tag{9.14}$$

The combination of equations 9.10 and 9.14 gives

$$\gamma_a = \frac{\delta U}{\delta A}, \tag{9.15}$$

where $\delta U/\delta A$ is defined as strain energy release rate.[9] This relation is used to calculate the adhesive fracture energy under linear conditions. But for nonlinear analysis, equations 9.14 and 9.15 are not valid, and equation 9.10 should be used to calculate γ_a, as does this chapter. The ratio of the adhesive fracture energy γ_a to the strain energy release rate $\delta U/\delta A$ may be used as a parameter to measure the nonlinearity. This ratio is a unity constant only under linear conditions. From equation 9.10, the ratio can also be expressed as the ratio of the difference between the work input and the strain energy stored to the latter during the debonding process

$$\gamma_a \Big/ (\frac{\delta U}{\delta A}) = \frac{\delta W - \delta U}{\delta U}. \tag{9.16}$$

Figures 9.5 and 9.6 shows that $(\delta W - \delta U)/\delta U$ varies as p_{cr} increases. $(\delta W - \delta U)/\delta U$ is near 1.0 at low pressure, because of no obvious nonlinearity under these conditions. It is interesting to note the relation for small h/a. Take $h/a = 0.05$ as an example. The value of $(\delta W - \delta U)/\delta U$ increases first and then decreases to a value near zero.

It is shown by this analysis that the larger the h/a value, the less significant is the nonlinear effect. This is because, for a certain critical pressure p_{cr}, the deflection involved for a thick geometry is smaller than the deflection for a thinner one. There are many factors that need to be taken into account in choosing the thickness of the blister specimen in the experiment.[9]. If the main purpose is to avoid a large nonlinear effect, the thick plate would be strongly recommended.

The nonlinear analysis is also conducted for rubber-like materials with different material parameters. The material is described by the Ogden-Tschoegl one-term model, that is,

$$W(\lambda_1, \lambda_2, \lambda_3) = \mu \frac{\lambda_1^\alpha + \lambda_2^\alpha + \lambda_3^\alpha}{\alpha}. \tag{9.17}$$

Please note that equation 9.17 becomes the neo–Hookean strain energy function when α takes a value of 2. The shear modulus for this material model can be expressed as

$$G = \frac{1}{2}\mu\alpha. \tag{9.18}$$

Three set constants are chosen in this way so that the shear modulus G remains the same

1 $\alpha = 5.0, \quad \mu = 40.64$ (psi);
2 $\alpha = 10.0, \quad \mu = 20.32$ (psi);
3 $\alpha = 0.1, \quad \mu = 20.32$ (psi).

The results are shown in Figures 9.6 through 9.8. Under the low pressure, the deformation is small, and there are no significant differences in the results corresponding to the different material constants. This is because the shear moduli G are the same and because the situation is almost linear. When higher pressure is applied, there are big differences.

The calculated γ_a may also depend on the size of the bonded plate unless the radius of the plate R is sufficiently large. Generally, the smaller the value of h/a and the smaller the deformation, the smaller the radius of the bonded plate needed to satisfy the "infinitely large" assumption. When $h/a = 0.05$ and $a = 0.4$ in., it is shown that plate radius $R = 0.8$ in. is large enough. Even then, there are some small effects of plate size on the volumes calculated; the effect on the specific adhesive fracture energy is even much smaller, because γ_a is calculated based on the volume increment during debond propagation, δV, not on volume V.[9] For this analysis, the dependence of results on radius R is checked, and the R used is proven sufficiently large. In other words, the result of this analysis can be considered as the result for an infinitely large specimen. In the real experiment, the "infinitely large" assumption may not be satisfied. However, with our finite element model it will not pose a serious problem in interpreting the experimental data.

9.4 Conclusion and Recommendation

A nonlinear elastic analysis of the blister test has been conducted with the finite element method. The nine-node axisymmetric, isoparametric element used for this analysis is formulated based on the total Lagrangian procedure for rubber-like material. The program is specially modified to be capable of treating deformation-dependent pressure loading in the blister test. The results show that the nonlinearity is significant in a blister test, especially for thin specimens. This would suggest that the nonlinear analysis should be introduced in the process of standardizing blister specimens for adhesive testing.

While the procedure of nonlinear analysis presented here is applied for blister testing, the same considerations can also be helpful for other adhesive bond analysis. Compared with other methods, numerical analyses, especially the finite element method, has many advantages in adhesive analysis. The significant advantage is that the finite element method can be applied to the nonlinear analysis where large deflection is involved. This is hard to achieve by simplified models. The adhesive fracture energy calculated by the finite element method can be very accurate.[9] The finite element method has its flexibility. This chapter analyzes an axisymmetric problem. The same method can be easily applied to two-dimensional, plain strain analysis of a blister test.[10,11] While a substrate is treated as a rigid plate in this chapter, the relatively soft substrate problem can also be analyzed with the finite element method.

Asphalt is considered a viscoelastic type material, although an appropriate material model is not available at present. A viscoelastic material model, (CBT model) may be adequate for this purpose.[21,22] Once a model is developed to describe the behavior of asphalt material, we can introduce the model into our finite element program, enabling us to conduct a nonlinear blister analysis on asphalt material. Based on the simulation result of the numerical analysis, the adhesive facture energy of an asphalt-aggregate system can be determined from experimentally measured p_{cr} (see Chapter 5).

It is strongly recommended that follow-up work on nonlinear viscoelastic analysis be conducted in conjunction with future work on the blister test.

Table 9.1: A comparison of linear results with results of other analyses.

h/a	$p_{cr}^2 a/E\gamma_a$ Bennett et. al.[7]	$p_{cr}^2 a/E\gamma_a$ Farris and Kerr[10]	$p_{cr}^2 \bar{a}/E\gamma_a$ This Analysis	$p_{cr}^2 a/E\gamma_a$
5.0			2.083	2.038
4.0	1.991	1.993		
3.5			2.044	2.000
2.0	1.675	1.778	1.855	1.816
1.0	1.057	1.186	1.276	1.249
1.0(fine mesh)	1.173			
0.5	0.413	0.485	0.517	0.506

Table 9.2: The results calculated for different values of a and δa

a (in.)	δa (in.)	$\bar{a}$ (in.)	γ_a j/m^2	$p_{cr}^2 a/E\gamma_a$	$p_{cr}^2 \bar{a}/E\gamma_a$
0.3637	0.0197	0.3737	0.4343	2.036	2.091
0.3637	0.0363	0.3823	0.4448	1.986	2.088
0.3834	0.0166	0.3918	0.4571	2.039	2.083

Note: $h/a = 5.0$, $p_{cr} = 0.5$ (psi).

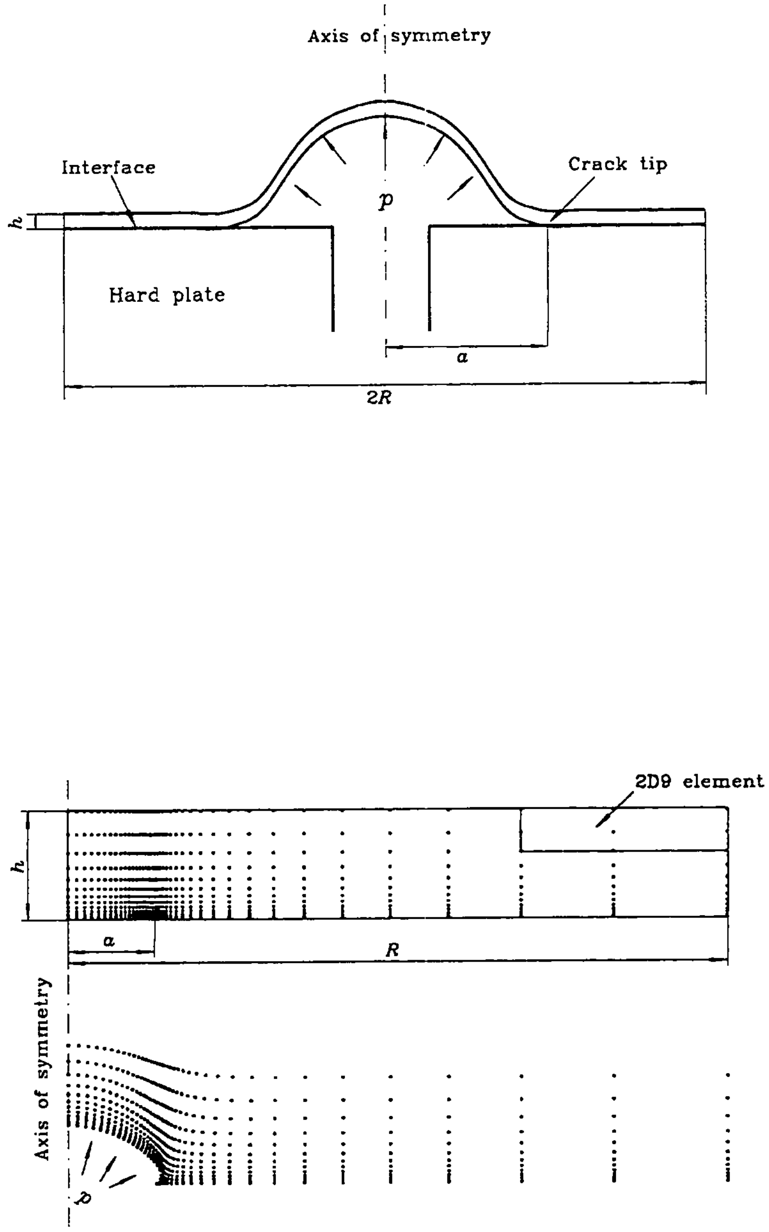

Figure 9.1: Circular specimen for blister test.

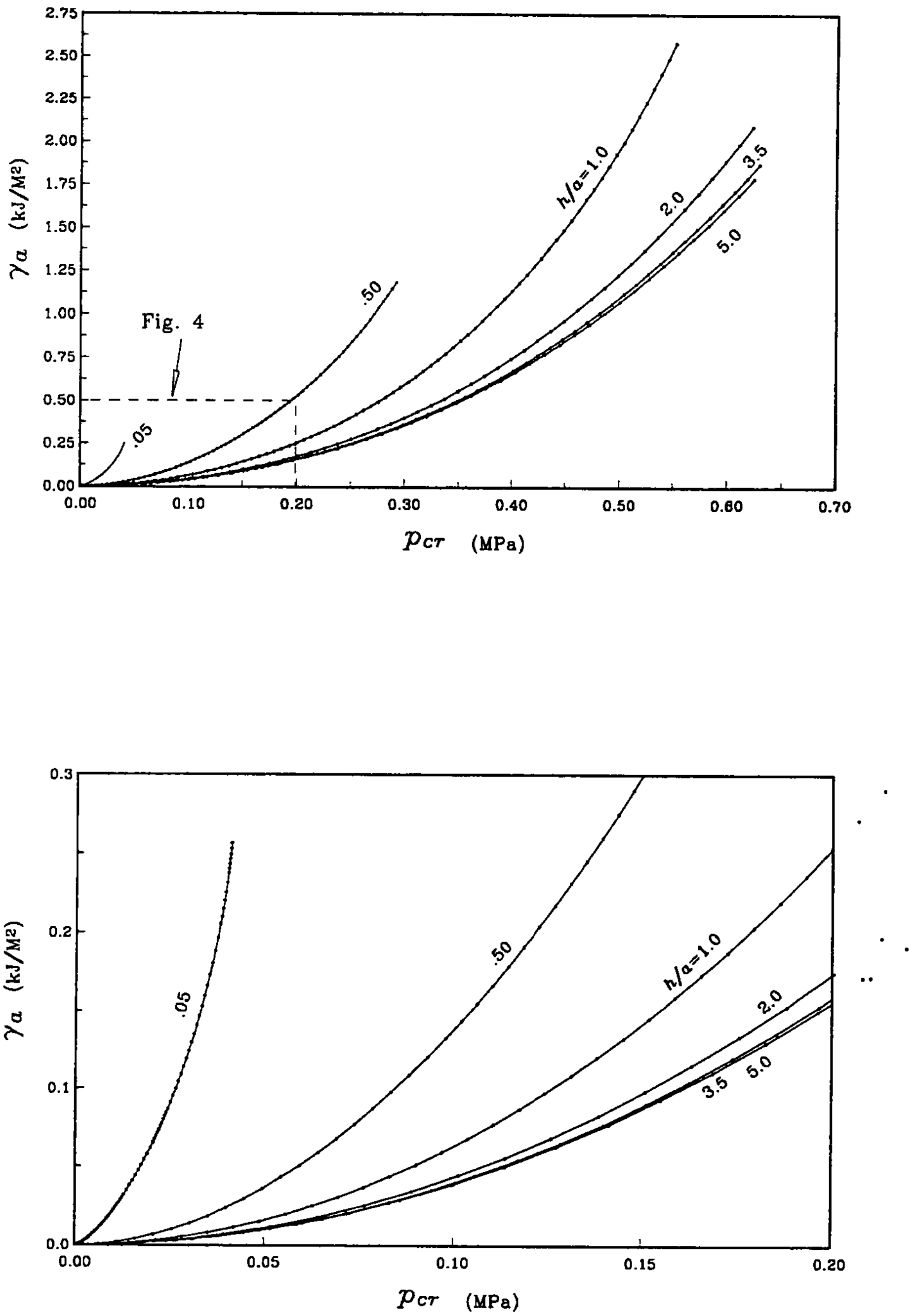

Figure 9.2: Finite element mesh model and deformed shape.

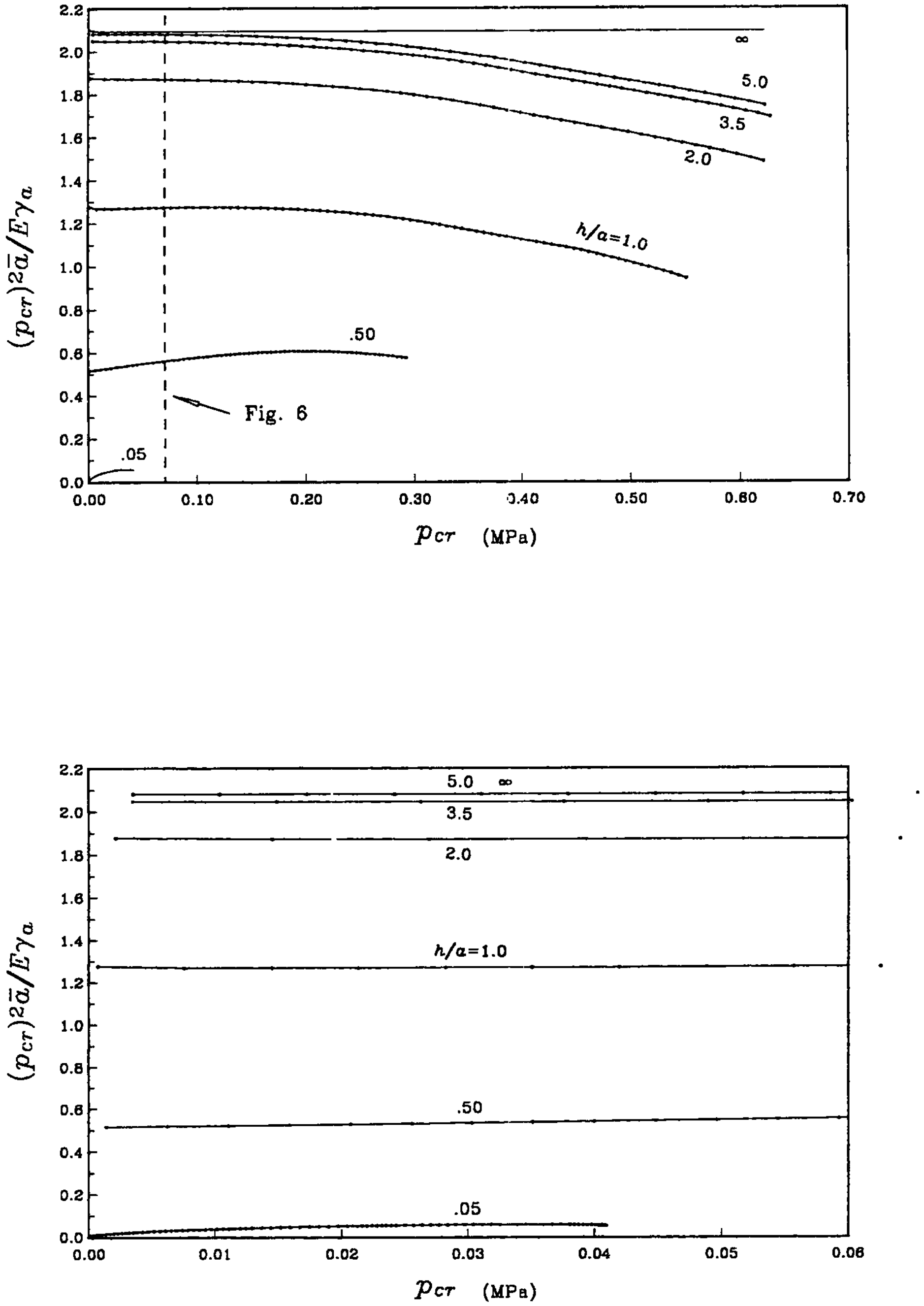

Figure 9.3: The relation between γ_a and p_{cr} for various h/a values.

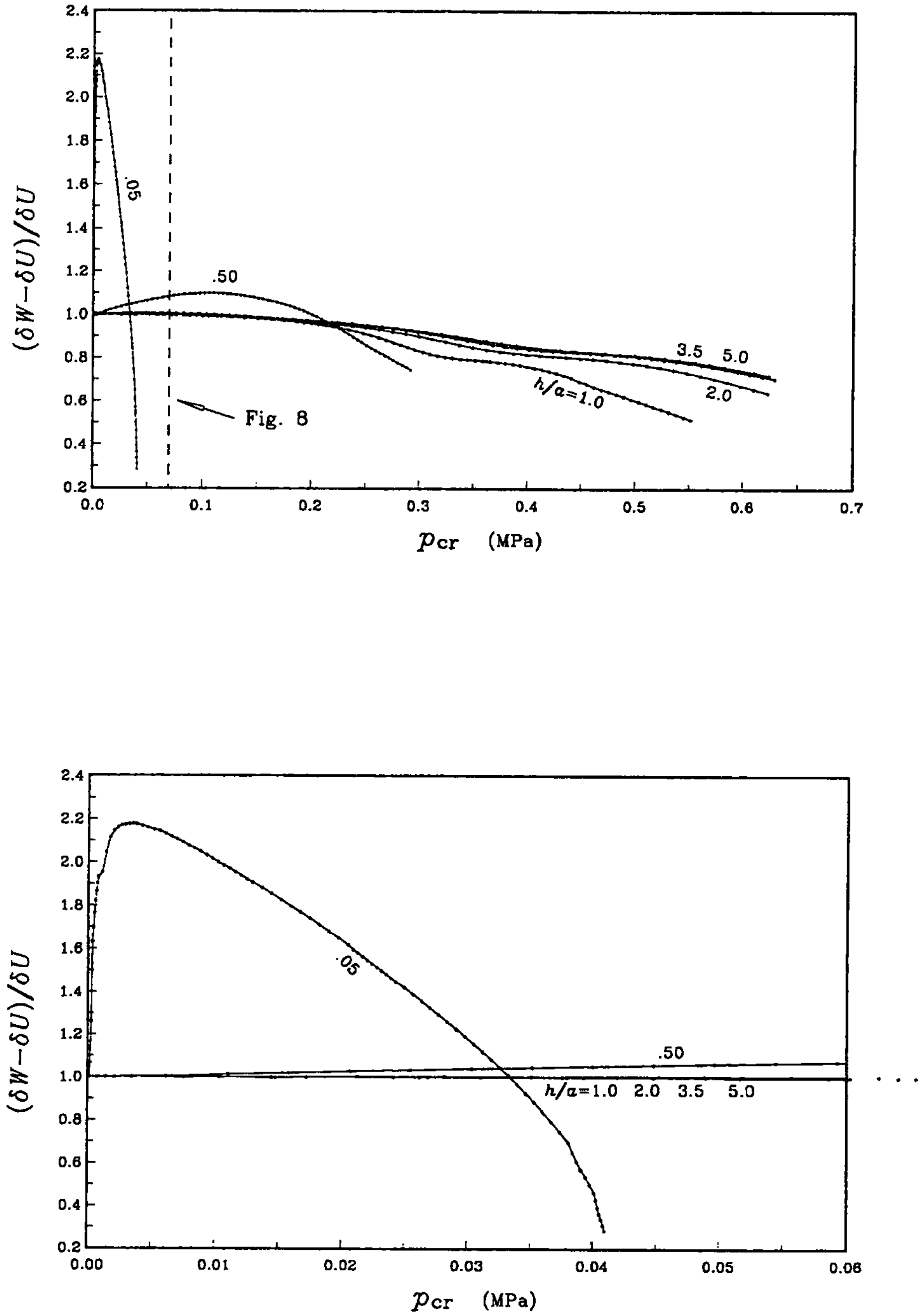

Figure 9.4: $p_{cr}^2\bar{a}/E\gamma_a$ versus p_{cr} for various h/a values.

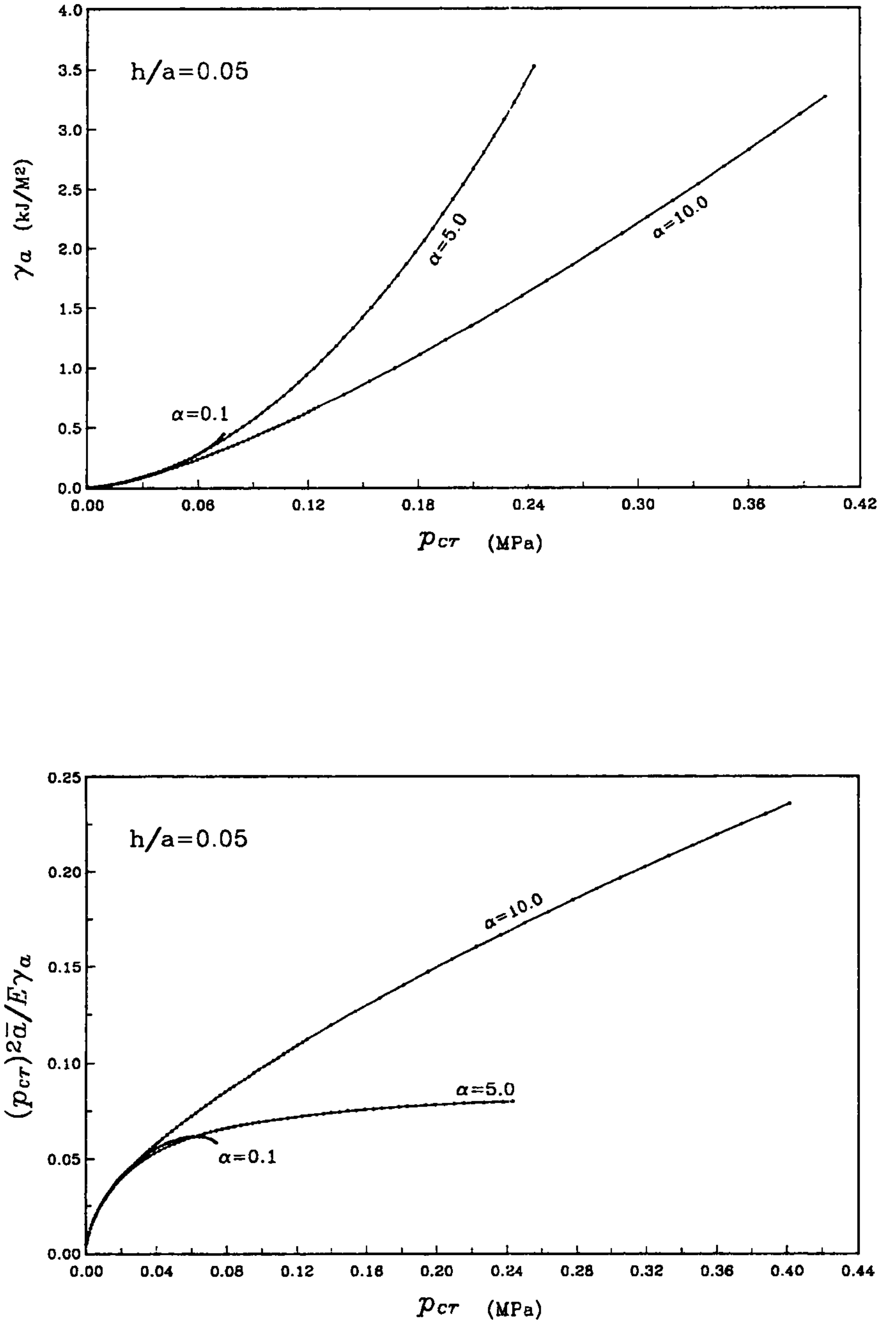

Figure 9.5: $(\delta W - \delta U)/\delta U$ versus p_{cr} for various h/a values.

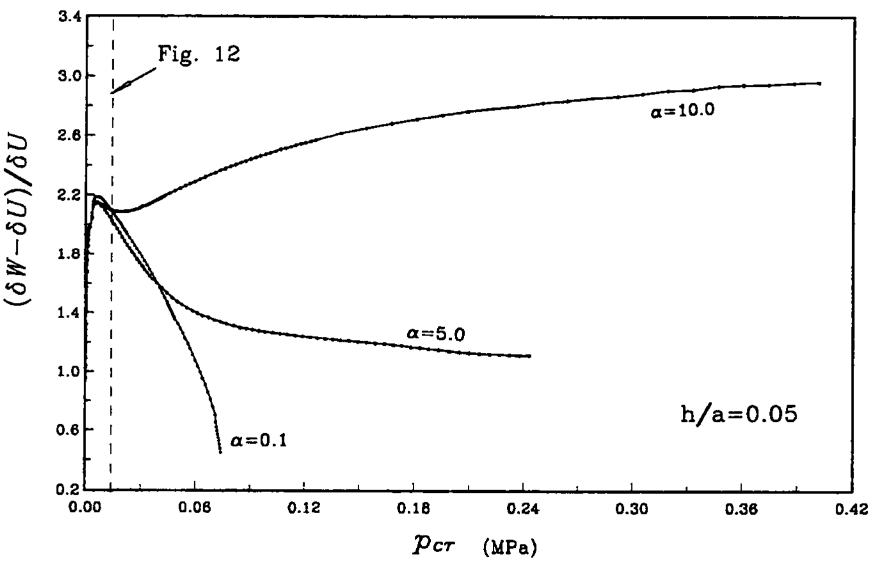

Figure 9.6: γ_a versus p_{cr} for different material constants.

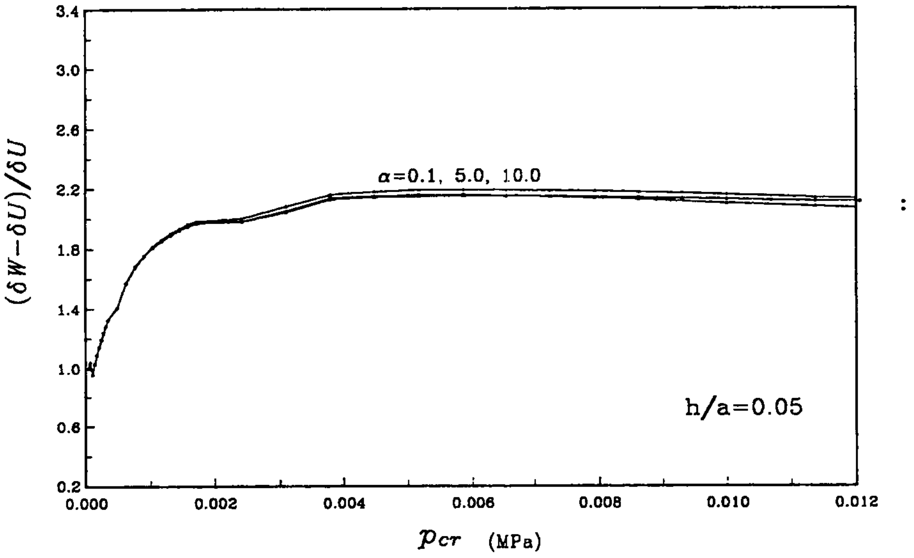

Figure 9.7: $p_{cr}^2 \bar{a}/E\gamma_a$ versus p_{cr} for different material constants.

References

1. K. M. Liechti, *Proceedings of International Congress on Experimental Mechanics*, Society for Experimental Stress Analysis, Westport, CT, June 1984, 815-820.

2. M. J. Napolitano and A. Moet, *ANTEC 89—47th Annual Technical Conference*, Society of Plastics Engineers, New York, NY May (1989), 555-557.

3. X. H. Jin, K. C. Tsay, et al., *Proceedings—The Electrochemical Society* **872** 37-47 (1987).

4. B. W. Cherry and P. B. Evely, *Polymer 85—An International Symposium on Characterization and Analysis of Polymers-Preprints* Royal Australian Chemical Institute, Polymer Division, Parkville, August (1985), 197-198.

5. B. J. Briscoe and S. S. Panesar, *Journal of Physics, D: Applied Physics*, **19**(5) 841-856 (1986).

6. D. P. Updike, *International Journal of Fracture* **12** 815-827 (1976).

7. S. J. Bennett, K. L. Devries, and M. L. Williams, *International Journal of Fracture*, **10** 33-43 (1974).

8. M. L. Williams, *Journal of Applied Polymer Science*, **13** 29-40 (1969).

9. G. P. Anderson, S. J. Bennett and K. L. Devries, *Analysis and Testing of Adhesive Bonds* Academic Press, New York (1977).

10. T. N. Farris and L. M. Keer, *International Journal of Fracture*, **27** 91-103 (1985).

11. M. L. Williams, *Journal of Applied Polymer Science*, **14** 1121–1126 (1970).

12. K. J. Bathe, *Finite Element Procedures in Engineering Analysis*, Prentice-Hall, Englewood Cliff, N.J. (1982).

13. B. M. Malyshev and R. L. Salganik, *International Journal of Fracture Mechanics*, **1** 114-128 (1965).

14. M. F. Kanninen and C. H. Popelar, *Advanced Fracture Mechanics*, Oxford University Press, New York (1985).

15. P. A. Kakavas, Ph.D. thesis, Chemical Engineering Department, University of Southern California, December 1987.

16. P. J. Blatz, S. C. Sharda and N. W. Tschoegl, *Translations of Society of Rheology*, **18** 145 (1973).

17. S. C. Sharda, P. J. Blatz, and N. W. Tschoegl, *Letters to Applied Engineering Science*, **2** 53 (1974).

18. R. W. Ogden, *Non-linear Elastic Deformation*, Ellis Horwood Limited, New York (1984).

19. W. V. Chang and S. H. Peng, *Nonlinear elastic analysis of butt-joint rubber specimen*, submitted to the 138th Rubber Division Meeting, ACS, Washington, D.C., October 9-12 (1990)

20. Y. C. Fung, *Foundations of Solid Mechanics*, Prentice-Hall, Englewood Cliffs, New Jersey (1965).

21. W. V. Chang, R. Bloch and N. W. Tschoegl, *Proceedings of the National Academy Science USA* **73** 981-983 (1976).

22. W. V. Chang, R. Bloch and N. W. Tschoegl, *Rheological Acta*, **15** 367-378 (1976).

Chapter 10

Conclusions and Recommendations

As mentioned before, the objectives of this research were these:

1. To develop novel performance related tests for asphalt binders.
2. To elucidate mechanisms that control the rigidity, cohesive strength, and adhesive strength of geometrically confined asphalt thin films.
3. To develop quantitative AE techniques for microdamage detection and cumulative damage quantification.

All the objectives have been accomplished. Key conclusions and recommendations are given in sections 10.1 and 10.2, respectively.

10.1 Conclusions

1. The working hypothesis of this research is that the properties of asphaltic concretes are strongly dependent on the bulk modulus of the asphalt and the cavitation resistibility in the asphalt phase and the asphalt-aggregate interface. The results of this research strongly support this hypothesis.
2. The utilities of the asphalt thin-film, poker chip test in simulating the stress state and the resulted cumulative damages in asphaltic concretes have been established. The stiffness and the tensile strength as determined from the poker chip test are consistent with those of asphaltic concretes
3. The mechanical properties of asphalt poker chip specimens depend on the LVE properties of the asphalt, the aspect ratio, S, and the thickness of the specimen, as well as the extent of cavitation in the specimen. It is important to point out that the

tensile properties of the asphalt poker chip depend on both thickness and the shape factor. By integrating stress analysis, mechanical tests, and AE tests, we are able to describe the effect of S, thickness, preparation conditions, loading rate, temperature, fatigue, etc., on the properties of the asphalt poker chip specimen in terms of the cavitation model.

4. Cavitation control and mitigation are the key factors to be considered for asphalt selection, asphalt modification, formulation development, process development, pavement preparation and rehabilitation, etc. The upper bounds for the stiffness and the strength of asphalt concretes based on our model are on the order of one million psi and one to ten thousand psi, respectively.

5. AE is a very sensitive and reliable technique for monitoring microdamage and healing processes in a poker chip specimen. AE is a valuable tool in detecting microfracture and has the potential to be an effective tool for quantifying cumulative damage. Fractography studies show that the damage pattern in fracture surfaces agrees well with the AE source identification results.

6. A special poker chip test was developed that we called the thermal mechanical scanning test to evaluate the thermal cracking resistance of AAD, AAG, and AAK asphalts. We found that the rupture temperature for AAG is higher than that for AAK, which is higher than that for AAD. The ranking is consistent with what was observed by T. Vinson of Oregon State University for asphaltic concretes made of the same SHRP asphalts.

7. The results of the thermal mechanical scanning test indicate that the thermal cracking temperature of an asphalt is sensitive to the extent of the cavitation in the material prior to the failure. Hence, it is a function of the loading history of the specimen. Nevertheless, the test provides a simple, efficient, and representative way to evaluate the thermal cracking resistance of asphalt in the pavement environment.

8. The AE-MTS testing system shows promise in monitoring the cumulative damages in asphalt concrete.

9. The AE/modified blister test developed in our laboratory provides a useful method to evaluate the resistance of asphalt-aggregate joints to environmentally-assisted debonding failures. This test, in conjunction with an appropriate stress analysis, will provide fundamental properties governing the adhesive joint strength.

10. LCAG is a simple and cost-effective test for surface characterization of asphalt binders.

10.2 Recommendations

1. The AE/poker chip test is strongly recommended as a part of the specification tests for asphalt binders to fully utilize the fundamental and practical values of the test. This can be accomplished with only a small amount of additional development work.
2. The thermal mechanical test is recommended as a routine test for evaluating the thermal cracking resistance of asphalt binders.
3. The LCAG and AE/blister tests show great potential in providing fundamental adhesion properties, as well as evaluating practical adhesive strength between asphalts and aggregates, especially when these meterials are subjected to adverse environmental conditions. However, more research is needed.

Asphalt Advisory Committee

Thomas D. Moreland, *chairman*
Moreland Altobelli Associates, Inc.

Gale C. Page, *vice chairman*
Florida Department of Transportation

Peter A. Bellin
Niedersachsisches Landesamt
für Strassenbau

Dale Decker
National Asphalt Paving Association

Joseph L. Goodrich
Chevron Research Company

Eric Harm
Illinois Department of Transportation

Charles Hughes
Virginia Highway & Transportation Research Council

Robert G. Jenkins
University of Cincinnati

Anthony J. Kriech
Heritage Group Company

Richard Langlois
Universite Laval

Richard C. Meininger
National Aggregates Association

Nicholas Nahas
EXXON Chemical Co.

Charles F. Potts
APAC, Inc.

Ron Reese
California Department of Transportation

Donald E. Shaw
Georgia-Pacific Corporation

Scott Shuler
The Asphalt Institute

Harold E. Smith
City of Des Moines

Thomas J. Snyder
Marathon Oil Company

Richard H. Sullivan
Minnesota Department of Transportation

A. Haleem Tahir
American Association of State Highway and
Transportation Officials

Jack Telford
Oklahoma Department of Transportation

George West
Shell Oil Company

Liaisons

Avery D. Adcock
United States Air Force

Ted Ferragut
Federal Highway Administration

Donald G. Fohs
Federal Highway Administration

Fredrick D. Hejl
Transportation Research Board

Aston McLaughlin
Federal Aviation Administration

Bill Weseman
Federal Highway Administration

8/16/93

Expert Task Group

Ernest Bastian, Jr.
Federal Highway Administration

Wayne Brule
New York State Department of Transportation

David Esch
Alaska Department of Transportation

Joseph L. Goodrich
Chevron Research Company

Woody Halstead
Consultant, Virginia Highway & Transportation Research Council

Gayle King
Bituminous Materials Company

Robert F. LaForce
Colorado Department of Transportation

Mark Plummer
Marathon Oil Company

Ron Reese
California Department of Transportation

Scott Shuler
The Asphalt Institute